Chemical Science

ROYAL SOCIETY OF CHEMISTRY

REVIEW

View Article Online
View Journal

Cite this: DOI: 10.1039/d6sc01450j

Photocatalysis beyond band gaps and hot carriers: toward a unified view of semiconductor and plasmonic systems

Rishi Verma, * Gunjan Sharma, Rohit Bansal, Charvi Singhvi, Saideep Singh and Vivek Polshettiwar *

Photocatalysis stands at the forefront of efforts to address global challenges in sustainable energy and environmental remediation. In this review, we critically examine the two major classes of heterogeneous photocatalysts-plasmonic materials and semiconductors-highlighting their fundamental distinctions, catalytic mechanisms, and potential for driving light-induced chemical transformations. We first explore the fundamentals of plasmonic materials and semiconductors, highlighting key distinctions and overlaps in their photophysical properties, elucidating how these differences govern their photocatalytic performance and reaction pathways. This review further explores practical examples of photocatalytic reactions, including CO_2 reduction, N_2 reduction, and dry reforming of methane (DRM), illustrating the versatility, catalytic efficiency, and inherent limitations of each class of materials. Additionally, we explore the excited-state dynamics of both plasmonic and semiconductor materials, with a focus on the underlying mechanisms that govern charge carrier behavior under light excitation. This review provides an overview of the present state of plasmonic and semiconductor photocatalysis, while also highlighting promising directions for future advancements. By exploring synergistic strategies that bridge these two classes of materials, it aims to unlock new pathways for light-driven chemical transformations, ultimately advancing catalytic performance for sustainable energy and environmental applications.

Received 19th February 2026
Accepted 2nd May 2026

DOI: 10.1039/d6sc01450j

rsc.li/chemical-science

1. Introduction

Photocatalysis has emerged as a vital tool in addressing some of the most pressing global challenges related to energy and the environment.[1–6] The disproportionate consumption of fossil fuels over the past century has led not only to the depletion of these finite resources but also to a sharp rise in atmospheric CO_2 levels, driving climate change and environmental problems.[1,2] As the world shifts towards more sustainable and cleaner energy sources, one promising approach is the use of solar energy to convert CO_2 into valuable chemicals and fuels through the process of photocatalysis. The ability to harness sunlight-an abundant, renewable, and almost limitless energy source- and convert it into chemical energy, offers an appealing route to mitigate carbon emissions while creating new pathways for green energy production. This process, often referred to as solar fuel production, presents an opportunity to decarbonize industries that are reliant on fossil fuels, while at the same time providing a sustainable alternative to traditional energy systems.[1–6]

Over the past few decades, significant progress has been made in developing materials capable of efficiently absorbing sunlight and driving chemical transformations. However, the challenge of improving catalytic efficiency remains, especially when dealing with complex multi-electron processes like CO_2 reduction or water splitting. The efficiency of a photocatalyst is highly dependent on the material's ability to interact with light, separate charge carriers, and drive specific reactions. Therefore, designing materials with optimal light absorption, charge transfer, and catalytic properties is crucial for the high efficiency of photocatalysts.[1–6]

With the advent of nanotechnology, new opportunities have arisen to engineer photocatalysts that can manipulate light and charge carrier dynamics at the nanoscale. Among the various photocatalytic systems that have been explored, two major categories have stood out: semiconductors,[7–150] and plasmonic photocatalysts.[151–435] These two classes of materials are often studied in isolation and are governed by fundamentally different photophysical principles with direct consequences for catalysis. While other classes, such as molecular photocatalysts, metal complexes, and biological systems like photosystems used in photosynthesis, are also highly relevant, this review focuses on semiconductors and plasmonic materials, as these two classes have emerged as the most extensively studied solid-state platforms for heterogeneous photocatalysis. Semiconductors and plasmonic metals differ not only in how they absorb light but also in how they manage and utilize the

Department of Chemical Sciences, Tata Institute of Fundamental Research, Mumbai, 400005, India. E-mail: rishi.verma@tifr.res.in; vivekpol@tifr.res.in

resulting excited states. Semiconductors rely on band-to-band transitions that generate relatively long-lived electron–hole pairs. Plasmonic materials, in contrast, exploit collective electron oscillations that lead to intense light–matter interactions, ultrafast carrier generation, and localized field effects. These distinct pathways set the stage for fundamentally different catalytic behaviors, motivating a careful side-by-side comparison.

This dichotomy highlights why a direct comparison is timely. A discussion on excitation mechanisms, carrier relaxation dynamics, and catalytic performance across both systems can clarify how their distinct photophysics translate into performance. It also provides design principles for next-generation catalysts that aim to integrate the long carrier lifetimes of semiconductors with the strong light–matter interactions of plasmonic nanostructures.

Semiconductor-based photocatalysts have been a foundation of photocatalytic research since the pioneering work on TiO_2 for water splitting by Fujishima and Honda in 1972.[7] Semiconductors, such as TiO_2, ZnO, CdS, and $BiVO_4$, are known for their ability to absorb photons and generate electron–hole pairs that can subsequently participate in redox reactions at the catalyst surface. Upon photon absorption, an electron is excited from the valence band to the conduction band, leaving behind a hole. These charge carriers (electrons and holes) can migrate to the surface and participate in oxidation and reduction reactions, enabling processes like water splitting and CO_2 reduction. The efficiency of semiconductor photocatalysts is highly dependent on factors such as the band gap, light absorption properties, charge carrier mobility, and the ability to suppress charge carrier recombination.[13,17,137]

Despite their widespread use, semiconductor-based photocatalysts face persistent challenges in harvesting solar energy efficiently. Many, such as TiO_2, are mainly active under ultraviolet (UV) light, which accounts for only ~5% of the solar spectrum.[22] Even when visible-light excitation occurs in certain semiconductors, it often produces less energetic charge carriers, limiting photocatalytic efficiency.[28] Their relatively low absorption coefficients further restrict overall light harvesting.[137] To address these issues, extensive strategies such as doping, defect engineering, and heterojunction formation have been explored to extend absorption into the visible region and enhance electron and hole separation.[44,62] Emerging designs, including 2D semiconductors, quantum dots, and core–shell nanostructures, show promise in improving light absorption and charge dynamics, thereby advancing the potential of semiconductor photocatalysts for scalable applications.[10,11]

On the other hand, plasmonic photocatalysis has attracted significant attention for its ability to harvest visible light through localized surface plasmon resonance (LSPR) in metal nanoparticles such as Au, Ag, Al, and Cu. Plasmonic nanoparticles can generate highly energetic charge carriers and strong local electromagnetic fields, enabling selective and efficient photocatalytic transformations.[151] They have been widely explored for reactions such as CO_2 reduction, water splitting, and nitrogen reduction.[155,186,404] However, plasmonic systems also face challenges, particularly related to the relatively short lifetimes of excited charge carriers (hot electrons) and the difficulty in controlling charge transfer processes.[152,161] Moreover, the scalability of plasmonic materials, given their reliance on precious metals, presents another challenge for widespread commercial use. Despite these hurdles, the unique ability of plasmonic photocatalysts to drive reactions under visible light and their tunable properties make them an exciting area of research with significant potential for future energy applications.

Thus, despite advances in photocatalyst design, both semiconductor and plasmonic systems face intrinsic limitations that hinder large-scale application. A comparative analysis of these two approaches is therefore crucial to highlight their respective strengths, limitations, and opportunities for synergistic innovation. In this review, we present a comprehensive comparison of plasmonic and semiconductor photocatalysts, focusing on their fundamental properties, including excitation mechanism, charge carrier dynamics, and excited-state lifetimes. We examine the distinct mechanisms by which these materials absorb and harness light, highlighting how these differences influence their photocatalytic efficiency and reaction pathways. Additionally, we highlight key photocatalytic applications, including CO_2 reduction, N_2 reduction, and dry reforming of methane (DRM), where both plasmonic and semiconductor photocatalysts have demonstrated their potential. By discussing the strengths and limitations of each system, we aim to identify promising avenues for future research and development, ultimately guiding the design of more efficient and sustainable photocatalytic materials for energy and environmental applications.

2. Fundamental concepts of semiconductor and plasmonic photocatalysts

The interaction of light with photocatalytic materials results in the generation of excited charge carriers, altering the electron density and influencing the material's catalytic properties. When a photon is absorbed, electrons in the material are promoted to higher energy states, which drive chemical reactions. Understanding the behavior of these excited carriers is crucial to optimizing photocatalytic performance. Key electronic properties such as energy levels, density of states, momentum, and the position of the Fermi level play significant roles in determining how efficiently these carriers contribute to reaction processes.

To comprehend these phenomena, it is essential to understand the underlying electronic structure of solids. Detailed mathematical treatments of band structure, density of states, momentum conservation, and the Fermi level are well established in solid-state physics texts and are therefore beyond the scope of this review.[436–439] Here, we provide only a brief introduction to establish a conceptual basis for the discussion that follows. The energy bands in a material dictate the range of energy of electron occupation, with the band gap defining the energy gap between the conduction band and valence band. The

band gap also dictates the photon energy required to generate electron–hole pairs. The Fermi level represents the electrochemical potential of electrons in the material, equivalently, the energy at which the Fermi-Dirac occupation probability equals one-half. In metals, it coincides with the highest occupied electronic state at absolute zero; in semiconductors, it lies within the band gap, and its precise position is determined by the doping level and temperature. Momentum conservation determines the efficiency of optical transitions, while the density of states (DOS) governs the availability of electronic states for excitation.[436–439] Together, these fundamental aspects of electronic structure determine the photophysical responses of semiconductors and plasmonic materials, including both their commonalities and distinctions.

2.1. Electrons in a semiconducting nanomaterial

Semiconductors are the most widely studied class of photocatalysts because their band structures naturally enable light-driven charge separation. When photons with energy greater than or equal to the band gap are absorbed, electrons are excited from the valence band to the conduction band, leaving behind holes (Fig. 1a).[137]

The electron–hole pairs generated through light excitation in semiconductors catalyze a variety of chemical reactions. The entire process, from the moment excitons are generated to when the charges participate in redox chemistry, can be delineated into three distinct stages:

(1) Photoexcitation: this initial stage involves the absorption of light by the semiconductor, resulting in the generation of excitons.

(2) Charge separation and diffusion: following photoexcitation, the excited charges (electron–hole pairs) must be effectively separated and diffused to the catalyst surface. Minimizing electron–hole recombination during this stage is critical to ensure that a greater number of charge carriers reach the surface.

(3) Charge utilization for redox reactions: in the final stage, the separated charges participate in redox reactions at the catalyst surface. To attain high efficiency in these reactions, it is essential to not only maintain a high charge carrier density but also promote stronger surface adsorption and activation on the catalyst, facilitating the efficient coupling of surface charges with targeted reduction or oxidation reactions.

To optimize the charge generation step, researchers are focused on developing catalysts capable of absorbing a broader spectrum of solar energy, thereby maximizing the number of photons converted into electron–hole pairs. However, having a high density of charge carriers on the surface does not guarantee efficient redox reactions. Enhancing the molecular-level catalytic activity and selectivity is essential for effective surface reactions.

The ability of photogenerated electrons and holes to take part in reduction and oxidation is mainly determined by the relative positions of the conduction band minimum (CBM) and the valence band maximum (VBM). For an overall photocatalytic

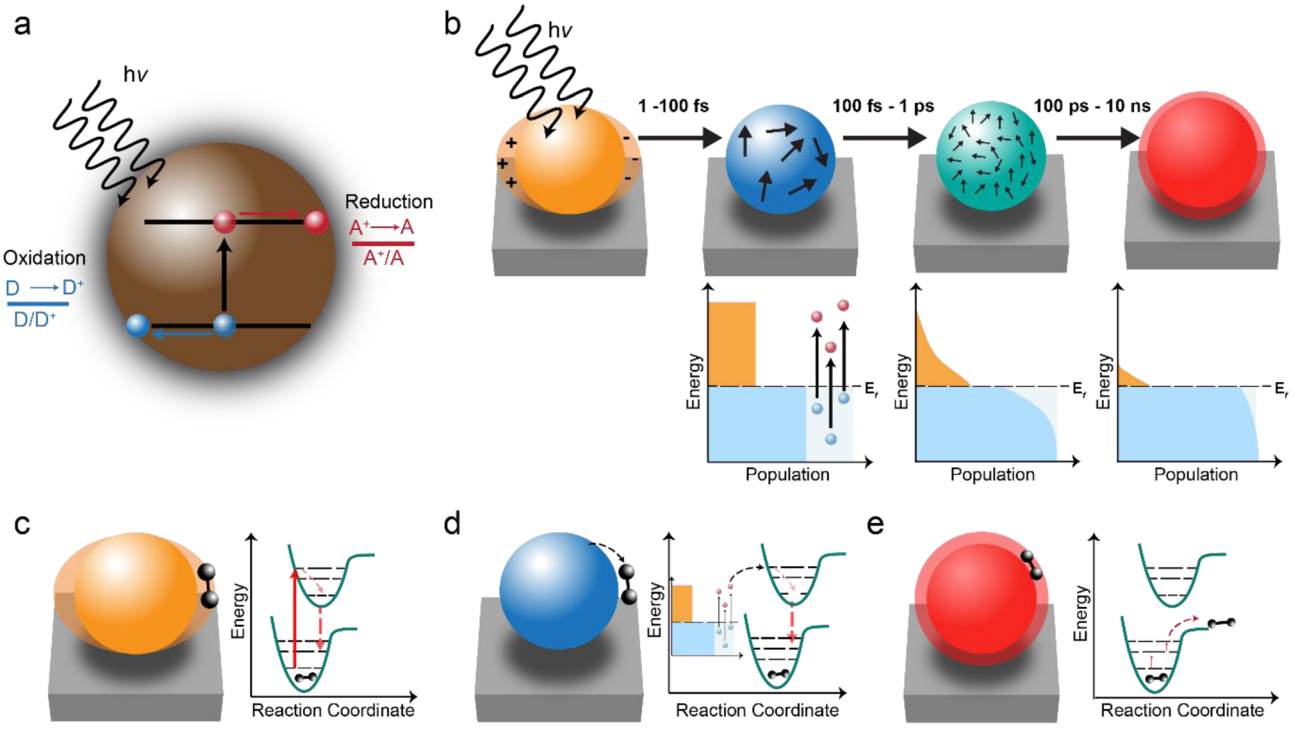

Fig. 1 Light-induced excitation in semiconductors and plasmonic materials. (a) Schematic of the fundamental mechanisms of photocatalytic processes on a pristine semiconductor, (b) schematic of relaxation processes following LSPR, showing typical timescales and the associated changes in electronic structure; schematic of plasmon-mediated effects: (c) near-field enhancement increases molecular excitation, (d) hot-carrier transfer facilitates surface reactions, and (e) localized heating raises vibrational excitation of molecules.

reaction to proceed, the CBM must lie at a higher energy than the reduction potential of the target species, while the VBM must lie at a lower energy than the oxidation potential of the corresponding species (Fig. 1a). If either of the band edges (CBM or VBM) fails to meet this criterion, sacrificial agents must be employed as alternative electron acceptors or donors to facilitate the required half-reaction.[14]

In pristine semiconductor photocatalysts, charge carrier generation, migration, and surface reactions occur on the same material, but each stage faces intrinsic limitations. Wide-band gap semiconductors (*e.g.*, TiO_2) are limited to UV absorption (~5% of the solar spectrum), while narrow-band gap materials (*e.g.*, CdS, Fe_2O_3) harvest visible light but often exhibit weaker redox potentials due to unfavorable band-edge positions.[11] Once generated, electrons and holes frequently recombine during migration because separation lacks a strong driving force. At the surface, slow reaction kinetics and limited catalytic activity further reduce efficiency, while accumulated charges may even degrade the semiconductor.[11,14] One important factor modulating charge dynamics is band bending at semiconductor surfaces and interfaces. Fermi-level equilibration between bulk and surface, or between different crystal facets, induces space charge regions and internal electric fields. These fields can steer electrons and holes toward different reaction sites, partially improving separation.[11] Facet engineering, ferroelectric polarization, dipole fields, and junction formation (metal–semiconductor or semiconductor–semiconductor) provide additional routes to enhance charge carrier separation. A more comprehensive discussion of these interfacial effects and their role in modulating charge dynamics can be found in a previous review.[11]

2.2. Electrons in a plasmonic nanomaterial

Plasmonic nanostructures exhibit unique optical properties and catalytically active surfaces, making them highly promising for solar photochemistry. At the heart of these materials is LSPR, a phenomenon observed in metallic nanomaterials such as Au, Ag, Al, Cu, *etc.* LSPR arises from the coherent oscillation of conduction electrons in response to electromagnetic fields, a process that enhances light–matter interactions.[151,152]

The LSPR arises when light interacts with metal nanoparticles smaller than the incident wavelength, inducing collective oscillations of surface electrons. The decay of these oscillations generates energetic hot carriers and heat on ultrafast timescales (Fig. 1b).[151,152] The optical response of plasmonic nanoparticles can be tuned by their size and shape, enabling efficient sunlight absorption and energy conversion. Hot electrons generated during LSPR dephasing can either transiently activate adsorbed molecules on the metal surface without permanent transfer or undergo plasmon-mediated electron transfer (PMET) to nearby semiconductors or molecules, driving reactions such as water splitting, CO_2 reduction, and organic transformations.[152,155] The relaxation of hot carriers occurs through electron–electron and electron–phonon scattering, leading to heat dissipation, which can also catalyze reactions on metal surfaces. In addition, LSPR creates intense near-field enhancements at particle edges or junctions, amplifying light absorption and scattering to boost catalytic efficiency.[152] Understanding these ultrafast carrier dynamics and their coupling with reactants is crucial for designing efficient plasmonic photocatalysts.[151,157,170]

2.3. Optical cross-sections of plasmonic nanomaterials

When metal nanoparticles are much smaller than the wavelength of light, their interaction with electromagnetic waves can be effectively described using the quasi-static approximation. This assumes that the electric field remains nearly uniform across the particle, allowing us to treat the problem electrostatically. A key result from this model is that the polarizability of a nanoparticle is maximized when the dielectric response of the particle resonates with the surrounding medium, a situation that gives rise to the LSPR. This resonant behavior of LSPR leads to strong light–matter interactions. It manifests as intense absorption and scattering peaks in the optical spectrum of the nanoparticles.[436–439]

The strength of these interactions is quantified through the absorption and scattering cross-sections, which depend on the polarizability. The scattering cross-section increases with the sixth power of the particle radius, while the absorption scales with the third power, making absorption dominant for smaller particles.[436–439] These relationships are given by:

$$C_{\mathrm{sca}} = \frac{k^4}{6\pi}|\alpha|^2 = \frac{8\pi}{3}k^4a^6\left|\frac{\varepsilon-\varepsilon_{\mathrm{m}}}{\varepsilon+2\varepsilon_{\mathrm{m}}}\right|^2 \quad (1)$$

$$C_{\mathrm{abs}} = k\mathrm{Im}[\alpha] = 4\pi ka^3\mathrm{Im}\left|\frac{\varepsilon-\varepsilon_{\mathrm{m}}}{\varepsilon+2\varepsilon_{\mathrm{m}}}\right| \quad (2)$$

Here, k is the wavevector of the incident light, α is the polarizability of the nanoparticle, a is the radius of the spherical nanoparticle, ε is the complex dielectric function of the nanoparticle, and ε_{m} is the dielectric constant of the surrounding medium. These expressions not only describe metal nanoparticles but also apply to dielectric spheres, although the resonant enhancement is most pronounced in metals due to their free electrons. While this dipole model works well for nanoparticles below ~100 nm, for larger particles where light's phase varies significantly across the structure, the full electrodynamic treatment known as Mie theory is required.[436–439]

2.4. Plasmon lifetime and decay of LSPR

The decay of plasmon excitations is a dynamic process that unfolds over multiple time domains, each governed by different physical mechanisms (Fig. 1b). In LSPR, a coherent many-body state of oscillating conduction electrons forms within the nanoparticle, effectively storing energy. This energy is then released in stages. In the first few femtoseconds (fs), coherence is lost through dephasing, which initiates the generation of non-thermal electrons and holes *via* Landau damping. These excited carriers may then relax by emitting photons (radiative decay) or through electron–electron collisions (non-radiative decay). This is particularly significant in plasmonic systems, where such decay pathways yield hot carriers that can drive

chemical reactions. Over the next 100 femtoseconds to several picoseconds (ps), these hot carriers formed *via* Landau damping redistribute their energy through electron–electron scattering, eventually establishing a thermalized Fermi–Dirac-like distribution. The final step occurs over hundreds of picoseconds to nanoseconds (ns), as electrons transfer their excess energy to the lattice *via* electron–phonon interactions, dissipating the stored energy as heat. The interplay of near-field enhancement, hot carrier generation, and localized heating makes plasmonic nanoparticles powerful tools in photocatalysis, where harnessing these energy flows can drive downstream chemical transformations with high efficiency (Fig. 1b).[151]

2.5. Plasmon-enhanced chemical transformation

Building on the fundamental processes of LSPR excitation and relaxation, this section provides a comparative analysis of plasmon-mediated catalytic reactions. In an ensemble of nanoparticles in a reactor, different LSPR effects often occur concurrently, and the excitation and relaxation characteristics of LSPR can be significantly influenced by the molecules adsorbed on the particle surface. By sequentially describing the key physicochemical processes involved in plasmon-mediated catalysis, we provide a framework for understanding their mechanisms and outcomes (Fig. 1c–e). The enhanced electromagnetic near-field associated with LSPR significantly increases light absorption, which leads to a higher probability of exciting reactants adsorbed on the plasmonic surface. Such heightened excitation can also affect nearby semiconducting interfaces in hybrid catalysts (Fig. 1c). However, successful catalytic reactions depend critically on the spectral overlap between the plasmonic nanostructure and the reactants or semiconductors. Additionally, upon photoexcitation of plasmonic nanoparticles, reactant molecules attached to their surfaces can be elevated to higher electronic energy levels due to charge transfer from the nanoparticles, leading to the formation of transient negative ions in case of electron transfer (Fig. 1d). In this excited negative ion state, reactant molecules may undergo geometric reorganization, altering bond angles and lengths, which can trigger chemical reactions. In plasmonic photocatalysis, even if a molecule does not react directly in its initial electronically excited state, it may still undergo a reaction while occupying a longer-lived vibrationally excited state generated during the relaxation process. A recent review by Cortés *et al.* discusses the electron transfer process from metal nanoparticles to the adsorbed molecule using a general framework based on the concept of electron scattering that encompasses the most important effects at the plasmonic metal–molecule interface.[158] Plasmonic materials can also act as a source of localized heat, enhancing chemical reaction rates. Traditional methods often struggle to achieve nanoscale thermal confinement, but plasmon-mediated heating presents a promising solution (Fig. 1e). This distinctive property results in the potential applications of plasmon-mediated catalysis across various reactions. The selected pathway by which the reaction will be catalysed is determined by various factors, including the properties of the metal nanoparticles, the reaction and reactants involved, and external conditions like band gap, heat transfer, dielectric properties, refractive index, and electron mobility.

The effectiveness of hot electron generation depends on efficient electron-surface interactions, which are promoted in systems with surface features that disturb translational symmetry, enhancing electron scattering and photon absorption. The subsequent generation of thermalized electrons through electron–electron scattering depends on the scattering rates, while the conversion of light energy to heat is governed by the electron–phonon scattering processes. Both processes are strongly influenced by the size of the metal nanoparticles. Smaller nanoparticles exhibit increased electron-surface interactions, raising the probability of hot electron generation and improving electron-driven catalysis. In contrast, larger nanoparticles more readily channel absorbed energy into lattice heating, leading to more pronounced photothermal effects, because reduced surface scattering and longer electron mean free paths favor bulk electron–phonon energy transfer over hot-carrier extraction.[151]

In summary, the photophysical foundations of these two material classes are defined by their distinct electronic structures: the discrete band gap of semiconductors and the collective electronic oscillations of plasmonic metals. While semiconductors drive catalysis through the generation and separation of relatively long-lived electron–hole pairs governed by band-edge potentials, plasmonic materials operate through the ultrafast generation of high-energy hot carriers and the creation of intense localized electromagnetic fields. By defining the specific stages of carrier generation, migration, and utilization, it becomes clear that the efficiency of these systems is intrinsically linked to their unique energy-relaxation timescales and optical cross-sections. Establishing this conceptual framework is a prerequisite for understanding how these materials can be tailored to meet the specific thermodynamic and kinetic requirements of complex chemical transformations.

Having established the fundamentals of semiconductors, excitons, and plasmonic excitation, we now turn our attention to practical applications. In the following sections, we will explore the similarities and differences in plasmonic and semiconductor systems and how these properties facilitate catalysis in significant reactions, including nitrogen reduction, CO_2 reduction, and dry reforming of methane. Finally, we will conclude with ultrafast studies on semiconductor and plasmonic materials, thereby linking the photophysical aspects previously discussed with observed catalytic phenomena in the literature across various reactions.

3. Semiconductor and plasmonic photocatalysts: a comparative perspective

The rational design of efficient photocatalytic systems demands a deep understanding of how semiconductor and plasmonic materials fundamentally differ in their interaction with light

and subsequent conversion of photon energy into chemical energy. While both classes of materials can harvest solar energy to drive chemical transformations, their underlying mechanisms are different, resulting from different electronic structures that give rise to distinct excitation pathways, energy landscapes, and catalytic behaviors. These differences represent fundamental physical principles that dictate the performance limits, optimization strategies, and ultimate applications of each material class.

Understanding these distinctions requires examining the microscopic processes that govern light–matter interactions, where classical and quantum effects dictate how absorbed energy is utilized. This section highlights the contrasting strengths and limitations of semiconductors and plasmonic materials, highlighting why their performance in photocatalysis differs fundamentally. A comparative evaluation of these two classes of photocatalysts thus provides insights into their mechanisms and potential applications.

3.1. Excitation mechanisms and energy landscapes

The initial steps following photon absorption define the trajectory of photocatalytic processes, but the nature of these primary excitations differs fundamentally between semiconductors and plasmonic materials. These contrasting excitation pathways govern charge carrier dynamics, energy relaxation, and ultimately catalytic behavior, establishing a central distinction between the two classes of photocatalysts.

3.1.1 Two excitation mechanisms. In plasmonic nanoparticles, photon absorption triggers a collective oscillation of electrons, enabled by the high free-electron density of metals (10^{22}–10^{23} cm^{-3}), which allows for a coherent response to the electromagnetic field (Fig. 1b).[152,154,163] The LSPR can be elegantly described using Maxwell's equations and classical electrodynamics.

This collective oscillation of conduction electrons arises from the intrinsic dielectric response of metals, which is strongly dependent on their free carrier density. When the frequency of incident light matches the natural oscillation of these electrons, a resonance condition is established. Under these conditions, the nanoparticle exhibits robust light–matter coupling, resulting in absorption and scattering cross-sections that can exceed the particle's geometric cross-sectional area by one to two orders of magnitude. This unique property results in the extraordinary optical response of plasmonic nanostructures and sets them apart from conventional semiconductors.

This collective excitation is short-lived, typically dephasing within 1–10 fs through Landau damping, wherein the coherent plasmon oscillation decays into excited charge carriers. The resulting hot carriers possess a broad, non-thermal energy distribution that extends well above the Fermi level (Fig. 1b). Such a wide energetic spread is often regarded as one of the defining advantages of plasmonic systems, as unlike semiconductor photoexcitation, where a single photon generates a single electron-hole pair at a specific energy, the collective nature of plasmon excitation yields hot carriers distributed across a broad range of energies from a single plasmon decay event.[160,171,181]

In contrast to plasmonic systems, semiconductor photoexcitation is governed by discrete optical transitions between well-defined electronic bands. Each absorbed photon generates a single electron–hole pair (or exciton) with specific energy and momentum, rather than a broad, collective excitation involving multiple electrons (Fig. 1a).[137] This distinction arises from the band structure, which imposes strict energy thresholds and allows only certain transitions. Momentum conservation further shapes absorption behavior: direct band gap semiconductors allow efficient vertical transitions in momentum space, whereas indirect band gap materials require phonon assistance, leading to weaker absorption and distinct edge characteristics.[137]

3.1.2 Energy landscapes. In terms of energy distribution, the contrasting excitation mechanisms of semiconductors and plasmonic materials produce fundamentally different energy landscapes with direct implications for catalysis. In plasmonic systems, the decay of collective oscillations yields hot carriers that occupy a broad range of energies, extending well beyond the equilibrium Fermi level (Fig. 2a).[160,171,181] This highly non-equilibrium distribution features populations in higher-energy states that would not be accessible under thermal conditions. This provides remarkable flexibility for photocatalysis, offering multiple energetic pathways for driving chemical reactions and enabling access to high-barrier processes that would be kinetically difficult under equilibrium conditions.

In semiconductors, the energy landscape is more discrete and predictable (Fig. 2b). Each absorbed photon produces carriers with specific energies that can be directly aligned with the redox potentials of targeted reactions, offering a level of

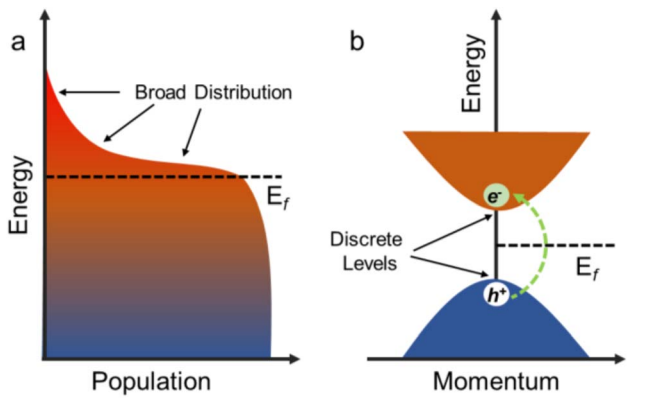

Fig. 2 Energy landscapes in plasmonic and semiconductor systems. (a) Non-equilibrium distribution of hot carriers in a plasmonic nanoparticle. The plot illustrates the carrier population following electron–electron scattering, showing a high-energy distribution relative to the Fermi level (E_f) before energy transfer to the lattice, (b) electronic band structure of a semiconductor plotted in momentum space. The schematic depicts the parabolic dispersion of the conduction band and valence band separated by a discrete band gap, defining the specific energy levels available for photogenerated carriers and exciton formation.

precision absent in plasmonic systems.[53,139] Furthermore, the coulombic attraction between electrons and holes introduces spatial correlation, giving rise to excitons with characteristic sizes and lifetimes. Free charge carriers in inorganic semiconductors can persist from nanoseconds to microseconds before recombination, depending on trap density, doping, and dimensionality, a timescale that is orders of magnitude longer than the femtosecond dynamics of plasmonic hot carriers.

3.1.3 The thermal effect advantage. The dissipation of absorbed energy also differs fundamentally between plasmonic and semiconductor systems. In plasmonic nanoparticles, nonradiative decay of LSPR rapidly channels energy into the lattice *via* electron–phonon coupling, producing strong and localized heating effects that can reach hundreds of degrees within nanometric domains (Fig. 1b).[151] Such intense local thermal gradients can strongly influence catalytic outcomes. By contrast, in semiconductors, excess photon energy above the band edge is more efficiently dissipated through carrier cooling into the lattice, where heat generation is comparatively modest and spatially delocalized, because of the low density of excited charge carriers.[26] This contrast highlights how plasmonic systems inherently couple optical excitation to pronounced local heating, while semiconductors maintain more distributed and less significant thermal responses. However, this comparative discussion assumes identical illumination conditions for both systems; actual thermal effects are strongly dependent on system parameters and light intensity.

3.1.4 The absorption advantage. The absorption characteristics of semiconductor and plasmonic photocatalysts highlight their fundamentally different excitation mechanisms, both in magnitude and in spectral response. Plasmonic nanoparticles, especially at their LSPR, can display absorption cross-sections far exceeding their physical dimensions. For example, a gold nanoparticle of only 50 nanometers in diameter can have extinction coefficients on the order of 10^9 M^{-1} cm^{-1}.[151] These tremendous values, several orders of magnitude higher than those typically achieved by semiconductor nanostructures, make plasmonic materials remarkably effective light harvesters even at very low loadings.

By contrast, semiconductor absorption is generally modest in intensity but offers distinct advantages. Near their band edge, semiconductor nanoparticles typically exhibit extinction coefficients in the range of 10^4–10^6 M^{-1} cm^{-1}.[107] While lower than plasmonic resonances, this absorption spans broader spectral ranges and is more strongly dictated by the band structure, yielding predictable energy thresholds and stable optical responses under varying surrounding conditions. Plasmonic nanomaterials exhibit absorption that is highly sensitive to their surrounding environment, with the peak position shifting as the dielectric properties of the medium change.[152,154]

3.2. Field effects in photocatalysis

The spatial distribution and temporal evolution of electric fields represent another fundamental distinction between plasmonic and semiconductor photocatalysts. These field effects profoundly influence how each system interacts with molecular adsorbates and determine the spatial extent over which catalytic enhancement occurs.

Plasmonic nanoparticles generate intense electromagnetic fields, creating a localized intense electric field region that can enhance electric field intensity by factors of 10^2 to 10^3 compared to the incident light (Fig. 1b and c).[151,152] This near-field enhancement emerges from the coherent oscillation of surface electrons, which creates regions of concentrated electromagnetic energy in the immediate vicinity of the nanoparticle surface. Unlike the uniform fields of plane waves, plasmonic near-fields are highly inhomogeneous, with intensity enhancement factors that can reach values of 10^4 to 10^6 at specialized locations called hotspots.[151,159] These hotspots represent electromagnetic singularities where field enhancement reaches its maximum intensity. They typically occur at sharp features such as particle tips, edges, and corners where charge accumulation is highest, or in narrow gaps between closely coupled nanoparticles where fields from multiple sources constructively interfere.[151,159] The spatial extent of plasmonic field enhancement decays extremely rapidly with distance from the nanoparticle surface. In most cases, the effect is confined to just 5–10 nanometers, creating an intensely localized activation zone. Molecules within this zone experience intense field enhancement, while those just slightly farther away remain virtually unaffected.[158] This distance dependence has profound implications for catalytic selectivity. The plasmonic enhancement zone acts like a molecular spotlight, selectively activating surface-bound species while leaving solution-phase molecules untouched (Fig. 1b and c). This spatial selectivity can be exploited to control reaction pathways, enhance weak molecular transitions that would otherwise be optically inactive, and create catalytic hot zones with precisely defined dimensions.

Semiconductor photocatalysts operate with an entirely different field paradigm, generating built-in electric fields through band bending phenomena that extend much deeper into the material and persist even in the absence of illumination.[16,25,26] When a semiconductor surface is exposed to an environment with a different chemical potential, charge redistribution occurs to achieve electrochemical equilibrium, creating space charge regions with associated static electric fields. The formation of these internal electric fields through band bending is a fundamental characteristic of the semiconductor systems, as shown by the example of upward and downward bending in an n-type semiconductor system (Fig. 3). While shown for an n-type semiconductor, similar electric fields also exist across various doping profiles and junction types in semiconductor systems.[11] While these fields are generally weaker than plasmonic hotspots, they extend over much larger distances, depending on the doping concentration and surface conditions. These built-in fields serve multiple functions in semiconductor photocatalysis. They drive photogenerated electrons and holes in opposite directions, reducing recombination probability and enhancing charge separation efficiency. They modulate surface reactivity by altering the energetic positions of surface states, affecting both adsorption energies and reaction kinetics. They also create junction potentials at interfaces between different materials, providing additional

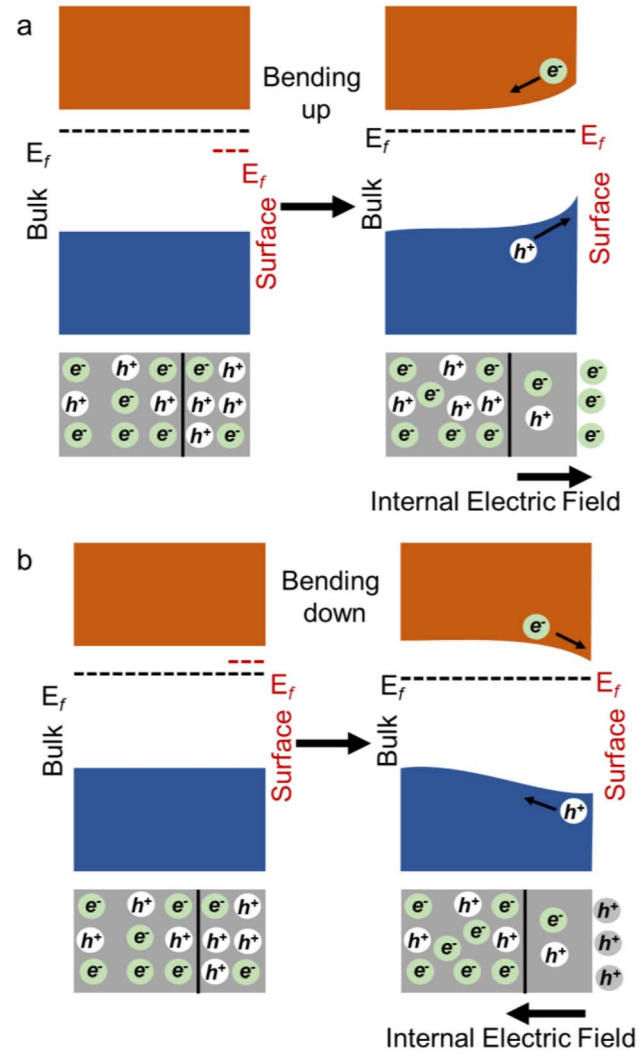

Fig. 3 Built-in electric field formation and band bending in semiconductors. Schematic of equilibration at an n-type semiconductor interface. (a) Upward band bending: charge redistribution creates an internal electric field that drives photogenerated holes to the surface and pushes electrons into the bulk, (b) downward band bending: the resulting field facilitates electron accumulation at the surface while driving holes toward the bulk.

driving forces for charge transfer and separation.[11] Unlike the dynamic, light-dependent fields in plasmonic systems, semiconductor built-in fields are largely static, changing only slowly with variations in surface chemistry, temperature, or surrounding conditions.

3.2.1 Molecular coupling. The interaction between electromagnetic fields and molecular adsorbates reveals fundamental differences in how plasmonic and semiconductor systems activate chemical reactions. Plasmonic–molecule coupling operates through several distinct mechanisms that depend critically on spectral matching and spatial proximity.[170] Resonant enhancement occurs when molecular electronic transitions coincide with the LSPR frequency, creating strong coupling between the plasmonic oscillation and molecular excitation (Fig. 1c). This resonance can dramatically increase molecular absorption cross-sections and enable excitation pathways that would be less likely under normal illumination conditions (Fig. 1c).[170] The coupling strength scales with the local field intensity, creating a strong incentive to position molecules at hotspot locations where field enhancement is maximized. Vibrational coupling represents another important pathway, where plasmonic fields couple to molecular vibrational modes through mechanisms similar to surface-enhanced Raman spectroscopy.[253] This coupling can selectively activate specific vibrational coordinates, potentially steering reactions along desired pathways by preferentially exciting vibrational modes that lead to target products. Hot carrier injection provides a third coupling mechanism, where energetic electrons generated by plasmon decay transfer directly into molecular orbitals (Fig. 1d).[170] This process can populate antibonding states that weaken chemical bonds or create transient negative ion states that facilitate bond breaking.[215] The efficiency of hot carrier injection depends on the energy alignment between hot carrier distributions and molecular acceptor states, as well as the coupling strength at the metal–molecule interface.

In semiconductors, molecule coupling is primarily governed by energetic alignment with the band edges, whereas in plasmonic systems, coupling depends on both the energy of hot carriers and resonant interactions with the local electromagnetic field. The key requirement is that molecular energy levels align appropriately with semiconductor band edges to enable efficient charge transfer (Fig. 1a). CBM must lie at a higher electronic energy than the reduction level of the target species, while the VBM must lie at a lower electronic energy than the corresponding oxidation level.[7,8,23] Surface states often serve as intermediates in semiconductor-molecule charge transfer, providing stepping stones that facilitate electron or hole transfer even when direct band-to-molecule transitions are energetically unfavorable. These surface states can be intrinsic features of the semiconductor crystal structure or extrinsic states created by surface defects, adsorbates, or chemical modifications. The built-in electric fields in semiconductors also influence molecular coupling by polarizing adsorbed species and stabilizing charged transition states.[8,11] Thus, while plasmonic and semiconductor systems exhibit distinct temporal, spatial, and energetic behaviors, they operate through fundamentally related mechanisms of molecule–material interaction.

3.3. Thermodynamic considerations

The thermodynamic landscape governing photocatalytic reactions reveals perhaps the most fundamental distinction between semiconductor and plasmonic systems. While both material classes must ultimately convert photon energy into chemical potential, they operate under different constraints that determine which reactions are accessible and how efficiently energy can be utilized.

Semiconductor photocatalysts operate within their catalytic capabilities that are fundamentally constrained by the fixed positions of their band edges, which set absolute limits on the reducing and oxidizing power of photogenerated carriers

(Fig. 1a).[8,11] The thermodynamic driving force for each process scales with the energy difference between the band edge and the redox potential: $\Delta G = -nF(E_{\text{band edge}} - E^{\circ}_{\text{redox}})$. This creates a rigid framework that determines which reactions are possible and which are forbidden. This thermodynamic constraint manifests in several practical limitations that have limited semiconductor photocatalysis. Wide-band gap semiconductors like titanium dioxide possess band edges positioned at highly favorable potentials for both water reduction and oxidation, making them excellent photocatalysts for water splitting. However, their large band gaps (3.2 eV for anatase TiO_2) restrict them to ultraviolet absorption, capturing less than 5% of the solar spectrum and severely limiting their practical efficiency.[20–22] Conversely, narrow-band gap semiconductors can harvest visible light but often suffer from unfavorable band edge positions. Materials like iron oxide (α-Fe_2O_3) absorb strongly in the visible region but possess a conduction band minimum that is insufficiently negative (*vs.* NHE) to reduce protons to H_2 without an external bias or sacrificial electron donors.[21] This fundamental trade-off between spectral coverage and thermodynamic driving force represents one of the central challenges in semiconductor photocatalyst design. The situation becomes even more complex when considering practical reaction conditions. Practical catalytic processes require overpotentials beyond the thermodynamic minimum to achieve reasonable reaction rates, further constraining the available energy window. Additionally, for metal oxide semiconductors, band edge positions shift by approximately −59 mV per pH unit due to surface protonation equilibria, a Nernstian response that creates pH-dependent constraints on thermodynamic driving forces.[8,14]

Plasmonic photocatalysts operate under an entirely different energetic paradigm. Rather than being constrained by fixed band positions, plasmonic systems generate hot carriers with a broad energy distribution that can potentially access multiple reaction pathways simultaneously (Fig. 2a).[152,181,203] This energetic flexibility represents both plasmonics' greatest strength and its most significant challenge. The energy distribution extends well above the Fermi level, potentially reaching energies of several electron volts and enabling access to reaction pathways that would be kinetically challenging under equilibrium conditions. The LSPR frequency can be tuned across the visible and near-infrared spectrum through careful control of nanoparticle size, shape, and composition, enabling spectral matching with target reactions or optimization for specific solar irradiation conditions.[151] This tunability extends to the hot carrier energy distribution itself, which can be modified through plasmon–molecule coupling or by engineering the local electromagnetic environment. However, this energetic freedom comes at a steep price. The broad energy distribution means that only a small fraction of hot carriers possesses the precise energy needed for any specific reaction, leading to inherent inefficiencies in energy utilization. Moreover, the rapid thermalization of hot carriers through electron–electron and electron–phonon scattering creates a fierce competition between energy utilization and energy dissipation.[165]

3.3.1 Energy conversion pathways. The temporal evolution of energy conversion reveals another fundamental distinction between semiconductor and plasmonic photocatalysts. Semiconductor systems operate primarily in steady-state regimes where photoexcitation, charge separation, and chemical utilization occur on similar timescales, typically ranging from nanoseconds to microseconds.[13,27] This temporal matching enables efficient energy conversion because carriers have sufficient time to migrate to surface reaction sites before recombining. Charge separation can be enhanced through band engineering, surface modification, or the creation of built-in electric fields.[11,44] Surface reaction kinetics can be improved through cocatalyst loading, facet engineering, or surface sensitization.[11,44] These approaches work because the relatively long carrier lifetimes provide multiple opportunities for intervention and optimization.

Plasmonic energy conversion, in contrast, operates in highly non-equilibrium, transient regimes where different processes occur on vastly different timescales. Plasmon excitation and dephasing occur within femtoseconds, hot carrier generation proceeds on timescales of 1–100 femtoseconds, thermalization occurs within picoseconds, and chemical reactions may require nanoseconds to microseconds for completion.[154,161,165] This temporal mismatch creates fundamental challenges in energy utilization that cannot be addressed through conventional optimization approaches. The transient nature of plasmonic processes demands entirely different optimization strategies focused on accelerating beneficial processes or slowing detrimental ones. Hot carrier injection must be accelerated through improved energy alignment and stronger coupling.[161,230] Thermalization can be slowed through quantum confinement effects or by creating energy bottlenecks in the electronic structure. Chemical reactions can be accelerated through field enhancement or by pre-activating reactant molecules through surface chemistry. Efficient transfer of hot electrons can be achieved by creating "antenna–reactor" catalysts.[220,248]

3.3.2 Activation barrier modification. The modification of reaction activation barriers in semiconductor and plasmonic photocatalysts fundamentally arises from the transfer of electronic energy from the catalyst to adsorbed molecules. In both systems, photogenerated electrons and holes interact with molecular orbitals, enabling bond activation and facilitating chemical transformations.

A semiconductor typically operates under a quasi-steady-state population under continuous illumination, where photoexcitation generates electron–hole pairs that can be spatially separated by built-in electric fields or junctions. These moderate fields, combined with surface states, can stabilize charged transition states or provide alternative reaction pathways with slightly lowered activation barriers.[32,54] Plasmonic systems, while relying on the same fundamental electron transfer principle, can provide additional, transient contributions due to intense local electromagnetic fields and thermal effects.[170] Hot carriers can directly populate antibonding orbitals, while near-field enhancements and transient local heating can temporarily increase the effective energy available

to adsorbed molecules. Vibrational excitation may also play a role, enhancing certain molecular motions and subtly steering reactions toward specific pathways.[253,286]

In essence, the underlying electron-transfer mechanism is shared between semiconductors and plasmonics. The apparent differences largely arise from the magnitude, localization, and temporal profile of the excitation: plasmonic systems often provide higher-energy, ultrafast, and spatially concentrated stimuli, whereas semiconductors offer more moderate but sustained activation.

3.4. Size-dependent catalytic activity and scalability

The relationship between particle size and photocatalytic performance unveils another major distinction between semiconductor and plasmonic systems, revealing how quantum mechanics and classical physics impose different scaling laws that govern optimization strategies and ultimate performance limits.

When semiconductor dimensions shrink to approach the exciton Bohr radius, which ranges from ~1 nm (*e.g.*, ZnO) to over 30 nm (*e.g.*, InAs, PbS) depending on the material, quantum confinement effects begin to dominate, fundamentally restructuring the electronic landscape and optical properties. This quantum size effect represents one of the most powerful tools in semiconductor photocatalyst design, enabling precise control over band gaps, absorption spectra, and redox potentials through simple size manipulation.[10] The implications of quantum confinement extend far beyond simple spectral tuning. Size reduction increases the overlap between electron and hole wavefunctions, enhancing oscillator strength and improving light absorption efficiency.[10] The density of states transforms from continuous (3D bulk) to increasingly discrete (2D, 1D, 0D), creating atomic-like energy levels in the smallest nanocrystals (Fig. 4). Most importantly for photocatalysis, quantum confinement shifts band edge positions, enabling fine-tuning of redox potentials to match specific reaction requirements.[10]

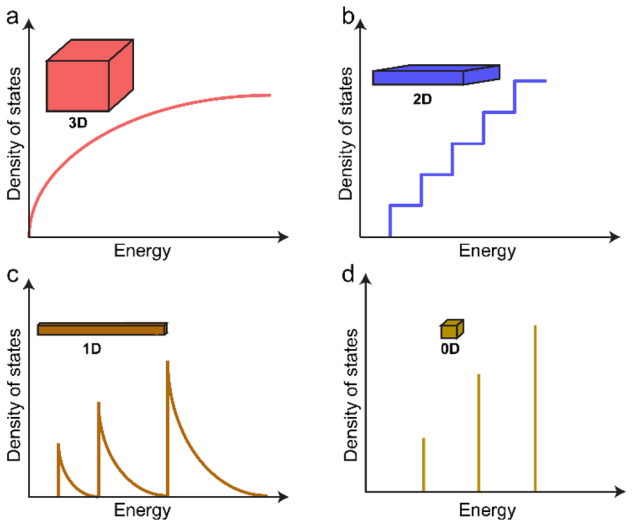

Fig. 4 Schematic representations of the density of states (DOS) as a function of energy for semiconductor crystals in different dimensions: (a) 3D bulk, (b) 2D, (c) 1D, and (d) 0D.

This size-energy connection provides semiconductor photocatalysts with remarkable design flexibility. A single material composition can be optimized for different reactions simply by controlling particle size during synthesis. Larger particles provide stronger light absorption and lower band gaps for visible light harvesting, while smaller particles offer higher energy carriers and more favorable redox potentials for challenging reactions. The ability to independently tune spectral response and energetic driving force represents one of semiconductor photocatalysis's greatest advantages. However, quantum confinement also introduces new challenges. Smaller particles exhibit increased surface area-to-volume ratios, leading to higher densities of surface defects that can act as recombination centers. The discrete energy levels in quantum dots can create energy bottlenecks that impede charge transport and extraction. Surface chemistry becomes increasingly important as surface atoms constitute larger fractions of the total particle, potentially altering electronic structure and catalytic behavior in unpredictable ways.

Plasmonic nanoparticles exhibit size-dependent properties that can be understood within classical electrodynamics for particles larger than approximately 2 nanometers. Unlike the quantum mechanical origins of semiconductor size effects, plasmonic size dependence emerges from classical electromagnetic phenomena, including retardation effects, surface scattering, and the balance between radiative and non-radiative decay pathways.[151] As plasmonic particles grow larger, several competing effects come into play. Retardation effects become significant when particle dimensions approach the wavelength of light, causing red shifts in LSPR frequency and changes in field distribution patterns. Radiative damping increases with particle size, becoming the dominant loss mechanism for particles larger than approximately 100 nanometers. While this radiative loss reduces the local field enhancement, it can actually improve far-field scattering efficiency, making larger particles more effective for light-scattering applications. For smaller particles below approximately 10–20 nm, where particle dimensions become comparable to or smaller than the bulk electron mean free path (~38 nm for Au, ~52 nm for Ag), surface scattering becomes increasingly important, contributing additional damping.[151] This surface scattering broadens LSPR linewidths and can shift resonance frequencies, but it also enhances hot carrier generation by increasing the probability of electron-surface interactions that break momentum conservation. The optimization of plasmonic particle size represents a delicate balancing act between competing factors. Intermediate sizes (50–80 nm for gold) often provide optimal field enhancement by balancing strong absorption with manageable damping losses. Smaller particles favor hot carrier generation and chemical interface damping, while larger particles excel in far-field applications and radiative processes. Unlike semiconductors, where quantum confinement provides a clear size–property relationship, plasmonic optimization requires careful consideration of the specific application and the relative importance of different enhancement mechanisms.

This exploration of fundamental comparison between semiconductor and plasmonic photocatalysts reveals not competing paradigms, but complementary approaches to solar energy conversion that can be synergistically combined to transcend the limitations of either system alone. Semiconductors offer the precision of quantum mechanics, discrete energy levels, predictable thermodynamics, and long-lived charge carriers that enable sustained catalytic processes. Plasmonic systems provide the power of collective excitation, intense electromagnetic fields, thermal effects, broad energy distributions, and ultrafast dynamics that can access high-barrier reactions and utilize the full solar spectrum. It should be noted, however, that these distinctions represent general trends rather than rigid boundaries, and exceptions exist where systems display properties that extend beyond this broad framework. The path forward lies not in choosing between these approaches, but in understanding how their distinct strengths can be combined to create architectures that combine controlled charge dynamics with strong optical field enhancement. The following sections will explore how these fundamental principles translate into catalytic applications and examine the emerging strategies for creating next-generation photocatalytic systems that integrate plasmonic and semiconductor functionalities.

4. Utilizing the excited charge carriers to drive chemical reactions

The transition from understanding photophysical principles to achieving practical chemical transformations is best illustrated through the lens of three globally significant reactions: CO_2 reduction, the dry reforming of methane (DRM), and N_2 reduction or fixation. These processes are not merely industrial targets but represent the frontline of the "Circular Carbon and Nitrogen Economy". As the global community seeks to mitigate the impacts of climate change and greenhouse gas emissions, the ability to upcycle CO_2 and CH_4 into high-energy fuels, or to produce ammonia *via* sustainable pathways, has become an environmental imperative. These reactions provide a critical framework for moving away from fossil-fuel-dependent chemistry toward a solar-driven chemistry where light acts as the primary energy source for industrial-scale synthesis.

From a fundamental chemical perspective, these three reactions serve as the ultimate benchmarks for catalytic performance because they involve the activation of some of the strongest chemical bonds found in nature. The thermodynamic stability of the C=O bond in CO_2, the C–H bond in CH_4, and the formidable N_2 triple bond (941 kJ mol^{-1}) creates kinetic barriers that are largely insurmountable for traditional catalysts at ambient temperatures. Mastering these transformations requires more than simple energy transfer; it demands the precise management of multi-electron and multi-proton pathways. These molecules, therefore, represent the most rigorous test of a photocatalyst's ability to manipulate high-energy transition states and control product selectivity in stable molecular species.

Furthermore, these reactions provide an ideal platform for comparing the distinct operational regimes of semiconductor and plasmonic architectures. Driving these high-barrier transformations necessitates winning the temporal race against charge relaxation, utilizing strategies such as hot-carrier injection, localized near-field enhancement, and defect-mediated molecular activation. By examining the nuances of CO_2 reduction, DRM, and N_2 reduction, we can evaluate how different photocatalytic systems utilize excited charge carriers to override traditional thermal limits.

4.1. CO_2 reduction with hydrogen

Solar-light-driven CO_2 conversion into valuable carbon-based products is an attractive strategy to mitigate greenhouse gas emissions and reduce dependence on fossil fuels.[440–449] The photocatalytic reduction of CO_2 on a semiconductor catalyst involves three main steps.[443,445] First is the creation of excited charge carriers. These photo-generated electrons and holes then migrate to the catalyst surface. Finally, the adsorbed CO_2 is reduced by the electrons, while the holes oxidize the reductant. For this process to be efficient, the presence of catalytic sites where CO_2 activation occurs is crucial for reaction kinetics. Potential products of this reaction include CO (2-electron reduction, −0.52 V), HCHO (2-electron reduction, −0.41 V), CH_3OH (6-electron reduction, −0.38 V), CH_4 (8-electron reduction, −0.24 V), higher hydrocarbons, *etc.*

The sunlight-driven reduction of CO_2 by H_2O is particularly promising for scalable energy storage and carbon-neutral production of high-energy fuels, with O_2 as the by-product.[440,450] However, this process is challenged by low efficiency and poor product selectivity, especially for high-value chemicals. Low efficiency is often due to the use of wide-band gap semiconductors that absorb only ∼4% of the solar spectrum (UV light) and suffer from high charge carrier recombination rates. An alternative reducing agent to H_2O is molecular H_2, which has a lower oxidation potential and helps avoid these issues.[451,452]

To improve the charge transfer efficiency in CO_2 reduction, various strategies have been developed, such as cocatalyst loading, heterojunction fabrication, interface activation, and surface catalytic site engineering. Engineering surface catalytic sites can extend light absorption, improve the separation of photogenerated electrons and holes, and thus facilitate surface redox reactions. For example, introducing spatially separated catalytic sites (cocatalyst) can enhance charge carrier transfer and surface redox reactions (Fig. 5a). Li *et al.*[453] prepared copper–cobalt dual catalytic site porous TiO_2, where Cu sites acted as reductive sites and Co sites as oxidative sites. The spatial separation of reactive sites on TiO_2's surface significantly promoted charge separation during catalytic reactions.

Fabricating heterostructure catalysts with favorable band alignment is also effective for achieving broad spectral responses and efficient charge separation. Depending on charge transfer directions, heterostructure catalysts are categorized as p–n junctions or Z-schemes.[454–458] In a p–n junction, photo-generated electrons are injected into the component with

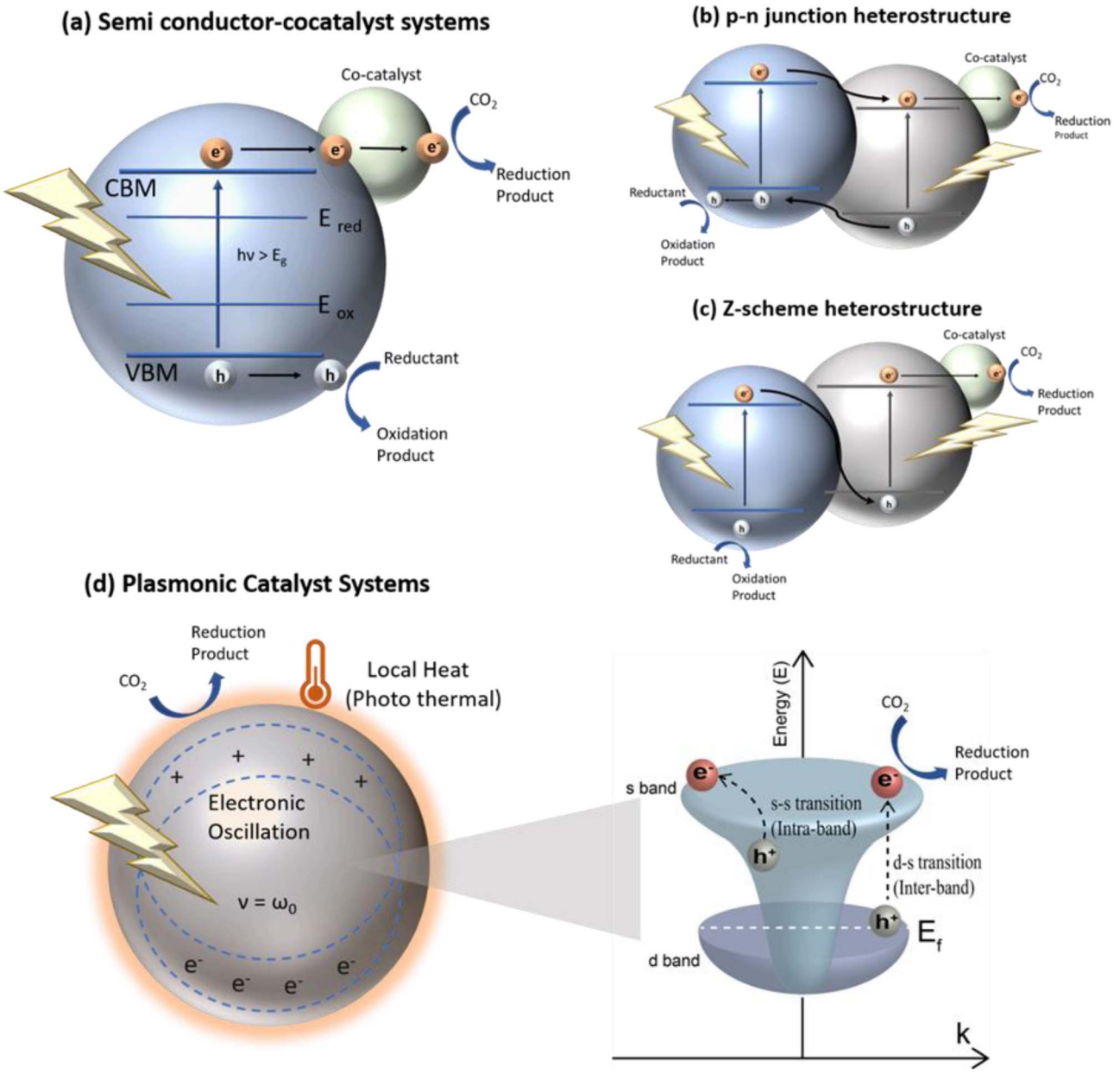

Fig. 5 Different photocatalytic systems for CO_2 reduction. (a) Single-semiconductor-based photocatalyst with cocatalyst, (b) p–n junction heterostructure photocatalyst, (c) Z-scheme heterostructure photocatalyst, (d) metal-based photocatalyst with localized surface plasmon resonance.

a lower CB edge, while photo-generated holes migrate to the component with a higher VB edge (Fig. 5b). In contrast, in a Z-scheme architecture, photo-generated electrons in the component with a lower CB edge recombine with holes in the component with the higher VB edge, either directly or indirectly, using a conductive intermediate or reversible redox shuttle (Fig. 5c).

Moreover, heterogeneous photocatalytic CO_2 reduction can also be carried out over metal catalysts like gold, silver, copper, and bismuth, mainly due to the LSPR effect.[459–461] Hot charge carriers are formed through intraband s-to-s or interband d-to-s transitions after the decay of LSPR (Fig. 5d). Both the local heat and hot charge carriers can contribute to CO_2 reduction.

Different strategies have been carried out to increase the lifetime of these charge carriers in both semiconductor and plasmonic photocatalysts. In oxide semiconductors, defect creation in the form of O vacancies offers dual advantages by offering trap sites for electrons and introducing mid-gap states, broadening the absorption spectrum of the semiconductors. For CO_2 reduction, they can be critical for activating CO_2 molecules or can help in stabilizing semiconductor and cocatalyst interfaces by special phenomena like strong metal–support interactions (SMSI). For example, black TiO_2 with dual

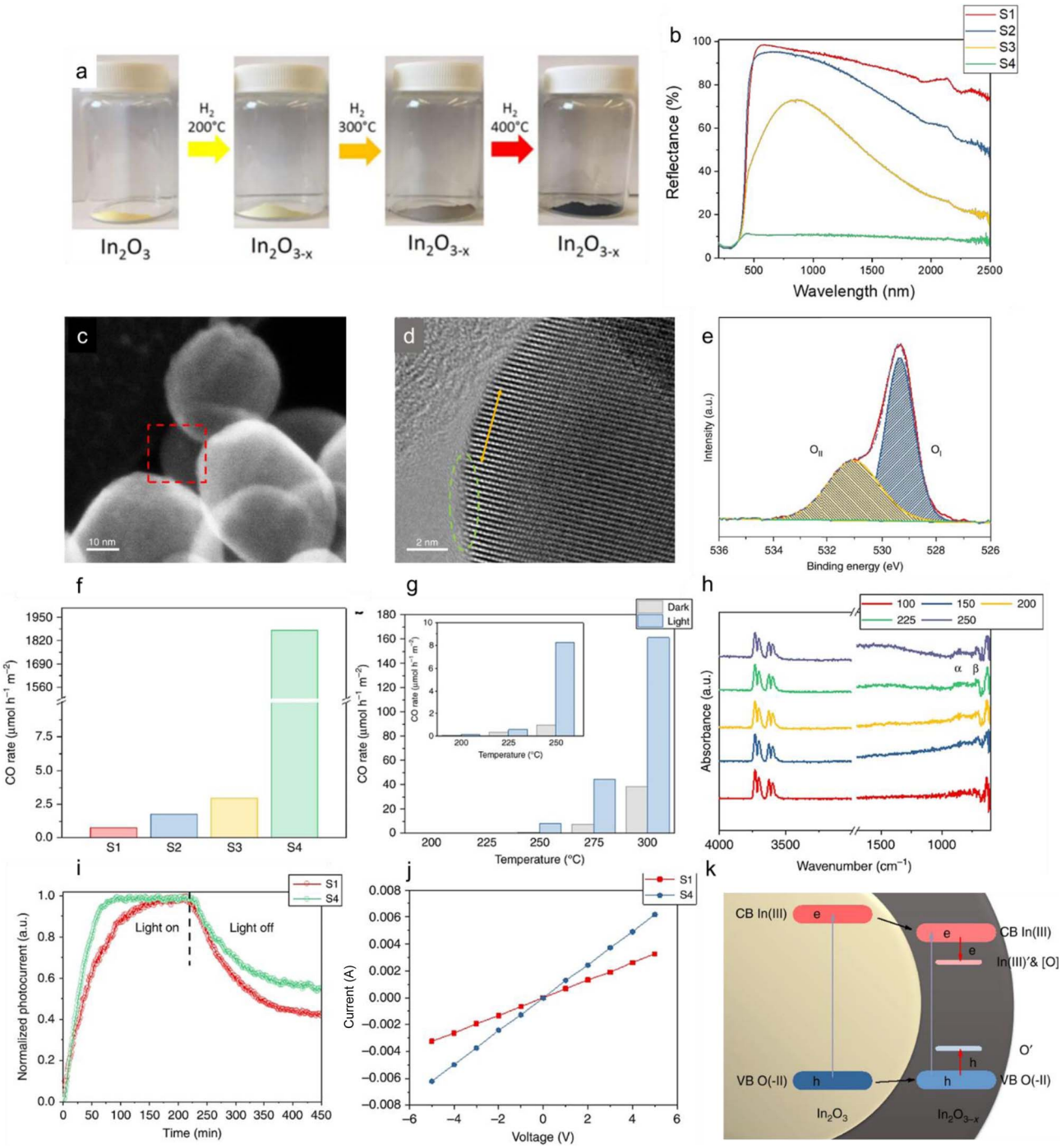

Fig. 6 Photocatalytic CO_2 hydrogenation over single-component In_2O_{3-x}. (a) Color changes from pale yellow to grey to black observed on hydrogenating stoichiometric In_2O_3 at 200, 300, 400 °C to form non-stoichiometric In_2O_{3-x} with monotonically increasing values of x with temperature, (b) optical reflectance spectra (UV-Vis-NIR), (c) STEM, and (d) HRTEM images of S4 at different magnifications. A dashed green circle indicates an amorphous phase, yellow arrow indicates the measured lattice spacing and the red square indicates the imaged position, (e) high-resolution O 1s core level XPS spectrum of S4, (f) photocatalytic CO_2 hydrogenation in a batch reactor. (g) Catalytic performance for S4 in a flow reactor at different temperatures, both with and without light irradiation, inset is the enlarged view of the catalytic performance for 200, 225, and 250 °C, (h) *in situ* DRIFTS spectra of S4 obtained under both H_2 and CO_2 (1 : 1) with increased temperatures, (i) photocurrent saturation and decay plot, (j) corresponding *in situ* I–V plot, (k) the In_2O_{3-x}/In_2O_3 heterostructure showing the In(III)′, [O] electron-trapping and O′ hole-trapping mid-gap energy states near the CB and VB edges, respectively. Reproduced with permission from ref. 463. Copyright 2020 Springer Nature.

active sites (Ni NPs and oxygen defects) was synthesized by Chen *et al.*[462] Surface dual sites acted as the binding sites of the CO_2 molecule and lowered its activation energy, while oxygen defect sites also trapped the electron and narrowed the band gap of TiO_2, collectively resulting in an 18-times higher acetaldehyde production than that catalyzed by P25. One such study

by Ozin *et al.*[463] focuses on the exploitation of O vacancy defects in In_2O_3 semiconductor nanoparticles for photothermal CO_2 hydrogenation (Fig. 6). The pale yellow In_2O_3 powder was converted to pitch-black by controlling its non-stoichiometry through hydrogen treatment at elevated temperatures (Fig. 6a). The optical reflectance spectra (UV-Vis-NIR) for S1–S4 showed a trend of gradually increasing absorption, broadening and red shifting of the ultraviolet absorption edge into the visible region with higher temperatures of the hydrogenation (Fig. 6b). High resolution transmission electron microscopy (HRTEM) confirmed the formation of these heterostructures having amorphous indium oxide In_2O_{3-x} interfaced with crystalline indium oxide In_2O_3 (Fig. 6c and d), which enabled the photothermal reverse water gas shift (RWGS) reaction with 100% selectivity. X-ray photoelectron spectroscopy (XPS) analysis revealed that oxygen vacancies increased with hydrogenation temperature, with S2, S3, and S4 corresponding to $In_2O_{2.8}$, $In_2O_{2.7}$, and $In_2O_{2.63}$, respectively (Fig. 6e). The black In_2O_{3-x}/In_2O_3 exhibited a CO production rate nearly three orders of magnitude higher than the yellow In_2O_3 under light, reaching 1874.62 μmol h^{-1} m^{-2} (Fig. 6f). Based on the enclosed thermocouple, the temperatures of S1–S3 are lower than 50 °C, and about 160 °C for S4. The local temperatures of all samples were estimated from the conversion of CO_2 to CO (yield, ppm), where S4 was found to be 262 °C in contrast to S1–S3 which were found to have much lower local temperatures (Fig. 6g). The effect of oxygen vacancies on CO_2 binding was analyzed using *in situ* diffuse reflectance infrared Fourier transform spectroscopy (DRIFTS) where a reaction pathway involving the CO_2 insertion and regeneration of oxygen vacancies was proposed (Fig. 6h). Photoconductivity measurements under vacuum and experimental conditions for S1 and S4 were performed to study the dynamics of photoexcited carriers.

The much faster photo-saturation of the excited electrons for S4 implied a stronger optical absorbance for S4 than S1. While the light was off, the photocurrents of S1 and S4 slowly decayed, with S4 requiring a much longer decay time than S1, which implied a higher population of oxygen vacancy traps for photoelectrons (Fig. 6i). The longer lifetime of the detected photoelectrons also meant a higher probability for the photoexcited electrons to participate in the reaction and thereby results in a better catalytic performance for S4. The same trend was observed under vacuum conditions, and the resulting *I–V* plot further confirmed the prolonged lifetime of photoexcited electrons for S4 (Fig. 6j). The oxygen vacancies [O] and coordinately unsaturated indium In′ sites and oxygen O′ sites in In_2O_{3-x} existed as mid-gap defect states in the band gap of In_2O_3.[107,464] These states were shown to be respectively situated near the oxide-based valence band and indium-based conduction band, with the charge-balancing electrons occupying mid-gap states and aiding in the separation of electron–hole pair and therefore facilitating photochemical conversion of CO_2 to CO (Fig. 6k).

It should be noted that the nature of defect sites is critical to determine the selectivity of the reaction, as it can change the charge carrier dynamics as well as the surface activity. In another report, when the defects were introduced in In_2O_3 using $NaBH_4$ instead of thermal treatment in an H_2 environment, the catalyst was hydroxy-terminated, leading to shifting the reaction pathway towards methanol.[465]

To enhance the efficiency of single-component semiconductors, various strategies such as forming heterojunctions between semiconductors and loading metal cocatalysts are employed. In a study by Li *et al.*,[466] graphdiyne (GDY)-modified In_2O_3 hybrid photocatalysts (denoted as GDY-IO) were synthesized using simple electrostatic attraction and thermal annealing methods (Fig. 7a). The GDY-IO composites not only showed significantly improved photocatalytic activity in the production of CO and CH_4 but also enabled the formation of C_{2+} hydrocarbons (such as C_2H_4, C_2H_6, C_3H_6, and C_3H_8) under atmospheric conditions. The introduction of GDY promoted the separation of excited carriers and enhanced the adsorption and activation of CO_2, which significantly lowered the kinetics barrier for CH* formation and favored hydrogenation and C–C coupling processes. TEM analysis revealed that the intimate two-phase interfacial contact between highly crystallized In_2O_3 and the amorphous GDY region (Fig. 7b and c) effectively improved interfacial charge transfer during the photocatalytic reaction.

High-resolution In 3d XPS spectra of In_2O_3 showed two peaks corresponding to In $3d_{5/2}$ and In $3d_{3/2}$. Notably, after coupling GDY with In_2O_3, these In 3d peaks shifted to higher binding energies compared to those of pristine In_2O_3 (Fig. 7d). A similar shift was observed in the O 1s spectra, indicating electron transfer from In_2O_3 to GDY upon contact (Fig. 7e). Furthermore, electron paramagnetic resonance (EPR) signals at the *g*-value of 2.003, along with O 1s XPS, demonstrated that the GDY-IO possessed a higher concentration of oxygen vacancies (O_v) than pristine IO. Notably, heterojunction fabrication between GDY and IO helped to improve the visible light absorption of In_2O_3 (Fig. 7f). Additionally, a significant decrease in the integrated density-of-states (DOS) in In_2O_3 after contact with GDY was observed, implying accelerated electron mobility from In_2O_3 to GDY (Fig. 7g).

The pristine In_2O_3 catalyzed both the RWGS reaction and the methanation reaction, producing CO and CH_4 as primary products. Interestingly, the GDY-IO composites exhibited a different product distribution under the same reaction conditions, generating not only CO and CH_4 but also C_{2+} hydrocarbons (C_2H_4, C_2H_6, C_3H_6, and C_3H_8) during the photocatalytic process (Fig. 7h). The GDY-IO composites showed negligible thermal effects since the photocatalytic performance tests were conducted at room temperature, with the final bulk reaction temperature below 120 °C.

The combination of GDY with In_2O_3 led to the weakest photoluminescence (PL) emission peak, likely due to the increased concentration of oxygen vacancies introduced by GDY, which provided more traps for capturing electrons and preventing electron–hole recombination. Consequently, the GDY-IO sample exhibited a longer transient fluorescence lifetime (~11 ns) compared to pristine In_2O_3 (~5.1 ns) and GN-IO (~8.5 ns) (Fig. 7i). Transient photocurrent response (Fig. 7j) and electrochemical impedance tests collectively indicated that the introduction of GDY indeed facilitated charge carrier

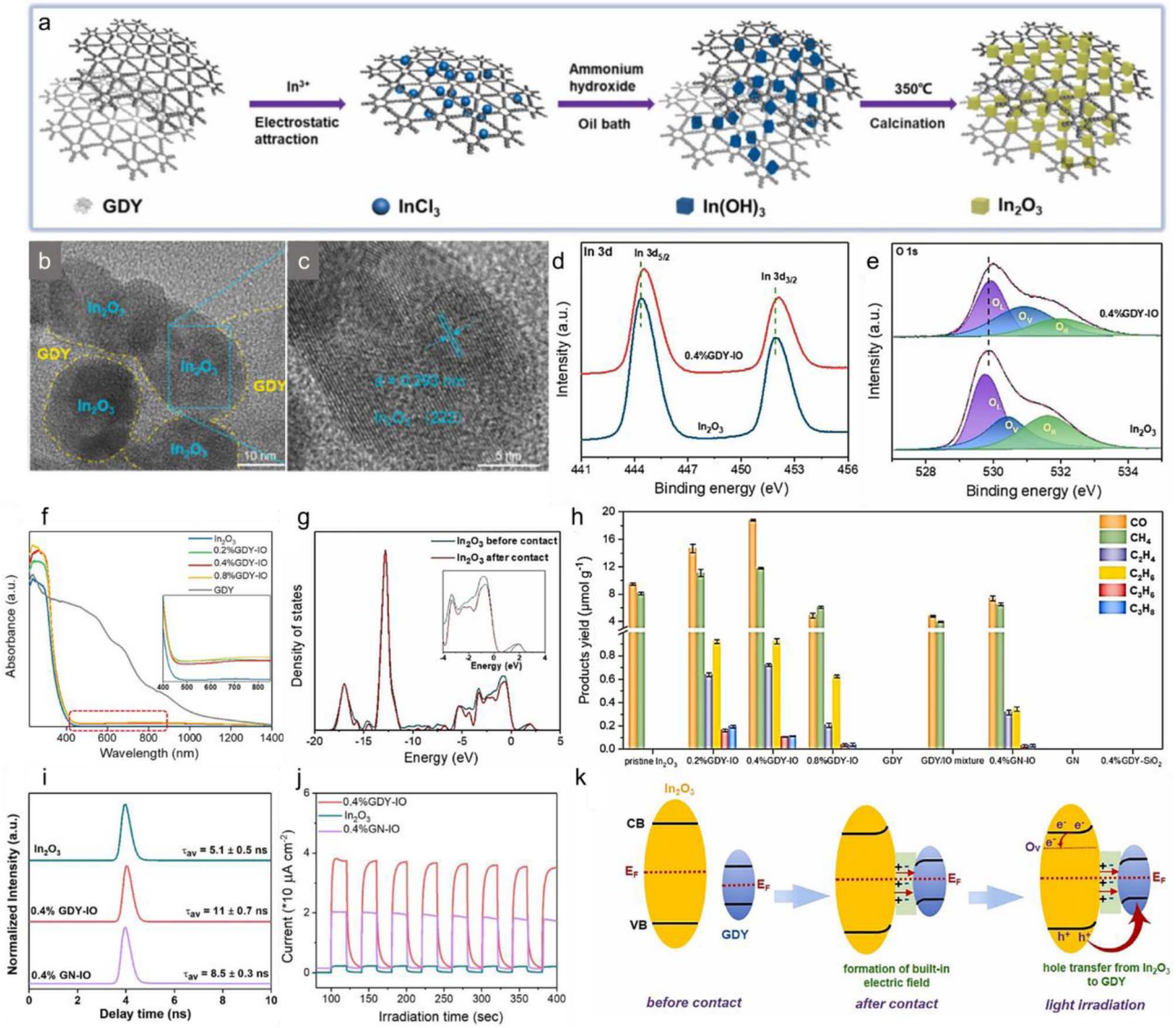

Fig. 7 Photocatalytic CO_2 hydrogenation over GDY-IO utilizing heterojunction. (a) Schematic illustration of the synthetic process for GDY-IO composites, (b) TEM and (c) HRTEM images of 0.4% GDY-IO composites, (d) high-resolution In 3d spectra and (e) O 1s spectra of In_2O_3 and 0.4% GDY-IO composite, (f) UV-Vis DRS spectra of In_2O_3, GDY, and GDY-IO composites, (g) density of states of In_2O_3 before and after contact with GDY, (h) products of photocatalytic CO_2 reduction on various catalysts, (i) time-resolved photoluminescence observed from selected red frames on single In_2O_3 particle, single 0.4% GDY-IO particle, and single 0.4% GN-IO particle, (j) transient photocurrent response curves, (k) schematic diagram for the electron transfer and the formation of built-in electric field between In_2O_3 and GDY upon their contact, and the holes transfer between In_2O_3 and GDY after light irradiation. Reproduced with permission from ref. 466. Copyright 2024 Elsevier.

separation. The combined *in situ* DRIFTS and density functional theory (DFT) results demonstrated that introducing GDY into In_2O_3 enhanced CO_2 adsorption and activation, leading to electron enrichment on the In_2O_3 surfaces near the oxygen vacancies, which together stabilize reaction intermediates and promote C–C coupling reactions.

Based on these observations, an electron transfer mechanism was deduced (Fig. 7k). When In_2O_3 and GDY were in contact, electrons transferred from In_2O_3 to GDY to reach the same Fermi level, creating a built-in electric field. Under light irradiation, the photogenerated holes from In_2O_3 were driven to transfer to GDY by the built-in electric field, while the photogenerated electrons were captured by the abundant surface oxygen vacancies in In_2O_3. As a result, the separation and transfer of photogenerated carriers in the GDY-IO composite are significantly improved. Most importantly, the photogenerated electrons in In_2O_3 migrated and accumulated at the surface oxygen vacancies, providing a high surface charge density to overcome the C=O activation and C–C coupling energy barriers, facilitating the transformation of CO_2 into C_{2+} hydrocarbons.

To enhance charge separation in photocatalysts, in addition to strategies like defect creation and heterojunction fabrication, noble metal loading is a simple and effective method. The

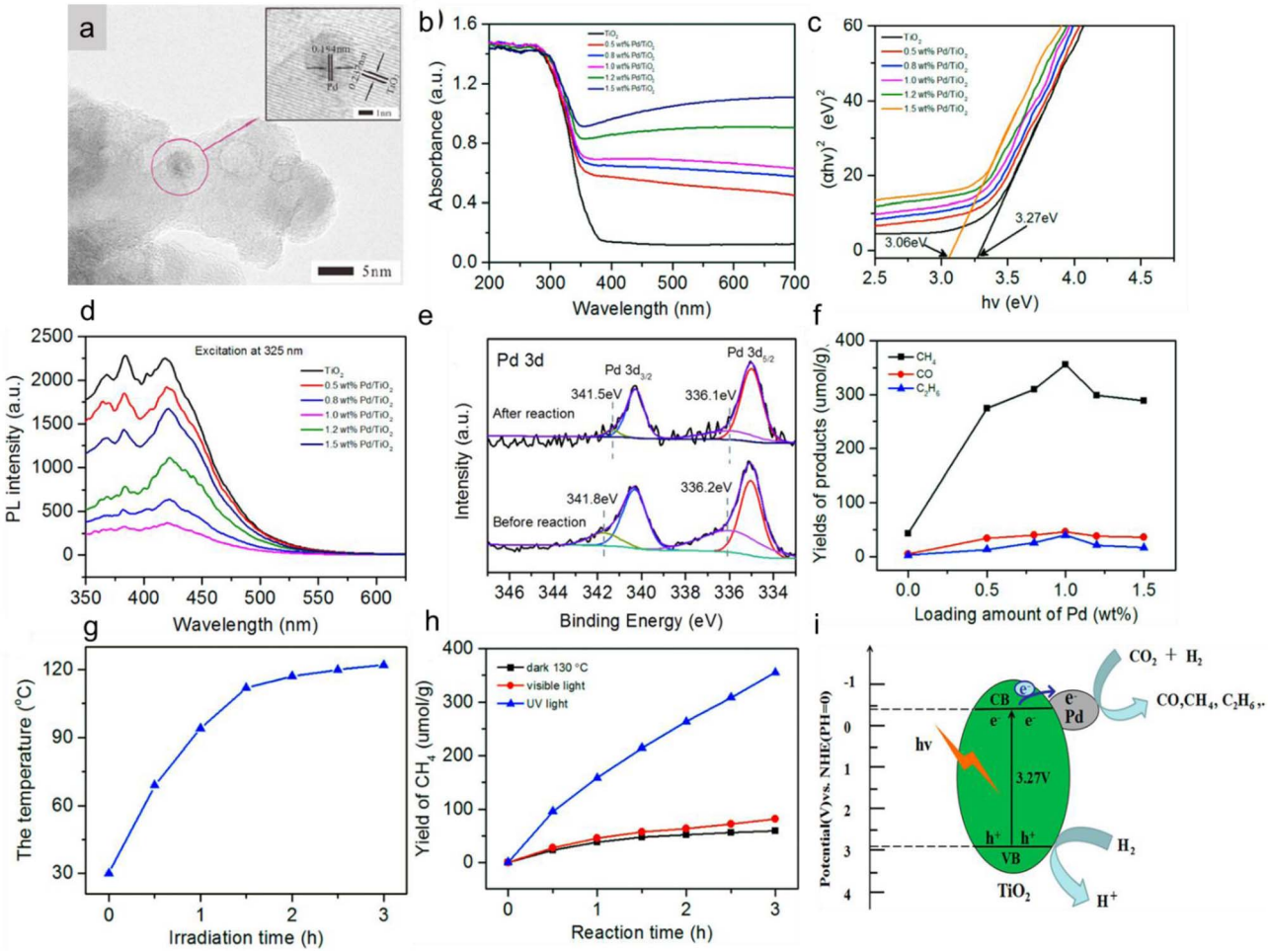

Fig. 8 Photocatalytic CO_2 hydrogenation over Pd/TiO_2 semiconductor-cocatalyst system. (a) HRTEM image of Pd/TiO_2, (b) UV-Vis absorption spectra of TiO_2 and Pd-loaded TiO_2 samples, (c) plot of $(\alpha h\nu)^2$ *vs.* photon energy ($h\nu$) for the direct optical band gaps of TiO_2 and Pd-loaded TiO_2, (d) PL spectra of TiO_2 and Pd/TiO_2 measured at an excitation wavelength of 325 nm, (e) X-ray photoelectron spectra of 1.0 wt% Pd/TiO_2 catalyst Pd 3d region, (f) relationship between the products and the loading amount of Pd after irradiation for 3 h, (g) change in temperature with irradiation time, (h) relationship between the yield of CH_4 and the reaction time using 1.0 wt% Pd/TiO_2 catalyst with different light sources, (i) schematic illustration of charge transfer over Pd/TiO_2 during the photoreaction. Reproduced with permission from ref. 467. Copyright 2017 American Chemical Society.

nature of metal-support interfaces and their electronic structure critically governs photocatalytic activity through strong metal-support interactions, plasmon-driven light-matter coupling, and charge-carrier trapping and transport dynamics in heterogeneous systems.[467–470] In a study by Liu *et al.*,[467] a series of TiO_2-supported palladium photocatalysts were synthesized using a glucose reduction method (Fig. 8). These photocatalysts exhibited high activity for the photocatalytic hydrogenation of CO_2, with a notable selectivity towards CH_4 formation. Pure TiO_2 consisted of spherical aggregates of small subparticles, uniform in size and shape, with nanoparticles averaging 30–40 nm in diameter. High-resolution TEM images revealed that palladium nanoparticles had a diameter of 3 nm, with lattice spacings corresponding to the (004) plane of anatase TiO_2 and the (200) plane of Pd (Fig. 8a). As Pd loading increased, the samples exhibited improved optical responses, with absorbance in the 380–700 nm range significantly higher than that of pure TiO_2, attributed to the LSPR of Pd nanoparticles (Fig. 8b). The band gap energy of pure TiO_2 was estimated at 3.27 eV, but after Pd loading, the absorption edge shifted, reducing the E_g value to 3.06 eV for 1.5 wt% Pd/TiO_2 (Fig. 8c). The photoluminescence intensity decreased with increasing palladium loading (up to 1.0 wt%), indicating improved charge separation and reduced recombination of photogenerated charges on the Pd-loaded TiO_2 surface (Fig. 8d). However, for Pd loadings above 1.0 wt%, PL intensity increased again, which was attributed to the formation of new recombination centers by excess palladium. XPS spectra revealed that PdO was also formed during catalyst preparation and storage, with a slight shift in the PdO peaks for the used catalyst (Fig. 8e), possibly due to the formation of Pd–C, as suggested by the increased C 1s area. When photocatalytic CO_2 hydrogenation was performed under batch conditions, CH_4 was the main product, along with some CO and C_2H_6. The yields of these products increased with Pd

loading up to 1.0 wt%, with the highest yields of CH_4, CO, and C_2H_6 being 355.62, 46.35, and 39.69 μmol g^{-1}, respectively, after 3 hours of irradiation (Fig. 8f). Excessive Pd loading reduced yields, possibly due to new recombination centers or a shielding effect that inhibited light harvesting.

To investigate the effect of light, experiments were conducted in the dark at 130 °C, which corresponded to the temperature reached under light illumination (Fig. 8g), and under visible light yielded only small amounts of CH_4, indicating that Pd-loaded TiO_2 was primarily active under UV light (Fig. 8h), as supported by UV-Vis spectra. These findings demonstrated that the photocatalytic hydrogenation of CO_2 was driven by a synergistic effect between the metal and the support. Based on these observations, a reaction mechanism was proposed: Upon UV light exposure, TiO_2 absorbed energy greater than or equal to its band-gap energy, generating photogenerated electron–hole pairs. Electrons in the CB and holes in the VB were partially transferred to the surface, where the electrons migrated to adjacent Pd nanoparticles. These electrons combined with chemisorbed CO_2 to form CO_2^-, enhancing charge separation and inhibiting recombination. The holes in the VB of TiO_2 were captured by reactive atomic hydrogen, forming H^+, which was dissociated at Pd sites by combining with electrons. Activated CO_2 molecules at Pd sites reacted with H^+ and electrons to produce the intermediate Pd–C═O. This intermediate could either desorb as CO or further react with dissociated H to form Pd–C, which then reacted with more H species to produce CH_4 (Fig. 8i).

Photo-thermal catalysis, which relies on the simultaneous action of light and heat, inevitably exposes materials to high temperatures where several intrinsic limitations arise. As discussed earlier in Section 3.2, efficient charge separation can be achieved due to the presence of a built-in electric field within semiconductor materials. However, under elevated temperatures (>300 °C), accelerated lattice vibrations induce thermal quenching of photogenerated carriers, structural stability becomes compromised, and surface-defect-mediated recombination is significantly intensified. Ferroelectric semiconductors offer a potential solution because their spontaneous polarization provides an internal electric field that can drive carrier separation, yet this advantage weakens at high temperatures due to inherently limited polarization strength and polarization collapse near the Curie temperature. These challenges require the need for strategies that stabilize ferroelectric polarization and suppress both bulk and surface recombination under harsh photo-thermal operating conditions. In a recent study by Kuang *et al.*,[70] the authors harnessed the same built-in electric field of a semiconductor material to increase the efficiency of the photo-thermal CO_2 hydrogenation reaction. In their work, they used a ferroelectric $PbTiO_3$ material that has a spontaneous polarization in it, and they did surface modification to increase the polarization effect to their advantage. They first synthesized cuboidal $PbTiO_3$ nanoparticles (PTO) by hydrothermal synthesis (Fig. 9a). The morphological and crystallinity characterizations of PTO revealed a brick like structure with exposed {001} facets on its top/bottom surfaces and {100} facets on the other four lateral facets. The intrinsic ferroelectric polarization electric field of PTO is oriented along the [001] direction (*c*-axis), hence the polarization direction of the synthesized PTO was perpendicular to its top/bottom surfaces (Fig. 9b). The measured ferroelectric characteristics of the PTO was found out to be, d_{33} = 38.2 pm V^{-1} with characteristic butterfly-shaped amplitude hysteresis and a phase reversal by piezoelectric force microscopy (PFM) (Fig. 9c). The COMSOL simulation model simulated the polarization electric field strength of PTO (Fig. 9d), suggesting a electric field of up to 0.7×10^{-2} V can be spontaneously generated within PTO. This spontaneous polarization electric field in PTO directed the photogenerated carrier toward opposite polarity (001) crystal surfaces, thereby inhibiting the carrier recombination in the bulk phase.[70]

However, the next challenge was to enhance and preserve this polarization at high temperatures. To achieve this goal, the authors doped Pt into the PTO by adding Pt precursor in the hydrothermal synthesis of PTO, forming PTPO. The choice of Pt was based on its ionic radius, which closely matches Ti^{4+} and allows substitution-induced lattice distortion to enhance polarization, as well as its electronic configuration, which introduces additional energy states that promote charge localization and provide multiple transport pathways for photogenerated carriers. Pt doping was found to leave the brick-like morphology and textural properties of PTO largely unchanged, yet it introduced notable structural and electronic modifications. XRD and EPR analyses collectively showed that Pt^{2+} substitutes Ti^{4+} sites in the $[TiO_6]$ octahedra and simultaneously generates oxygen vacancies, leading to lattice distortion along the polar *c*-axis. This distortion is most pronounced at 2% Pt, which correlates with the strongest enhancement of ferroelectric polarization. PFM measurements show an increase in the effective piezoelectric coefficient from 38.2 pm V^{-1} in pure PTO to 57.2 pm V^{-1} in 2%-PTPO, confirming polarization amplification (Fig. 9e). In addition, Pt-induced impurity states cause a red-shift in optical absorption and reduce the band gap, while preserving the n-type semiconductor nature of PTO.

The PTPO and PTO were then tested for CO_2 hydrogenation reaction in flow. Catalytic testing showed that Pt doping had virtually no effect on the thermocatalytic CO_2 hydrogenation performance, with Pt-doped PTO and pristine PTO exhibiting nearly identical activity under heat-only conditions (Fig. 9f). However, under photo-thermal operation, Pt doping produced a pronounced enhancement, with 2%-PTPO delivering the highest CO_2 conversion efficiency of 66.7 mmol g^{-1} h^{-1} CO and 3.6 mmol g^{-1} h^{-1} CH_4, a 2.2-fold enhancement in electron transfer efficiency compared to pure PTO (Fig. 9f). Since thermocatalysis depends mainly on surface chemistry, the unchanged thermal performance indicates that Pt does not significantly alter surface-active sites. In contrast, the improvement under photo-thermal conditions reflects Pt-induced polarization amplification, which promotes more efficient photogenerated carrier separation.

While Pt doping enhanced internal polarization, the lack of active surface sites and the prevalence of surface carrier recombination remain significant bottlenecks. To address these, the authors leveraged the intrinsic ferroelectric properties of 2%-PTPO to drive the facet-selective photodeposition of

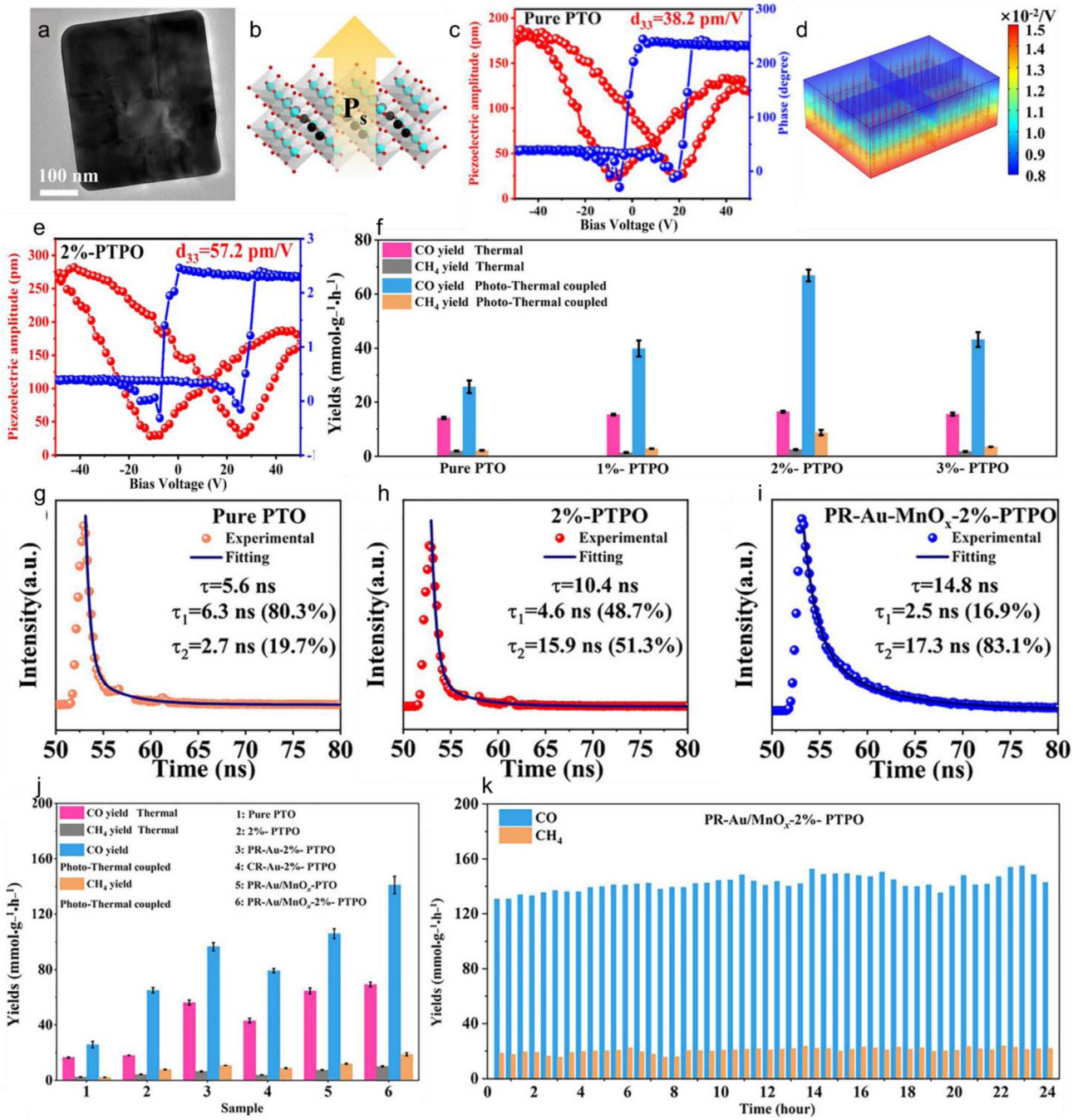

Fig. 9 Ferroelectric polarization and surface engineering for enhanced photo-thermal CO_2 hydrogenation. (a) TEM image, (b) schematic of the direction of polarization electric field, (c) amplitude and phase hysteresis loops, (d) COMSOL simulated polarization electric field, of pure PTO, (e) amplitude and phase hysteresis loops of 2%-PTPO, (f) thermal (400 °C)/photo-thermal coupled (400 °C, light intensity = 20 mW cm^{-2}) CO_2 hydrogenation performance of pure PTO and *x*%-PTPO (*x* = 1, 2, 3), (g–i) TRPL spectroscopy of pure PTO, 2%-PTPO, and PR-Au/MnO_x-2%-PTPO, respectively, (j) thermal (400 °C)/photo-thermal coupled (400 °C, light intensity = 20 mW cm^{-2}) catalytic CO_2 hydrogenation performance of PR-Au/MnO_x-2%-PTPO and its control samples, (k) continuous photo-thermal coupled catalytic CO_2 hydrogenation testing of PR-Au/MnO_x-2%-PTPO. Reproduced with permission from ref. 70. Copyright 2025, Wiley-VCH GmbH.

dual cocatalysts. By utilizing the spontaneous polarization of the PTO matrix, photogenerated electrons and holes were directionally migrated to opposing {001} facets, allowing for the spatial isolation of Au nanoparticles (electron traps) and MnO_x nanosheets (hole traps). This strategic placement transformed the crystal into a spatially isolated redox system, preventing the recombination of charge carriers at the surface. The synergy between Pt doping and dual-cocatalyst loading significantly optimized the thermodynamic and kinetic profiles of the catalyst. DFT calculations and *in situ* XPS confirmed that the inclusion of Au and MnO_x not only lowers the CO_2 adsorption energy, from −0.27 eV in pure PTO to a much more favorable

−2.57 eV in the dual-loaded system, but also acts as a powerful driving force for charge transfer. Comprehensive carrier dynamics studies, including *in situ* Kelvin probe force microscopy, time-resolved photoluminescence (TRPL), and temperature-dependent PL, provide quantitative evidence for this enhanced performance.

Photoluminescence spectroscopy revealed that the exciton binding energy, a key indicator of recombination probability, dropped dramatically from 216.7 meV in pure PTO to just 103.6 meV in the PR-Au/MnO_x-2%-PTPO system. This reduction was mirrored in the TRPL data, where the average carrier lifetime increased from 5.6 ns to 14.8 ns (Fig. 9g–i). Furthermore, *in situ* XRD and high-temperature catalytic testing demonstrated that Pt doping elevates the Curie temperature from 550 °C to 650 °C. This ensured that the material retains its crucial ferroelectric tetragonal phase at elevated reaction temperatures, maintaining the polarization-led carrier separation necessary for high-efficiency solar-to-fuel conversion.

The catalytic performance of the PR-Au/MnO_x-2%-PTPO system demonstrated the practical success of this bulk-surface engineering strategy, particularly in demanding high-temperature environments. At 400 °C, the optimized catalyst achieved a remarkable photo-thermal coupled CO_2 conversion rate of 140.8 mmol g^{-1} h^{-1}, significantly outperforming its mono-cocatalyst and unmodified counterparts while maintaining exceptional structural integrity over a 24-hour stability test (Fig. 9j and k). Most notably, the catalyst excels where traditional ferroelectrics fail; while pure PTO experienced a decline in photo-activity at 550 °C due to a ferroelectric-to-paraelectric phase transition, the Pt-doped samples retain their tetragonal phase and spontaneous polarization up to 650 °C. Consequently, at 550 °C, PR-Au/MnO_x-2%-PTPO delivers a CO_2 conversion rate of 235.7 mmol g^{-1} h^{-1} for CO, nearly double the efficiency of its purely thermal catalytic performance, proving that Pt doping effectively extends the operational temperature window for ferroelectric-enhanced catalysis.

Ultimately, this study highlights how the built-in electric field, as a fundamental property inherent to a material's crystal structure and electronic alignment, can be precisely exploited to overcome the most persistent kinetic challenges in complex chemical reactions. It underscores that by tailoring internal polarization alongside surface architecture, one can harness the internal electronic forces of ferroelectrics to drive high-performance solar-to-fuel conversion.[70]

Apart from acting as cocatalysts and increasing the electron–hole separation in semiconductors, metals can also act as light harvesters and form hot charge carriers through LSPR, which can further boost the catalytic performance. In a study by Liu *et al.*,[471] plasmonic Rh nanoparticles demonstrated significant photocatalytic properties by reducing activation energies and exhibiting strong product photo-selectivity in CO_2 hydrogenation reactions (Fig. 10). This design exemplifies a supported plasmonic metal on an insulating oxide, where the metal nanostructures function as bifunctional centers for both photon harvesting and surface catalysis. The Rh photocatalyst, consisting of 37 nm Rh nanocubes (Fig. 10a) dispersed on Al_2O_3 with a 1.02% mass loading (Rh/Al_2O_3), showed that under mild illumination, the activation energies for CO_2 hydrogenation were lowered by approximately 35% compared to thermal activation energies (Fig. 10e and f). Specifically, the selectivity for CH_4 over CO was remarkably enhanced, achieving over 86% under blue light and more than 98% under UV light, with reaction rates doubling the thermocatalytic rates at 350 °C.

The Rh nanocubes, with precisely tunable size and LSPR wavelength, had sharp corners that concentrated light and liberated hot carriers. The study found that the LSPR of Rh nanocubes, which was 334 nm (3.71 eV) in ethanol, was broadened and blue-shifted when placed on porous Al_2O_3 (Fig. 10b). Unlike Au nanoparticles, which produced only CO regardless of illumination, Rh nanoparticles exhibited high selectivity towards CH_4 production only under illumination (Fig. 10g). This difference arose because the weaker oxygen binding on Au surfaces prevented C–O bond cleavage in CHO intermediates, whereas the stronger O adsorption energy on Rh stabilized these intermediates and enabled their dissociation toward CH_4 formation.[471]

Dark thermocatalytic reactions on Rh nanoparticles showed moderate selectivity with a CH_4 ratio of approximately 60 : 40 across different temperatures and reaction rates. However, under UV illumination, the CH_4 production rate was significantly enhanced, with a photo-selectivity exceeding 95% (Fig. 10c). This high selectivity persisted even under H_2-deficient conditions during illumination but dropped in the dark, indicating that the selective production of CH_4 was driven by light rather than thermal effects or excess H_2.

The study confirmed that the high photo-selectivity was not due to local heating but was attributed to the selective activation of CHO intermediates by plasmon-generated hot electrons. Under UV illumination at ~1 W cm^{-2}, the reaction rate showed a super-linear dependence on light intensity, with an exponent of $n = 2.1$ at 623 K and 2.4 at 573 K, suggesting multiple excitations of vibrational modes by hot electrons (Fig. 10d). The reaction kinetics of CO_2 hydrogenation on Rh and Au photocatalysts were investigated, revealing that the activation energy (E_a) for CH_4 production under UV light was reduced to 50.4 kJ mol^{-1} compared to 78.6 kJ mol^{-1} under thermocatalytic conditions. This reduction in E_a was also observed for CO production on the Au photocatalyst, decreasing from 55.8 kJ mol^{-1} in the dark to 39.5 kJ mol^{-1} under visible light.

They concluded that the transfer of hot electrons from plasmonic metal nanoparticles to specific intermediates selectively activates certain reaction pathways by interacting with anti-bonding orbitals, thus providing a method to control the selectivity of catalytic processes. In contrast, in thermocatalytic reactions, phonons activate both CHO and CO intermediates, leading to comparable production rates of CH_4 and CO on the ground-state reaction coordinate (Fig. 10h).

The previous study demonstrated that the plasmonic resonance of Rh nanoparticles is confined to the UV region. However, red-shifting the plasmonic resonance further into the visible region could enhance the photocatalyst's effectiveness within the solar spectrum. Assembling plasmonic nanoparticles into closely packed clusters to create 'hot spots' through plasmonic coupling is one approach that could lead to more

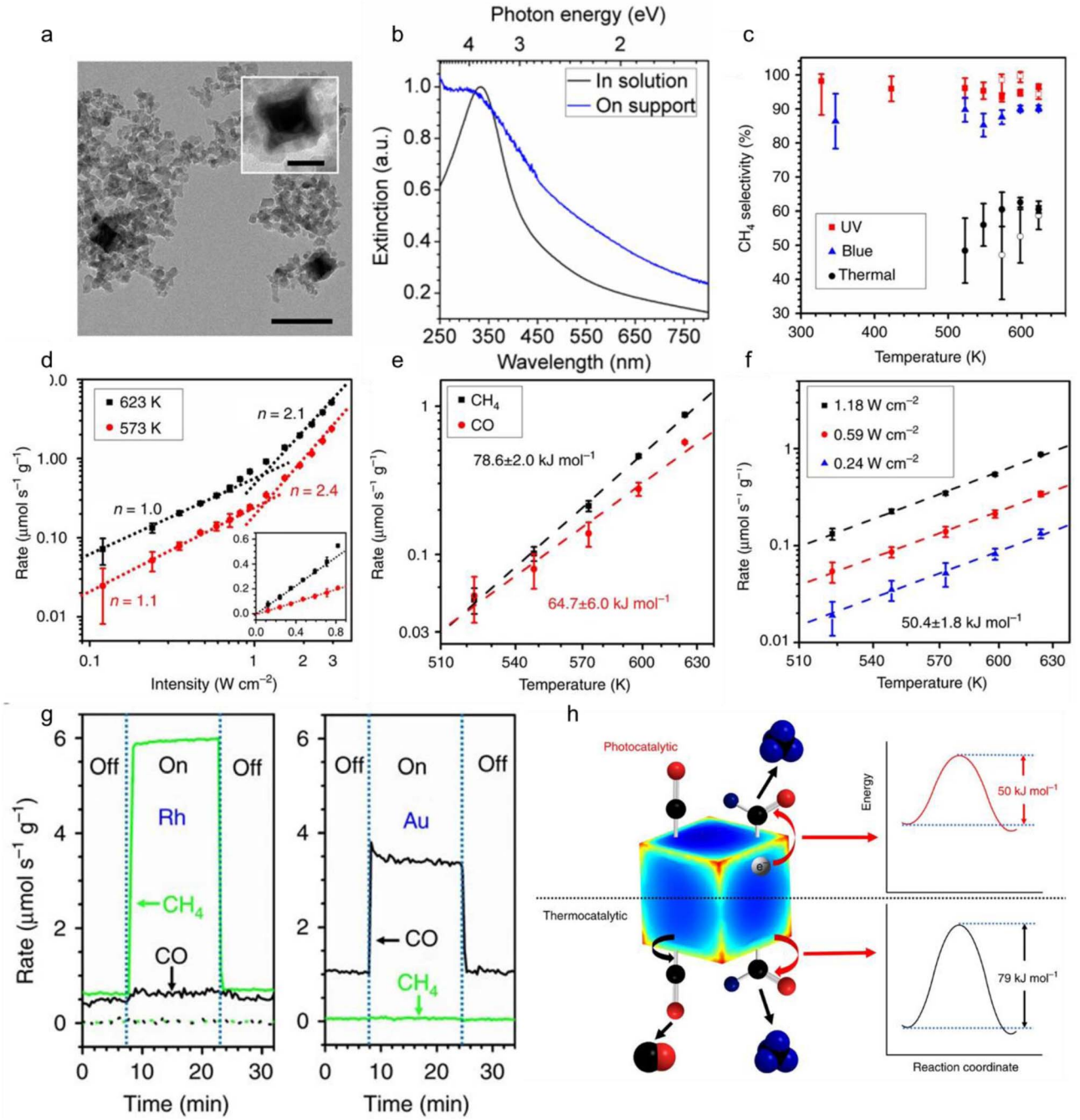

Fig. 10 Plasmon driven selectivity for CO_2 hydrogenation over Rh/Al_2O_3 photocatalyst. (a) TEM images of the Rh/Al_2O_3 photocatalyst. Scale bar, 100 nm (inset: 25 nm), (b) extinction spectra of rhodium nanocubes, (c) selectivity towards CH_4 of the thermo- (black circles) and photocatalytic reactions under ultraviolet (365 nm, red squares) and blue (460 nm, blue triangles) illumination as a function of temperature under H_2-rich ($CO_2 : H_2 = 1 : 5.5$, solid symbols) and H_2-deficient ($CO_2 : H_2 = 1 : 3.1$, open symbols) conditions. (d) rates of CH_4 photo-production as a function of ultraviolet light intensity at 623 (black squares) and 573 K (red circles). (e) Thermocatalytic reaction rates of CH_4 (black squares) and CO (red circles) production on Rh/Al_2O_3 as a function of temperature, (f) photoreaction rates for CH_4 production on Rh/Al_2O_3 under 1.18 (black squares), 0.59 (red circles) and 0.24 W cm^{-2} (blue triangles) ultraviolet illumination as a function of temperature, (g) rates of CH_4 (green) and CO (black) production at 623 K on Rh/Al_2O_3 or Au/Al_2O_3 (solid lines) and Al_2O_3 (dotted lines) under dark and ultraviolet illumination at 3 W cm^{-2}, (h) the thermocatalytic reaction activates both CO–Rh bonds and CH–O bonds to produce CO and CH_4, respectively. Reproduced with permission from ref. 471. Copyright 2017 Springer Nature.

selective and efficient CH_4 production from CO_2 hydrogenation, even under direct or mildly concentrated sunlight.

Conventional plasmonic nanocatalysts have intense but narrow absorption spectra. In our lab, we focus on developing antenna–reactor systems using a unique broadband-absorbing 'black gold'[226] to enhance plasmonic absorption and broaden the absorption profile in the visible region through plasmonic coupling and 'hot spot' formation. We designed dendritic

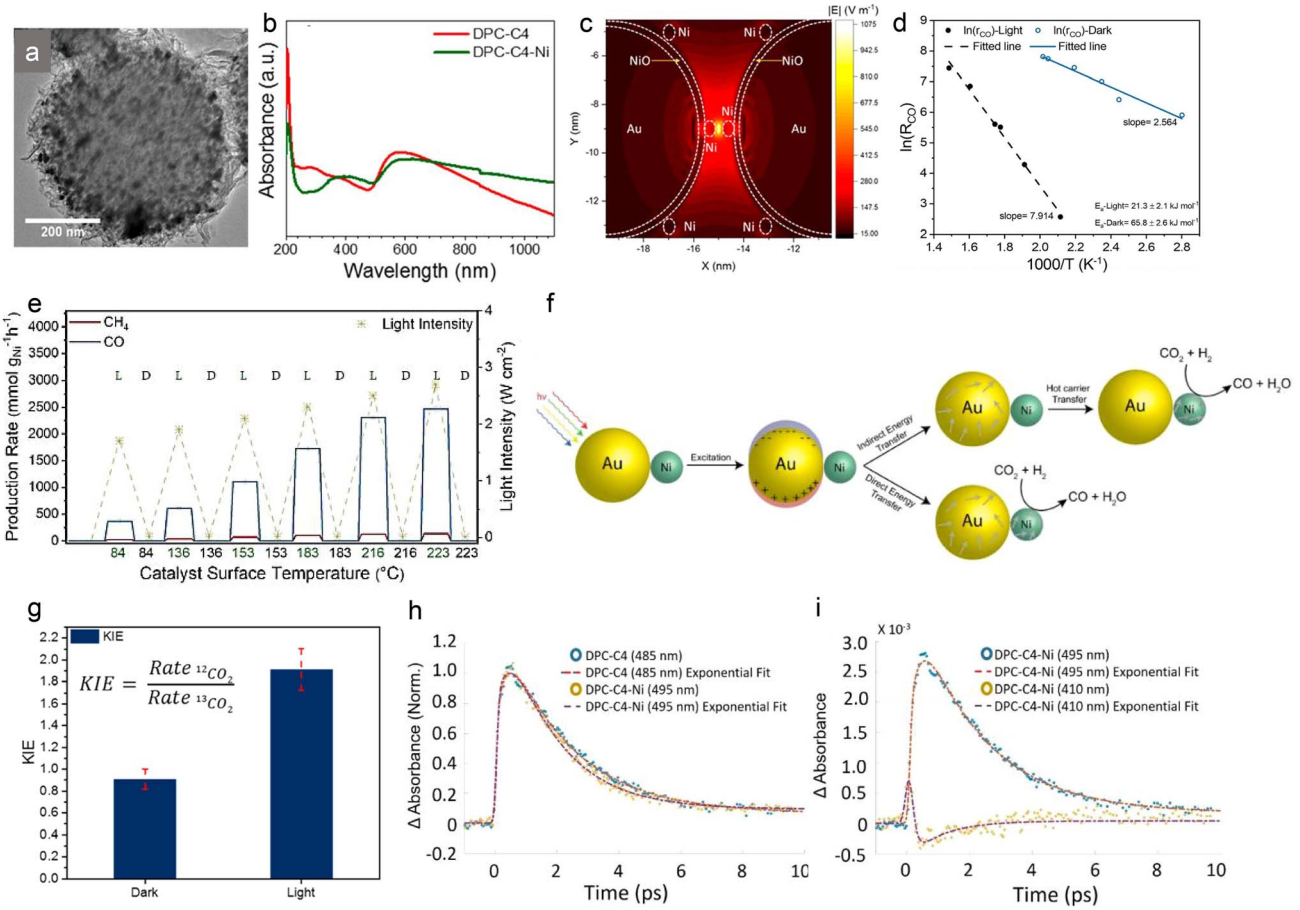

Fig. 11 Photocatalytic CO_2 hydrogenation over black gold-Ni antenna–reactor system. (a) TEM image of DPC-C4-Ni, (b) UV-DRS spectrum of DPC-C4 and DPC-C4-Ni, (c) electric field intensity (V m^{-1}) in DPC-C4-Ni using FDTD simulation, (d) Arrhenius plot for E_{app} of the CO_2 hydrogenation in the dark and light, (e) production rate of CH_4 and CO in light at various intensities and in dark at different temperatures, (f) schematic of direct *vs.* indirect energy transfer processes that can result in hot-electron population in a Ni reactor, (g) KIE for CO_2 hydrogenation, measured in dark and light, (h) kinetic trace extracted at the maximum of the winglet for both samples, (i) kinetic trace extracted at the minimum of bleach observed at around 410 nm for DPC-C4-Ni. Reproduced with permission from ref. 248. Copyright 2023 American Chemical Society.

plasmonic colloidosomes (DPC) of Au loaded with nickel sites (DPC-C4-Ni)[248] (Fig. 11). This design is an example of antenna–reactor geometry where plasmonic metal functions as a light harvester and the other metal functions as an active site for catalysis. DPC-C4-Ni was synthesized by loading Au nanoparticles on dendritic fibrous nanosilica (DFNS) over four cycles (Fig. 11a). DPC-C4-Ni absorbed broadband light from the solar spectrum (Fig. 11b) and generated intense localized hot spots with strong electric fields, as shown by the finite difference time domain (FDTD) simulations (Fig. 11c). When DPC-C4-Ni was illuminated with visible light, it became highly catalytically active, enabling CO_2 hydrogenation using solar energy (Fig. 11e). We conducted CO_2 hydrogenation reactions at various light intensities and temperatures, observing a superlinear dependence of CO production on light intensity with a power law exponent of 5.6. This behavior was characteristic of multielectron-driven plasmonic reactions. The apparent activation energy (E_{app}) for the reaction under light was 21.3 ± 2.1 kJ mol^{-1}, significantly lower than the E_{app} of 65.8 ± 2.6 kJ mol^{-1} in the dark, indicating a substantial decrease in the activation energy barrier (Fig. 11d). The observed photo enhancement in CO production also suggested the involvement of a nonthermal pathway in CO_2 hydrogenation, with the thermal effect playing a minimal role.

This hypothesis was further supported by an increase in the kinetic isotope effect (KIE), the ratio of photocatalytic rates for the $^{12}CO_2$ and $^{13}CO_2$ isotopes (Fig. 11g). The enhanced KIE was a distinct signature of the nonthermal activation of reactions. In DPC-C4-Ni, the hypothesis was that the hot electrons were either generated in Ni after LSPR decay (a direct mechanism) or charges were transferred from Au to Ni (an indirect mechanism) (Fig. 11f). A fraction of these hot electrons interact with reactant CO_2, activating it and lowering the activation energy barrier. Additionally, during the damping of black gold LSPR, electrons in the nickel d-band could be excited to higher energy levels (hot electrons), and hot-electron transfer from Au to Ni could occur, filling the Ni d-band.

To study the involvement of hot electrons and their transfer mechanism to Ni sites, we performed ultrafast transient absorption spectroscopy (TAS) measurements. The formation of hot carriers and elastic electron–electron scattering was observed, with estimated processes occurring at 302 ± 63 fs and

419 ± 107 fs for DPC-C4 and DPC-C4-Ni, respectively (Fig. 11h). The first decay, related to electron–phonon scattering time, was estimated to be 2.16 ± 0.11 ps for DPC-C4 and 1.64 ± 0.12 ps for DPC-C4-Ni. The reduced electron–phonon lifetime in DPC-C4-Ni suggested changes in the plasmon electronic structure consistent with hot carrier transfer from Au to Ni. A negative signal centered at 410 nm in the DPC-C4-Ni sample, absent in DPC-C4, corresponded to the Ni d–d transitions (Fig. 11i). The negative signal indicated a decrease in empty states in the Ni d-band, consistent with hot-electron donation from Au to Ni. These findings suggested that the indirect hot-electron generation mechanism played a dominant role in Ni's electronic changes and, consequently, its catalytic behavior.[248]

As discussed in the earlier example of DPC-C4-Ni, one way to enhance the catalytic activity of plasmonic nanostructures is to integrate plasmonic metals with catalytically active metals to form antenna–reactor bimetallic heterostructures.[181,472–476] Another example of such a strategy is a study by Xie *et al.*[477] in which the authors explored surface-alloyed Au@AuRu plasmonic nanoparticles loaded on graphitic carbon nitride (g-C_3N_4) to create a bimetal-semiconductor heterojunction (Au@AuRu/g-C_3N_4) (Fig. 12). This catalyst was designed for efficient hot-electron-induced CO_2 hydrogenation under mild conditions. By doping a low content of catalytically active Ru atoms into the surface of Au nanoparticles (Fig. 12a–c), the production selectivity was significantly enhanced, shifting from 63.1% CO to 98.4% CH_4 (Fig. 12e). The efficiency of CO_2 methanation reached 103 μmol g^{-1} h^{-1} under light at 150 °C, far exceeding its performance in dark reactions (Fig. 12d) and surpassing that of reference catalysts Au/g-C_3N_4 and Au@Ru/g-C_3N_4 (Fig. 12e).

The photothermal CO_2 hydrogenation performance of Au@AuRu/g-C_3N_4 at low temperatures surpassed that of noble metal (Au, Pd, Rh, Ru) and oxide (In_2O_3)-based photocatalysts reported in the literature. The production rate under visible light (400 nm < λ < 650 nm) was superior to that under ultraviolet light (λ < 400 nm), demonstrating that the LSPR effect of Au plays a crucial role in promoting CO_2 conversion (Fig. 12f). This was also evident from the light intensity dependence study (Fig. 12e). Hydrogen temperature-programmed desorption (H_2-TPD) and CO_2/CO desorption experiments were conducted to evaluate the adsorption capacities of various catalysts. Ru-modified Au@AuRu/g-C_3N_4 and Au@Ru/g-C_3N_4 showed enhanced H_2 adsorption and dissociation, as well as stronger CO_2 and CO adsorption compared to their counterparts, facilitating efficient CO_2 conversion to CH_4. g-C_3N_4 was also found to adsorb CO_2 weakly (~91 °C) (Fig. 12h).

Transient absorption spectroscopy was employed to provide direct evidence of electron transfer from Au@AuRu NPs to g-C_3N_4 (Fig. 12i). Unlike Au/g-C_3N_4, Au@AuRu/g-C_3N_4 exhibited a slower electron injection process after 15 ps, attributed to the surface states in the AuRu shell retaining electrons for a longer duration before injecting them into the semiconductor. At 1 ns, the residual electron signal in Au@AuRu/g-C_3N_4 was 69.39% of the initial value, while this ratio for Au/g-C_3N_4 was only 33.17%. This indicated that hot electrons generated by Au were transferred to the AuRu shell and then injected into g-C_3N_4 in Au@AuRu/g-C_3N_4, prolonging the lifetime of the plasmon-induced electrons and enhancing the catalytic reaction (Fig. 12j). The accumulated hot electrons on g-C_3N_4 promoted the activation of CO_2 adsorbed on the metal/semiconductor interfaces. Based on *in situ* DRIFT results, CO_2 was converted into CO, which was then adsorbed on the metal surface for further hydrogenation to form CH_4 (Fig. 12k).[477]

Light-driven chemical transformations on plasmonic nanostructures have traditionally utilized noble metals like Ag and Au due to their efficient plasmonic properties in the visible range. However, given the high cost and scarcity of these metals, there have been efforts to explore more abundant alternatives such as Al, Cu, and Fe. A significant challenge with these metals is their tendency to form oxide layers due to spontaneous oxidation, and their plasmon resonances often lie in the UV region, unlike the visible plasmonic resonances of Au, Ag, and Pt.

Halas *et al.*[238] developed a notable plasmonic Al@Cu_2O antenna–reactor heterostructure using earth-abundant materials, aiming to harness charge-carrier generation for the catalytic conversion of CO_2 into CO under milder conditions compared to purely thermally driven processes (Fig. 13). This study highlighted Al as a plasmonic antenna that enhances reactivity on adjacent materials, in this case, the semiconducting oxide Cu_2O. The Al@Cu_2O heterostructure showed better external quantum efficiencies (EQE) for CO formation. In contrast, increasing irradiation intensities on pure Cu_2O did not improve EQE, highlighting the unique advantage of the plasmonic Al core. A combination of experimental investigations and theoretical simulations was employed to distinguish the respective roles of plasmon-induced charge carrier generation and photothermal heating in driving the photocatalytic reverse water–gas shift reaction (rWGS) on Al@Cu_2O.

Electron microscopy and elemental analysis revealed that the pristine Al nanocrystals (Al NCs) had a nominal diameter of 100 nm (Fig. 13a). To form the plasmonic antenna–reactor nanoparticles, a ~15 nm thick Cu_2O shell was grown around the Al core, which was separated from the Al metal by a 2–4 nm self-limiting amorphous Al_2O_3 layer. The UV-Vis-NIR extinction spectrum showed a dipolar plasmon mode at 465 nm for pristine Al NCs, which shifted to ~550 nm after the Cu_2O shell growth. The rate of CO formation catalyzed by Al@Cu_2O was significantly higher than that of Cu_2O and pristine Al without the reactive Cu_2O shell, especially under higher illumination intensities (Fig. 13b). The study also investigated the steady-state heating of the photocatalysts under illumination using high-resolution spatial and temporal mapping of temperature variations. At a maximum visible light intensity of 10 W cm^{-2} in air, the Al NCs/γ-Al_2O_3 catalyst surface reached temperatures upwards of 175 °C. Despite this heating, the photocatalytic rWGS on Al@Cu_2O was characterized by higher product selectivity and yields under illumination at comparable temperatures (Fig. 13c). Notably, the average steady-state surface temperature of 175 °C was below the 200 °C onset temperature for product formation in thermal-driven rWGS, yet it achieved a significantly higher overall reaction rate.

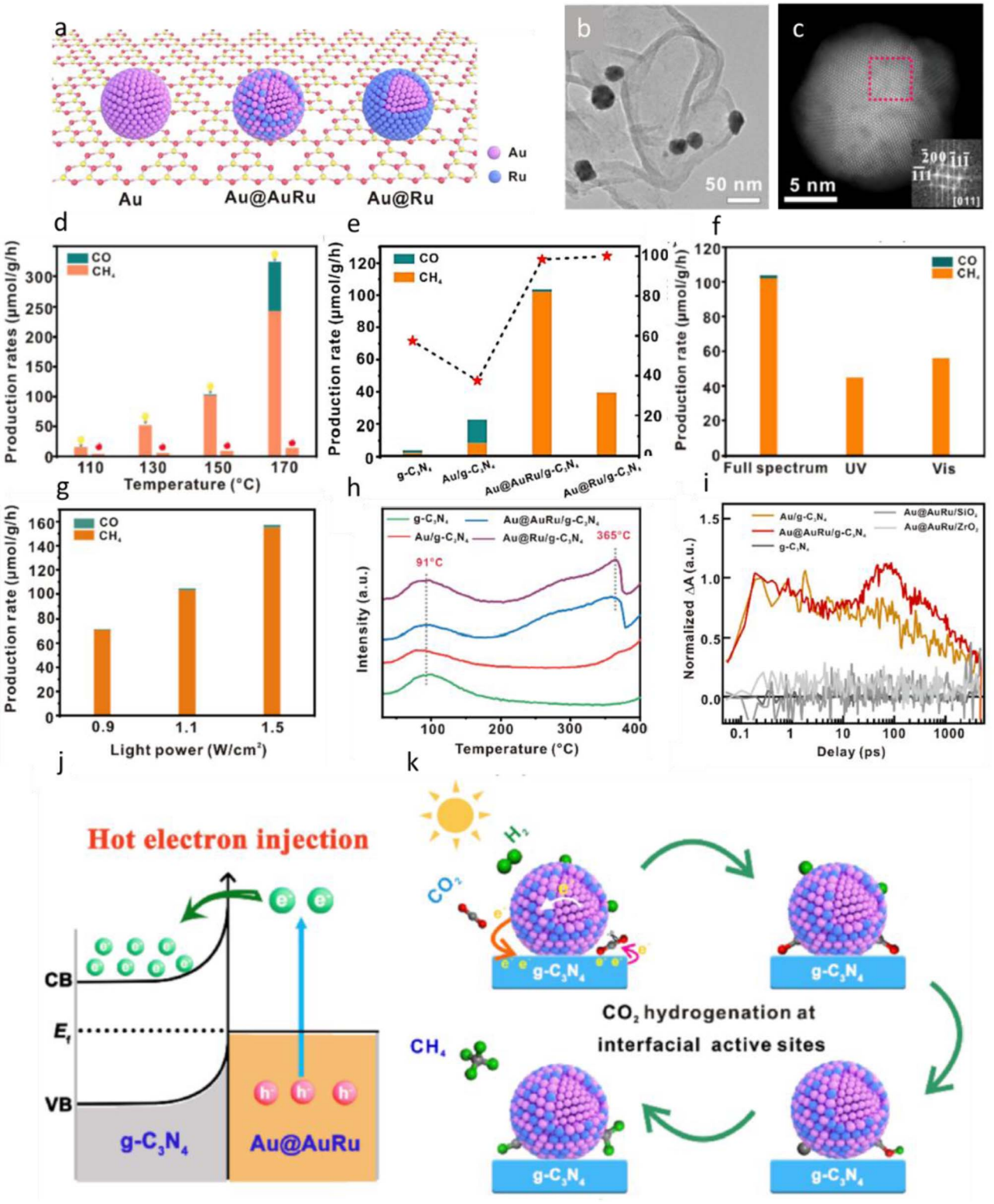

Fig. 12 Photocatalytic CO_2 hydrogenation over Au@AuRu/g-C_3N_4 plasmon–semiconductor hybrid. (a) Schematic illustration of different metal NPs supported on g-C_3N_4, (b) TEM image of Au@AuRu/g-C_3N_4, (c) atomic-resolution HAADF-STEM image of Au@AuRu NPs. (d) Production rates over Au@AuRu/g-C_3N_4 in the dark and under irradiation at different temperatures for 4 h, (e) production rates over different catalysts at 150 °C under illumination, (f) production rates obtained by the prepared catalysts under the light of different wavelengths (UV: $\lambda < 400$ nm, Vis: 400 nm $< \lambda <$ 650 nm), (g) the production rates of Au@AuRu/g-C_3N_4 at 150 °C under different light powers, (h) CO_2-TPD curves of g-C_3N_4, Au/g-C_3N_4, Au@AuRu/g-C_3N_4, and Au@Ru/g-C_3N_4, (i) normalized transient absorption kinetics traces for Au/g-C_3N_4, Au@AuRu/g-C_3N_4, Au@AuRu/ZrO_2, Au@AuRu/SiO_2, and g-C_3N_4, (j and k) schematic illustration of hot electron injection and catalytic process. Reproduced with permission from ref. 477. Copyright 2022 Elsevier.

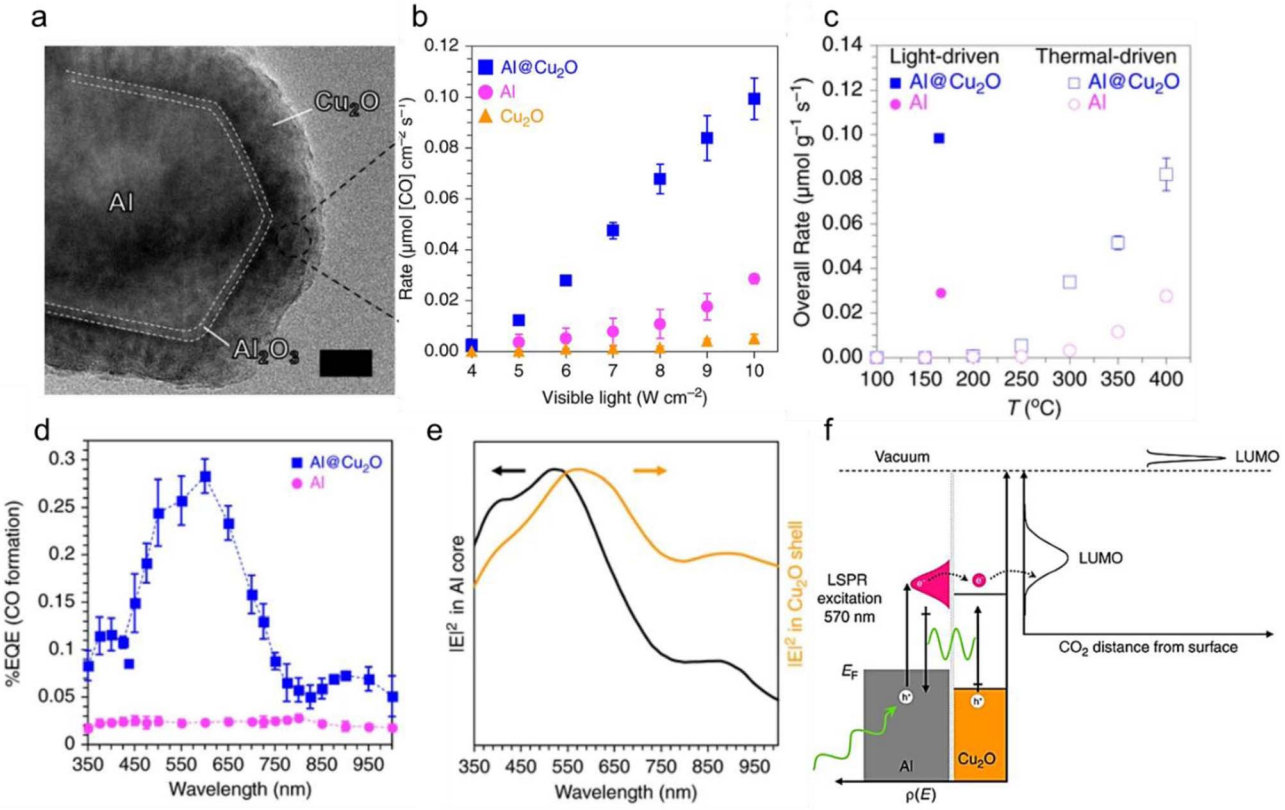

Fig. 13 Photocatalytic CO_2 hydrogenation over plasmon–semiconductor antenna–reactor Al@Cu_2O. (a) High-resolution TEM image of Al and of Al@Cu_2O nanoparticles, scale bar: 20 nm, (b) the impact of visible light intensity on the rate of CO formation on photocatalysts prepared from Cu_2O, Al NCs and Al@Cu_2O, (c) the overall rate of products formation as a function of applied temperature in purely thermal-driven (light off) rWGS for oxide supported Al NCs and Al@Cu_2O (unfilled data points). For comparison, the reaction rates during the light-induced process (10 W cm^{-2}) are shown at the corresponding recorded temperatures for oxide-supported Al NCs and Al@Cu_2O (filled data points), (d) the measured EQE as a function of illumination wavelength for oxide-supported Al@Cu_2O compared to Al *vs.* illumination wavelength, (e) numerically calculated local electric field strength $|E(r)|^2$ in Al core (left axis) and Cu_2O shell (right axis), (f) energy band diagram of Al@Cu_2O for plasmon-mediated carrier generation for injection into unoccupied state of CO_2 for C–O bond activation. Reproduced with permission from ref. 238. Copyright 2017 Springer Nature.

Further analysis revealed that coating Al NCs with a Cu_2O shell substantially enhanced EQE, particularly around the dipolar plasmon resonance at ~570 nm (Fig. 13d). The wavelength-dependent CO formation was compared with local electric field enhancement, calculated by finite element method (FEM) (Fig. 13e). The study demonstrated that the rate of carrier generation from plasmon decay was directly proportional to the plasmon-induced internal electric field enhancement. The Finite Element Method (FEM) simulations showed that the calculated electric field enhancement ($|E(r)^2|$) in both the Al core and the Cu_2O shell qualitatively matched the measured EQE spectrum (Fig. 13e). The twin mechanisms of carrier generation, direct or indirect energy transfer, both contributed to enhanced hot-carrier densities for chemical transformations. To isolate the influence of the plasmonic core, a model structure was created where the Al core was replaced with a dielectric Al_2O_3 sphere of the same size. In this scenario, the local electric field enhancement in the Cu_2O shell did not reproduce the experimental EQE spectrum, validating the role of the Al antenna in carrier generation through plasmon decay.

The higher efficiency of light-assisted rWGS on Al@Cu_2O compared to pristine Al NCs was attributed to the concurrent enhancement in surface catalytic activity and carrier generation rates. The energy diagram and schematic of the proposed elementary steps for plasmon-induced carrier-assisted rWGS on Al@Cu_2O were illustrated (Fig. 13f). The negative electron affinity of CO_2 posed a challenge for electron injection to form CO_2^-, the first and most difficult step in CO_2 activation. However, CO_2 adsorption on Cu_2O surfaces led to charge redistribution, reducing the energy barrier for transient electron transfer to unoccupied states of adsorbed CO_2, thus facilitating CO_2 activation.

The study concluded that the unique selectivity observed during light-induced processes on Al@Cu_2O could be explained by plasmon-induced selective C–O bond activation and nonthermal desorption of CO from reactive surface sites. Although a 2–4 nm amorphous Al_2O_3 shell enveloped the Al core, hot-carrier tunneling to the oxide surface remained feasible, facilitated by the abundant defect states within the Al_2O_3 layer. The study provided evidence for this hot-carrier

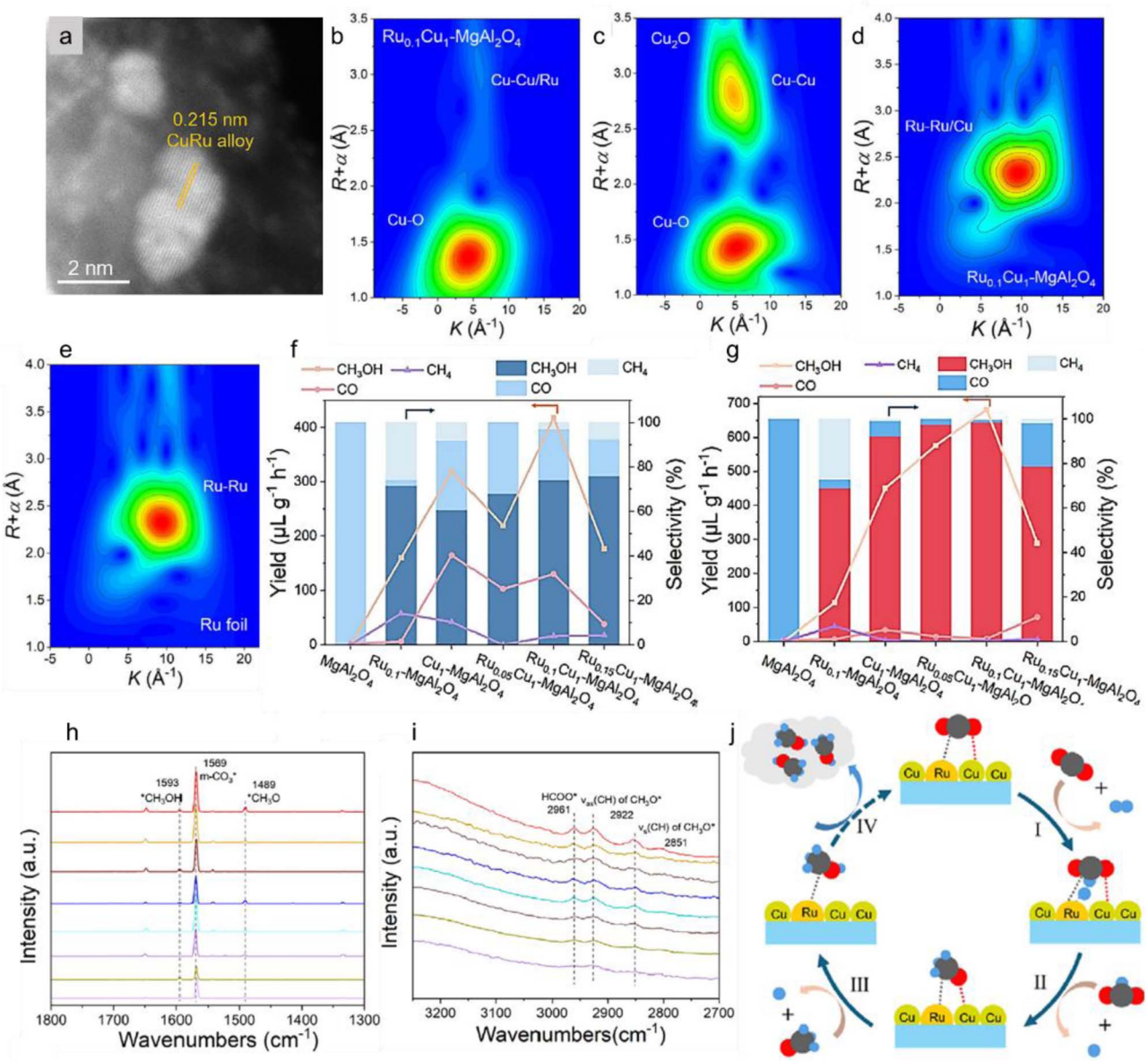

Fig. 14 Structural and performance characterization of the RuCu alloy catalyst for photothermal CO_2 hydrogenation. (a) HAADF-STEM image of $Ru_{0.1}Cu_1$-$MgAl_2O_4$, (b–e) WT-EXAFS contour plots of activated $Ru_{0.1}Cu_1$-$MgAl_2O_4$, in comparison with Cu_2O, Ru foil which were used as reference materials, (f) thermal catalytic performance of the Ru_xCu_y-$MgAl_2O_4$ catalyst, (g) photothermal catalytic performance of the Ru_xCu_y-$MgAl_2O_4$ catalyst, (h and i) *In situ* DRIFTS obtained for activated $Ru_{0.1}Cu_1$-$MgAl_2O_4$ catalytic hydrogenation of CO_2, (j) schematic illustration of intermediate adsorption and conversion on RuCu catalytic sites during CO_2 hydrogenation. Reproduced with permission from ref. 162. Copyright 2026 Wiley-VCH GmbH.

tunneling mechanism through the direct dissociation of adsorbed CO_2 on pristine Al NCs under visible light at ambient conditions.

Overall, this work demonstrated that the efficiency of resonance energy transfer in plasmon-enhanced photocatalysis primarily depends on the overlap between the LSPR absorption of the plasmonic metal and the optical transitions in the nearby semiconductor. Two mechanisms for resonance energy transfer were discussed: near-field enhancement associated with radiative plasmon decay and dipole–dipole coupling in non-radiative plasmon-induced resonance energy transfer (PIRET). While the FEM simulation results were interpreted in the context of near-field enhancement, the study acknowledged the plausibility of PIRET as well.[238]

Plasmonic catalysts have shown immense promise in CO_2 conversion processes; however, their widespread application is significantly hindered by a heavy reliance on noble metals like Au and Ag. To find more sustainable alternatives, many researchers have pivoted toward Al and Cu, as both metals exhibit strong LSPR in the visible range. Yet, these non-noble alternatives suffer from poor stability and are notoriously prone to oxidation, which degrades their catalytic efficacy over

time. In a recent study, Ye *et al.*[162] addressed this fundamental stability-performance trade-off by developing an alloy-based catalyst utilizing Cu and Ru. By strategic alloying, they not only mitigated the oxidation issues inherent to copper but also harnessed the resulting system for the efficient photothermal conversion of CO_2 specifically into methanol. This system represents a bimetallic plasmonic alloy or alloy-based antenna–reactor, where the electronic coupling between a plasmonic metal and a transition metal is strategically utilized to enhance both catalytic stability and selectivity.

The synthesis of the CuRu catalysts was performed using a wet impregnation–precipitation method on a $MgAl_2O_4$ support prepared *via* lyophilization, resulting in highly dispersed metal species that were initially invisible to XRD but clearly resolved through HAADF-STEM. The HAADF-STEM images reveal bright contrast regions corresponding to CuRu alloy nanoparticles uniformly distributed across the support (Fig. 14a). To resolve the local atomic environment, Wavelet-Transformed EXAFS (WT-EXAFS) was employed; the 2D contour plots distinguished a dominant Cu–O coordination at 1.5 Å and a Cu–Ru/Cu signal at 2.2 Å, revealing a sophisticated electronic coupling where Cu exists in a partially oxidized state ($Cu^{\delta+}$) stabilized by metallic Ru (Fig. 14b–e). This synergy was further validated by *in situ* irradiated XPS and CO-DRIFTS, which show a light-induced electron transfer from Ru to Cu, effectively "pumping" electrons to maintain the active metallic Cu^0 state and preventing deactivation. Consequently, the alloy exhibits a LSPR band at ~590 nm that not only broadens light absorption but also facilitates a potent photothermal conversion, providing the localized thermal energy and electronic environment necessary for the selective hydrogenation of CO_2 to methanol under mild conditions.

The catalytic evaluation of the Ru_xCu_y-$MgAl_2O_4$ system highlighted the transformative impact of the RuCu alloy on both activity and selectivity, particularly when transitioning from purely thermal to photothermal conditions. While thermal catalysis yields were comparatively low (Fig. 14f), the $Ru_{0.1}Cu_1$ catalyst demonstrated superior performance under visible light (640 μL g^{-1} h^{-1}), significantly outperforming its monometallic counterparts in the selective hydrogenation of CO_2 to methanol (Fig. 14g). To understand the surface kinetics driving this selectivity, *in situ* DRIFTS was employed to monitor the intermediates under reaction conditions. The vibrational bands of *HCOO at 1593 and 2961 cm^{-1} were observed, while peaks at 1489, 2851, and 2922 cm^{-1} were attributed to methoxy species (*CH_3O) (Fig. 14h and i). These results confirmed a stepwise hydrogenation pathway from CO_2 to CH_3OH *via* formate and methoxy intermediates (Fig. 14j). Furthermore, the catalyst showcased exceptional long-term stability, maintaining its production rate over a 60-hour continuous test, which was attributed to the Ru to Cu electron transfer that preserves the Cu sites in their reduced, active form against oxidative poisoning. Ultimately, the mechanism was driven by the Cu LSPR-induced photothermal effect, which supplied localized heat to lower the activation barrier, while the RuCu electronic synergy manages the surface intermediates to ensure high methanol selectivity and sustained durability.

This study demonstrated that the RuCu alloy system successfully bypasses the inherent instability of copper-based plasmonics through strategic electronic coupling. By leveraging the synergistic antenna–reactor geometry, the results highlight that the reactor metals in such configurations do not merely serve as active catalytic sites but play a critical role in stabilizing the plasmonic metal against oxidative deactivation.[162]

4.2. CO_2 reduction with water

Hydrogen gas is widely used to reduce CO_2. However, conventional H_2 production methods, such as steam reforming ($H_2O + CH_4 \rightleftharpoons 3H_2 + CO$) and petroleum cracking, are energy-intensive and generate substantial greenhouse gas emissions. To minimize the CO_2 emissions from H_2 production, alternative technologies for CO_2 reduction are urgently required. Photocatalytic CO_2 reduction using water presents an attractive solution to both energy and environmental challenges. Achieving CO_2 reduction under visible light, which accounts for 45% of solar energy, using water instead of organic electron donors or H_2 gas, is a key objective in photocatalysis. Significant efforts have focused on developing highly efficient photocatalysts for this purpose.[104,189,209,243,478–541]

The photocatalytic conversion of CO_2 with H_2O involves two critical half-reactions: the reduction of CO_2 by photogenerated electrons and protons, and the oxidation of H_2O by photogenerated holes. Strategies like doping, defect engineering, and heterostructure fabrication have been employed to enhance the efficiency of conventional semiconductors.[527–536] For instance, Xie *et al.*[527] reported atomically thin layers of sulfur-deficient $CuIn_5S_8$ with charge-enriched Cu–In dual sites, demonstrating near 100% selectivity for CH_4 production from CO_2 under visible light (Fig. 15). The $CuIn_5S_8$ single-unit-cell layers achieved a CH_4 evolution rate of 8.7 μmol g^{-1} h^{-1}, attributed to the formation of a highly stable Cu–C–O–In intermediate. The defects in the catalyst design acted as trapping sites for photogenerated electrons or holes, thereby improving carrier separation. The atomically thin 2D layers provided abundant low-coordinated dual-metal sites, allowing simultaneous M–C and M–O bond formation, stabilizing intermediates, and enhancing reaction selectivity towards CH_4. High-resolution transmission electron microscopy (HRTEM) (Fig. 15a) showed the high orientation along the [001] projection, and atomic force microscopy (AFM) confirmed single-unit-cell thickness (~1.07 nm). The defects were characterized by electron spin resonance (ESR) signal ($g = 2.003$) (Fig. 15b) and an upshift in the S 2p XPS peak, indicating the presence of S vacancies (Fig. 15c). The electronic band structures of V_S-$CuIn_5S_8$ were analyzed using synchrotron radiation photoemission spectroscopy (SRPES) (Fig. 15d), and UV-Vis spectra (Fig. 15e) revealed suitable band gaps and band edge positions for CO_2 reduction and O_2 evolution under visible light (Fig. 15f). Compared to pristine $CuIn_5S_8$, the sulfur-deficient layers exhibited a 5.4-fold increase in CH_4 evolution rate and near 100% selectivity for CH_4 over CO (Fig. 15g). V_S-$CuIn_5S_8$ showed enhanced visible-light absorption, higher surface photovoltage (SPV) peak intensity

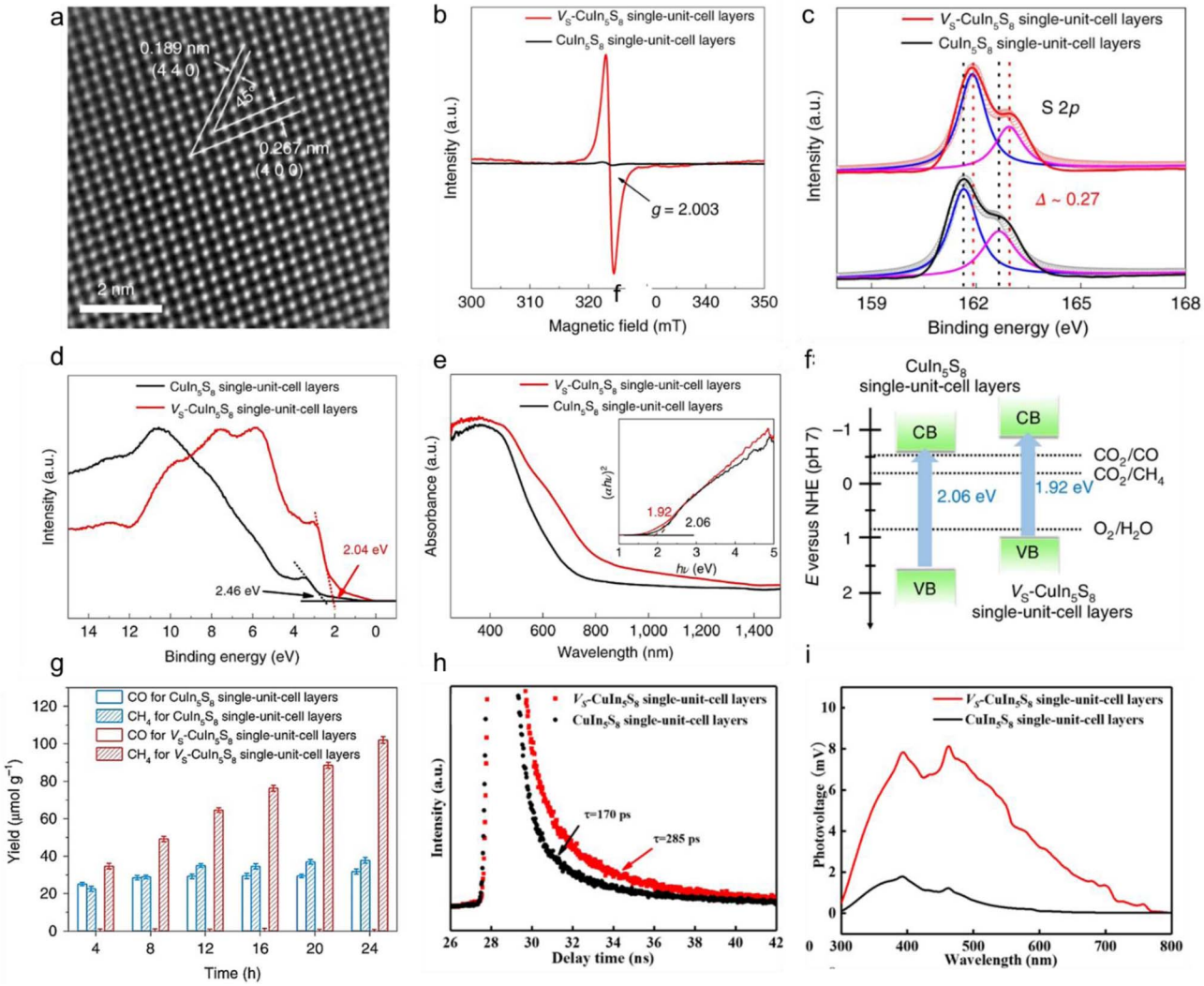

Fig. 15 Photocatalytic CO_2 reduction to CH_4 mediated by vacancy-rich atomically thin $CuIn_5S_8$ layers. (a) HRTEM image showing the interplanar distances, and the corresponding dihedral angle, (b) EPR spectra, in which the signal at $g = 2.003$ corresponds to the S vacancies, (c) XPS spectra of S 2p for the V_S-$CuIn_5S_8$ single-unit-cell layers and the pristine $CuIn_5S_8$ single-unit-cell layers, (d) SRPES valence-band spectra, in which valence-band maxima are located at 2.04 and 2.46 eV below the Fermi level, (e) UV-Vis diffuse reflectance spectra. (inset) Obtained band gaps of 1.92 eV and 2.06 eV, (f) schematics illustrating the electronic band structures, (g) products of photocatalytic CO_2 reduction for the V_S-$CuIn_5S_8$ single-unit-cell layers (red bars) and the pristine $CuIn_5S_8$ single-unit-cell layers (blue bars), (h) fluorescence emission decay spectra, (i) surface photovoltage (SPV) spectra of V_S-$CuIn_5S_8$ single-unit-cell layers and the pristine $CuIn_5S_8$ single-unit-cell layers. Reproduced with permission from ref. 527. Copyright 2019 Springer Nature.

(Fig. 15i) as well as lower PL peak intensity relative to the pristine $CuIn_5S_8$ single-unit-cell layers. The time-resolved fluorescence spectra showed extended carrier lifetimes, indicating improved charge separation (Fig. 15h). *In situ* Fourier transform infrared spectroscopy (FTIR) highlighted that CO intermediates on V_S-$CuIn_5S_8$ surfaces were rapidly protonated to CHO*, preventing CO desorption and favoring CH_4 formation. DFT calculations demonstrated that charge-enriched Cu–In dual sites stabilized COOH* intermediates more effectively than Cu single sites, reducing energy barriers and enabling spontaneous protonation to CH_4. This work highlighted the potential of rationally designed defect-engineered atomically thin semiconductor sheets with dual-metal sites to modulate reaction pathways, improving the activity and selectivity of CO_2 photoreduction.[527]

Among semiconductors, metal oxyhalide ultrathin nanosheets (UTNs) are particularly promising for CO_2 reduction due to the unique heterogeneity in their crystal structure. These materials feature both covalent metal–oxygen bonding and soft ionic metal–halide bonding coexisting within a two-dimensional layer. This arrangement creates an anisotropic charge distribution between the metal–oxygen layer and metal–halogen slices, resulting in a preferentially oriented internal electric field within the 2D metal oxyhalide layer.[489,504,528]

When defect engineering is applied to selectively disrupt halide or oxygen atoms, it induces a synergistic effect by exposing unsaturated surface metal atoms and enhancing the

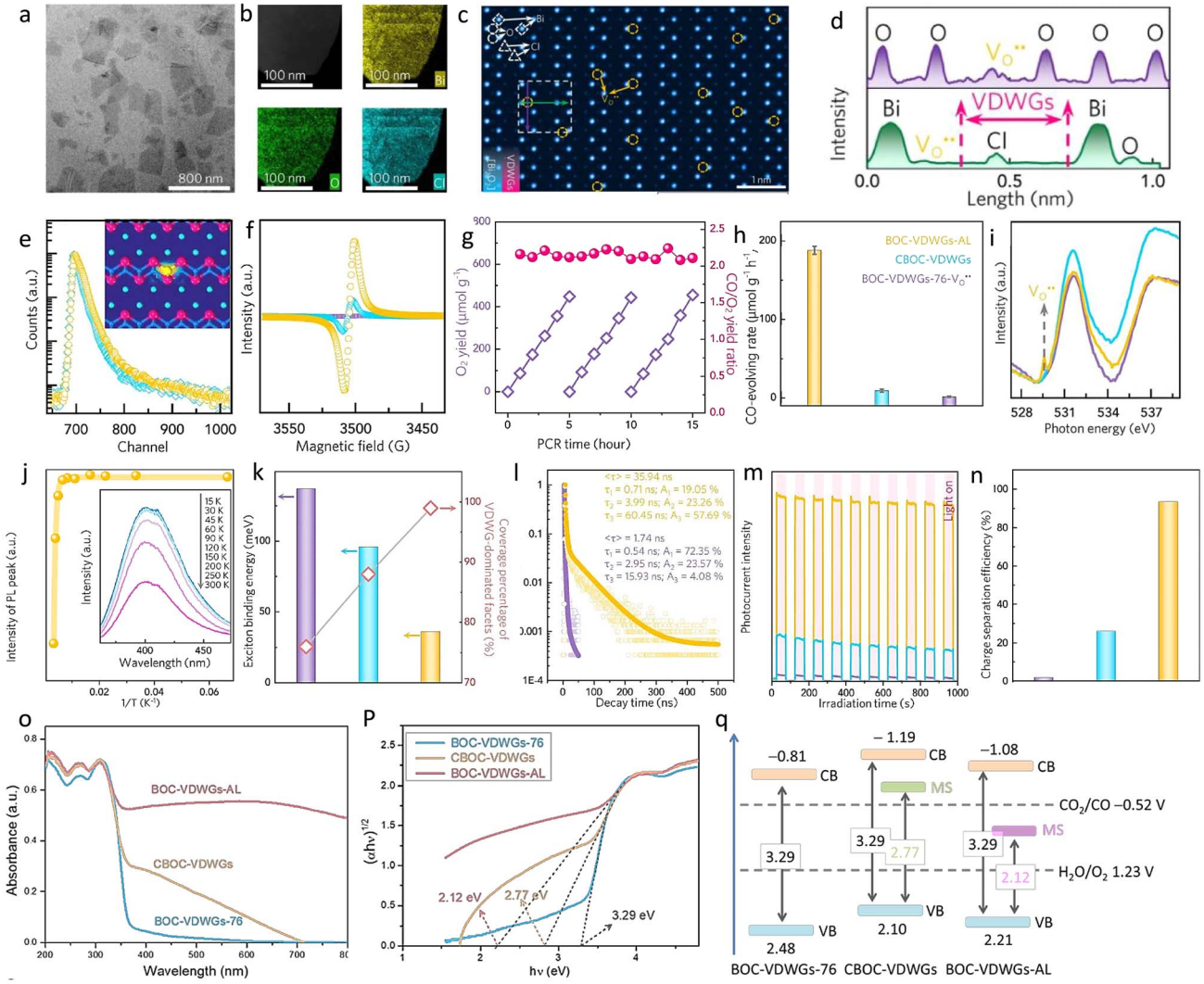

Fig. 16 Photocatalytic CO_2 reduction to CO over van der Waals gap-rich BiOCl atomic layers. (a) TEM image, (b) dark-filed STEM image and elemental mappings, (c) aberration-corrected HAADF-STEM image, (d) intensity profiles (taken along the lines of c) of BOC-VDWGs-AL, (e) PAS, (f) EPR, (g) yield of O_2 detected during pure-water PCR photocatalyzed by BOC-VDWGs-AL, as well as the calculated yield ratio of CO to O_2, (h) comparison of CO-evolving rate of BOC-VDWGs-AL, CBOC-VDWGs, and BOC-VDWGs-76, all under visible light in the presence of pure-water and CO_2, (i) O K-edge XANES of BOC-VDWGs-AL, CBOC-VDWGs, and BOC-VDWGs-76, (j) PL of BOC-VDWGs-AL, (k) comparisons of E_b and VDWG coverage percentage of BOC-VDWGs-AL, CBOC-VDWGs, and BOC-VDWGs-76, (l) time-resolved PL of BOC-VDWGs-AL and BOC-VDWGs-76, (m) transient photocurrent responses and (n) bulk charge separation efficiencies of BOC-VDWGs-AL, CBOC-VDWGs, and BOC-VDWGs-76, (o) UV-visible absorption spectra, (p) plots of $(\alpha h\nu)^{1/2}$ *versus* energy ($h\nu$) for the band-gap energies, (q) band structure alignments of BOC-VDWGs-AL and BOC-VDWGs-76. Reproduced with permission from ref. 528. Copyright 2021 Springer Nature.

internal electric fields. This coupling significantly improves charge separation efficiency and catalytic performance in metal oxyhalide UTNs. Zhang *et al.*[528] explored van der Waals gaps (VDWGs) and defects for photocatalytic CO_2 reduction and reported an efficient pure water CO_2-to-CO conversion using sub-3-nm-thick BiOCl nanosheets enriched with van der Waals gaps on their two-dimensional facets (Fig. 16). Unlike bulk BiOCl, these atomic layers with abundant VDWGs showed significantly reduced exciton binding energy (from 137 to 36 meV) and a 50-fold increase in charge separation efficiency. VDWGs facilitated the formation of VDWG-Bi-VO$^{\bullet\bullet}$-Bi defect sites, which optimized CO_2 activation, *COOH splitting, and *CO desorption. This system achieved a photocatalytic CO_2 reduction (PCR) rate of 188.2 μmol g^{-1} h^{-1} under visible light in pure water without requiring cocatalysts, hole scavengers, or organic solvents (Fig. 16g and h). The nanosheets, with 99% VDWG exposure achieved through gas-phase exfoliation, demonstrated enhanced electron–hole separation due to weakened exciton binding and the formation of active VDWG-Bi-VO$^{\bullet\bullet}$-Bi sites (Fig. 16a–d). Positron annihilation spectroscopy (PAS) showed a lifetime of 195 ps (Fig. 16e), EPR showed a peak centered at $g = 2.004$ (Fig. 16f), and X-ray absorption near-edge structure (XANES) revealed an additional peak centered at 529.6 eV (Fig. 16i), confirming the presence of VDWG-Bi-VO$^{\bullet\bullet}$-Bi defects, which were positively proportional to VDWGs coverage percentage. This defect structure enhanced CO_2-to-CO

conversion, with a stoichiometric $CO:O_2$ evolution ratio of ~2.14 : 1 (Fig. 16g and h). Steady-state PL measurements across temperatures demonstrated reduced exciton binding energy (E_b) due to high VDWG coverage, which facilitated charge carrier separation and suppressed recombination (Fig. 16j and k). The VDWGs offered channels along which electrons and holes can diffuse and then separate. In addition, the VDWGs-dominated surfaces possess abundant unsaturated atoms or architectures that can efficiently trap electrons or holes to inhibit their recombination. Time-resolved PL measurements showed a 20.7-fold longer charge carrier lifetime for BOC-VDWGs-AL compared to conventionally exfoliated nanosheets (Fig. 16l). Similarly, an 11.5-fold higher photocurrent (Fig. 16m) and a smaller electrochemical impedance arc evidenced efficient bulk charge carrier separation with high VDWG coverage (Fig. 16n).

The VDWG-Bi-VO$^{\bullet\bullet}$-Bi defect also imparted BiOCl, which is normally photoactive only under ultraviolet light, with optical absorption across the entire visible light spectrum (Fig. 16o). This occurs because VDWG-Bi-VO$^{\bullet\bullet}$-Bi introduces intraband states between the conduction and valence bands, narrowing the band gap and enabling the absorption of long-wavelength visible-light photons (Fig. 16p). Ultraviolet photoelectron spectra (UPS) revealed that BOC-VDWGs-AL possesses a valence band maximum of 2.21 eV, providing sufficient potential to photo catalytically oxidize H_2O into O_2 (Fig. 16q).

These findings highlight the transformative role of VDWGs in ultrathin BiOCl nanosheets. The high VDWG coverage enabled ultralow E_b and catalytically active VDWG-Bi-VO$^{\bullet\bullet}$-Bi sites, achieving superior PCR performance using visible light, pure water, and CO_2. This innovative VDWG engineering approach adds a new dimension to the optimization of layered photocatalysts, surpassing traditional strategies like defect engineering, doping, or single-atom loading.[528]

Compared to monometallic oxyhalides, bimetallic oxyhalides remain relatively underexplored. In a recent study, Chen *et al.*[529] employed a novel top-down wet-chemistry desalination approach to remove the alkali-halide salt layer within the complex bulk precursor structure of $Pb_{0.6}Bi_{1.4}Cs_{0.6}O_2Cl_2$ (PBCOC) (Fig. 17). This process successfully produced a new two-dimensional ultrathin bimetallic oxyhalide, $Pb_{0.6}Bi_{1.4}O_2Cl_{1.4}$ (PBOC). The desalination process, achieved *via* simple ultrasonication in deionized water, dissolved the Cs–Cl layer (Fig. 17a), delaminating the parental PBCOC structure into ultrathin PBOC layers. Scanning electron microscopy (SEM), scanning transmission electron microscopy (STEM), and energy dispersive spectroscopy (EDS) analyses validated the reduced Cs and Cl concentrations (to 0.05% and 21.73%, respectively), indicating successful leaching (Fig. 17b). STEM imaging revealed a layered ABBA stacking arrangement in PBOC, with mirror-symmetry-mediated stacking interactions and van der Waals bonding between layers (Fig. 17c).

The ultrathin PBOC exhibited a narrower band gap (2.82 eV) than bulk PBCOC (3.14 eV), as demonstrated by UV-Vis diffuse reflectance spectroscopy (Fig. 17d). Mott–Schottky analysis indicated an N-type semiconductor behavior, with CBM positions of −0.34 V (Fig. 17i). These band edge positions favored both CO_2 reduction and O_2 evolution (Fig. 17l). Enhanced charge separation and transport were confirmed by electrochemical impedance spectroscopy (EIS) (Fig. 17h), PL spectroscopy (Fig. 17j), and transient photocurrent measurements (Fig. 17g), with PBOC showing lower emission responses and longer charge carrier lifetimes.

Under Xe lamp irradiation (420 nm filter) with 1500 ppm CO_2, PBOC achieved superior photocatalytic performance, producing CO and CH_3OH at rates of 17.91 μmol g^{-1} and 26.53 μmol g^{-1} in 4 hours, 7.2 and 7.3 times higher than PBCOC (Fig. 17e and f). Continuous O_2 production (~48.69 μmol g^{-1} in 4 hours) was also observed, attributed to the oxidation of H_2O. This performance exceeded that of BiOCl nanosheets and other benchmark photocatalysts, highlighting the role of Pb–Bi co-occupancy in enhancing interfacial and electronic properties. The DFT calculations revealed that Pb incorporation reduces the band gap compared to BiOCl while inducing significant polarization effects that promote charge separation. Partial density of states (PDOS) analysis revealed increased electronic states at the conduction-band edge due to Pb–Bi co-occupancy (Fig. 17k). The synergistic effects of rich catalytic centres, enhanced charge conductivity, and structural stability are crucial in achieving remarkable CO_2 reduction performance, providing insights into the design of next-generation photocatalysts.[529]

In a report by Chen *et al.*,[530] they discovered that the high surface area and low charge recombination characteristics of doped 2D materials could significantly enhance photocatalytic activity. Among various metal sulfides, they investigated SnS_2, a naturally occurring bronze-colored n-type semiconductor with a narrow band gap (2.2–2.4 eV) known as mosaic gold. The material's narrow band gap, combined with an average photocarrier diffusion length of approximately 0.19 μm and high quantum yield, provided two distinct advantages for visible-light-driven photocatalysis. Chen *et al.* synthesized a carbon-doped SnS_2 nanostructure (referred to as SnS_2-C) to improve photocatalytic performance by suppressing charge recombination and enhancing charge transport (Fig. 18).[530] The powder X-ray diffraction (p-XRD) peaks for SnS_2-C were broader than those of SnS_2, indicating a nanocrystalline and partially amorphous structure. The (001) interplanar spacing of SnS_2-C was calculated as 0.604 nm, slightly larger than that of SnS_2 (0.585 nm), suggesting lattice expansion caused by carbon doping. The HRTEM images supported these findings, showing increased interplanar spacing in SnS_2-C. EDX and HAADF imaging confirmed uniform distribution of Sn, S, and C in SnS_2-C (Fig. 18a and b). A reduction in the band gap was observed for SnS_2-C (2.34 eV) compared to SnS_2 (2.43 eV) (Fig. 18c). The UPS analysis revealed a work function of 4.4 eV for SnS_2-C, higher than the 4.16 eV of SnS_2. This shift indicated a change in band edge positions, which is favorable for multi-electron CO_2 reduction (Fig. 18h). XPS analysis revealed binding energy shifts in SnS_2-C, confirming lattice distortions caused by carbon incorporation (Fig. 18d). PL (Fig. 18f) and time-resolved PL (TRPL) (Fig. 18g) measurements provided insights into charge carrier dynamics. SnS_2-C exhibited a nearly threefold lower PL intensity compared to SnS_2, indicating reduced recombination

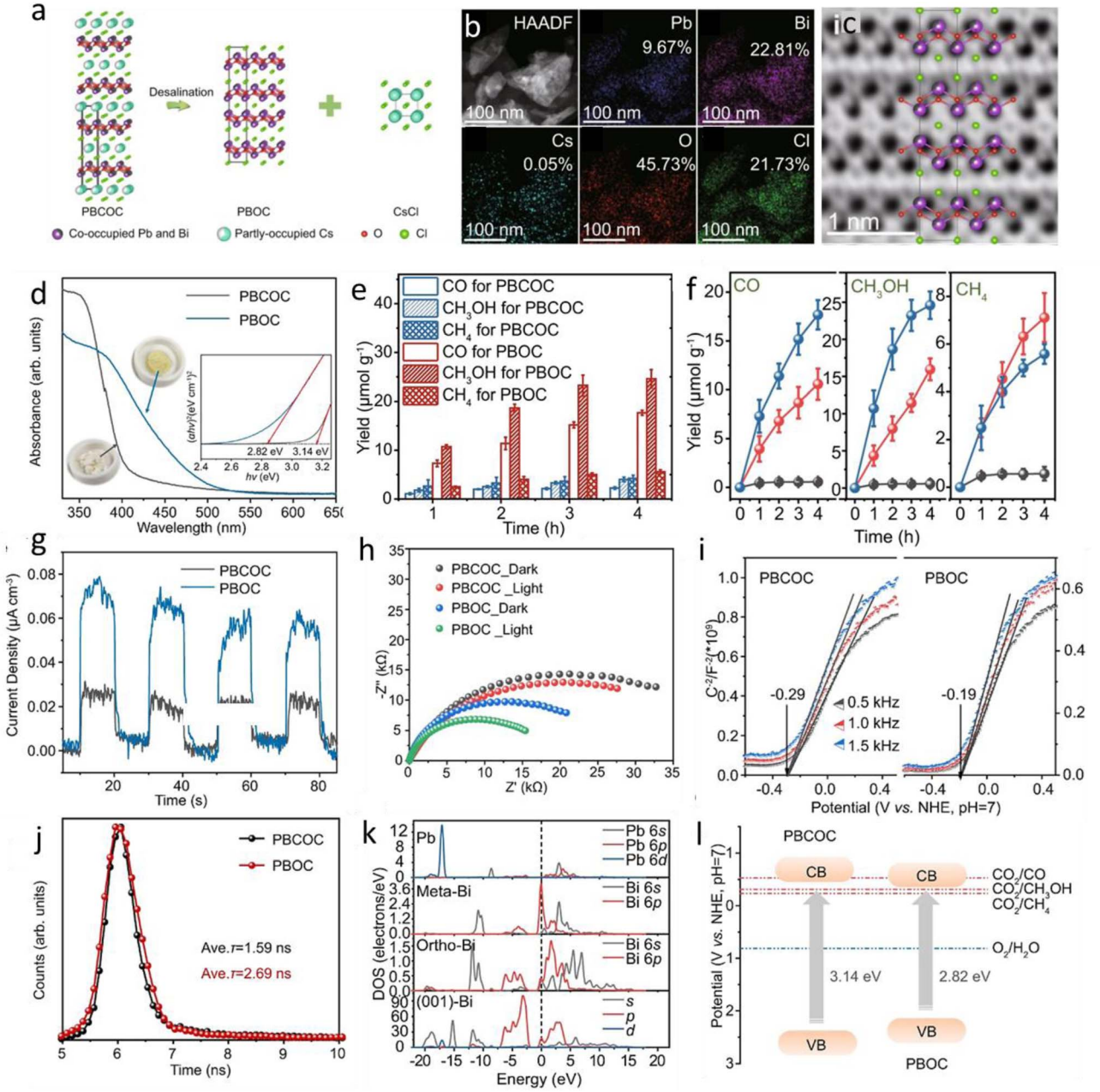

Fig. 17 Photocatalytic CO_2 reduction over desalinated bimetallic oxyhalide ($Pb_{0.6}Bi_{1.4}O_2Cl_{1.4}$). (a) Schematic illustration of ultrathin PBOC layers synthesis from PBCOC *via* desalination strategy, (b) STEM-EDS elemental-mapping images and the corresponding element atomic concentrations, (c) atom-resolved inverse FFT BF-STEM images, with the labeled zone axis, (d) UV-Vis diffuse reflectance spectra. (inset) Corresponding optical images and obtained band gaps of 2.82 and 3.14 eV, (e) photocatalytic CO_2RR products under full-spectrum light irradiation, (f) photocatalytic CO_2 reduction activities of the ultrathin PBOC in N_2 (grey ball), atmospheric CO_2 (red ball), and pure CO_2 (blue ball) under full-spectrum light irradiation, (g) transient photocurrent densities with light on/off cycles under full spectrum in 0.1 M Na_2SO_4 electrolyte solution at an applied potential of 0.5 V *vs.* Ag/AgCl electrode, (h) electrochemical impendence spectroscopy, (i) Mott–Schottky plots, (j) time-resolved fluorescence spectra. Ave. τ is the average fluorescence lifetime, (k) the partial density of states (PDOS) calculated using DFT, (l) schematic illustration of the electronic band structures, and grey arrows represent the electron transition process under the light irradiation. Reproduced with permission from ref. 529. Copyright 2022 Springer Nature.

of photoinduced charge carriers. TRPL spectra revealed shortened lifetimes for photogenerated electrons and holes in SnS_2-C, suggesting efficient carrier separation due to nonradiative pathways facilitated by carbon doping. Under visible light, SnS_2-C exhibited a maximum cumulative acetaldehyde yield of approximately 125.66 μmol/100 mg_{cat} after 14 hours, compared to 0.55 μmol/100 mg_{cat} for SnS_2 (Fig. 18e). The solar fuel photochemical quantum efficiency (PCQE) of SnS_2-C was calculated to be ~0.72%. Mechanistic insights revealed that carbon doping helped in extending the absorption band into

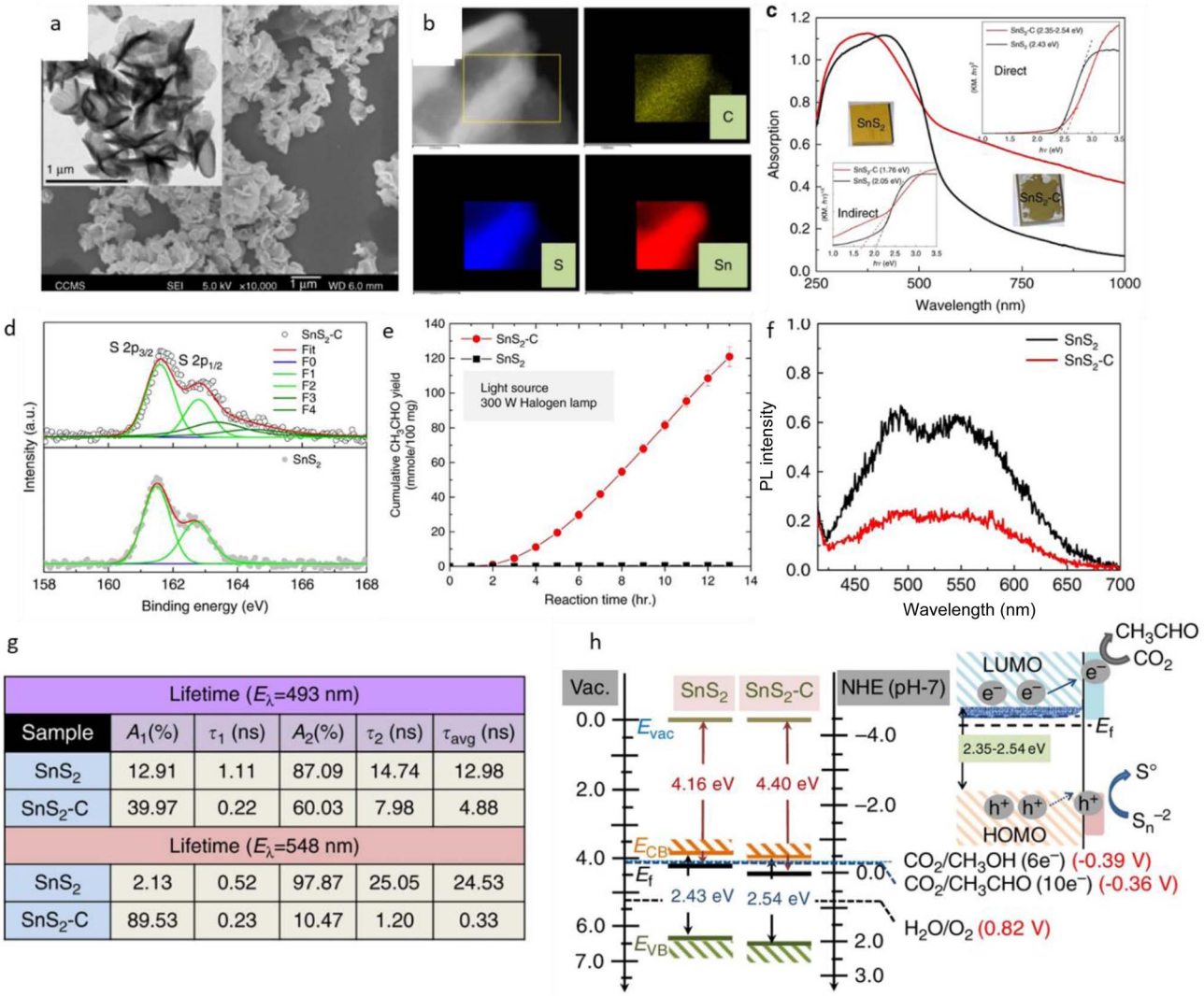

Lifetime (E_λ=493 nm)					
Sample	A_1(%)	τ_1 (ns)	A_2(%)	τ_2 (ns)	τ_{avg} (ns)
SnS_2	12.91	1.11	87.09	14.74	12.98
SnS_2-C	39.97	0.22	60.03	7.98	4.88
Lifetime (E_λ=548 nm)					
SnS_2	2.13	0.52	97.87	25.05	24.53
SnS_2-C	89.53	0.23	10.47	1.20	0.33

Fig. 18 Photocatalytic CO_2 reduction over carbon-doped SnS_2. (a) SEM images of SnS_2-C, (b) high-angle annular dark-field (HAADF) image and EDX elemental mapping of C, S, Sn from selected area for SnS_2-C, (c) UV-Vis diffuse reflectance and (insets) Tauc plots with both direct and indirect fittings, (d) high-resolution XPS S 2p spectra of SnS_2-C and SnS_2, (e) cumulative acetaldehyde formation yield of SnS_2-C and SnS_2, (f) normalized PL spectra of SnS_2-C and SnS_2, (g) summary table of TRPL slow, fast, and average lifetime calculated at both 493 and 548 nm emissions, (h) band edge positions and photocatalytic reaction mechanism: comparative band diagram of SnS_2-C and SnS_2, together with a proposed electron–hole separation of photo-excited electron–hole pairs in SnS_2-C. Reproduced with permission from ref. 530. Copyright 2018 Springer Nature.

the longer wavelength range, promoting CO_2 adsorption and reducing the dissociation barrier for the reduction process.

Simulation studies suggested that the conduction band position of SnS_2-C aligned favorably with the onset reduction potential energy of CO_2, enabling a ten-electron reduction process critical for acetaldehyde production (Fig. 18h). The band edge tuning and microstrain-induced new electronic states in SnS_2-C enhanced electron migration to the surface. Meanwhile, photogenerated holes reacted with water molecules, forming oxygen, hydrogen peroxide, or hydroxide radicals, further driving the reaction.

In summary, Chen *et al.*[530] concluded that the enhanced photocatalytic performance of SnS_2-C resulted from a combination of structural and electronic modifications, including high surface area, reduced photocarrier diffusion length, improved charge separation, and favorable band edge positions. These factors collectively enabled efficient visible-light-driven CO_2 reduction and selective acetaldehyde production through a multi-electron transfer process.[530]

Other than doping and defect creation, there have been reports of heterostructure fabrication and metal cocatalyst loading to improve the lifetime of charge carriers in semiconductors. Yu *et al.*,[531] presented a simple one-pot method to develop core-triple shell Mn, C-codoped ZnO hollow spheres photocatalysts for CO_2 reduction. In this design, Mn ions with switchable valence states acted as "ionized cocatalysts", enhancing CO_2 adsorption and light harvesting. They also facilitated the transfer of photogenerated electrons from the

ZnO conduction band to drive CO_2 reduction, a process maintained by the reversible oxidation states of Mn ions. This approach bypasses the challenges of cocatalyst loading and ensuring intimate contact, as the ionized cocatalysts are embedded within the ZnO lattice, serving as active sites for CO_2 activation.

Using a coordination polymer (CP) strategy, Mn, C-codoped ZnO core-triple shell hollow spheres (Mn, C-ZnO CTSHSs) were synthesized through a solvothermal method followed by controlled air annealing (Fig. 19). Characterization revealed that Mn ions substitute Zn in the ZnO lattice (Fig. 19a), acting as active centers for CO_2 reduction while suppressing competitive hydrogen evolution. *In situ* XPS demonstrated that Mn ions restore their initial oxidation state post-reaction by capturing photogenerated electrons, showcasing a light-switchable cocatalytic behavior (Fig. 19h). This mechanism underscored the durability and efficiency of Mn as an ionized cocatalyst for practical applications.

Photocatalytic experiments revealed that the 2% Mn, C-ZnO CTSHS catalyst achieved the highest CO_2 reduction activity, producing CO at a rate of 0.83 μmol g^{-1} under simulated solar light (Fig. 19d and e). Excessive Mn doping (*e.g.*, 5%) introduced defect states that acted as charge recombination centers, reducing efficiency. The system's apparent quantum efficiency (AQE) aligned with its light absorption spectrum (Fig. 19c). The enhanced light absorption was attributed to the hollow structure, which enabled multiple light reflections, and Mn doping, which introduced impurity states that narrowed the ZnO band

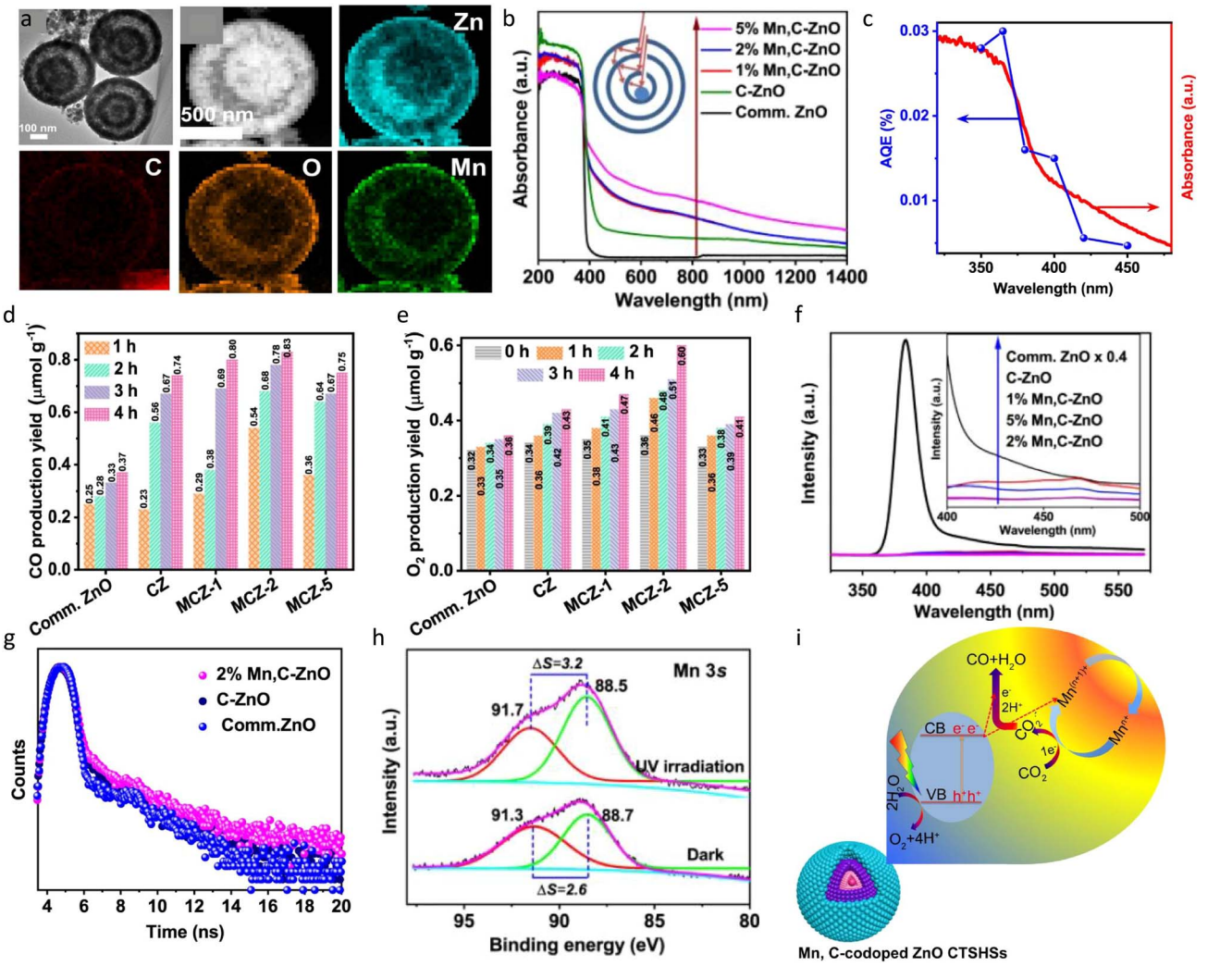

Fig. 19 Photocatalytic CO_2 reduction over Mn, C-codoped ZnO core-triple shell hollow spheres. (a) TEM images of the Mn, Zn-CPSs after calcination for 3 h, HAADF-STEM image of Mn, C–ZnO and EDS mapping of the sample, (b) UV-Vis light absorption of the prepared photocatalysts and the inset represents the multiple reflection effect of the incident light inside the hollow cavities, (c) wavelength dependence of the AQE and the UV-Vis absorption spectrum of 2% Mn, C-ZnO sample, (d and e) photocatalytic CO_2 reduction performance of comm. ZnO and the prepared samples: time course of a CO and O_2 production yields, (f) PL spectra of photocatalysts at excitation wavelength of 380 nm, (g) TRPL spectra of the samples, (h) *in situ* XPS analysis showed Mn 3s profiles for CO_2-adsorbed Mn, C-ZnO CTSHS samples. The multiple splitting of Mn 3s (ΔS) is used to calculate the average oxidation state of Mn ions within the structure, (i) schematic illustration of CO_2 activation and reduction over Mn, C-codoped ZnO sample. Reproduced with permission from ref. 531. Copyright 2021 Springer Nature.

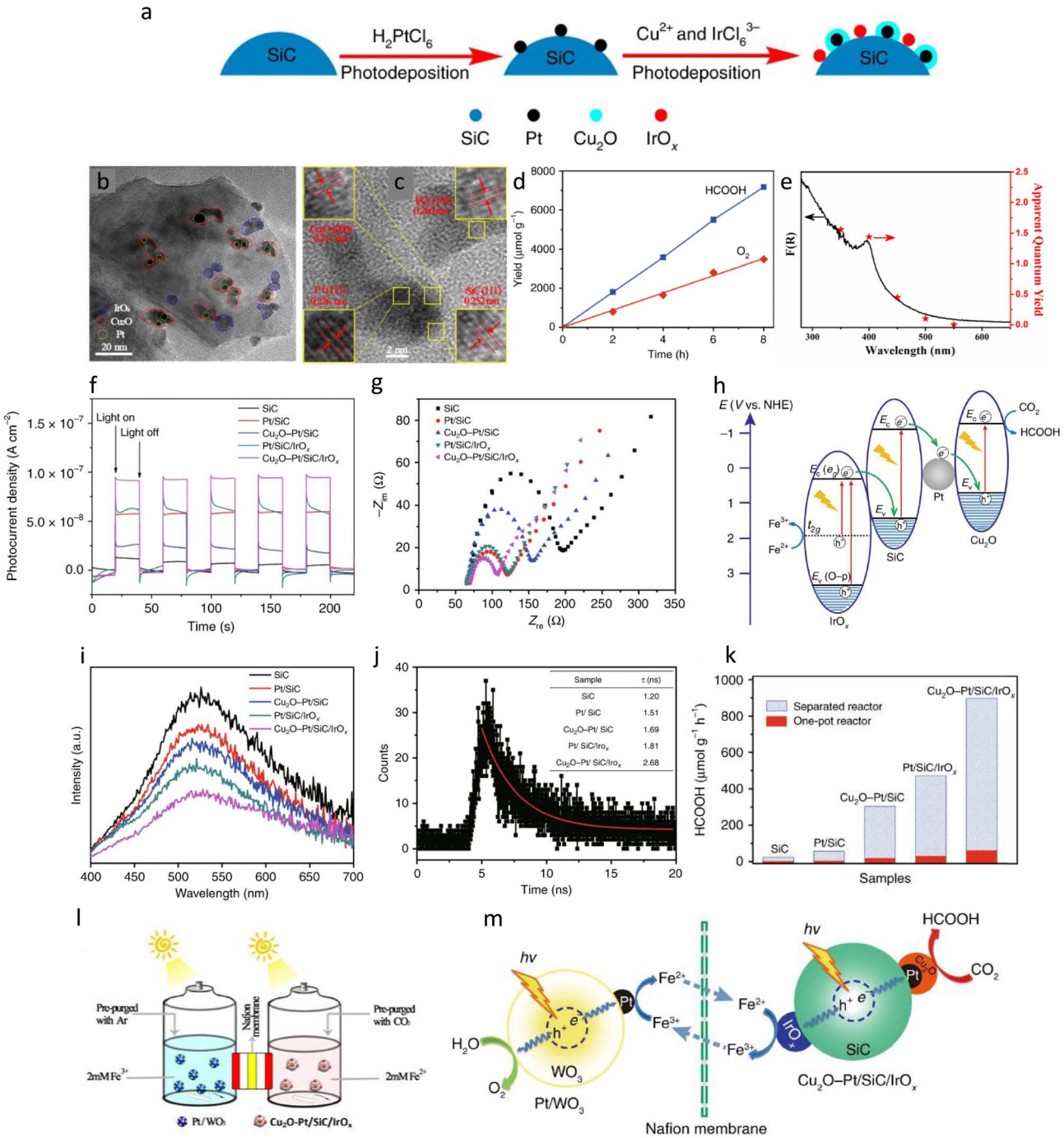

Fig. 20 Photocatalytic CO_2 reduction over direct and indirect Z-scheme heterostructure-coupled Cu_2O-Pt/SiC/IrO_x photosystem. (a) Schematic representation of Cu_2O-Pt/SiC/IrO_x synthesis *via* controlled photo-deposition, (b) TEM and (c) HRTEM images of Cu_2O-Pt/SiC/IrO_x, (d) evolutions of HCOOH and O_2 as a function of illumination time, (e) the apparent quantum yield of HCOOH evolution with the wavelength of irradiation light for the separated reaction system, (f) periodic on/off photocurrent response, (g) AC Impedance, (h) the electron transfer processes in Cu_2O-Pt/SiC/IrO_x under light illumination, (i) PL spectra for different photocatalysts, (j) time-resolved photoluminescence spectroscopy of Cu_2O-Pt/SiC/IrO_x, (k) comparison for the HCOOH evolution between in the spatially separated reaction system and in the conventional one-pot reactor with different samples as the reduction side photocatalyst, (l) schematic diagram of the spatially separated Z-scheme system, (m) the proposed mechanism of the separated system for the efficient CO_2 reduction and O_2 evolution. Reproduced with permission from ref. 457. Copyright 2020 Springer Nature.

gap (Fig. 19c). Additional electronic transitions, such as ligand-to-metal and metal-to-ligand charge transfers, further improved light harvesting. The PL spectra confirmed suppressed charge recombination, with the 2% Mn, C-ZnO catalyst showing the lowest PL intensity and longest charge carrier lifetime (1.1 ns) (Fig. 19f). Electrochemical impedance spectroscopy revealed

reduced charge transfer resistance (R_{ct}) in Mn-doped samples, promoting efficient charge carrier migration. The Mn species also significantly enhanced CO_2 adsorption, attributed to surface oxygen species and Mn ions replacing Zn in the lattice. *In situ* XPS under light and dark conditions showed Mn ions alternately transferring electrons to CO_2 molecules and regenerating their oxidation states upon light irradiation (Fig. 19h). This light-switchable behavior is crucial for maintaining catalyst activity without external treatments. The Mn ions also acted as Lewis base centers, facilitating CO_2 adsorption and activation through a single-electron transfer to form CO_2^- intermediates. Subsequent proton-coupled electron transfer leads to CO production (Fig. 19i). These findings validated Mn ions as durable and efficient ionized cocatalysts in a light-responsive system.

In summary, the core-triple-shell Mn, C-codoped ZnO hollow spheres synthesized *via* a one-pot method exhibited superior photocatalytic performance due to their structural and functional advantages, including enhanced light absorption, efficient charge separation, and abundant active sites. The Mn species played a pivotal role in CO_2 activation through electron transfer while regenerating their oxidation states under light. This study underscores the potential of hollow-structured materials and light-switchable cocatalysts for sustainable CO_2 reduction and clean energy applications.[531]

Despite different structural modifications, the efficiency of CO_2 photoreduction remained less, to enhance the efficiency of artificial photosynthesis, Li *et al.*[457] developed a Cu_2O-Pt/SiC/IrO_x composite using controlled photodeposition techniques (Fig. 20). This composite was integrated into an artificial photosynthetic system featuring a Nafion membrane that separated the reduction and oxidation half-reactions. The system demonstrated exceptional photocatalytic performance under visible light, converting CO_2 into HCOOH and water into O_2 with yields of 896.7 and 440.7 μmol g^{-1} h^{-1}, respectively, nearly in stoichiometric proportions.

This remarkable efficiency is attributed to the direct and indirect Z-scheme electronic structures of the composite. The direct Z-scheme facilitates efficient charge separation and prolonged carrier lifetimes, while the spatially separated reduction and oxidation units prevent product back-reactions. Unlike many photocatalysts that require sacrificial agents (*e.g.*, triethanolamine or EDTA) to function, this system achieves sustainable and efficient photocatalysis without such additives.

Silicon carbide (SiC), a metal-free semiconductor with a moderate band gap (2.4 eV) and suitable conduction band energy (∼−1.1 V), is ideal for multi-electron CO_2 reduction reactions. However, its low hole mobility and lack of active sites for CO_2 adsorption hinder its photocatalytic performance. To address these challenges, the Cu_2O-Pt/SiC/IrO_x hybrid photocatalyst was designed with IrO_x for photo-oxidation and Cu_2O-Pt for photoreduction (Fig. 20a). This configuration enhanced charge carrier lifetimes and CO_2 adsorption, significantly boosting efficiency.

The artificial system utilized two separate reaction chambers mimicking natural photosynthesis. One chamber, equipped with Cu_2O-Pt/SiC/IrO_x and Fe^{2+}, drives CO_2 reduction, while the other, containing Pt/WO_3 and Fe^{3+}, facilitates water oxidation (Fig. 20l). A Nafion membrane ensures selective ion transfer between chambers, optimizing reaction efficiency. The Cu_2O-Pt/SiC/IrO_x composite achieved a remarkable HCOOH yield of 896.7 μmol g^{-1} h^{-1}, which is 527 times higher than pristine SiC (Fig. 20d). The system also maintained a stoichiometric ratio of O_2 evolution, confirming its reliability. The photocatalytic activity of the spatially separated system was approximately 15 times greater than that of the one-pot reaction system for each photocatalyst (Fig. 20d). In the one-pot system, the re-oxidation of HCOOH by O_2 likely contributed to the lower production of HCOOH and O_2. Additionally, Fe^{3+} competes with CO_2 for generated electrons, and Fe^{2+} competes with H_2O for photogenerated holes. However, the impact of Fe^{2+} was likely less significant than that of Fe^{3+}, as HCOOH and O_2 evolution were even lower in the absence of added Fe^{3+} and Fe^{2+}. The AQY of HCOOH evolution for the optimal Cu_2O-Pt/SiC/IrO_x sample aligned well with its optical absorption spectra. Under 400 nm light irradiation, the AQY of HCOOH evolution reached approximately 1.44% (Fig. 20e).

Detailed analyses, including TEM analysis, revealed the strategic spatial distribution of Pt, Cu_2O, and IrO_x on the SiC surface, promoting efficient electron transfer (Fig. 20b and c). Cu_2O-Pt exhibited intimate contact, while IrO_x was randomly deposited, ensuring optimal charge separation and migration. The PL (Fig. 20i) and time-resolved spectroscopy (Fig. 20j) confirmed reduced charge recombination rates and enhanced carrier lifetimes for the composite. Cu_2O-Pt/SiC/IrO_x exhibited the highest photocurrent (Fig. 20f) and the lowest AC impedance (Fig. 20g), indicating superior electron transfer and charge separation efficiency. However, a slight inconsistency arises for Cu_2O-Pt/SiC and Pt/SiC, where the photocurrent and AC impedance trends do not fully align with their photocatalytic activity. This discrepancy suggested that photocatalytic activity depended not only on charge transfer and separation efficiency but also on the surface chemistry of the photocatalysts. Furthermore, Mott–Schottky and UV-Vis analyses demonstrated the Z-scheme mechanism, where photogenerated electrons and holes were effectively utilized to drive the desired reactions (Fig. 20h). When light illuminated the system, electrons from the conduction band of IrO_x (+0.35 V) transferred to the valence band of SiC (+1.40 V). Simultaneously, electrons in the CB of SiC (−1.08 V) moved to Pt nanoparticles and then to the VB of Cu_2O (+0.70 V), where they combined with the holes generated in Cu_2O. This process, known as the direct Z-scheme, resulted in electrons accumulating in the CB of Cu_2O (−1.28 V), where they reduced CO_2 to HCOOH [$E(CO_2/HCOOH) = -0.61$ V]. Meanwhile, the holes in IrO_x (+1.85 V) oxidized Fe^{2+} to Fe^{3+} [$E(Fe^{2+}/Fe^{3+}) = +0.77$ V]. In the water oxidation chamber, visible light excited Pt/WO_3, causing electrons in the CB of WO_3 (+0.74 V) to migrate to Pt, where they reduced Fe^{3+} back to Fe^{2+} (Fig. 20m). At the same time, the holes in the VB of WO_3 (+2.06 V) oxidized water to produce oxygen [$E(H_2O/O_2) = +1.23$ V]. This study underscores the significance of combining direct and indirect Z-scheme mechanisms with spatial separation for artificial photosynthesis. The hybrid system not only addresses the

limitations of pristine SiC but also achieves sustainable and economically viable CO_2 reduction and water oxidation.[457]

The size and choice of cocatalyst nanoparticles are critical for charge separation and CO_2 activation, as previously demonstrated. In a notable study, Liu *et al.*[532] developed a single-atom catalyst consisting of isolated cobalt atoms incorporated into Bi_3O_4Br atomic layers to facilitate charge transfer, carrier separation, and CO_2 adsorption and activation. Thus, reducing the CO_2 activation energy by stabilizing COOH* intermediates and shifting the rate-limiting step from COOH* formation to CO* desorption. The optimized catalyst, leveraging cobalt single atoms and ultrathin Bi_3O_4Br layers, achieved a CO production rate of 107.1 μmol g^{-1} h^{-1}; approximately 4 and 32 times higher than atomic-layer and bulk Bi_3O_4Br, respectively.

The ultrathin configuration of Bi_3O_4Br reduced bulk charge carrier recombination due to shorter diffusion distances and provided a high ratio of unsaturated surface atoms, enhancing interfacial reactions and product selectivity. TEM images confirmed a 1.89 nm thickness of Bi_3O_4Br layers (Fig. 21a), while elemental mapping (Fig. 21b and c) revealed a uniform distribution of cobalt atoms (0.8 wt%). The XPS analysis showed cobalt atoms predominantly in the +2 oxidation state (Fig. 21d). The band gap energy decreased from 2.29 eV in Bi_3O_4Br to 2.21 eV in Co-Bi_3O_4Br, improving light absorption by introducing dopant energy levels (Fig. 21g and h).

The detailed energy-level positions of the VB edges, determined from XPS VB spectra (Fig. 21f and o), were both 1.06 eV. Consequently, the CB potentials of Bi_3O_4Br and Co-Bi_3O_4Br-1 were calculated to be −1.23 eV and −1.15 eV, respectively,

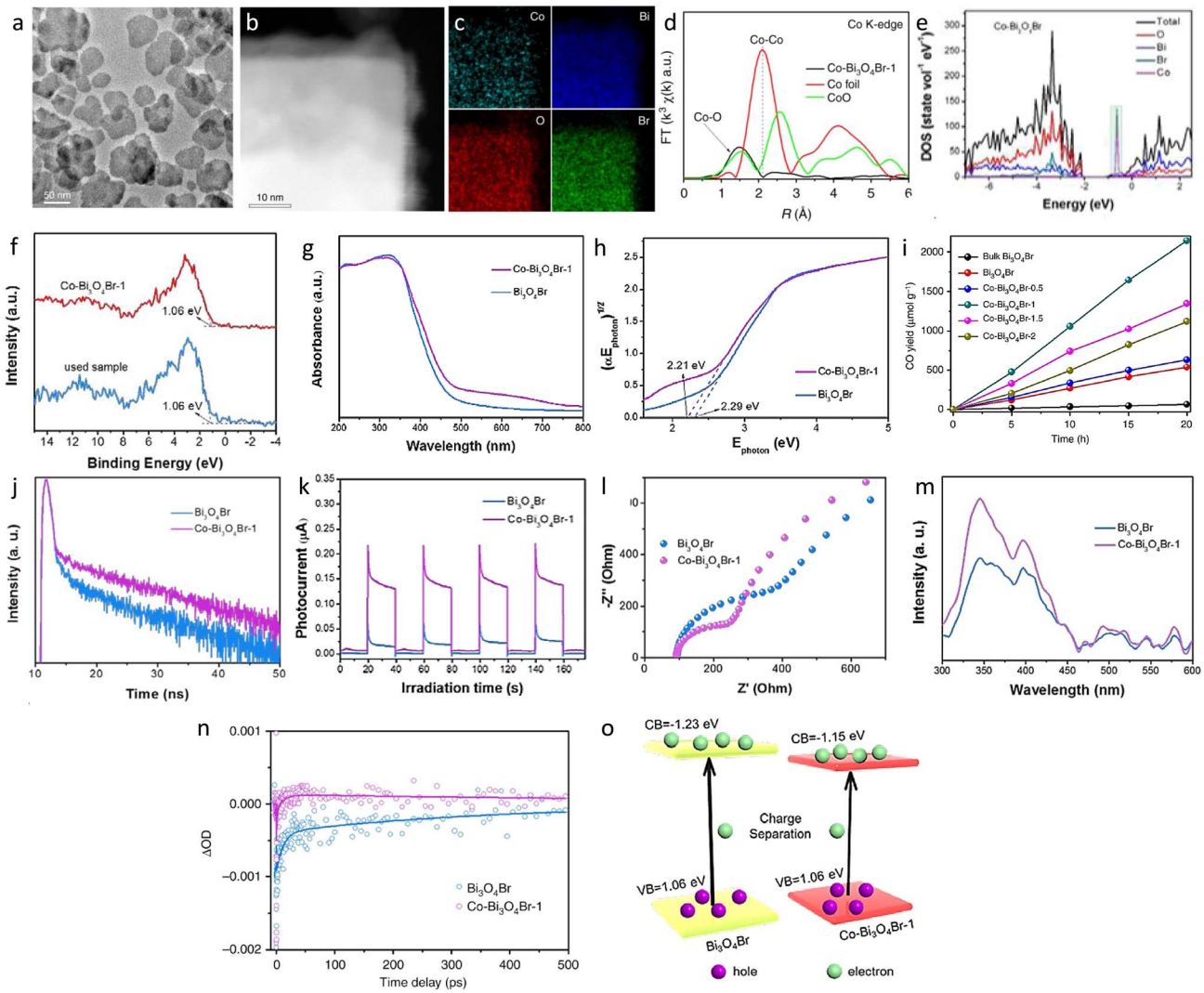

Fig. 21 Photocatalytic CO_2 reduction over isolated single atom cobalt in Bi_3O_4Br atomic layers. (a) Schematic representation of Cu_2O-Pt/SiC/IrO_x synthesis *via* controlled photo-deposition, (b) TEM and (c) STEM image and EDS mapping images of Co, Bi, O, and Br, (d) EXAFS spectra of Co K-edge, (e) calculated density of states of Co-Bi_3O_4Br, (f) XPS valence band spectra of the Bi_3O_4Br and Co-Bi_3O_4Br-1, (g) UV/Vis diffuse reflection spectra, (h) Tauc plot of Bi_3O_4Br and Co-Bi_3O_4Br-1, (i) photoreduction of CO_2 into CO over Bi_3O_4Br and Co-Bi_3O_4Br materials, (j) time-resolved transient PL decay, (k) transient photocurrent responses; (l) electrochemical impedance spectroscopy pure Bi_3O_4Br and Co-Bi_3O_4Br-1, (m) surface photovoltage spectra, (n) ultrafast TA spectra of Bi_3O_4Br and Co-Bi_3O_4Br-1, (o) schematic band structure obtained according to the results in (f) and (h). Reproduced with permission from ref. 532. Copyright 2019 Springer Nature.

meeting the thermodynamic requirements for CO_2 reduction to CO. Additionally, DFT calculations indicated an increased density of states in the band gap for Co-Bi_3O_4Br, further confirming the facilitated transition of photogenerated electrons to the new energy levels (Fig. 21e). Ultrafast TA spectroscopy provided key insights into charge carrier dynamics (Fig. 21n). The biexponential fitting of TA spectra revealed two distinct time constants: τ_1, representing electron capture from the CB into trap states, was approximately 12 ps for Bi_3O_4Br and 11 ps for Co-Bi_3O_4Br. Meanwhile, τ_2, corresponding to recombination between trapped electrons and VB holes, showed a significant increase from 400 ps in Bi_3O_4Br to 1 ns in Co-Bi_3O_4Br, indicating a ~2.5-fold improvement in carrier lifetime. This prolonged lifetime allowed trapped electrons more opportunities to participate in CO_2 photoreduction, enhancing catalytic efficiency.

The Co-Bi_3O_4Br catalyst exhibited superior photocatalytic activity, achieving a 20-hour CO yield of 2142.1 μmol g^{-1} with trace methane production (Fig. 21i). It simultaneously oxidized water to O_2 at an average rate of 56 μmol g^{-1} h^{-1}, maintaining a near-stoichiometric CO : O_2 ratio of 2. The apparent quantum yields reached 0.91% at 380 nm and 0.36% at 400 nm. Additional analyses, including SPV spectroscopy (Fig. 21m), photocurrent (Fig. 21k), and electrochemical impedance (Fig. 21l) measurements, confirmed enhanced charge separation, which was the reason for high CO_2 reduction efficiency. The findings highlight the potential of single-atom catalysts in ultrathin layers to achieve high-efficiency, selective solar-driven CO_2 conversion.[532]

The efficiency of CO_2 reduction relies not only on effective charge separation and transfer but also on the catalyst's ability to adsorb and activate CO_2 molecules at its surface. Semiconductor materials offer an additional advantage in this regard, as their surfaces can be engineered to introduce oxygen vacancies that enhance CO_2 adsorption and thereby improve reduction performance. In this context, Zhang *et al.*[53] addressed the limitation of poor CO_2 adsorption by designing periodic oxygen vacancies to create periodic frustrated Lewis pairs (PFLPs) on the surface of bimetallic semiconductor oxide $SrNb_2O_6$ photocatalysts. In this configuration, the two metal centers play complementary roles: Sr^{2+} acts as a Lewis acid, polarizing the oxygen atoms of CO_2, while Nb^{4+} functions as a Lewis base, interacting with the carbon atom to bend and activate the molecule, ultimately facilitating more efficient electron transfer.

The synthesis utilized electrospinning to produce $SrNb_2O_6$ nanofibers, which were subsequently vacuum-annealed in ethanol to generate surface oxygen vacancies (OVs). Comprehensive characterization using EPR confirmed the presence of OVs, while XPS analysis revealed a critical electronic shift in the O 1s spectrum, exhibiting a lattice oxygen peak at 530.6 eV and a vacancy-induced peak at 531.4 eV. This defect engineering triggered a partial reduction of Nb^{5+} to Nb^{4+}, creating a bimetallic surface where Sr^{2+} (empty 5s orbital) acts as the Lewis acid, and Nb^{4+} (free 4d electron) acts as the Lewis base (Fig. 22a). Atomic-resolution ABF-STEM confirmed that these vacancies are periodically arranged, resulting in regular lattice contractions along the [100] direction that maintain the "frustrated" state necessary for high catalytic reactivity.[53]

The photocatalytic performance of the $SrNb_2O_{6-x}$ nanofibers highlighted the transformative impact of PFLP engineering on CO_2 conversion efficiency and selectivity. Among the series of catalysts tested, $SrNb_2O_{6-x}$-3 emerged as the optimal candidate, achieving a CO production rate of 65.9 μmol g^{-1} h^{-1} under UV-visible light, which is a 3.35-fold enhancement over pristine $SrNb_2O_6$ (Fig. 22b), while simultaneously boosting CO selectivity to 98.7%. Furthermore, the catalyst demonstrated long-term stability, retaining activity over four sequential cycles with no detectable changes in crystal structure or PFLP electronic states, as confirmed by post-reaction XRD and XPS fitting (Fig. 22c). For practical scalability, the authors conducted outdoor experiments under natural sunlight focused by a Fresnel lens, where the $SrNb_2O_{6-x}$-3 sample maintained a CO evolution rate of 25.5 μmol g^{-1} h^{-1}, significantly outperforming the 6.1 μmol g^{-1} h^{-1} observed for pure $SrNb_2O_6$ (Fig. 22d and e). This superior activity is underpinned by an increase in CO_2 uptake values; the $SrNb_2O_{6-x}$-4 sample exhibited an adsorption capacity of 16.0 cm^3 g^{-1}, a 5.2-fold improvement over the unmodified nanofibers (3.1 cm^3 g^{-1}), attributed to the robust coordination between the Sr^{2+}/Nb^{4+} pairs and CO_2 molecules (Fig. 22f).

The photocatalytic mechanism of the $SrNb_2O_{6-x}$-3 nanofibers was driven by a sophisticated "push–pull" synergy between the periodic frustrated Lewis pairs. Ultraviolet-visible spectroscopy and UPS measurements reveal that the oxygen vacancies introduced critical midgap defect states primarily derived from Nb 4d orbitals, which not only extended light absorption but also dramatically enhanced carrier separation by trapping photogenerated electrons at the Nb^{4+} sites. *In situ* FT-IR and Raman spectroscopy provide real-time evidence of this superior kinetics; while pristine $SrNb_2O_6$ suffers from a sluggish conversion of *COOH intermediates (1595 cm^{-1}), the $SrNb_2O_{6-x}$-3 sample facilitates a rapid transition from CO_2 to CO, preventing surface poisoning (Fig. 22g and h). As illustrated in the proposed mechanism (Fig. 22i), the Sr^{2+} Lewis acid site captures CO_2 through its empty 5s orbitals (the "pull"), while the adjacent Nb^{4+} Lewis base site donates photoinduced electrons to the carbon atom to drive the rate-determining step of *COOH formation. This localized electron accumulation at the Nb sites eventually triggers a charge-repulsive "push" effect, effectively ejecting the produced *CO from the surface. Gibbs free energy calculations confirm this pathway, showing a significantly reduced activation barrier for CO_2 hydrogenation (0.57 eV *vs.* 0.83 eV), establishing a highly efficient catalytic cycle sustained by the PFLP-induced electronic frustration. This work showed that by bridging semiconductor photophysics with the chemical specificity of frustrated Lewis pairs, we can effectively bypass traditional kinetic barriers, managing the delicate balance between reactant activation and product desorption to achieve high-performance catalysis.[53]

We have discussed examples of studies targeting better utilization of charge carriers, but the first step is the generation of free carriers from excitons. The question is whether we can tune that initial transition, and this is what Xu *et al.*[19] achieved

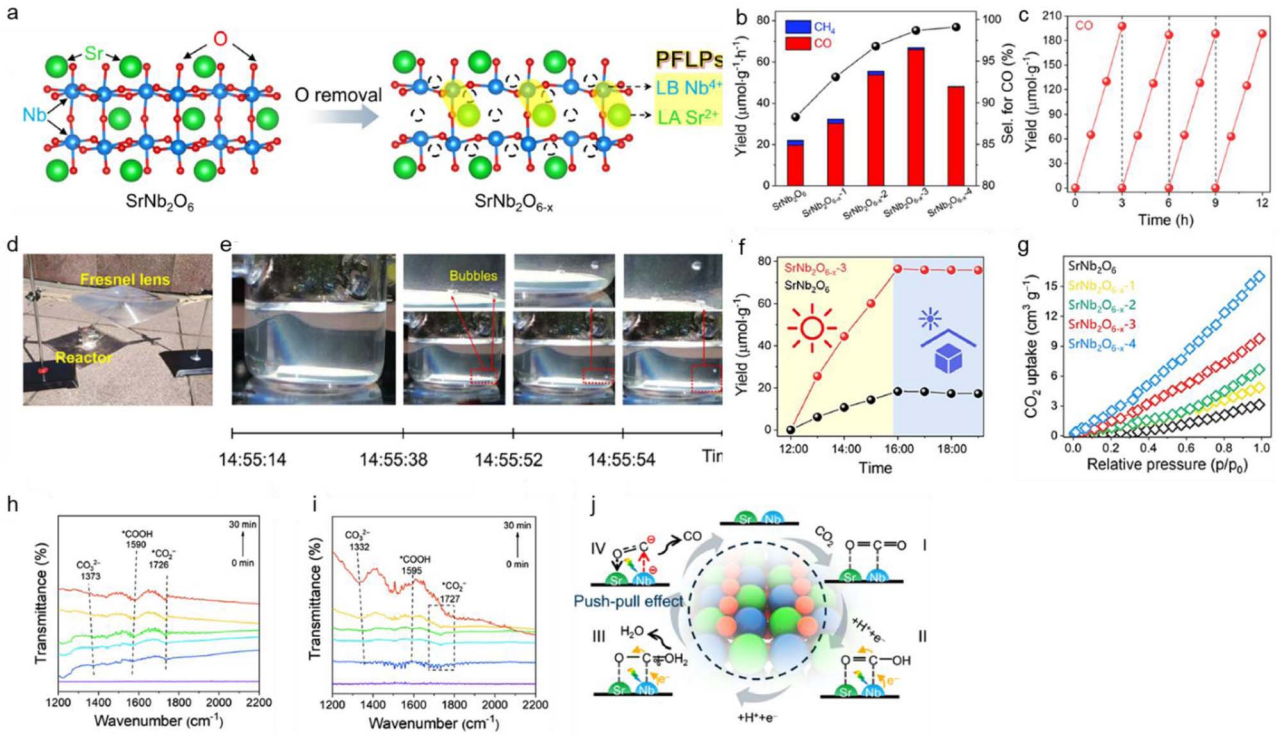

Fig. 22 PFLP-engineered bimetallic $SrNb_2O_6$ for enhanced sunlight-driven CO_2 photocatalysis. (a) Schematic illustration of the structure change from the $SrNb_2O_6$ to the $SrNb_2O_{6-x}$ decorated with PFLPs, (b) CO and CH_4 production rates of photocatalytic CO_2 reduction over $SrNb_2O_{6-x}$-1–4 and $SrNb_2O_6$ under UV-visible light irradiation (320 nm < λ < 780 nm); black dots expressing the corresponding CO-product selectivities of these samples, (c) cycling measurements for CO_2 photoreduction to CO over $SrNb_2O_{6-x}$-3, (d) photograph image of the photocatalytic reactor for CO_2 reduction in an outdoor condition upon natural light irradiation focused by the Fresnel lens, (e) photograph images of the CO evolution through the outdoor CO_2 photoreduction reaction in the way of solid–liquid condition by using 0.1 M potassium bicarbonate solution as the CO_2 precursor, (f) CO production rates of the outdoor CO_2 photoreduction over $SrNb_2O_{6-x}$-3 and $SrNb_2O_6$ upon the focused sunlight irradiation (solid–gas condition), (g) CO_2 adsorption isotherms at 298 K. *In situ* FT-IR spectra of (h) $SrNb_2O_6$ and (i) $SrNb_2O_{6-x}$-3 during photocatalytic CO_2 reduction with water vapor under UV-visible light irradiation for 0 to 30 min, (j) a possible four-step reaction mechanism for the photocatalytic reduction of CO_2 to CO based on the synergistic effect of PFLPs distributed on $SrNb_2O_{6-x}$. Reproduced with permission from ref. 53. Copyright 2025, American Chemical Society.

in their work by focusing on the supercritical CO_2-induced exciton effect in $BiFeO_3$ for photocatalytic CO_2 reduction. While traditional photocatalytic theories often overlook the excitonic aspect of the photoexcitation process, this study posits that the competition between bound excitons and free carriers is a crucial determinant of catalytic performance. By exploring strategies for exciton dissociation through the introduction of structural disorder, the researchers aimed to bridge the gap between initial light absorption and the generation of the free electrons and holes necessary for surface reactions.[19]

The synthesis utilized a supercritical carbon dioxide (SC CO_2) treatment to exfoliate bulk $BiFeO_3$ into ultrathin 2D nanosheets. TEM images confirm the successful transformation into transparent, few-layer structures (Fig. 23a) while the AFM studies showed that the resulting nanosheets possess a thickness primarily between 2.4 and 4 nm, representing roughly 6 to 10 atomic layers. Interestingly, HRTEM and Geometric Phase Analysis (GPA) reveal that the SC CO_2 process does more than just exfoliate; it induces a lattice strain. This structural distortion is accompanied by the formation of oxygen vacancies (Ov) as evidenced by XPS and EPR. To probe how these oxygen vacancies alter the fundamental photophysics of the system, the authors employed femtosecond transient absorption spectroscopy (Fig. 23b–d). In the untreated $BiFeO_3$, the TAS spectra exhibit a double-exponential decay, which is characteristic of a system dominated by a large exciton effect where carriers remain largely bound (Fig. 23b and d). However, the sample treated at 12 MPa shows a distinct shift to a triple-exponential decay model (Fig. 23c and d). In this optimized sample, the TAS kinetics reveal a more complex life cycle for the photoexcited species: the initially generated electrons undergo an ultrafast relaxation from the conduction band into exciton-mediated trap states (Fig. 23e). Unlike the bulk material, the presence of oxygen vacancies in the 2D nanosheets provides a second relaxation step where these excitons are effectively "destabilized" and dissociated into free carriers (Fig. 23e). The TA measurements specifically highlight that the 12 MPa-treated sample possesses a longer photoexcitation recovery lifetime compared to those treated at higher pressures (14 and 16 MPa), which showed only double-exponential decay (Fig. 23d). This suggests that there is a precise density of oxygen vacancies required to facilitate this exciton-to-free-carrier transition.

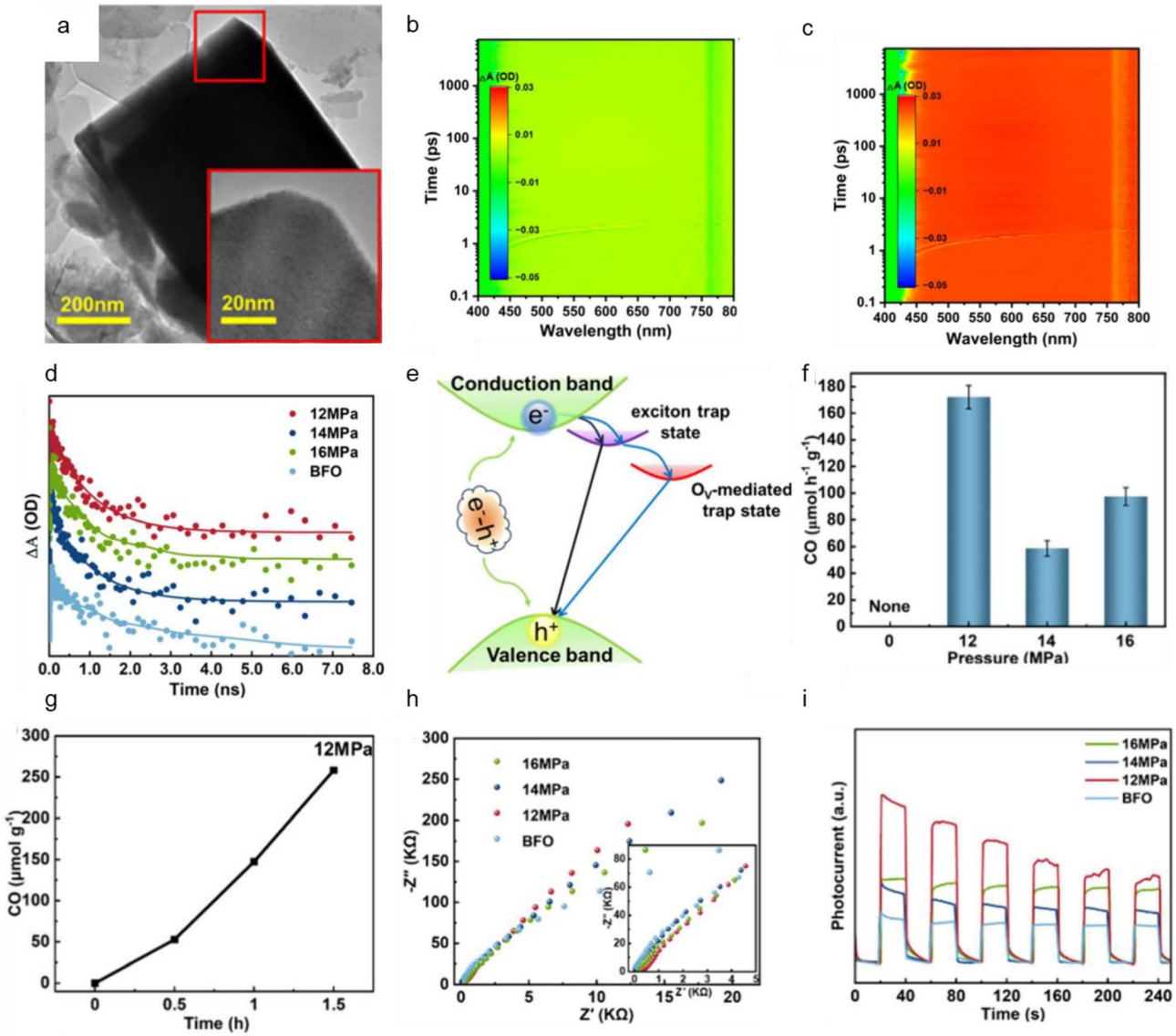

Fig. 23 Defect-engineered $BiFeO_3$ for enhanced sunlight-driven CO_2 photocatalysis. (a) Low-magnification TEM image of $BiFeO_3$ treated with SC CO_2 at 12 Mpa, The 3D plot of fs-TA spectra of (b) untreated $BiFeO_3$, (c) treated $BiFeO_3$ at 12 MPa of SC CO_2, (d) the rise portion of the normalized PIA kinetic curves of $BiFeO_3$ treated with SC CO_2 under different pressure, near ≈605 nm, (e) schematic diagram of the photophysical process of exciton and O_V-mediated trap states, (f) the yield distribution of photoreduction product CO in 1.5 h, (g) the amount of CO produced by CO_2 is a function of the irradiation time of $BiFeO_3$ treatment at different pressures, (h) EIS Nyquist plots for $BiFeO_3$, (i) photocurrent responses of $BiFeO_3$. Reproduced with permission from ref. 19. Copyright 2025, American Chemical Society.

The impact of this enhanced exciton dissociation was clearly reflected in the photocatalytic performance and electrochemical evaluation. The $BiFeO_3$ nanosheet was highly selective for the reduction of CO_2 to CO, with the 12 MPa-treated catalyst delivering the highest yield (Fig. 23f and g). This peak performance was corroborated by a series of electrochemical tests: the 12 MPa sample exhibited the strongest photocurrent response and a reduced semicircle radius in electrochemical impedance spectroscopy, signifying significantly higher charge transfer efficiency (Fig. 23h and i). While the 2D morphology inherently shortens carrier migration distances, the authors conclude that it is the oxygen vacancy-mediated dissociation, unique to the 12 MPa treatment, that provided the surge in carrier concentration necessary to outperform the samples treated at higher pressures. By successfully bridging ultrafast photophysical insights with tangible catalytic outputs, this work demonstrated that the efficiency of CO_2 reduction is not merely a matter of light absorption or surface area, but is fundamentally governed by the ability to engineer defect states that can forcibly decouple bound excitons.[19]

The cocatalyst offers various opportunities for enhancing CO_2 photoreduction efficiency, as we discussed in previous examples. One key property of metal cocatalysts is LSPR. However, the hot carriers produced *via* the LSPR effect in metal photocatalysts have a much shorter lifetime compared to those generated in semiconductors, making CO_2 reduction with H_2O

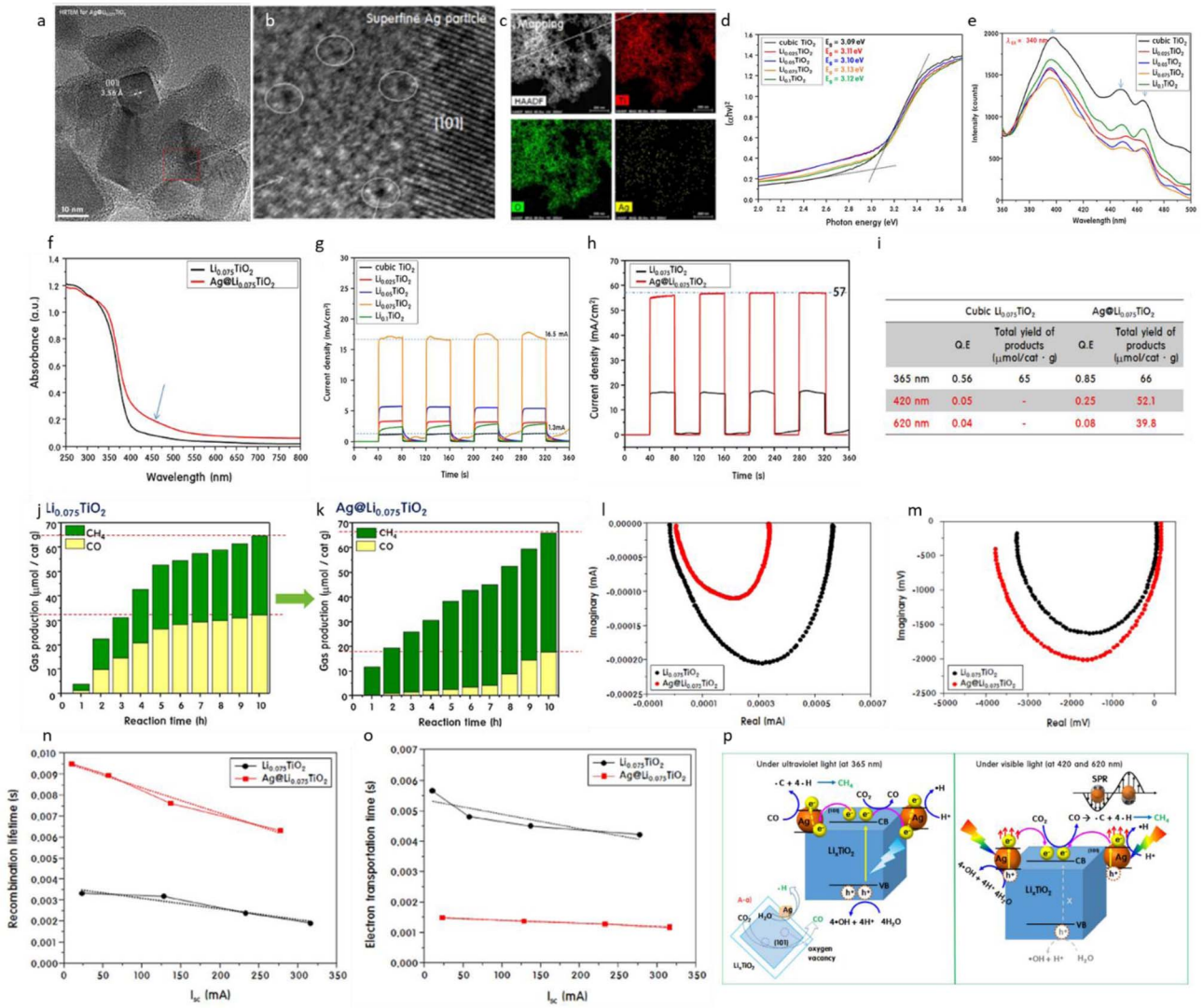

Fig. 24 Photocatalytic CO_2 reduction using the surface plasmon resonance effect of superfine silver nanoparticles anchored on lithium titanium dioxide nanocubes. (a–c) HRTEM images of Ag@$Li_{0.075}TiO_2$ particle and EDS Mapping, (d) Tauc plots of TiO_2 and Li_xTiO_2 particles, (e) PL spectra; (f) UV-Vis spectra of Li_xTiO_2 and Ag@Li_xTiO_2 particles, (g) photocurrent curves of TiO_2 and Li_xTiO_2 particles, (h) photocurrent of $Li_{0.075}TiO_2$ and Ag@$Li_{0.075}TiO_2$ particles, (i) quantum efficiency obtained from the IPCE spectra according to the irradiation wavelength for Li_xTiO_2 and Ag@$Li_{0.075}TiO_2$ particles, (j and k) catalytic performances for CO_2 photoreduction on $Li_{0.075}TiO_2$, and Ag@$Li_{0.075}TiO_2$ particles under UV-light irradiation, (l) IMVS and (m) IMPS curves for $Li_{0.075}TiO_2$ and Ag@Li_xTiO_2 particles, (n) recombination lifetime and (o) electron transport time determined from IMVS and IMPS curves, respectively, (p) expected mechanisms for the photoreduction of CO_2 to CH_4 on Ag@Li_xTiO_2 particle under UV- and visible light irradiations. Reproduced with permission from ref. 533. Copyright 2018 Elsevier.

more challenging. To solve this problem, combining plasmonic metal nanostructures with semiconductors (such as TiO_2) has been a widely used method by which the lifetime of hot charge carriers is prolonged. Kang *et al.*[533] investigated the strong SPR effect of Ag particles anchored on cubic-phase Li_xTiO_2 for the CO_2 photoreduction reaction (Fig. 24). This system represents a multifunctional plasmonic–semiconductor heterostructure, where the synergy between a defect-engineered oxide support and a noble-metal cocatalyst is utilized to shift product selectivity toward reduced hydrocarbons. Their study highlighted three significant aspects: First, they successfully synthesized cubic TiO_2, which activated the [101] facet. Second, Frenkel defects were introduced into some lattices by incorporating Li^+ ions, creating oxygen vacancies. These vacancies increased CO_2 adsorption and accelerated the rate-determining step in CO_2 reduction, facilitating its conversion to CO, the initial reduction product. The vacancies also helped in decreasing the band gap and charge recombination rate, as shown by the UV-Vis and PL spectra, respectively (Fig. 24d and e). Finally, they enhanced photocatalytic activity by loading Ag nanoparticles onto the Li_xTiO_2 cubic surface (Fig. 24a–c), leveraging SPR effects to selectively convert CO_2 to CH_4.

Quantitative results revealed that Ag@$Li_{0.075}TiO_2$ particles yielded 49 μmol g^{-1} of CH_4 after 10 hours of reaction under UV light. This represented an 8.2-fold increase compared to cubic TiO_2 (6 μmol g^{-1}) and a 1.5-fold increase compared to

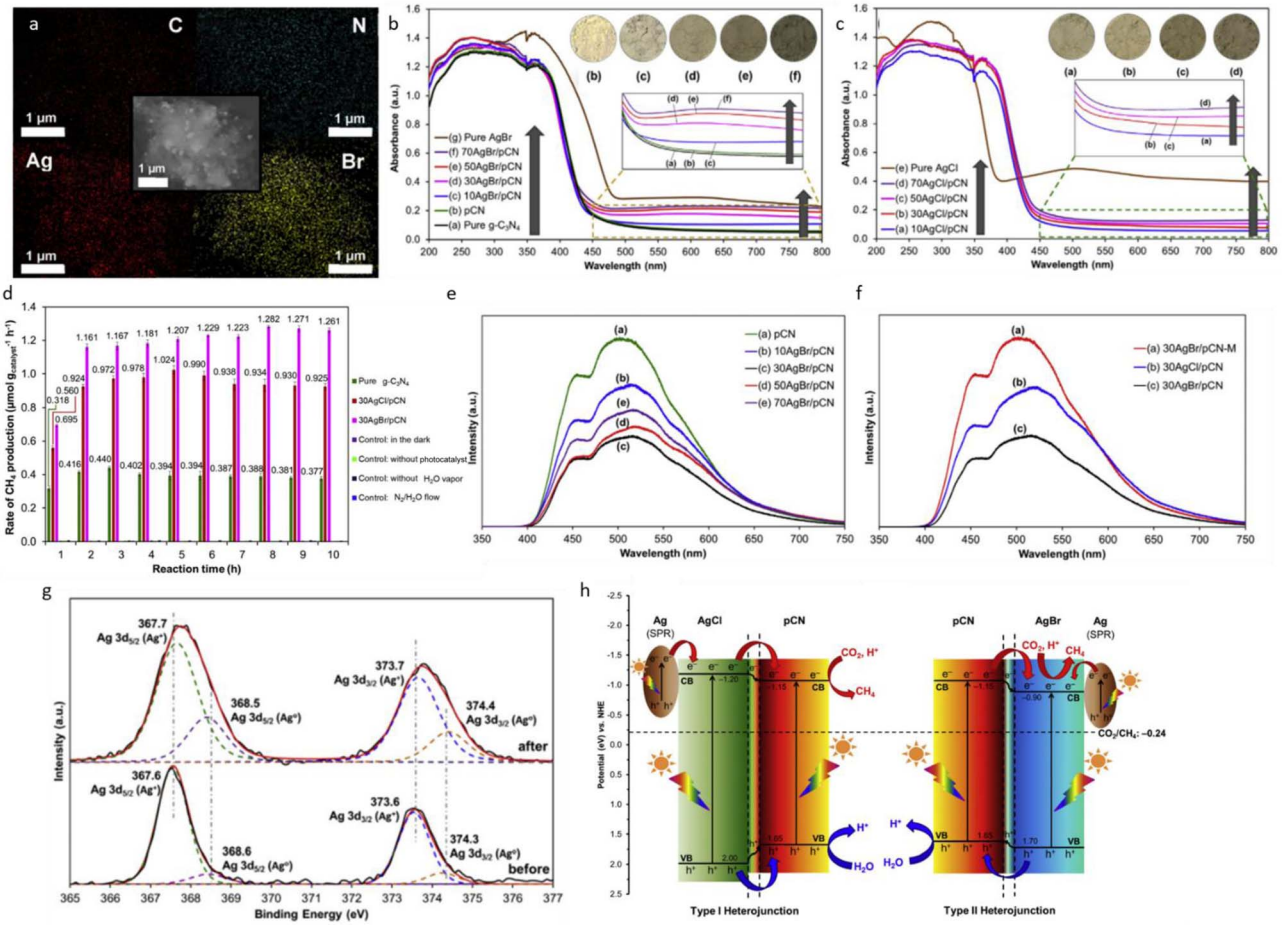

Fig. 25 Photocatalytic CO_2 reduction over heterostructured AgX/g-C_3N_4 nanocomposites. (a) EDX mapping of C, N, Ag, Br, and Cl elements for AgBr/pCN. Insets show the corresponding FESEM images of the AgBr/pCN sample for elemental mapping, (b and c) UV-Vis absorption spectra of the as-synthesized samples: AgBr/pCN and AgCl/pCN hybrid heterostructures. Insets show the digital photographs and the enlarged region of visible light absorption of the samples, (d) time dependence of the rate of CH_4 production over pure g-C_3N_4, 30AgBr/pCN and 30AgCl/pCN samples, (e) PL spectra of pCN and AgBr/pCN hybrid heterostructures, (f) PL spectra of 30AgBr/pCN, 30AgBr/pCN-M and 30AgCl/pCN samples, (g) XPS survey (Ag 3d) spectra of the 30AgBr/pCN before and after the photocatalytic reaction, (h) schematic illustration of the band structures of Ag/AgCl/pCN and Ag/AgBr/pCN hybrid nanocomposites for the photoreduction of CO_2 with H_2O to CH_4 under the light irradiation. Reproduced with permission from ref. 534. Copyright 2016 Elsevier.

$Li_{0.075}TiO_2$ (33 μmol g^{-1}). Additionally, the activity remained stable under visible light (420 and 620 nm), producing 42 and 34 μmol g^{-1} of CH_4, respectively, after 10 hours. Without Ag nanoparticles, cubic TiO_2 and Li_xTiO_2 exhibited a CH_4 : CO product ratio of approximately 1 : 1, showing no selectivity. However, with Ag loading, the ratio shifted to 3 : 1, favoring CH_4 production (Fig. 24j and k). Kang *et al.*[533] attributed the enhanced photocatalytic performance to the LSPR effect of Ag nanoparticles, which is evident by the increase in absorption across visible regions upon loading Ag (Fig. 24f). Under SPR, light trapping on the metal surface and electron excitation into the photocatalyst resulted in significant photocurrent increases (Fig. 24g and h). Specifically, Ag@$Li_{0.075}TiO_2$ exhibited a photocurrent density of 57 mA cm^{-2} under visible light, 3.5 times higher than $Li_{0.075}TiO_2$, which was attributed to the stable integration of Ag particles with $Li_{0.075}TiO_2$. The HRTEM and elemental mapping confirmed the even distribution of Ag, Ti, and O atoms on the particle surface (Fig. 24a–c).

The study confirmed CH_4 as the dominant product under UV and visible light. Using Ag@$Li_{0.075}TiO_2$, approximately 98% CH_4 (20 μmol g^{-1}) was produced after 10 hours of reaction under UV light (Fig. 24j and k). The quantum efficiency of Ag@$Li_{0.075}TiO_2$ also increased significantly across wavelengths. Under 365 nm UV light, the quantum efficiency rose from 0.56 for $Li_{0.075}TiO_2$ to 0.85 for Ag@$Li_{0.075}TiO_2$. Similar enhancements were observed under 420 and 620 nm visible light (Fig. 24l).

Impedance measurements as well as intensity modulated photocurrent/photovoltage spectroscopies (IMVS and IMPS) revealed slower electron–hole recombination (Fig. 24n) and faster electron transport times (Fig. 24o) in Ag@$Li_{0.075}TiO_2$ compared to $Li_{0.075}TiO_2$, attributed to the electron trapping and plasmonic resonant energy transfer properties of Ag. Mechanistically, under UV irradiation, Li_xTiO_2 absorbed UV light, transferring electrons from its valence band to the conduction band. Ag trapped these electrons, maintaining charge separation. CO_2 was reduced at the conduction band or Ag surface to

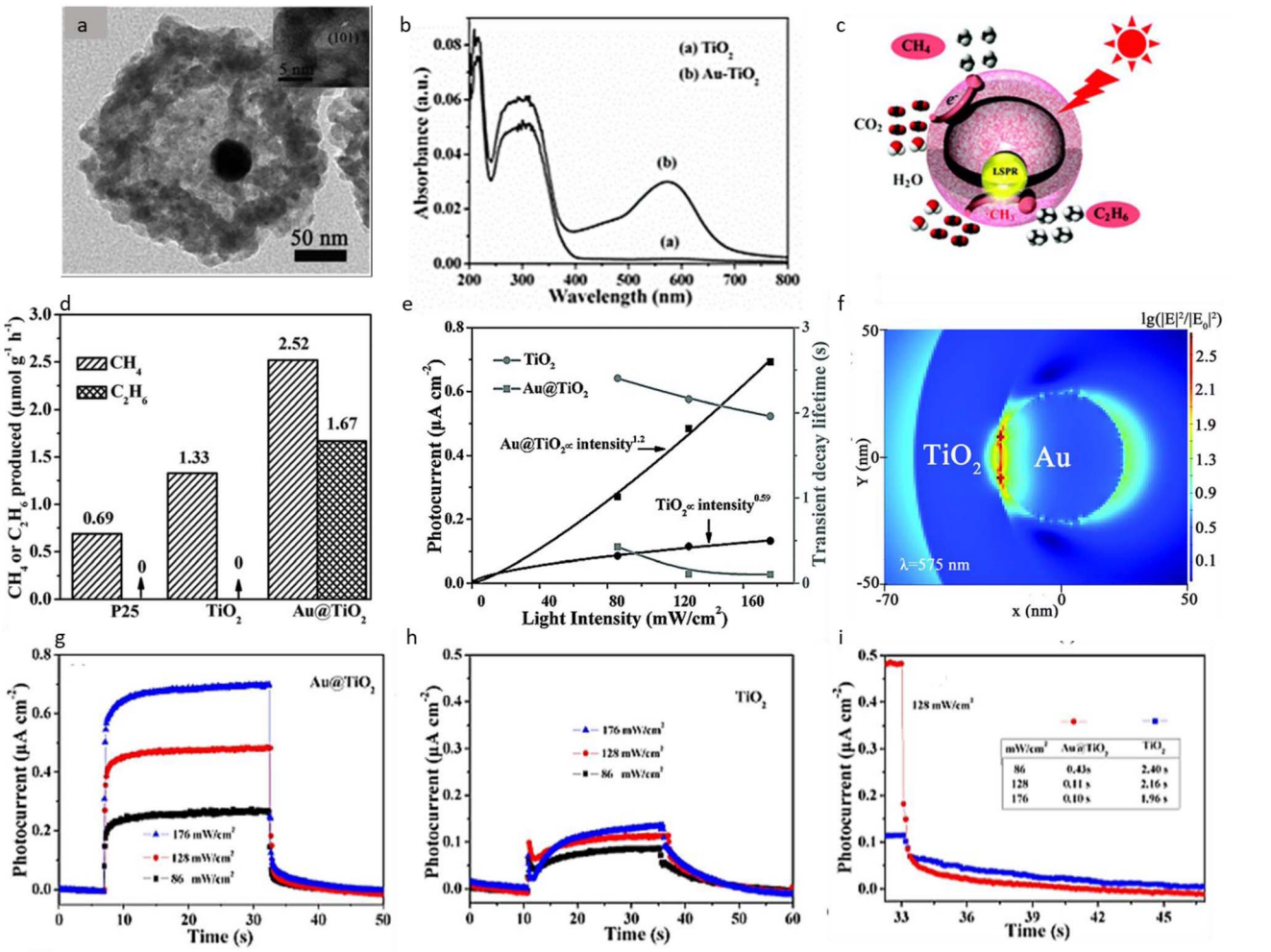

Fig. 26 Photocatalytic CO_2 reduction over plasmon–semiconductor hybrid Au@TiO_2 yolk–shell hollow spheres. (a) TEM images, (b) UV-Vis diffuse reflectance spectra of TiO_2 hollow spheres and Au@TiO_2 yolk–shell hollow spheres, (c) schematic for the mechanism of CO_2 reduction, (d) comparison of photocatalytic activity for CO_2 reduction over P25, TiO_2 hollow spheres, and Au@TiO_2 yolk–shell hollow spheres, (e) photocurrent responses as a function of light intensity and transient decay lifetime of surface trap states, (f) the spatial distribution of local EM field enhancement on the x–y plane for Au@TiO_2 yolk–shell hollow spheres from an FDTD simulation, (g and h) photocurrent responses, (i) the comparison of photocurrent of Au@TiO_2 yolk–shell hollow spheres TiO_2 and hollow spheres with light intensity of 128 mW cm^{-2}, the table is the transient decay lifetime of surface trap states of Au@TiO_2 yolk–shell hollow spheres and hollow spheres under light irradiation with different intensities. Reproduced with permission from ref. 535. Copyright 2015 Royal Society of Chemistry.

CO or CO_2^- intermediates, which further reacted with protons to form CH_4. Under visible light, Ag absorbed photons and transferred electrons to the Li_xTiO_2 conduction band *via* SPR, reducing CO_2 (Fig. 24p). This work provided a comprehensive framework for leveraging SPR effects, oxygen vacancies, and cubic morphology to improve the efficiency and selectivity of CO_2 photoreduction reactions.

A cocatalyst can also be loaded onto a semiconductor using a precursor, forming a hybrid Z-scheme-metal cocatalyst system. For instance, Yong *et al.*[534] developed a visible-light-active silver halide (AgX, where X = Cl or Br) photocatalyst by depositing it onto protonated graphitic carbon nitride (pCN) through a sonication-assisted deposition–precipitation method at room temperature (Fig. 25). This system is also an example of a multifunctional plasmonic–semiconductor heterostructure. Photoreduction of the silver halides resulted in the formation of Ag as a plasmonic metal cocatalyst. The choice of halide ions influenced the band energies and the electron dynamics of the system.

The photocatalytic performance was tested for CO_2 reduction to CH_4 under low-power daylight bulb illumination at ambient conditions. The 30AgBr/pCN nanocomposite demonstrated superior photocatalytic activity, producing CH_4 at 10.92 μmol per g catalyst, outperforming both single-phase AgBr and pCN by factors of 34.1 and 4.2, respectively (Fig. 25d). Additionally, the performance of AgBr/pCN was 1.3 times higher than AgCl/pCN, attributed to enhanced surface plasmon resonance effects and a heterojunction structure that facilitated efficient charge transfer and separation.

Structural characterization showed that AgX crystals transformed into nanoparticles on the pCN surface, as confirmed by FESEM and TEM. EDX mapping revealed a uniform distribution

of elements, including C, N, Ag, Br, and Cl (Fig. 25a). The incorporation of AgX nanoparticles did not significantly alter the absorption edge of pCN but slightly enhanced its visible-light absorption. The band gap energy of AgBr (2.6 eV) enabled it to absorb more visible light compared to AgCl (3.2 eV), contributing to better photocatalytic performance (Fig. 25b and c).

Photoluminescence analysis indicated that 30AgBr/pCN effectively suppressed electron–hole recombination, which was not the case with physically mixed samples, correlating its high photocatalytic activity with efficient charge transfer (Fig. 25e and f). After multiple reaction cycles, XPS analysis confirmed a partial reduction of AgX to metallic Ag, enhancing the SPR effect (Fig. 25g). The hybridization of AgX with pCN created heterojunction interfaces, with AgBr forming a Type II heterojunction that facilitated spatial separation of charge carriers. This configuration improved charge transfer efficiency and suppressed recombination, driving the reduction of CO_2 to CH_4 through the well-aligned energy bands of pCN, Ag, and AgBr (Fig. 25h). The thermodynamic properties of AgBr, including a conduction band potential more negative than the CO_2/CH_4 reduction potential, allowed effective electron transfer to reduce CO_2. Concurrently, the oxidation of H_2O provided protons for the reaction, completing the photocatalytic cycle. These advancements underline the significance of AgX incorporation in improving photocatalytic efficiency and product yield.[534]

LSPR not only generates excited charge carriers in plasmonic metals but also enhances the electric field, significantly influencing photocatalytic reactions. Zou *et al.*[535] demonstrated this with Au@TiO_2 yolk–shell hollow spheres, where an electric field generated by LSPR boosted electron–hole pair generation, suppressed charge recombination, and improved the CO_2 photoreduction yield. This system is an example of a plasmonic–semiconductor heterostructure. The LSPR-induced electromagnetic field around Au nanoparticles enhanced the separation of charge carriers in the TiO_2 shell, enabling the formation of high-grade hydrocarbons like ethane (C_2H_6), rarely seen in prior CO_2 reduction systems.

This study highlights the importance of LSPR-mediated electric fields in driving multi-electron and proton transfer reactions, a crucial step toward producing valuable carbon species. The researchers synthesized Au@TiO_2 yolk–shell hollow spheres (Fig. 26a and c). Optical analysis showed a significant red-shift in the LSPR peak (575 nm) of Au@TiO_2, compared to bare Au nanoparticles (540 nm), due to the high refractive index of TiO_2 (Fig. 26b). Under UV-visible light, bare TiO_2 hollow spheres exhibited moderate activity for CO_2 photoreduction (CH_4: 1.33 μmol g^{-1} h^{-1}). In contrast, Au@TiO_2 enhanced CH_4 production (2.52 μmol g^{-1} h^{-1}) and facilitated C–C coupling to generate ethane (C_2H_6: 1.67 μmol g^{-1} h^{-1}) (Fig. 26d). This improvement was attributed primarily to the LSPR-mediated local EM field, which amplified charge carrier generation and reduced recombination losses.

The study also ruled out significant electron transfer between Au and TiO_2 due to the minimal contact between the yolk and shell. Instead, the enhanced photocatalytic activity was driven by the intense local electric field generated by LSPR. The FDTD simulations confirmed that the electric field strength was highest near the Au nanoparticles, leading to a localized increase in charge carrier density within the TiO_2 shell (Fig. 26f). This field concentration promoted the dimerization of CH_3 radicals, favoring C–C coupling and ethane formation. Regions farther from the Au core primarily facilitated CH_4 generation due to insufficient $^{\bullet}CH_3$ radical concentration. The photocurrent response further validated the role of the LSPR effect. Au@TiO_2 exhibited a significant enhancement in photocurrent compared to bare TiO_2, confirming increased charge carrier generation (Fig. 26e and g–i). This work highlights the potential of plasmonic nanostructures like Au@TiO_2 in photocatalytic CO_2 reduction, offering insights into designing catalysts for artificial photosynthesis. By leveraging LSPR to enhance charge dynamics and promote complex reaction pathways, researchers can pave the way for efficient solar-driven fuel production systems.[535]

The previous study established the role of electric field enhancement in driving CO_2 photoreduction. In another study, Long *et al.*[536] demonstrated the long-range redox reactivity of plasmon-generated hot electrons from gold nanorods for solar-driven CO_2 conversion. They designed a series of Au NR@ZnO core–shell photocatalysts with tunable shell thicknesses to achieve efficient solar-to-CH_4 conversion, where hot electrons drive the photoreduction on the polar ZnO shell (Fig. 27). This system is an example of a multifunctional plasmonic–semiconductor heterostructure. Polar ZnO was selected as an electron acceptor for two main reasons: its surface polarity deforms CO_2 and lowers its LUMO level, and its abundant hydroxyl groups and Brønsted acidic protons near CO_2 adsorption centers aid the CH_4 generation. This prevented the formation of CO_2^- species and thermodynamically favored CH_4 production under solar light. Au NR@ZnO samples were synthesized using a low-temperature solution process, with varying precursor ratios enabling control over ZnO shell thickness (Fig. 27a). SEM and TEM images confirmed clear boundaries between the Au core and ZnO shell, with an average Au NR aspect ratio of 3 : 1 (Fig. 27b). Photocatalytic activity tests revealed that the highest CH_4 and CO production rates were 17.12 μmol h^{-1} $(g_{Au})^{-1}$ and 32.4 μmol h^{-1} $(g_{Au})^{-1}$, respectively (Fig. 27d–f). When normalized to ZnO content, the activity variation across different shell thicknesses was minimal, confirming that ZnO thickness did not directly affect photocatalytic efficiency (Fig. 27e). Under visible light, CH_4 was the primary product, while CO was exclusively produced under ultraviolet light, illustrating that the Au core and ZnO shell synergistically enhance photocatalytic activity (Fig. 27f).

Transient absorption spectroscopy provided detailed insights into the charge transfer dynamics in the Au NR@ZnO system (Fig. 27j). In the steady-state UV-Vis spectrum, two characteristic plasmon peaks corresponding to the transverse and longitudinal modes of Au NRs were observed at 534 nm and 688 nm (Fig. 27c). Upon encapsulation with ZnO, a blue shift in the longitudinal peak was noted, attributed to changes in the surrounding dielectric constant. In the transient absorption spectra, bleaching at 534 nm and 688 nm confirmed the

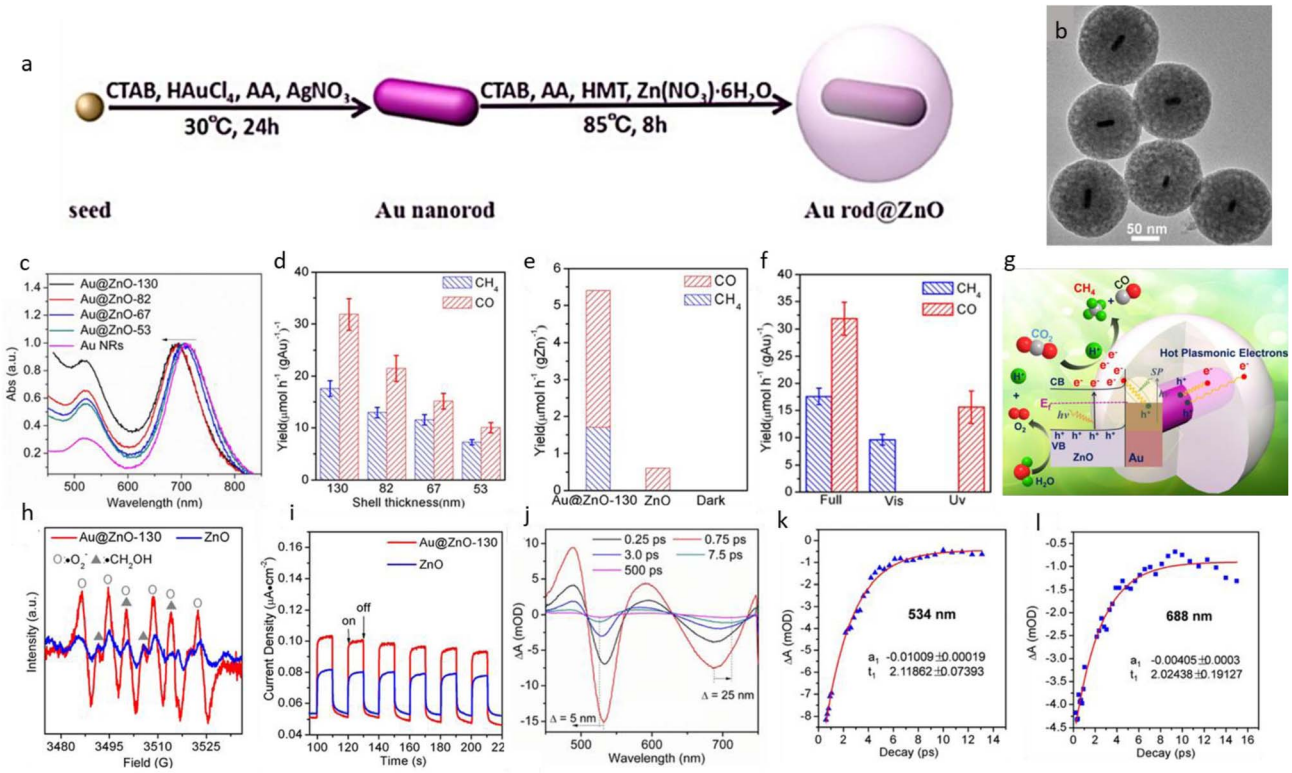

Fig. 27 Photocatalytic CO_2 reduction over plasmon–semiconductor hybrid Au NR@ZnO core–shell nanostructures. (a) The schematic diagram of the fabrication procedure of Au NR@ZnO samples, (b) TEM image of Au NR@ZnO-130 sample, (c) UV-Vis spectrum, (d) shell thickness-depended photocatalytic activity of Au NR@ZnO-*x* samples for photocatalytic reduction of CO_2 under solar light irradiation, (e) different catalysts, (f) under different light irradiation, (g) schematic description of the generation, injection and long-range reactivity of hot electrons for the solar-to-hydrocarbon conversion, (h) the EPR spectra of Au NR@ZnO and pure ZnO samples dispersed in DMPO and methanol solution under solar light irradiation, (i) the photocurrent–time curves of Au NR@ZnO and pure ZnO samples, (j) transient absorption spectra of the Au NR@ZnO after excitation by 400 nm pulse. Electron decay kinetics at (k) 534 nm, (l) 688 nm. Reproduced with permission from ref. 536. Copyright 2020 Wiley-VCH GmBH.

excitation of plasmon modes, while a red-shifted positive absorption peak at 470 nm indicated a volume expansion of the hot particles, reducing electron density and plasmon frequency (Fig. 27j). A significant blue shift in the bleach at 534 nm, reaching up to 130 meV, was much larger than that observed for pure Au NRs (0.15 meV). This indicated a strong interaction between the Au core and ZnO shell, suggesting efficient coupling and charge transfer.

The recovery of plasmon bleach signals provided critical data on electron relaxation dynamics. At 534 nm, the bleach recovery followed a monoexponential decay with a relaxation time of 2.1 ps, corresponding to electron–phonon interactions. Similarly, the relaxation time at 688 nm was significantly longer than that of pure Au NRs (<1 ps), highlighting the prolonged lifetime of hot electrons in the Au NR@ZnO system (Fig. 27k and l). This extended lifetime enhances the likelihood of photoexcited electrons participating in catalytic reactions (Fig. 27g).

Spin trap EPR confirmed the generation of $^{\bullet}O_2^-$ and $^{\bullet}CH_2OH$ radicals, further supporting the involvement of photoinduced electrons (Fig. 27h). Electrochemical analyses demonstrated a twofold enhancement in photocurrent and a reduction in charge transfer resistance for Au NR@ZnO compared to pure ZnO (Fig. 27i). The well-distributed Au NR@ZnO core–shell structure exhibited strong synergistic effects for CO_2 photoreduction. The LSPR of Au NRs extended light absorption into the visible range, driving the eight-electron CO_2 reduction reaction for CH_4 generation. While ZnO shell thickness did not influence the production rate, its role in prolonging electron lifetimes enhanced overall efficiency. This work highlights the potential of the Au NR@ZnO system for solar-driven CO_2-to-hydrocarbon conversion.[536]

The research on semiconductor-plasmon hybrid systems highlights a significant gap in the understanding of purely plasmonic photocatalysts for artificial photosynthesis. Zhao *et al.*[459] demonstrated that quantum-sized Au NPs were capable of photocatalytically reducing CO_2 to CO using H_2O under low-intensity irradiation at 420 nm (Fig. 28). This is an example of a purely plasmonic metal-catalysed process. This process utilized electron–hole pairs generated predominantly from interband transitions, leading to a CO production rate of 4.73 mmol g^{-1} h^{-1} with ~100% selectivity. This rate was approximately 2.5 times higher than that observed during CO_2 reduction with H_2 under similar conditions. The enhanced activity is attributed to surface Au–O species formed during H_2O decomposition, which improved rate-determining steps,

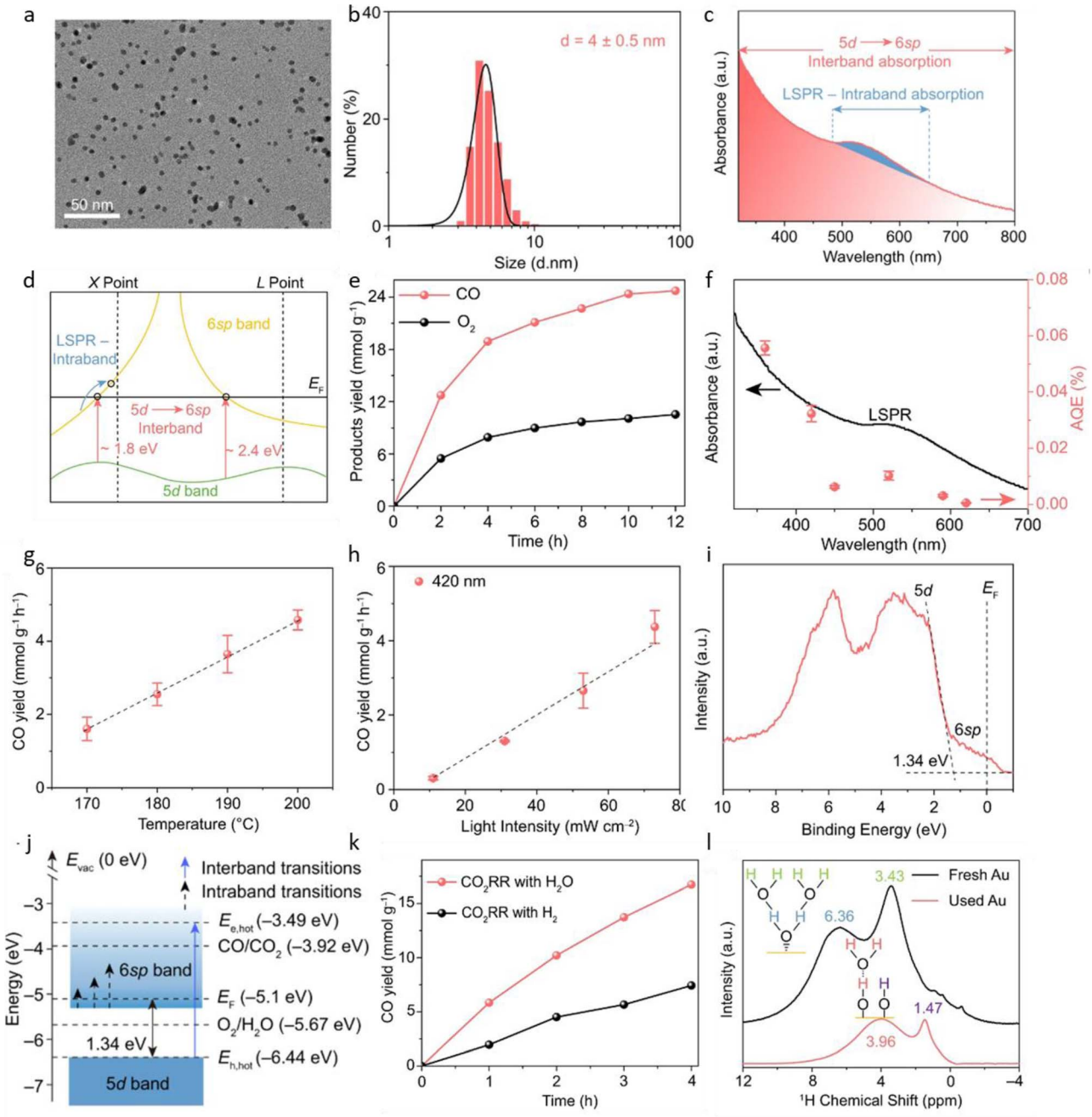

Fig. 28 Photocatalytic CO_2 reduction over Au nanoparticles by interband transitions. (a) TEM image, (b) particle size distribution of Au NPs, (c) UV-Vis absorption spectrum of the Au NPs with interband and intraband absorption, (d) schematic diagram of interband and intraband (LSPR) transitions, (e) CO and O_2 productions over Au NPs with 420 LED light irradiation at 200 °C, (f) wavelength-dependent AQEs of the Au photocatalyst, (g) the reaction temperatures and (h) light intensity-dependent CO production rate on Au NPs under 420 nm LED light irradiation, (i) valence-band XPS spectrum of Au, (j) schematic illustration for the electronic band structure of the ~4 nm Au NPs, (k) photocatalytic CO_2RR performance on Au NPs with H_2O or H_2 under 420 nm light illumination at 200 °C. The volume ratio of H_2 to CO_2 is 4 : 1 in the gas mixture, (l) ^{1}H ssMAS-NMR spectra of Au samples before (black curve) and after CO_2RR (3 h reaction, red curve). Reproduced with permission from ref. 459. Copyright 2022 Springer Nature.

reduced energy barriers for *CO desorption and *OOH formation, and facilitated the production of CO and O_2.

In contrast to the LSPR effect, the hot electron–hole pairs derived from interband transitions exhibit higher redox potentials and longer lifetimes. These features are advantageous for H_2O oxidation and CO_2 reduction. The quantum-sized Au NPs (~4 nm) (Fig. 28a and b) with unique interband excitations under visible light irradiation demonstrated their potential for photocatalytic CO_2 conversion. Their UV-Vis absorption spectrum spanned 320–800 nm, with a small

peak at 520 nm attributed to the LSPR effect, while the dominant interband absorption band extending to 800 nm results from 5d–6sp transitions (Fig. 28c).

Theoretical calculations revealed two types of interband excitations: transitions from the 5d band to states near the Fermi level and transitions to unoccupied 6sp band states above the Fermi level (Fig. 28d). Under monochromatic LED light at 420 nm, photocatalytic experiments achieved CO evolution of up to 4.73 mmol g^{-1} h^{-1} and O_2 evolution of 1.98 mmol g^{-1} h^{-1} (Fig. 28e). The apparent quantum efficiency peaked at 520 nm due to LSPR-enhanced light absorption, although interband transitions at shorter wavelengths also contributed significantly, confirming that the CO_2-to-CO conversion process is driven mainly by interband-generated hot electrons (Fig. 28f).

Time-resolved photoluminescence analysis showed a carrier lifetime of ~0.2 ns, which was much longer than the ~30 fs typical of LSPR-generated carriers. This extended lifetime facilitated efficient charge transfer, improving photocatalytic activity. The photothermal effect on catalytic CO_2 reduction using Au NPs was negligible because the 420 nm LED light used (73 mW cm^{-1}) had a low intensity, even lower than solar intensity. The sample temperature only increased from 24 °C to 33 °C under irradiation. Therefore, CO_2-to-CO conversion on Au NPs was likely driven by photogenerated electrons (Fig. 28h). However, a linear increase in the photocatalytic CO production rate with reaction temperature (Fig. 28g) suggested that heat input enhanced the photocatalytic CO_2 reduction activity, likely due to the higher populations of adsorbates in excited vibrational states at elevated temperatures. Valence-band XPS spectra demonstrated that the electronic band structure of Au NPs was well-suited for CO_2 reduction and H_2O oxidation (Fig. 28i). Specifically, the hot electron energy under 420 nm light was more positive than the reduction potential of CO/CO_2, while the hot hole energy was more negative than the oxidation potential of O_2/H_2O, enabling simultaneous CO_2 reduction and H_2O oxidation (Fig. 28j). *In situ* FTIR spectroscopy revealed the accumulation of surface-adsorbed H_2O and *COOH species on the Au surface during the reaction. Replacing H_2O with H_2 resulted in a halving of the CO yield, underscoring the critical role of H_2O in the CO_2 reduction process (Fig. 28k). Further analysis using solid-state NMR and other techniques showed that immobilized H_2O dissociates into *OH species on the Au surface under illumination, forming Au–O species that enhanced the efficiency of CO_2 reduction (Fig. 28l).

The proposed reaction mechanism involves photogenerated hot electrons and holes driving the dissociation of H_2O and the reduction of CO_2. Theoretical and experimental findings collectively highlight the importance of interband transitions and surface Au–O species in improving the efficiency of CO_2 reduction using quantum-sized Au NPs and H_2O. These insights offer a promising direction for the development of purely plasmonic photocatalysts for artificial photosynthesis.[459]

Throughout the preceding sections of this review, we have emphasized that the localized electric field inherent to plasmonic systems is not merely a secondary consequence of excitation, but a primary driver of catalytic performance. Further expanding on this idea, Xiong *et al.*[412] demonstrated the critical role of these near-field effects in achieving high-efficiency, broadband artificial photosynthesis using an Au-rod/CuPd-alloy core–shell architecture. This architecture represents a bimetallic core–shell plasmonic heterostructure. By utilizing the intense localized electric field at the CuPd surface, the authors successfully utilized low-energy NIR photons to drive the multielectron reduction of CO_2 to CH_4 with nearly 100% selectivity.

This catalyst design strategically positions the CuPd alloy shell as a dual-function cocatalyst that simultaneously captures CO_2 molecules and positions them within the most intense regions of the plasmon-induced local field (Fig. 29a). The synthesis involved the epitaxial growth of a single-crystal CuPd shell onto Au nanorods, a structure confirmed by the preservation of ordered lattice fringes and reduced coordination numbers in XANES/EXAFS spectra, ensuring that the active Pd and Cu sites were optimally located on the outermost surface. The light-harvesting capability of these core–shell composites was a crucial feature of their performance. The UV-Vis extinction spectra (Fig. 29b and c) revealed characteristic transversal and longitudinal LSPR modes at 510 and 740 nm, respectively. Crucially, the researchers found that precise control of the CuPd shell thickness enabled a significant broadening of the absorption profile into the NIR region. This ensured that the high-density CO_2 adsorbates were continuously energized by enhanced local fields across the entire solar spectrum, bridging the gap between light absorption and molecular transformation.

The CH_4 production rate exhibited a volcano-shaped dependence on the CuPd shell thickness, highlighting a critical optimization threshold where the density of surface active sites was maximized without inducing excessive electron–phonon scattering (Fig. 29d). The AQE profile also displayed a nearly perfect overlap with the Au-rod LSPR extinction spectrum, providing insight into the role of low-energy NIR photons in driving the multielectron reduction process (Fig. 29e). To understand the how low-energy photons overcome the energy barrier to carry out the reaction, the authors utilized *in situ* near-ambient pressure X-ray photoelectron spectroscopy (NAP-XPS) and monitored electronic fluctuations in real-time. The analysis of the Cu 2p and Pd 3d core levels (Fig. 29f and g) revealed a distinct three-stage electronic response under illumination: a fast, reversible accumulation of hot electrons above the Fermi level, coupled with a slower, irreversible photoreduction of the metal sites. This dual-process enrichment, characterized by an instantaneous decrease in binding energy upon light exposure, effectively elevated the chemical potential of the catalytic surface, thereby benefiting catalysis.

The authors then performed DFT calculations on the PDOS, which revealed that the localized electric field played a transformative role in CO_2 activation (Fig. 29h). The field induced the emergence of quasi-isolated trap states above the Fermi level, which extended the lifetime of hot electrons and facilitated a multiphoton absorption process. This allowed electrons to be re-excited by consecutive NIR photons until they gain sufficient energy to trigger the CO_2RR. Furthermore, natural orbitals for chemical valence (NOCV) analysis demonstrated that the

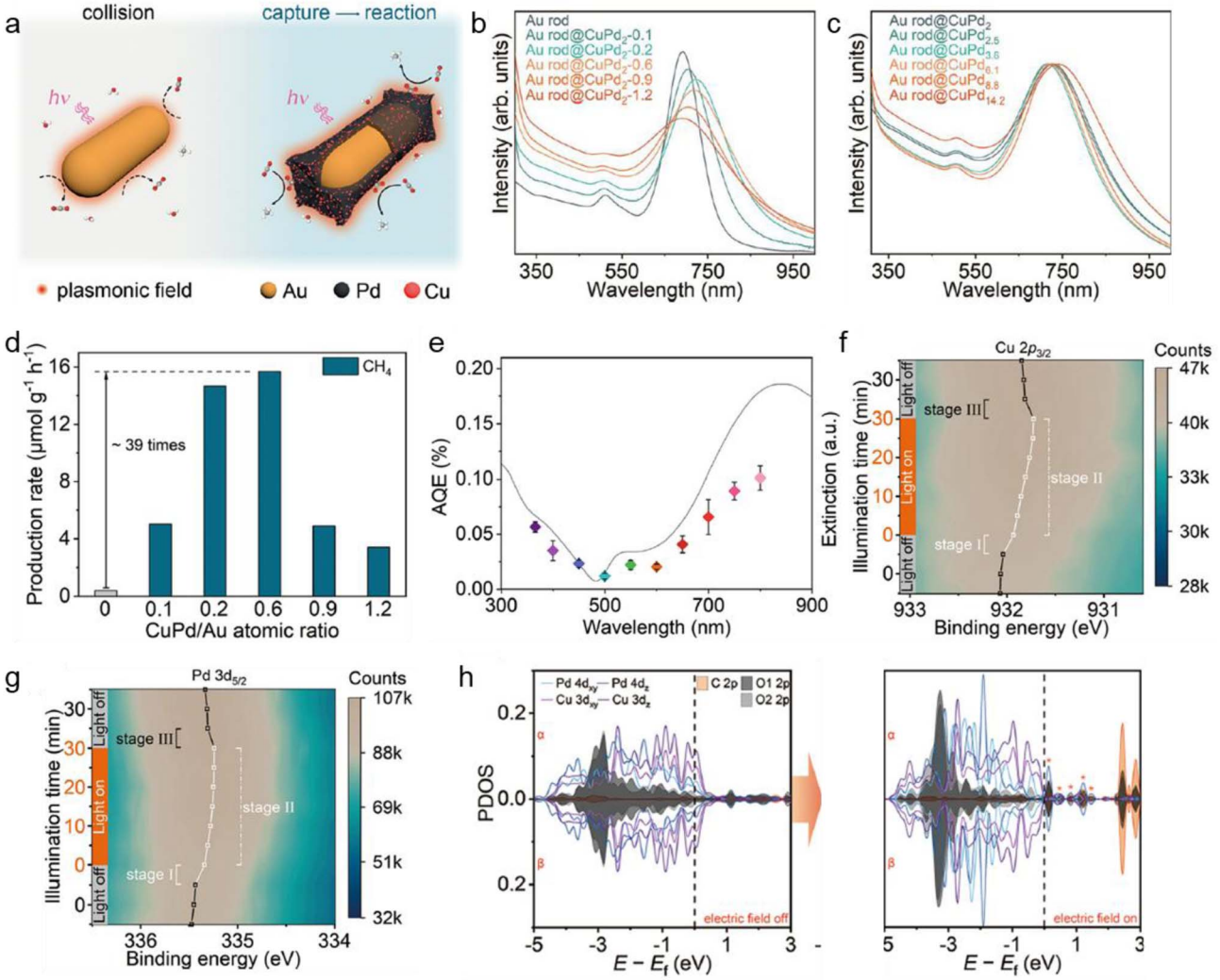

Fig. 29 Photocatalytic CO_2 reduction over Au-rod/CuPd-alloy core–shell photocatalyst. (a) Schematic illustration of the role of CuPd cocatalyst in capturing CO_2 molecules. UV-Vis extinction spectra of Au rod and Au rod@CuPd with (b) different CuPd shell thicknesses and (c) different Cu/Pd molar ratios, (d) average production rates of CH_4 over Au rod@$CuPd_2$ with different shell thicknesses, (e) calculated AQEs (color dots) over Au rod@$CuPd_2$ under different monochromatic light illumination, in reference to its UV-Vis extinction spectrum (black line). *In situ* NAP-XPS contour plot of (f) Cu $2p_{3/2}$ and (g) Pd $3d_{5/2}$. The squares and lines in black and white indicate unilluminated and illuminated conditions, respectively. (h) The projected density of states of CO_2 adsorbed on a CuPd (100) surface in the absence (left) and presence (right) of electric field pointing toward the surface. The main quasi isolated trap states are marked with orange asterisks. Reproduced with permission from ref. 412. Copyright 2023 Springer Nature.

electric field dictated a highly selective orbital-specific electron redistribution. When the field pointed toward the surface, electrons were specifically driven into the antibonding π* orbitals of CO_2, weakening the C–O bond and increasing its length. In contrast, the field provided negligible assistance for O–H bond cleavage in H_2O molecules. The assistance of the local electric field in facilitating the directional electron transfer to CO_2 molecules resulted in nearly 100% selectivity toward hydrocarbons.

The authors further improved the efficiency of the process by designing a spherical gas–solid reactor, which recaptured and reflected scattered light onto the catalyst surface. This architectural optimization facilitated enhanced multiphoton absorption, resulting in a CH_4 production rate of 0.55 mmol g^{-1} h^{-1}. This study used a unique idea of "orbital tuning" by the local field, which effectively overrides competing reaction pathways, establishing a sophisticated method for selective artificial photosynthesis using low-energy photons.[412]

4.3. Dry reforming of methane

Another promising reaction for CO_2 conversion using Hydrogen is the dry reforming of methane (DRM, $CH_4 + CO_2 \rightleftharpoons 2CO + 2H_2$). DRM converts CO_2 and CH_4 into syngas, a mixture of CO and H_2, in a thermodynamically uphill reaction that is advantageous for sustainable energy storage. The resulting syngas can be used as feedstock in processes such as Fischer–Tropsch synthesis and oxo processes. Additionally, since CO_2 and CH_4 together account for 90% of greenhouse gas emissions, DRM

offers the potential to address two major sources of global warming simultaneously.

The thermal DRM process has been extensively studied over the past few decades. However, the high temperatures required (600–1000 °C) and the massive energy consumption involved lead to the re-emission of CO_2, as fossil fuels are burned to generate the necessary heat. To overcome these challenges, photo-assisted DRM has emerged as a promising alternative.[223,542–553] This approach relies on innovative nanoscale catalyst designs that are crucial for effective sunlight harvesting while also being resistant to coke formation.

Despite the wide band gap of many semiconductors favoring catalytic reactions thermodynamically, it also limits the conversion efficiency of solar irradiation. For instance, traditional TiO_2 can only utilize UV photons. However, Hu *et al.*[552] introduced black TiO_2, which featured broad-spectrum absorption, making it suitable for harvesting visible light, which constitutes the majority of natural solar irradiation (Fig. 30). The visible light absorption in black TiO_2 was attributed to deep energy wells created by oxygen vacancies in the lattice (Fig. 30c) or the presence of Ti^{3+} in hydrogenated rutile TiO_2. These defects created a donor level approximately 1.30 eV below the CB edge, which aligned with the energy of visible photons.

Although the CO_2/CO redox potential is marginally more negative than the TiO_2 conduction band edge at room temperature, it shifts to a more positive value above 150 °C, surpassing the CB edge and thereby favoring CO_2 reduction to CO at elevated temperatures. The redox potential of CO/CH_4, however, remained more negative than the energy level of Ti^{3+} at room temperature and above, satisfying the energy requirement for CH_4 oxidation to CO (Fig. 30e).

Furthermore, platinum was incorporated into the TiO_2 *via* impregnation, serving as an active site due to its high conductivity (Fig. 30a). Under illumination with AM 1.5, the photo-driven yields after subtracting thermal contributions) of H_2 and CO (after subtracting thermal contributions) reached 95 and 191 mmol g_{cat}^{-1} h^{-1} at 550 °C, 135 and 299 mmol g_{cat}^{-1} h^{-1} at 650 °C, and 208 and 258 mmol g_{cat}^{-1} h^{-1} at 700 °C (Fig. 30b). The higher CO yield compared to H_2 resulted from the reaction between CO_2 and H_2, which consumed H_2 while producing CO. The relationship between quantum efficiency and wavelength further demonstrated that wavelengths from 395 nm to 950 nm contributed to photo-assisted DRM (Fig. 30d). In this way, the integration of a Pt/black TiO_2 catalyst with a light-diffusing SiO_2 substrate surface resulted in a highly efficient visible light photocatalytic process for CO_2 reforming of methane. This approach achieved photo CO and H_2 yields that were 1000 times greater than previously reported values.[552]

Another wide-band gap semiconductor, Strontium titanate ($SrTiO_3$ or STO) has been explored by Miyayuchi *et al.*[553] as a photocatalyst for the DRM reaction (Fig. 31). However, its

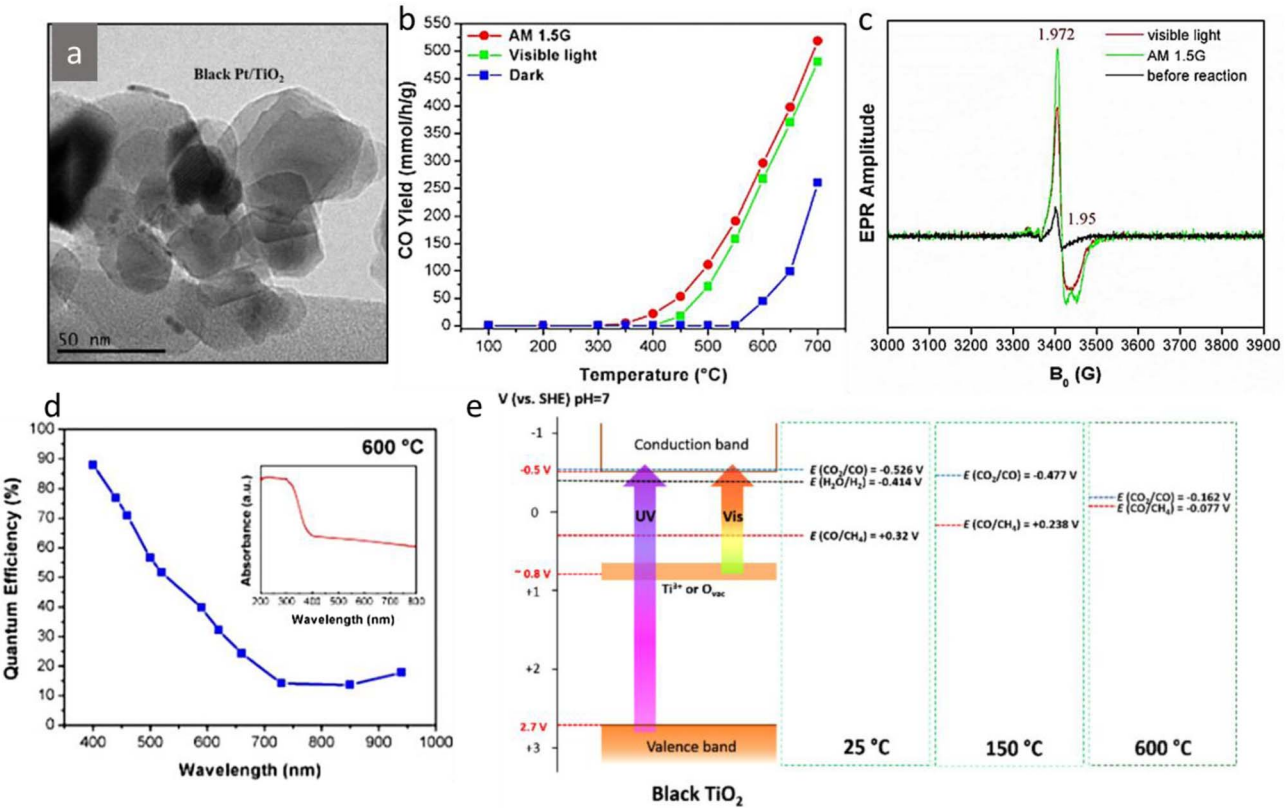

Fig. 30 Photocatalytic dry reforming of methane over defected semiconductor-cocatalyst system Pt/black TiO_2. (a)TEM image of Pt/black TiO_2 catalyst, (b) CO yields from CRM over Pt/black TiO_2 catalyst dispersed on the light-diffuse-reflection surface of a SiO_2 substrate, (c) EPR of the catalysts, (d) QE *versus* wavelength (λ), (e) relationship between band structure of black TiO_2 and redox potentials of CO_2 reforming of CH_4 (CRM). Reproduced with permission from ref. 552. Copyright 2016 American Chemical Society.

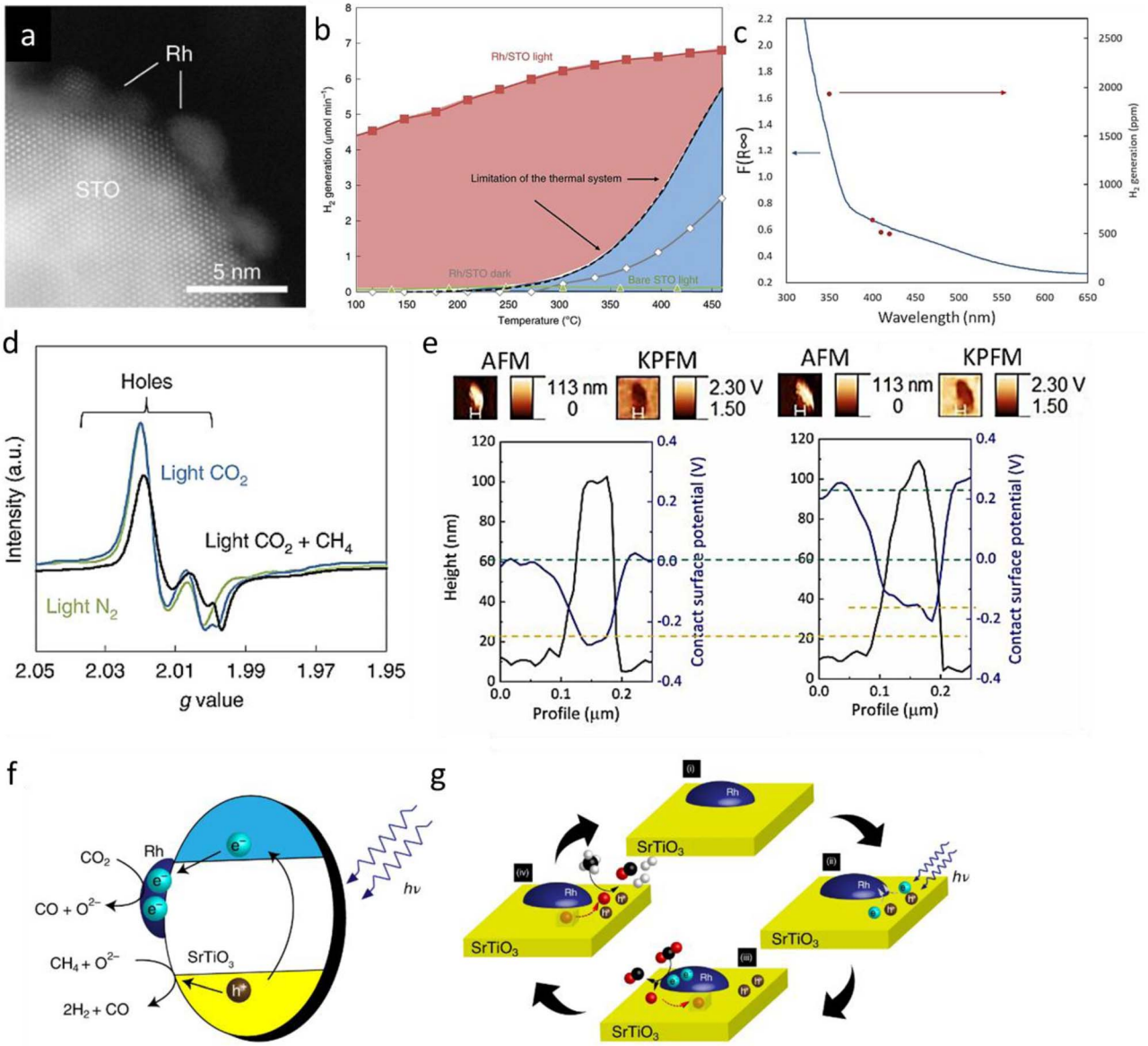

Fig. 31 Photocatalytic dry reforming of methane over doped semiconductor-cocatalyst Rh/STO system. (a) A magnified HAADF-STEM image of Rh/STO, (b) Rh/STO under light irradiation (red squares), the limitation of the thermal system for DRM when using a generic catalyst (dashed line), Rh/STO under dark conditions (grey line with white diamonds) and bare STO under light irradiation (green line with green triangles), (c) UV-Vis spectrum of Rh-STO (F: optical absorption drawn by blue line) and action spectrum of DRM activity (red circles), (d) EPRspectroscopy of Rh/STO under light irradiation in N_2, CO_2 or CH_4/CO_2 atmosphere conditions, (e) Kelvin probe force microscope (KPFM) analysis on the Rh loaded STO single crystal (110), before UV light irradiation (left), and during UV light irradiation (right), (f) a band diagram that shows generation of electron–hole pairs in STO and expected redox reactions, (g) schematic dynamics of charge carriers and oxygen ions. Reproduced with permission from ref. 553. Copyright 2020 Springer Nature.

efficiency is generally low due to rapid electron–hole recombination. The deposition of highly dispersed Rh nanoparticles on STO (Fig. 31a) dramatically increased the catalytic activity, achieving a hydrogen production rate of 4.5 μmol min^{-1} under visible light illumination(Fig. 31b). This rate significantly surpassed the limitations of thermocatalysis, indicating the involvement of hot-carrier chemistry alongside the photothermal effect under illumination. Additionally, the wavelength-dependent activity showed that the reaction was particularly enhanced at wavelengths below 380 nm, which corresponded to the band gap energy of STO (3.2 eV) (Fig. 31c). This finding supported the hypothesis that the DRM reaction was primarily driven by the band gap excitation of STO.

Kelvin probe force microscopy (KPFM) analysis of an STO single crystal with a (110) facet covered with Rh nanoparticles revealed a more pronounced Fermi-level upshift in STO than in the Rh nanoparticles under photo illumination (Fig. 31e). This difference in Fermi-level shift further promoted electron transfer from STO to Rh. In the synthesized Rh/STO composite nanoparticles, photoillumination led to STO domains with

concentrated holes and Rh domains with concentrated electrons. The presence of holes in the photoexcited STO domains was confirmed through *in situ* EPR at −173 °C (Fig. 31d). EPR signals observed around $g = 1.97$–1.99 and 2.01 corresponded to trapped electrons (Ti^{3+} species) and trapped holes (O^-), respectively. While trapped hole peaks in the valence band of STO were clearly detected in both Rh/STO and bare STO under ultraviolet irradiation, trapped electron signals in the conduction band were absent in Rh/STO, suggesting that the excited electrons in STO's conduction band were injected into the rhodium particles.

These injected electrons in rhodium facilitated charge separation (Fig. 31f and g) and were trapped by CO_2 to produce CO. The remaining O^{2-} ions were integrated into the STO lattice, as verified by isotope trace analysis. Meanwhile, the photogenerated holes in STO's valence band migrated to the rhodium interface, where they reacted with CH_4. The O^{2-} ions from CO_2 and the holes near the STO-rhodium interface further react with methane to produce H_2. This process also eliminated residual carbon from methane cracking by reacting it with oxygen ions generated during CO_2 reduction, resulting in stoichiometric products and conferring highly stable anti-coking properties. The trapped holes in STO domains accelerated CH_4 oxidation, enhancing the DRM reaction. Remarkably, the Rh/STO composite nanoparticles retained their catalytic activity and morphology even after 10 hours of reaction under light illumination.[553]

Halas *et al.*[223] synthesized plasmonic Cu nanoparticles decorated with single-atom Ru (SA-Ru) and investigated their potential for the DRM reaction (Fig. 32). This design is an example of antenna–reactor geometry. The low Ru loading in these composite nanoparticles did not affect the surface plasmon resonance of the Cu nanoparticles. This design leveraged both the photothermal effect and hot-carrier chemistry of the SA-Ru/Cu system to enhance the DRM reaction.

Under white light illumination (19.2 W cm^{-2}) without external heating, the catalytic activity of the SA-Ru/Cu nanoparticles significantly increased with higher SA-Ru loading (Fig. 32b). This enhancement was attributed to the local electronic inhomogeneity at the reactor site, which could facilitate hot-carrier generation. The system achieved a turnover frequency of 34 mol H_2 mol Ru^{-1} s^{-1} and demonstrated

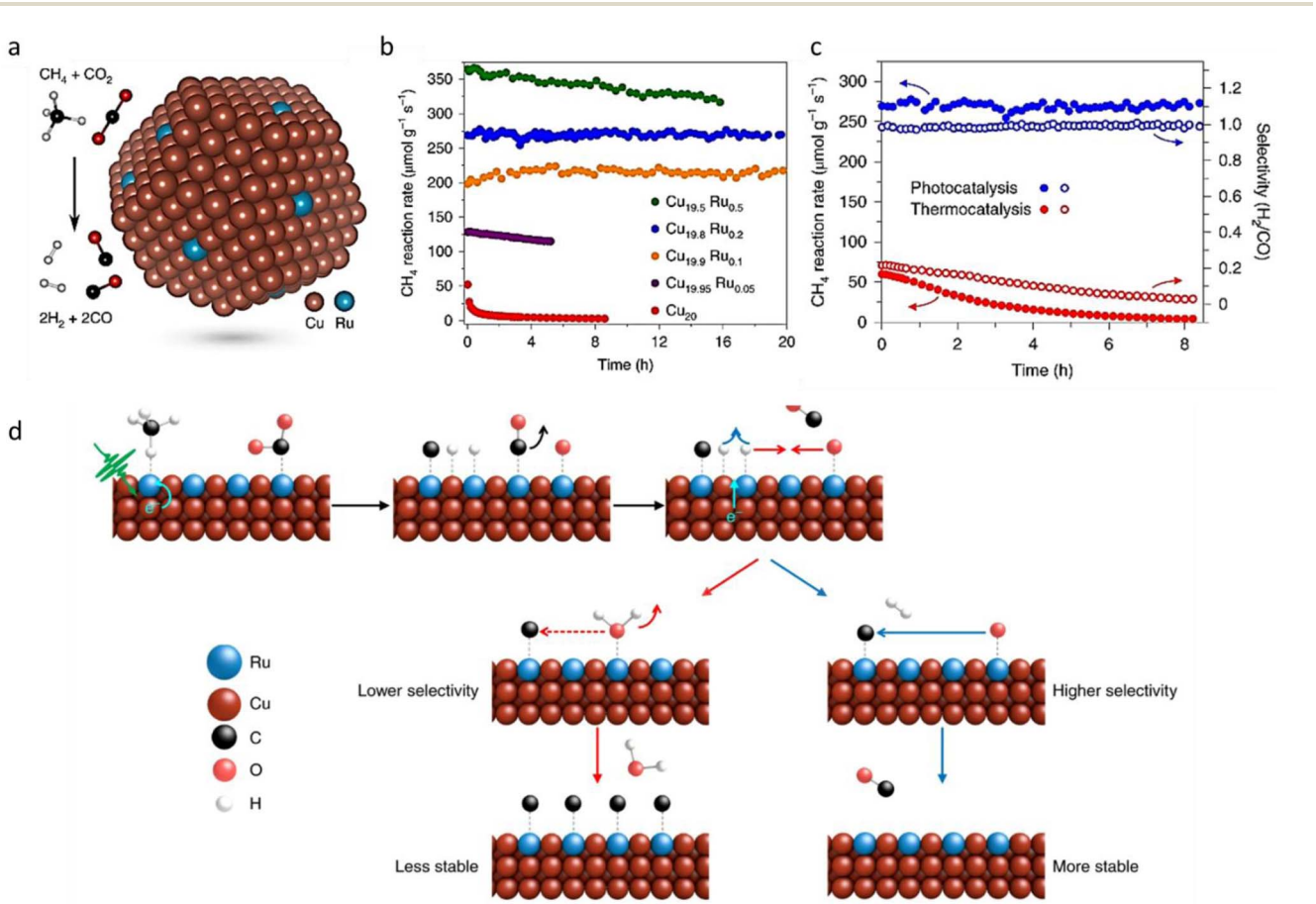

Fig. 32 Photocatalytic dry reforming of methane over Cu-single atom Ru antenna reactor system. (a) Schematic of a Cu-single-atom Ru surface alloy catalyst with the dry reforming reactants and products shown on the left, (b) reaction rate and long-term stability of photocatalytic DRM under 19.2 W cm^{-2} white light illumination as a function of Ru concentration of the photocatalyst nanoparticles, (c) long-term stability (filled circles), and selectivity (open circles) for photocatalysis, (d) schematics of enhanced selectivity and stability in photocatalysis *via* the DIET mechanism. Reproduced with permission from ref. 223. Copyright 2020 Springer Nature.

photocatalytic stability over 50 hours. The combination of the single-atom doped structure and hot-carrier generation was proposed to be critical for achieving high efficiency and coking resistance. Adding a minimal fraction of Ru ($Cu_{19.95}Ru_{0.05}$) nearly tripled the initial photocatalytic reaction rate compared to pure Cu nanoparticles, and significantly improved stability, maintaining 90% of the initial activity after 5 hours of continuous operation. Raman spectroscopy indicated reduced coke formation, and the $Cu_{19.95}Ru_{0.05}$ sample showed increased selectivity for the DRM process by promoting the DRM rate and suppressing the reverse water–gas shift (rWGS) reaction (Fig. 32a).

When comparing thermocatalytic and photocatalytic activities, it was found that the photocatalytic reaction rate under white-light illumination was more than four times higher than the thermocatalytic rate at the same surface temperature of 1000 K, suggesting that the primary mechanism for photocatalytic DRM was hot-carrier-mediated (Fig. 32c). Thermocatalytic activity rapidly declined due to coking, while photocatalysis remained stable. The incorporation of plasmon-enhanced H_2 desorption induced by electronic transitions (DIET),[554,555] likely contributed significantly to the improved selectivity and stability observed in photocatalysis compared to thermocatalysis. The suppression of the rWGS reaction through enhanced H_2 desorption prevented water formation, leading to a higher concentration of mobile O_{ads} species capable of effectively scavenging C_{ads} upon illumination (Fig. 32d). These combined effects highlighted the effectiveness of the SA-Ru/Cu system in facilitating efficient and stable photocatalytic DRM processes under light irradiation without external heating.[223]

In the previously discussed work, the light intensity needed to drive the reaction was quite high, around 19.2 W cm^{-2}, possibly leading to temperatures reaching approximately 1000 K.[223] This made it difficult to distinguish between non-thermal and photothermal effects. However, recent advancements have led to the development of a Ni–Co-loaded plasmonic catalyst for photocatalytic DRM that requires lower light power. Wang *et al.*[556] fabricated a series of ultra-small, non-noble NiCo bimetallic quantum dots on SiO_2 to study their thermal and photothermal catalytic performance in DRM (Fig. 33). This design is an example of antenna–reactor geometry. It was found that partially substituting Ni with Co in the NiCo alloy (Fig. 33a) reduced the thermocatalytic DRM performance. However, *in situ* irradiation DRIFTS, *in situ* irradiation EPR, and finite element method simulations showed that energetic hot carriers were excited in $NiCo/SiO_2$, which directly activated CO_2 and CH_4. This helped overcome the thermodynamic barrier and promoted the generation of *CHO for CO rather than *C, thereby avoiding coking.

The NiCo alloy QDs were ultra-small, with an average size of less than 3 nm (Fig. 33a). The binding energy of Co shifted downwards while that of Ni shifted upwards in $NiCo/SiO_2$, indicating electron donation from Ni to Co within the NiCo alloy QDs. For bimetallic NiCo catalysts, the light absorption capability was further enhanced, particularly for 1.2Ni-0.3Co/SiO_2, which exhibited maximum light absorption (Fig. 33c). The synergy in the bimetal alloy improved photon absorption, leading to increased generation of energetic hot carriers. While $1.5Ni/SiO_2$ demonstrated the highest thermocatalytic DRM performance among all the samples, Co in the bimetallic alloy suppressed the activation of CO_2 and CH_4, as confirmed by DRIFTS and DFT analyses. In these analyses, the carbonate peaks corresponding to CO_2 adsorption were lower in the bimetallic catalyst. Trends in reactant adsorption and CO desorption energies supported similar conclusions. Interestingly, 0.3Ni-1.2Co/SiO_2, which was inactive in thermocatalysis, was able to trigger the reaction upon light illumination (Fig. 33b and d), demonstrating a strong synergistic effect within the bimetal alloy under light irradiation despite its negative effect on thermocatalytic DRM.

The primary driving force for photothermal catalytic DRM over $1.5Ni/SiO_2$ remained thermal energy, which enhanced the reaction rate without altering the reaction pathway. However, for 1.2Ni-0.3Co/SiO_2, a distinct peak centered at 1238 cm^{-1} emerged under light irradiation, which was absent during thermocatalysis. This peak was attributed to the presence of the reactive intermediate CO_2^-. *In situ* EPR under light illumination also confirmed the presence of CO_2^- in the photothermal catalytic DRM process, as noticeable EPR peaks were observed when 1.2Ni-0.3Co/SiO_2 was illuminated in the presence of CO_2, but these peaks were absent in the dark (Fig. 33e). This provided strong evidence that energetic hot carriers were excited on 1.2Ni-0.3Co/SiO_2, directly activating CO_2 in the photothermal catalytic DRM process.

Additionally, heat on the surface of metal nanoparticles is generated by the decay of low-energy hot electrons. The highest temperature observed in the 1.2Ni-0.3Co/SiO_2 sample suggested the greatest number of excited hot carriers on the bimetallic QDs, leading to the maximum probability of energetic hot carriers. FEM simulations were conducted to study the electric field distribution of monometallic and bimetallic catalysts (Fig. 33f), providing a better understanding of the excitation of energetic hot carriers on the bimetallic catalyst. The results indicated that the intensity of the electric field, and therefore the density of high-energy electrons, was consistently higher in NiCo bimetallic catalysts compared to Ni and Co monometallic catalysts irradiated at different light wavelengths and resulted in higher photocatalytic performance (Fig. 33g). The work was crucial in understanding how reaction pathways can change for photocatalytic and thermocatalytic systems.[556]

This section reviewed photocatalytic DRM over semiconductor and plasmonic catalysts, emphasizing their complementary advantages and practical considerations. Semiconductor systems provide effective charge separation and structural stability, often operating efficiently under moderate illumination, whereas plasmonic systems can harness hot-carrier and photothermal effects, typically requiring higher light intensities to achieve comparable activity. These observations suggest that, while both catalyst classes can drive DRM effectively, rational design of light absorption, carrier dynamics, and cocatalyst integration remains key to optimizing efficiency and selectivity.

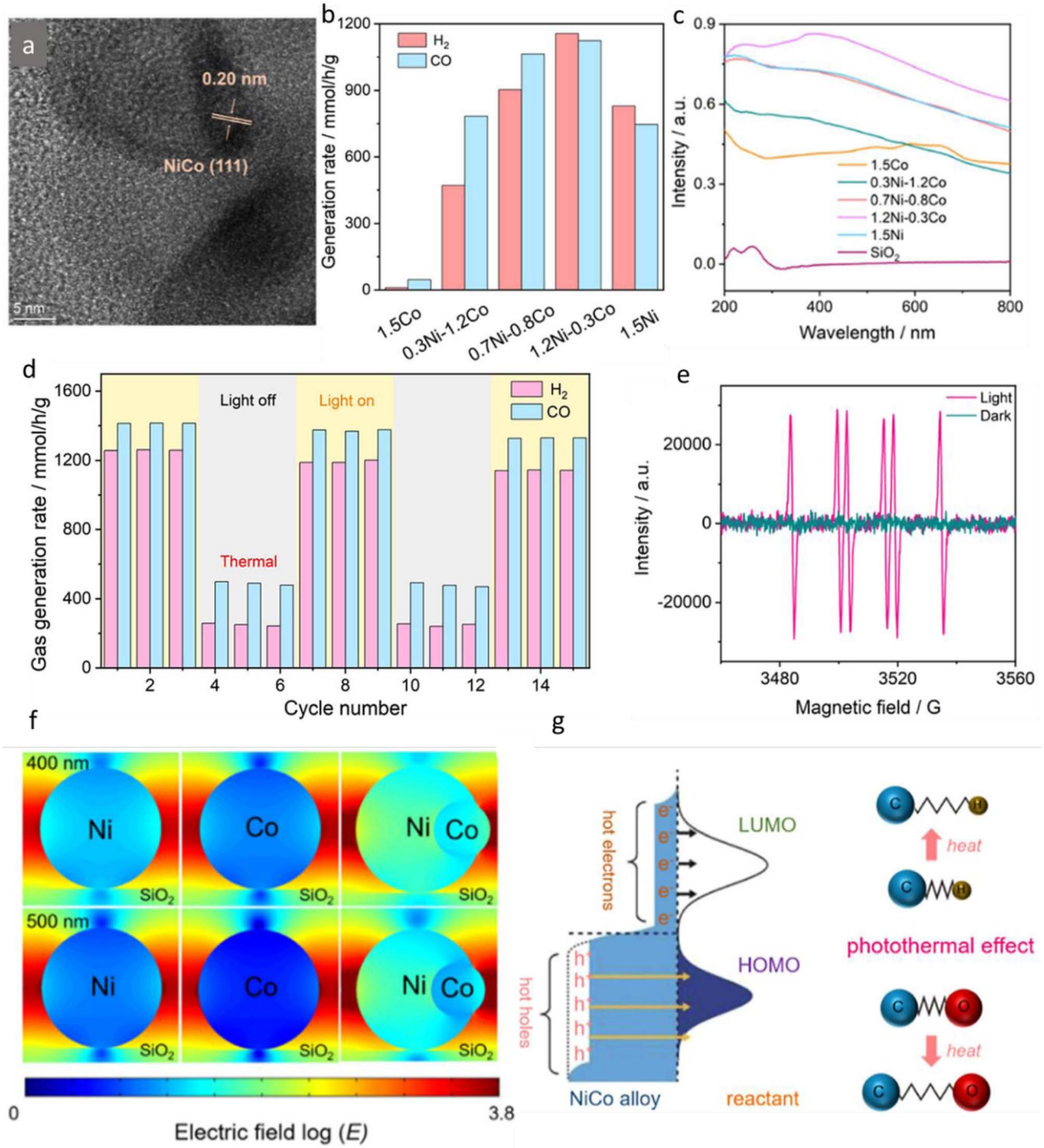

Fig. 33 Photocatalytic dry reforming of methane over NiCo antenna–reactor system. (a) HRTEM image of 1.2Ni-0.3Co/SiO_2, (b) photo contribution to photothermal catalytic DRM performance at the external heating temperature of 700 °C, (c) UV-Vis spectra of the prepared samples, (d) DRM performance with light on and off (700 °C) each cycle corresponds to a 20 min duration for GC monitoring of the effluent products, (e) *in situ* EPR of 1.2Ni-0.3Co/SiO_2 in the presence of CO_2 under light illumination and in the dark using 5,5-dimethyl-1-pyrroline-N-oxide (DMPO) as the trapping agent, (f) FEM profiles of enhanced electric fields over monometallic and bimetallic catalysts, (g) photothermal effect on the NiCo bimetal alloy catalyst. Reproduced with permission from ref. 556. Copyright 2023 American Chemical Society.

4.4. N_2 reduction to NH_3

Directly converting CO_2 into value-added chemicals is one way to deal with the global climate crisis. The other way is to find greener alternatives to industrial processes driven thermally, accompanied by large CO_2 emissions. Ammonia (NH_3) production was revolutionized in the early 20th century by the development of the Haber–Bosch process, which continues to be the primary industrial method for ammonia synthesis to this

day. This process produces around 200 million tons of NH_3 annually and consumes 1–3% of the world's electricity and 3–5% of its natural gas due to its reliance on methane-derived H_2 and the significant energy required to operate at 400–500 °C and 150–250 atm pressure.[557] Despite being an exothermic reaction ($\Delta H = -92$ kJ mol^{-1}), high temperatures are necessary to attain an economically feasible N_2 conversion rate of approximately 15% per reactor pass. This high-temperature requirement stems from the extraordinary strength of the N≡N triple bond (941 kJ mol^{-1}).[558]

The use of water as a hydrogen source could significantly reduce the carbon footprint of NH_3 synthesis, but it would require temperatures exceeding 1000 °C in thermal catalysis, making it impractical. Solar energy, abundant in many parts of the world, especially in equatorial regions, offers a promising alternative.[559–596] Utilizing solar energy through semiconductor photocatalysis could enable NH_3 synthesis under near-ambient conditions. However, most photocatalysts for N_2 fixation, similar to those used for photocatalytic CO_2 reduction and water splitting, exhibit low activities and poor selectivity. These low rates are due to the slow N_2 activation kinetics and the

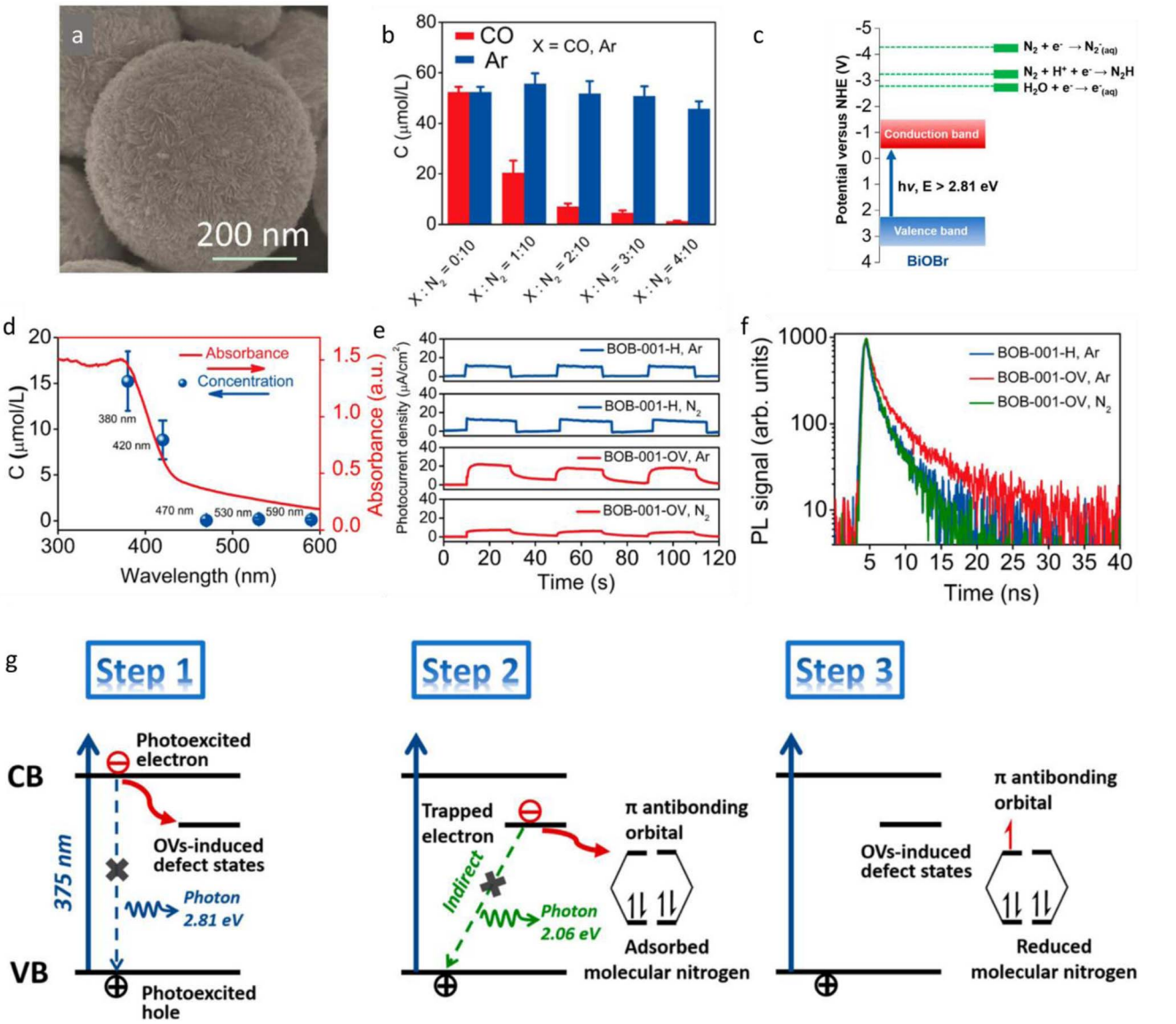

Fig. 34 Photocatalytic N_2 fixation over defective semiconductor system BiOBr-OV. (a) SEM image of the as-prepared BiOBr, (b) effect of CO on the photocatalytic fixation of N_2 over BOB-001-OV, (c) electronic energy-level diagram of BOB-001-OV, (d) N_2 fixation by BOB-001-OV under monochromatic light along with its light absorption spectra, (e) transient photocurrent responses of different BiOBr photocatalysts, (f) room-temperature PL spectra decay curves of the as-prepared BiOBr photocatalysts, (g) schematic illustration for enhanced interfacial electron transfer processes induced by OVs. OVs-induced defect states first dynamically trap the directly excited electrons from the CB of BiOBr, thus suppressing the direct recombination of charge carriers (Steps 1 and 2). Subsequently, the indirect recombination of trapped electrons with photoexcited holes is also suppressed as the trapped electrons could efficiently be transferred to populate the empty antibonding orbitals of adsorbed N_2 (Step 3). Reproduced with permission from ref. 601. Copyright 2015 American Chemical Society.

limited availability of charge carriers needed to drive the reduction of adsorbed N_2 and water oxidation. As a result, the quantum yields for photocatalytic N_2 fixation are low, with solar-to-chemical conversion efficiencies around 0.1%.

Photocatalytic N_2 fixation faces greater challenges compared to H_2 evolution and CO_2 reduction, mainly due to the high-energy intermediates required for N_2 reduction, such as N_2^- or N_2H. For example, the reduction potential for N_2^- formation is as negative as −4.2 V *vs.* NHE, making it inaccessible for traditional semiconductors (TiO_2, ZnO, Fe_2O_3, and CdS) without the assistance of organic scavengers or precious metal cocatalysts.[597–600] Defect engineering has emerged as an effective strategy to enhance the photocatalytic activity of semiconductors by creating defects that serve as trapping centers for electrons and holes and act as active sites for the reaction.

In this context, Zhang *et al.*[601] synthesized {001} facet-exposed BiOBr nanosheets with oxygen vacancies (OVs) using a simple solvothermal method (Fig. 34). A reference photocatalyst without OVs (BOB-001-H) was obtained by annealing BOB-001-OV in an oxygen-saturated atmosphere at 300 °C. BOB-001-H showed no significant NH_3 production with or without N_2 after 60 minutes, whereas BOB-001-OV produced a significant amount of NH_3 (104.2 μmol h^{-1} g_{cat}^{-1}), and its wavelength-dependent activity closely matched the absorption profile (Fig. 34d). The addition of the electron scavenger $AgNO_3$ significantly suppressed the N_2 fixation activity of BOB-001-OV, indicating that the primary active species were the photoexcited electrons.

Despite the CB potential of BiOBr being incapable of N_2 reduction or solvated electrons formation (Fig. 34c), theoretical calculations revealed that the OVs on the BiOBr surface could

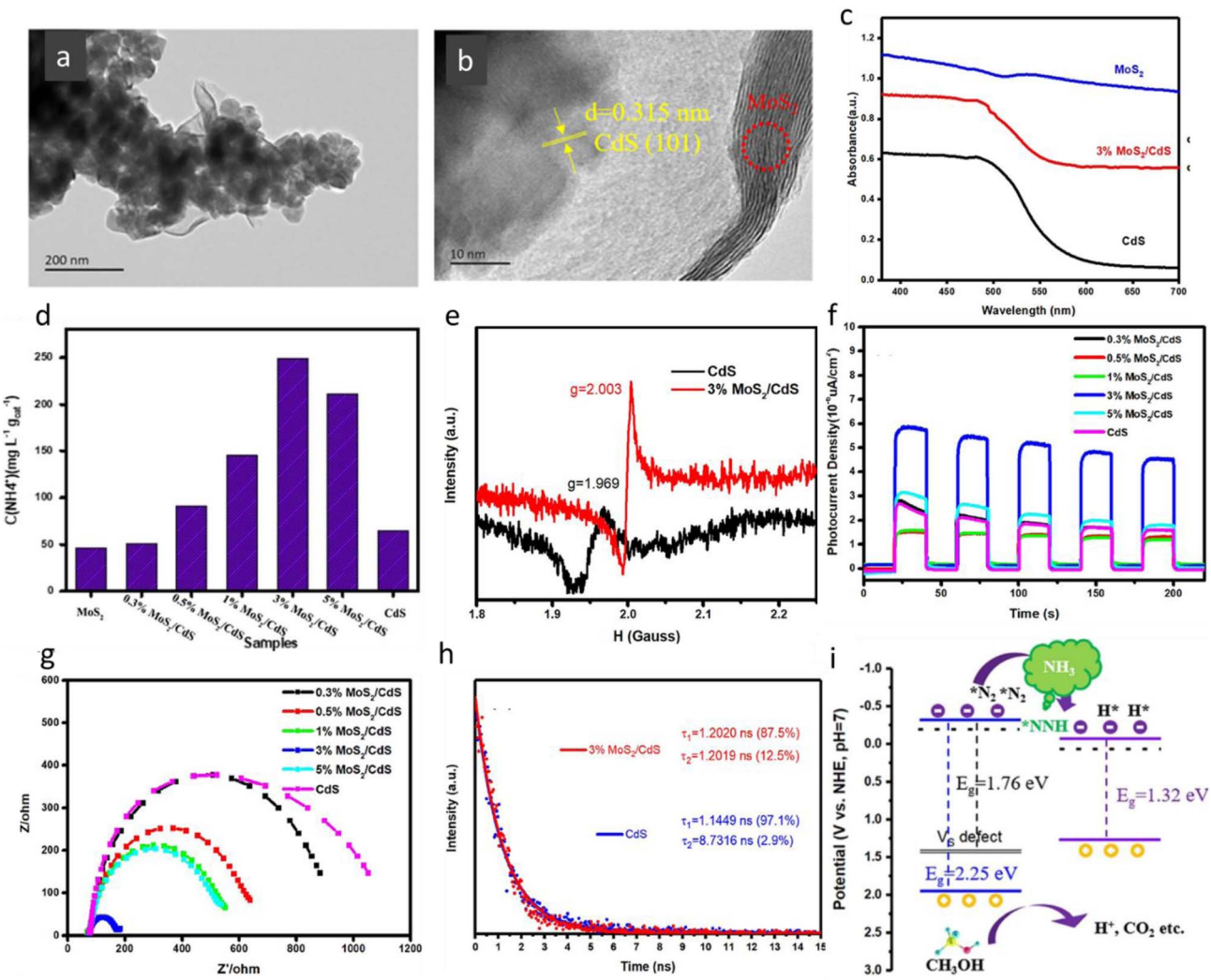

Fig. 35 Photocatalytic N_2 reduction over MoS_2/CdS semiconductor heterojunction system. (a) TEM and (b) HRTEM images of 3% MoS_2/CdS composites, (c) UV-Vis DRS spectra of the as-prepared MoS_2, CdS, and MoS_2/CdS composites, (d) Photocatalytic NH_4^+ production rates for MoS_2, CdS, and MoS_2/CdS composites containing different amounts of cocatalysts (0.3, 0.5, 1, 3, and 5%) under visible light irradiation, time course of NH_4^+ production, (e) EPR spectra of CdS and MoS_2/CdS heterojunctions, (f) transient photocurrent response, (g) Nyquist plots of EIS, (h) TR PL spectra of CdS and MoS_2/CdS heterojunctions, (i) schematic illustration of band structures and the proposed photocatalytic mechanism of N_2 reduction at MoS_2 and CdS heterojunctions. Reproduced with permission from ref. 602. Copyright 2022 American Chemical Society.

adsorb and activate N_2, modifying its electronic properties and hence reduction potential. The N_2 reduction efficiency of BOB-001-OV was highly dependent on the presence of OVs. N_2 temperature-programmed desorption (N_2-TPD) experiments showed a single desorption peak for BOB-001-OV, related to chemisorbed N_2, while no N_2 adsorption was observed for BOB-001-H. The NH_3 yield of different BOB-001-OV samples was linearly related to the N_2-TPD peak area, suggesting that both N_2 adsorption and reduction were dependent on the number of OVs.

Further experiments confirmed the role of OVs in promoting interfacial charge transfer (Fig. 34g). When the interfacial charge transfer was blocked by coating BOB-001-OV with an insulating SiO_2 layer, NH_3 production was significantly suppressed. Additionally, the introduction of CO in the gas mixture gradually inhibited NH_3 generation, indicating that CO, with its stronger adsorption on OVs, competes with N_2 (Fig. 34b). PL revealed that the OVs in BOB-001-OV acted as initial electron acceptors, increasing the lifetime of charge carriers and promoting interfacial electron transfer to adsorbed N_2 (Fig. 34f). Transient photocurrent measurements further supported this, showing a significant interaction between surface OVs and N_2, confirming the role of OVs in enhancing photocatalytic N_2 fixation (Fig. 34e).[601]

Heterojunction fabrication can also achieve effective charge transport and vacancy stabilization, as demonstrated by Chen *et al.*[602] in their study on MoS_2/CdS heterojunctions (Fig. 35a and b) with abundant sulfur vacancies for photocatalytic N_2 reduction (Fig. 35). The presence of sulfur vacancies in these heterojunctions was confirmed using UV-vis diffuse-reflectance spectroscopy (Fig. 35c) and EPR (Fig. 35e). Under visible light irradiation for 4 hours, the 3% MoS_2/CdS heterojunctions achieved a significantly higher NH_3 production (249.7 mg L^{-1} g^{-1}), outperforming pure MoS_2 (45.9 mg L^{-1} g^{-1}) and pristine CdS (64.5 mg L^{-1} g^{-1}) by 5.4 and 3.9 times, respectively (Fig. 35d). XPS analysis revealed that MoS_2 and CdS are well-connected, with electron transfer occurring from CdS to MoS_2, as indicated by the slightly higher binding energies of Cd^{2+} in the 3% MoS_2/CdS sample compared to CdS alone. The MoS_2/CdS samples also showed increased light absorption capacity with higher MoS_2 content (Fig. 35c). The band gaps of MoS_2 and CdS were calculated to be approximately 1.32 eV and 2.25 eV, respectively, with a defect-induced band gap close to 1.74 eV for 3% MoS_2/CdS, attributed to sulfur vacancies originating from CdS.

EPR data further confirmed the formation of additional sulfur vacancies in the MoS_2/CdS heterojunctions, with a shift in the EPR signature from $g = 1.969$ to 2.003, indicating a change in the coordination environment of Cd (Fig. 35e). The intensity of the EPR signal in the 3% MoS_2/CdS sample was higher than that of CdS, demonstrating an increase in sulfur vacancies. The transient photocurrent measurements revealed that the 3% MoS_2/CdS heterojunctions exhibited the highest photocurrent density, indicating the most efficient separation of photoexcited carriers (Fig. 35f). The EIS results showed that adding MoS_2 to CdS reduced the semicircle diameter in the EIS spectrum, indicating improved conductivity and electron transfer (Fig. 35g). The PL spectra also demonstrated efficient charge separation in the MoS_2/CdS heterojunctions, with a decrease in PL intensity and a longer decay time for the 3% MoS_2/CdS sample compared to CdS alone (Fig. 35h). The average PL lifetime of the 3% MoS_2/CdS heterojunction was shorter (1.2020 ns) than that of CdS (2.5465 ns), suggesting improved conductivity and faster electron migration after combining with MoS_2. The Mott–Schottky analysis revealed that the ECB of MoS_2, CdS, and 3% MoS_2/CdS were −0.06, −0.31, and −0.28 V *versus* NHE, respectively. The sulfur vacancies in the 3% MoS_2/CdS heterojunctions served as active sites for the chemical adsorption of N_2 molecules, facilitating electron transfer into the reverse-bond π orbitals of adsorbed N_2, thereby weakening the N–N triple bond (Fig. 35i). These findings underscore the importance of sulfur vacancies and enhanced charge transfer efficiency at MoS_2/CdS heterojunctions in improving N_2 fixation efficiency.[602]

The band gap of traditional semiconductors often does not align well with the N_2 reduction potentials, which has spurred interest in plasmon-mediated N_2 reduction and enhancing hot electron injection into N_2 antibonding orbitals. Xiong *et al.*[281] demonstrated that surface plasmons can provide sufficient energy to activate N_2 through a dissociative mechanism when water and incident light are present (Fig. 36). Theoretical simulations suggested that the electric field enhanced by surface plasmons, along with plasmonic hot electrons and interfacial hybridization, played a crucial role in N_2 dissociation. Specifically, AuRu core-antenna nanostructures, which had a broad light absorption cross-section and active sites, achieved an ammonia production rate of 101.4 μmol g^{-1} h^{-1} at room temperature and 2 atm pressure without any sacrificial agents. This design is an example of antenna–reactor geometry.

The N≡N bond cleavage occurs *via* indirect hot-electron injection into molecular orbitals or direct excitation of N_2 into vibrational/electronic states. In both cases, N_2 must be chemisorbed near the plasmonic metal to retain hot-electron energy and form an active metal-adsorbate complex. The AuRu core-antenna nanostructures showed a higher concentration of Ru at the antenna regions, confirming the formation of AuRu alloy antennas deposited on the Au core (Fig. 36a). These AuRu nanostructures significantly outperformed bare Au nanoparticles in catalytic ammonia production (Fig. 36b). With Ru incorporated up to 31%, the ammonia production rate increased to 101.4 μmol g^{-1} h^{-1}, about 7.3 times higher than that of bare Au nanocrystals. However, with 39% Ru content, light harvesting decreased significantly, reducing N_2 fixation activity (Fig. 36b). The N_2 fixation catalyzed by $AuRu_{0.31}$ nanostructures exhibited a nearly linear power law dependence on light intensity, indicative of a single charge-carrier reaction (Fig. 36c). The wavelength-dependent AQEs of $AuRu_{0.31}$, measured under various monochromatic light irradiations, aligned well with the full extinction spectra range of AuRu nanostructures, indicating high light utilization efficiency (Fig. 36d).

Without water, DRIFTS showed no change, confirming hydrogen in ammonia came from water. Upon water addition, ammonia bands appeared, and the absence of N–N vibrations

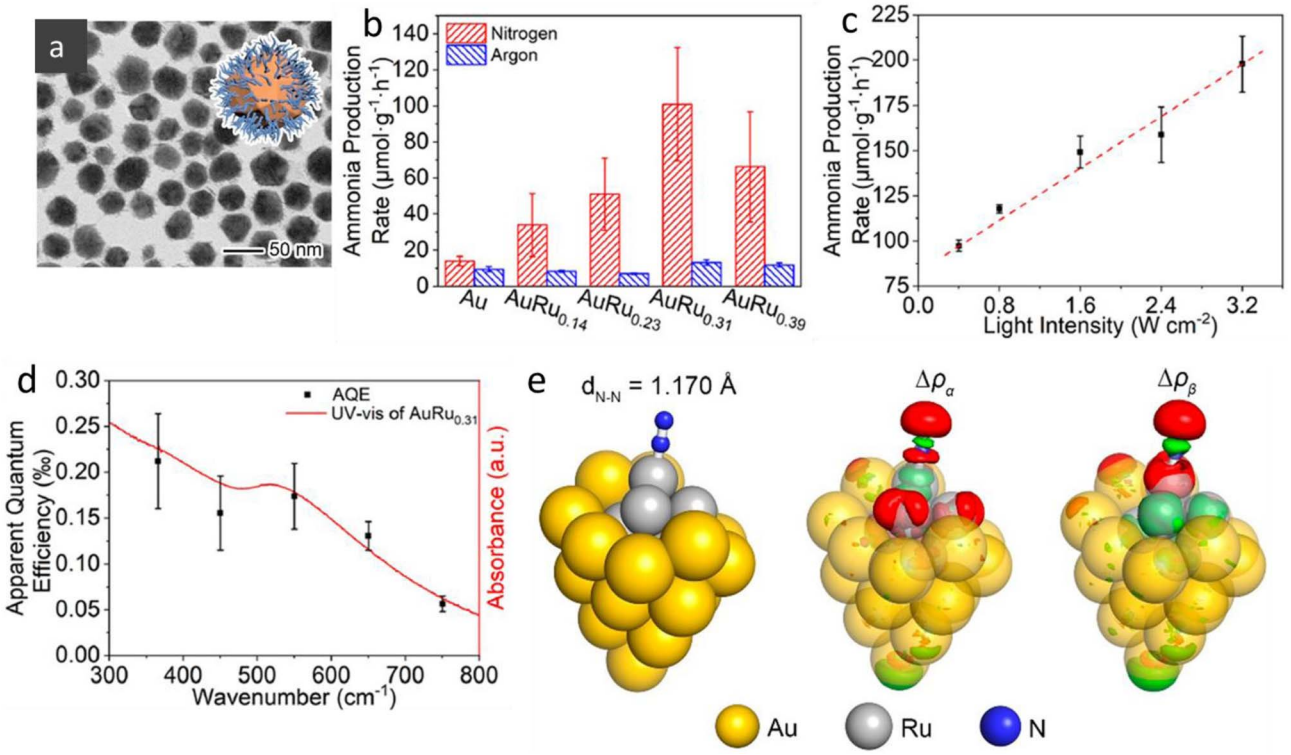

Fig. 36 Photocatalytic N_2 reduction over plasmonic Au–Ru antenna–reactor system. (a) TEM image of $AuRu_{0.31}$ core-antenna nanostructures, (b) catalytic ammonia production rates by bare Au, $AuRu_{0.14}$, $AuRu_{0.23}$, $AuRu_{0.31}$, and $AuRu_{0.39}$ in the first 2 h, (c) photocatalytic ammonia production rates by $AuRu_{0.31}$ in the first 2 h under different light intensity, (d) calculated AQEs for N_2 fixation over $AuRu_{0.31}$, with its UV-Vis extinction spectrum (red line) as a reference, (e) optimized structures of N_2 adsorbed on $Ag_{22}Ru_6$ cluster, both charged by 1e and experienced with an electric field of 1.0×10^8 V m^{-1}. The electron density difference for α (spin-up) and β (spin-down) is normalized, and the absolute isovalue is set to 0.02. The red and green colors represent an increase and decrease in electron density, respectively. Reproduced with permission from ref. 281. Copyright 2019 American Chemical Society.

excluded an associative pathway. XPS revealed atomic N chemisorption (395.3 eV) and hydrogenated species (=NH, –NH_2) at 397.2–398.0 eV. Simulations showed end-on N_2 adsorption on $Au_{22}Ru_6$ (1.128 Å) elongating to 1.170 Å under electric field and charge effects, indicating that local fields drive N_2 activation through electron transfer into antibonding orbitals (Fig. 36e).[281]

When a plasmonic metal nanocrystal interacts with an n-type semiconductor, a Schottky barrier forms at the nanocrystal–semiconductor interface. This barrier acts as a filter, allowing hot electrons to pass through the interface while blocking their reverse movement, thus facilitating efficient electron–hole separation. These composite systems benefit from high light-harvesting efficiency, stable activity, low electron–hole pair recombination rates, and tunable responses across the visible to near-infrared (NIR) spectrum.

In a study by Ye *et al.*[603] Au nanocrystals anchored on ordered ultrathin TiO_2 nanocavity arrays (NCAs) with abundant oxygen vacancies (denoted Au@TiO_2 NCA) demonstrated that LSPR from the Au nanocrystals under NIR irradiation effectively drove the fixation of N_2 to NH_3 under mild conditions (Fig. 37). This system also represents a multifunctional plasmonic–semiconductor heterostructure, where the synergy between a defect-engineered oxide support and a noble-metal cocatalyst is utilized. The Au nanoparticles were uniformly arranged on the TiO_2 nano cavity array (NCA) using a solid-state dewetting process (Fig. 37a and b). This setup optimized the total surface energy of the metallic Au thin film and TiO_2 substrate. TiO_2 NCAs served both as a support for the plasmonic Au nanoparticles and as active sites for N_2 adsorption and reduction.

The process worked as follows: (1) hot electrons excited from the plasmonic Au nanocrystals overcame the Schottky barrier and were injected into the TiO_2 NCA conduction band; (2) these hot electrons then diffused to the OV defect states of the TiO_2 and were trapped; (3) the trapped hot electrons on the TiO_2 NCA surface reduced the adsorbed N_2, leading to ammonia production (Fig. 37g). The FDTD simulations showed that the LSPR-induced electric field intensity at the Au/TiO_2 interface was amplified by a factor of 5 near the Au nanoparticle (Fig. 37d). XPS analysis confirmed the presence of OVs on the TiO_2 NCA surface, which acted as N_2 adsorption sites and introduced additional energy bands in the band gap. This facilitated electron transfer across the rutile TiO_2-Au nanoparticle interface, enhancing N_2 reduction to NH_3. TiO_2 nano tube array (NTA) and TiO_2 NCA both exhibited strong absorption below 400 nm due to their large 3.0 eV band gap and weak interband transitions in the NIR region (Fig. 37c). In contrast, Au@TiO_2 NCA showed an absorption peak at 1010 nm due to the LSPR effect of the Au

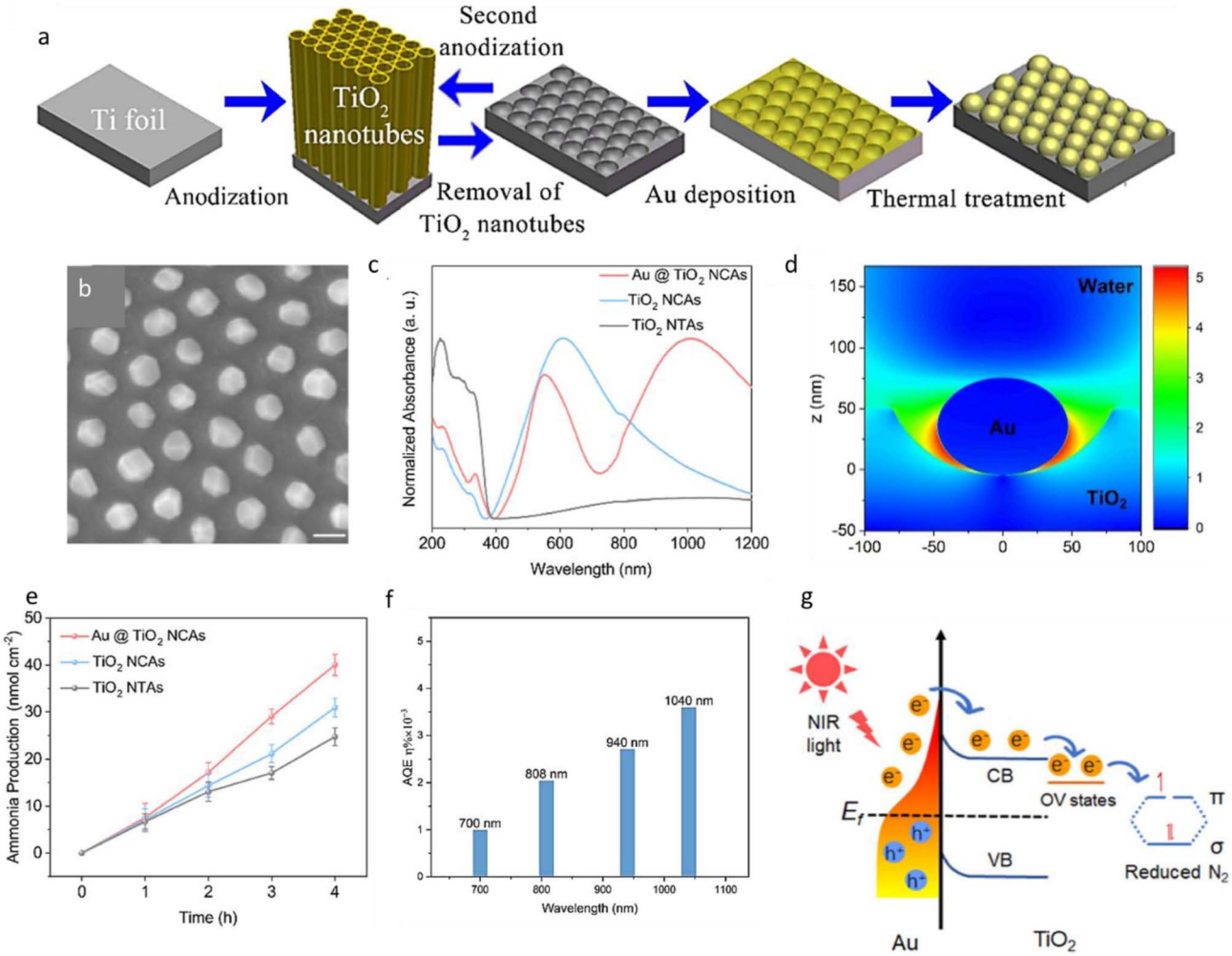

Fig. 37 Photocatalytic N_2 reduction over plasmonic–semiconductor hybrid Au–TiO_2 system. (a) Schematic outline of the fabrication processes for ordered and uniform Au@TiO_2 NCA, (b) SEM image of the assembled Au nanoparticle arrays after thermal treatment. Scale bar: 100 nm, (c) UV-Vis-NIR absorption of TiO_2 NTAs, TiO_2 NCAs, and Au@TiO_2 NCAs, (d) FDTD simulation of electric field enhancement over Au@TiO_2 NCAs, (e) time-dependent photocatalytic ammonia production under NIR light illumination and N_2 flow, (f) AQE of NH_3 production on Au@TiO_2 NCA as a function of wavelength, (g) illustration of the synergistic effect of the surface OVs and plasmonic Au NPs for photocatalytic N_2 fixation on Au@TiO_2 NCAs. Reproduced with permission from ref. 603. Copyright 2023 American Chemical Society.

nanoparticles. Additional absorption peaks at 605 and 550 nm were attributed to light interference through the thin TiO_2 nanomembrane.

The NH_3 production rate of 6.2 nmol cm^{-2} h^{-1} for TiO_2 NTA and 7.7 nmol cm^{-2} h^{-1} for TiO_2 NCA was observed (Fig. 37e). The improved performance of TiO_2 NCA, which has an ultrathin membrane, suggested that surface OVs enhance N_2 activation and interfacial electron transfer from the TiO_2 surface to adsorbed N_2 molecules. The addition of Au nanoparticles further increased the catalytic activity, with Au@TiO_2 NCA achieving an NH_3 production rate of 10.1 nmol cm^{-2} h^{-1}. This was confirmed by ion chromatography.

The synergistic interaction of surface OVs and Au nanoparticles in Au@TiO_2 NCA enhanced NH_3 production. Hot electrons generated by the Au LSPR were injected into TiO_2 and trapped at OV-induced defect states, activating adsorbed N_2 for reduction (Fig. 37g). Concurrently, water oxidation on Au consumed hot holes. Au@TiO_2 NCA showed slightly higher activity under $\lambda > 400$ nm than under NIR light, as the NIR LSPR band overlaps the visible region, generating more hot electrons for transfer to TiO_2 OVs. The best N_2 fixation occurred under full-spectrum irradiation due to combined UV-excited TiO_2 electrons and Au LSPR-induced hot carriers. The excited N_2 π^* orbitals were stabilized by OV bands in TiO_2, facilitating NH_3 formation. The alignment between AQEs and the absorption spectrum confirmed that N_2 photofixation was mainly driven by Au LSPR absorption (Fig. 37f).[603]

While heterostructures like plasmonic metal–semiconductors can improve hot charge carrier separation, many of these carriers are lost when crossing the Schottky barrier. Wang *et al.*[604] introduced a Schottky barrier-free plasmonic semiconductor photocatalyst, MoO_{3-x}, which excels in N_2 photofixation (Fig. 38). This material not only served as an active site for N_2 chemisorption but also utilized LSPR to generate hot

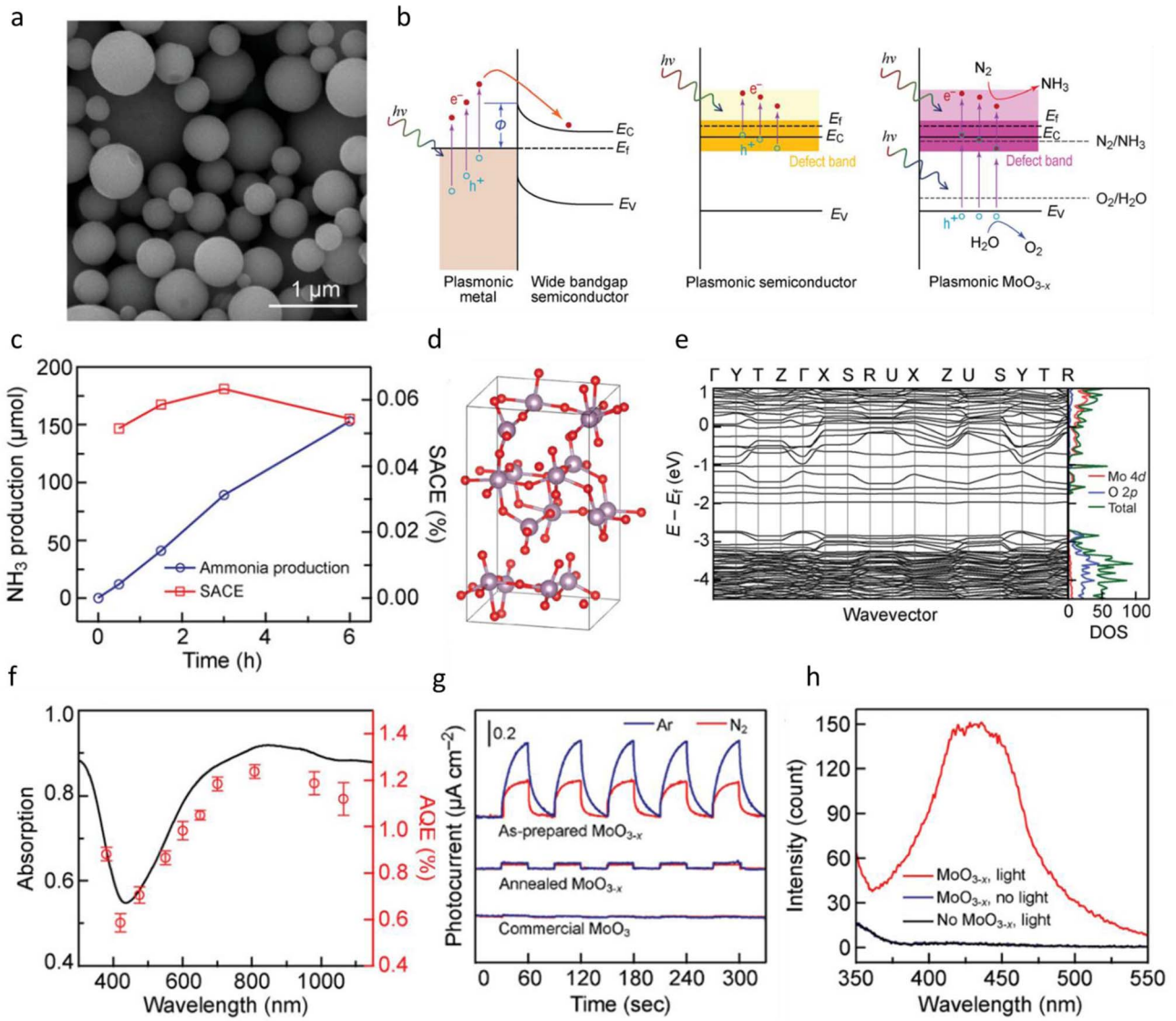

Fig. 38 Photocatalytic N_2 reduction over Schottky barrier-free plasmonic semiconductor MoO_{3-x} system. (a) SEM image of the MoO_{3-x} spheres prepared at 350 °C, (b) schematics illustrating the band structures of a conventional plasmonic metal–semiconductor hybrid photocatalyst (left), a plasmonic semiconductor photocatalyst (middle), and the plasmonic MoO_{3-x} photocatalyst in this work (right), (c) time-dependent NH_3 production amounts (left axis) and SACEs (solar to ammonia conversion efficiency) for ammonia production (right axis), (d) crystal structure of a MoO_{3-x} model used in the DFT calculation. The red spheres represent the O atoms after relaxation. (e) DFT-calculated band structure and densities of states for the model shown in (d), (f) action spectrum of the MoO_{3-x} spheres for N_2 photofixation. The light absorption spectrum is plotted against the left axis, while the AQEs are plotted against the right axis, (g) photocurrent responses of the different materials recorded in Ar and N_2 atmosphere, respectively. The visible light illumination was switched on and off repeatedly, (h) $^{\bullet}OH$ detected through the fluorescence emission after the reaction for 60 min under the different reaction conditions. Reproduced with permission from ref. 604. Copyright 2022 Wiley-VCH GmbH.

charge carriers. Plasmonic MoO_{3-x} showed impressive photoreactivity for NH_3 production, with an apparent quantum efficiency exceeding 1% up to a wavelength of 1064 nm, and a 0.057% efficiency in solar-to-ammonia conversion without any hole scavenger (Fig. 38c).

Recent studies have revealed LSPR in various semiconductors with adequate charge carrier densities.[604–608] To better understand the electronic structure and N_2 adsorption behavior of MoO_{3-x}, a comprehensive density functional theory study was conducted. Intrinsic MoO_3 displayed a wide band gap of over 2.29 eV, but the presence of oxygen vacancies introduced defect states close to the conduction band. This allowed for the free movement of electrons from these defect states to the conduction band, contrasting with the transfer of hot electrons from the metal to the semiconductor in traditional metal–semiconductor hybrid plasmonic photocatalysts. The calculations showed that the Fermi level is well above the defect band, indicating metallic characteristics with free charge carriers in MoO_{3-x} (Fig. 38d and e). Scattering spectra of MoO_{3-x} spheres (300–600 nm) showed consistent peak positions (Fig. 38a). Their

dielectric response, modeled *via* the Drude–Lorentz approach using carrier densities from Mott–Schottky analysis, matched experimental data. The negative real dielectric values in the visible-NIR range confirmed that the observed scattering peaks originated from LSPR rather than dielectric resonance.

Hot electrons were traced as superoxide anions ($^{\bullet}O_2^-$), formed when O_2 gas was introduced into the reaction solution instead of N_2. The photogenerated electrons reacted with O_2 to form $^{\bullet}O_2^-$, while photogenerated holes were consumed by DMSO. The presence of $^{\bullet}O_2^-$ was confirmed using 4-chloro-7-nitrobenzofurazan (NBD-Cl) acetonitrile solution, which showed an absorption peak at 470 nm. To confirm hot electrons' role in the N_2 reduction reaction, $AgNO_3$ was added as an electron scavenger. The N_2 photofixation reaction was completely inhibited by $AgNO_3$, and Ag nanoparticles were observed on the recovered photocatalyst, indicating that the suppression was due to hot electrons being consumed by Ag^+ ions. Fluorescence measurements of hydroxyl radicals ($^{\bullet}OH$) were used to detect hot holes. In the standard N_2 photofixation system, hot holes, generated by reacting with OH^-, were detected by adding terephthalic acid (TA), which fluoresces at 425 nm when reacting with $^{\bullet}OH$. Hot holes were only detected when both MoO_{3-x} spheres and the light source were present, consistent with the hot electron detection results (Fig. 38h). The Schottky-barrier-free nature of MoO_{3-x} is expected to minimize hot charge carrier loss. Electrochemical investigations confirmed the generation and consumption of hot charge carriers. MoO_{3-x} spheres displayed clear photocurrent signals in both Ar and N_2 atmospheres, confirming hot electron generation from OV-induced LSPR (Fig. 38e). In contrast, commercial MoO_3 and annealed MoO_{3-x} showed negligible photocurrent signals. The photocurrent signal's shark fin-like shape was attributed to photogenerated electron trapping at OVs, causing a delay in the signal's generation and reduction. Notably, changing from an Ar to an N_2 atmosphere halved the photocurrent, likely due to electron consumption in the N_2 reduction reaction.

Chemisorption of N_2 was essential for photofixation. Commercial MoO_3 showed a single desorption peak near 100 °C, indicating physisorption, whereas MoO_{3-x} exhibited an additional peak around 400 °C due to N_2 chemisorption at OV sites. Light absorption of MoO_{3-x} spheres decreased with longer calcination, correlating with reduced N_2 fixation, confirming the key role of OVs in catalysis. MoO_{3-x} spheres achieved superior N_2 photofixation owing to their Schottky-barrier-free structure, enabling efficient charge transport. Chemisorbed N_2 at OV sites was activated under illumination, where carrier oscillations induced LSPR. LSPR decay generated hot electrons and defect-state holes; the holes oxidized H_2O to O_2, while the electrons reduced N_2 to NH_3 (Fig. 38b).[604]

Building upon the established advantages of single-phase Schottky-barrier-free (SBF) systems, recent research has pivoted toward enhancing the efficiency further by improving the light absorption and charge carrier utilization. One such study was reported by Wang *et al.*[605] in which the authors engineered a MoO_{3-x}/Ag heterostructure (Fig. 39a), designed to achieve broadband solar harvesting through the synergistic coupling of vacancy-induced and metallic LSPR modes (Fig. 39b). This catalyst is an example of Schottky barrier-free plasmonic semiconductor and plasmonic metal heterostructure photocatalyst. Critically, this architecture maintained an SBF nature by ensuring ohmic interfacial contact rather than a traditional rectifying junction. KPFM and work function analyses demonstrated that the Ag work function facilitated a downward bending of the MoO_{3-x} conduction band, rendering the interface electronically "transparent" to hot carrier migration (Fig. 39c). This band alignment enabled the unhindered injection of plasmonic hot electrons from the Ag nanoparticles into the MoO_{3-x} host, as evidenced by a 15 meV Fermi level shift under illumination, nearly double the shift observed in the pristine oxide.

The catalytic activity of this SBF architecture was most evident in its wavelength-dependent nitrogen photofixation (PCNF) performance. By optimising the Ag loading to 10 mol%, the researchers successfully balanced plasmonic hot-carrier generation with reduced light scattering, achieving a record-high solar-to-chemical conversion efficiency (SCCE) of 0.41%. A critical mechanistic "fingerprint" was observed in the correlation between the light absorption and the AQE spectra (Fig. 39d and e), specifically, the AQE enhancement peaks at approximately 466 nm, precisely matching the LSPR of the incorporated Ag nanoparticles. This alignment provided direct evidence that the ohmic contact facilitated the efficient utilization of Ag-generated hot electrons for N_2 reduction. The best PCNF performance with an NH_3 yield of 0.78 ($\pm$0.08) mmol g_{cat}^{-1} h^{-1} and a SCCE of 0.14% ($\pm$0.01%) was achieved (Fig. 39f). Furthermore, the SBF nature and associated low activation energy allowed the system to leverage plasmonic photothermal effects. This synergy between broadband absorption, barrier-free transport, and photothermal assistance demonstrated how precise interfacial engineering can overcome the kinetic bottlenecks of traditional slurry-based photocatalysis.

To enhance light utilization and mass transfer, the MoO_{3-x}/Ag nanospheres were immobilized within a porous poly(vinyl alcohol) (PVA) substrate *via* freeze-drying. As shown in the backscattered SEM imaging (Fig. 39g), this interlaced network provided a high surface area for catalyst distribution while maintaining a thin, hydrophilic water layer that minimised NIR light attenuation and facilitated rapid N_2 diffusion to the active sites. By utilizing a bilayer configuration, elevating the catalyst-loaded PVA film above the water surface using a foam support (Fig. 39h), the authors minimised NIR light attenuation by water and bypassed the mass-transfer limitations typical of slurry reactors. This architecture allowed N_2 molecules to penetrate an ultrathin water layer to reach the active sites, resulting in a 30% performance boost over submerged monolayer systems. While the mass-normalised NH_3 yield followed a volcano-shaped dependence on catalyst loading, the overall SCCE remained consistently higher in the film system compared to the powder. Most notably, the AQE across the entire visible-to-NIR spectrum was significantly enhanced in the film system (Fig. 39i), proving that the integration of Schottky-barrier-free nanospheres into a porous, triphase-like interface

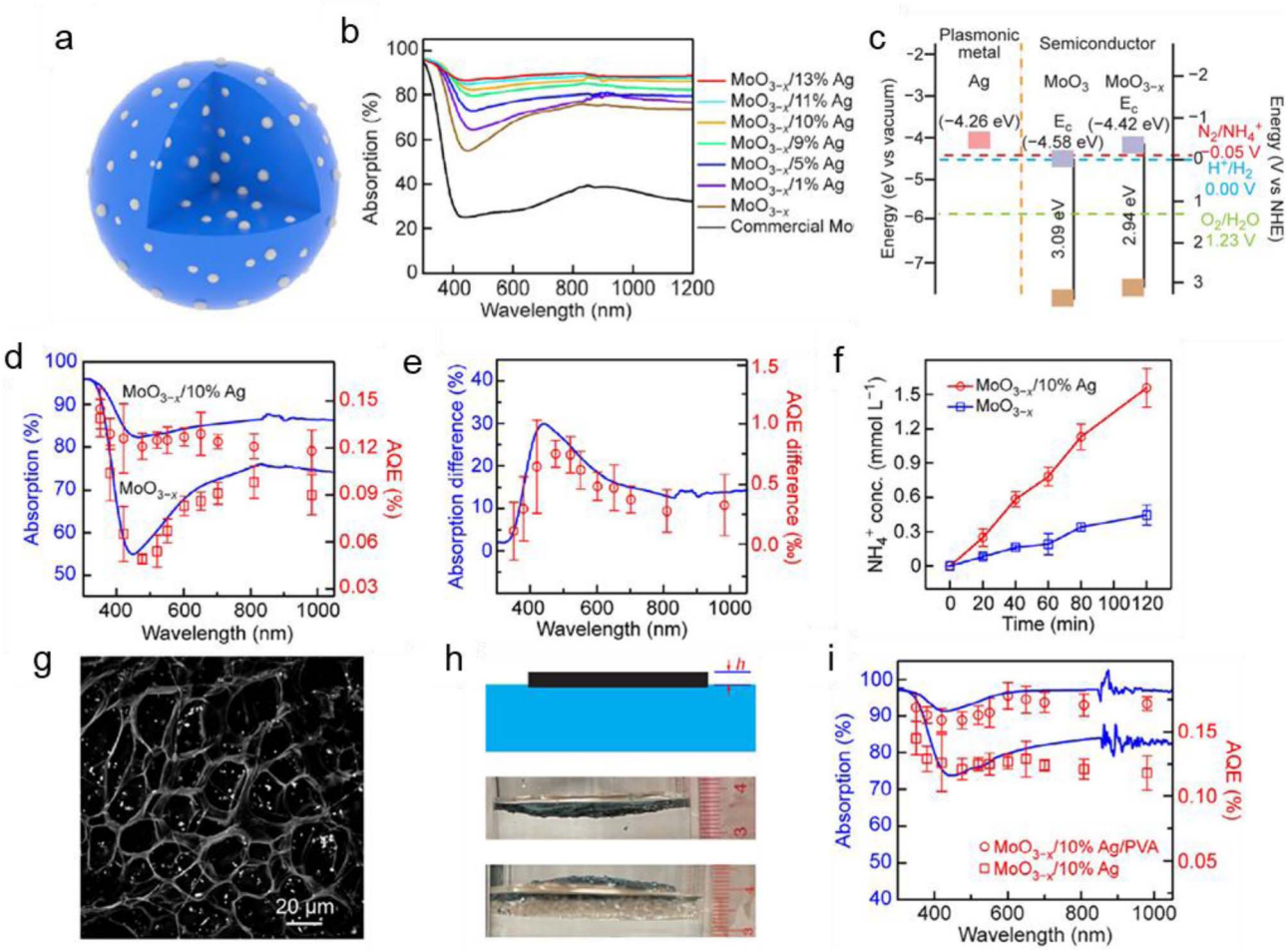

Fig. 39 Photocatalytic N_2 reduction over Schottky barrier free plasmonic semiconductor MoO_{3-x}/Ag system. (a) Schematic illustrating the structure of a MoO_{3-x} nanosphere loaded with Ag nanoparticles, (b) light absorption spectra of commercial intrinsic MoO_3 nanoparticles and the MoO_{3-x}/Ag samples with 0, 1, 5, 9, 10, 11, and 13% Ag, (c) electronic band energy levels of plasmonic Ag and MoO_{3-x} synthesized, (d) light absorption (left axis) and measured AQE (right axis) spectra of the MoO_{3-x} and MoO_{3-x}/10% Ag samples under the optimized conditions, (e) light absorption difference (left axis) and AQE difference (right axis) of the MoO_{3-x}/10% Ag sample with respect to the MoO_{3-x} sample under the optimized conditions, (f) time-dependent production of NH_3 for the MoO_{3-x}/10% Ag sample under the optimized conditions, (g) high-magnification SEM image of the solar absorber film obtained with the backscattered electron detection mode, (h) interface structure between the solar absorber film and water. From top to bottom: the ideal interface, monolayer interface, bilayer interface, (i) light absorption (left axis) and measured AQE (right axis) spectra of the powder and film systems. Reproduced with permission from ref. 605. Copyright 2025 Wiley-VCH GmbH.

effectively maximises both photon delivery and reactant accessibility.[605]

Expanding the scope of SBF systems, Wang *et al.*[206] recently reported a WO_3-based system that integrates hydrogen doping, oxygen vacancy engineering, and transition metal doping. Through a systematic screening of dopants (Mo, Bi, Ce, Fe, and V) and hydrothermal optimisation, the authors identified Mo-$H_{0.23}WO_{3-x}$ nanoplates (NPLs) as the most potent configuration for simultaneous N_2 fixation and H_2O_2 production. Morphological analysis revealed a well-defined rectangular nanoplate structure (Fig. 40a), while the synergistic presence of OVs and Mo sites, confirmed *via* EPR, XPS, and STEM-EDS, facilitated broadband light harvesting extending deep into the NIR region (Fig. 40b). Electronic structure analysis using Mott–Schottky and XPS valence band measurements (Fig. 40c) demonstrated that while Mo doping has a negligible impact on the overall band positions, it significantly enhances the charge transport dynamics. The conduction band and valence band potentials remained thermodynamically aligned for the coupled generation of NH_3 and H_2O_2, yet the Mo-modified $H_{0.23}WO_{3-x}$ exhibited the highest charge carrier density and photocurrent response among the series. Furthermore, the OVs were shown to serve a dual role: inducing the SBF-plasmonic state while simultaneously providing high-affinity sites for the chemisorption and activation of N_2 molecules.

The catalytic efficacy of these $H_{0.23}WO_{3-x}$-based nanoplates was evaluated through the simultaneous photofixation of N_2 and the generation of H_2O_2. Among the evaluated series, the Mo-$H_{0.23}WO_{3-x}$ configuration delivered the most robust bifunctional performance, achieving NH_3 and H_2O_2 production

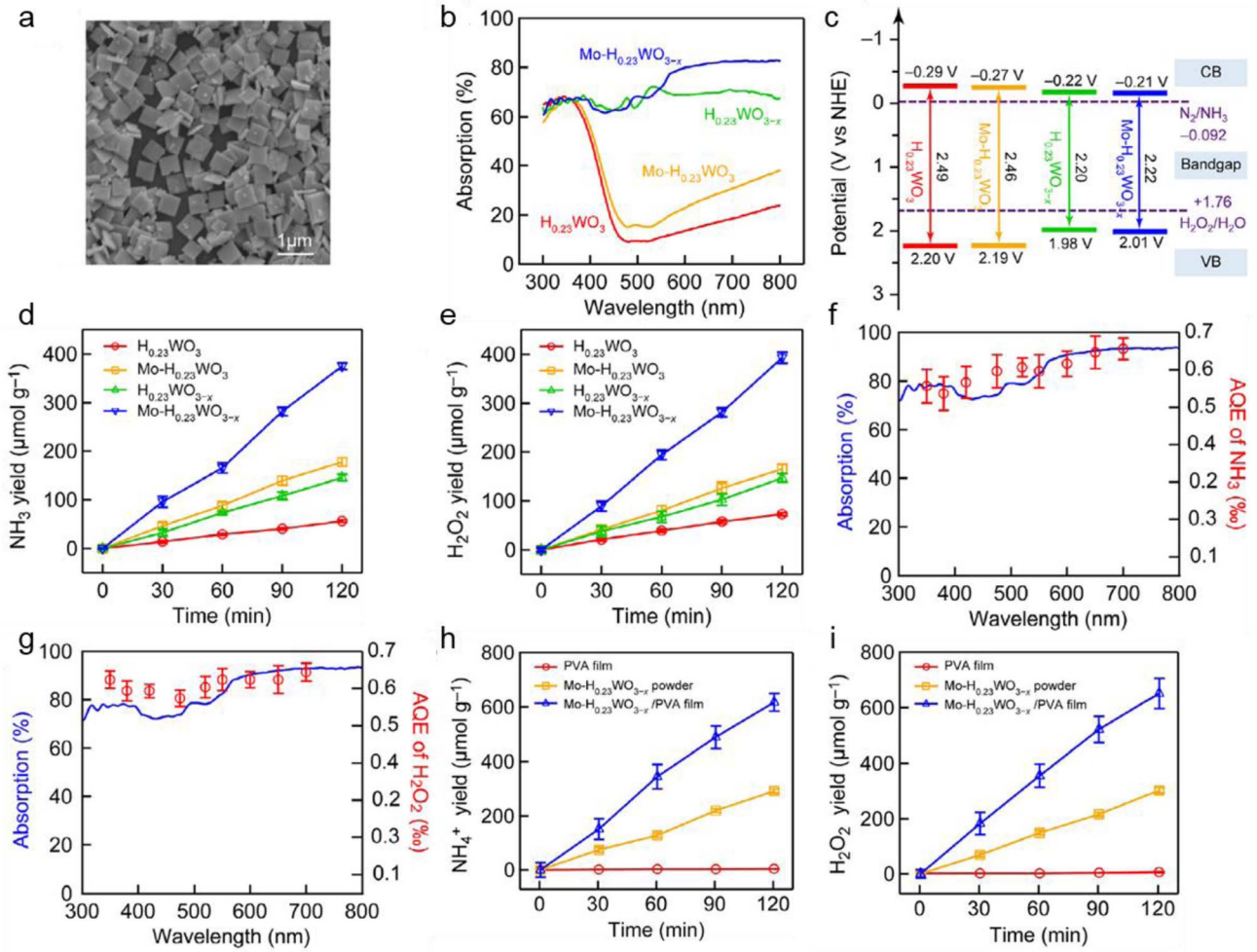

Fig. 40 Photocatalytic N_2 reduction over Schottky barrier-free Mo-$H_{0.23}WO_{3-x}$ photocatalyst. (a) SEM image of the Mo-$H_{0.23}WO_{3-x}$ NPLs, (b) DRS data of the $H_{0.23}WO_3$-based NPLs, (c) electronic band alignments of the $H_{0.23}WO_3$-based NPLs. Time-dependent yields of (d) NH_3 and (e) H_2O_2 for the $H_{0.23}WO_3$-based NPLs under the simulated solar light illumination. Light absorption spectra (blue line, left axis) and measured AQEs for (f) NH_3 (red dots, right axis) and (g) H_2O_2 (red dots, right axis) of the Mo-$H_{0.23}WO_{3-x}$ NPLs. Time dependent yields of (h) NH_3 and (i) H_2O_2 over the PVA film, Mo-$H_{0.23}WO_{3-x}$ powder, and Mo-$H_{0.23}WO_{3-x}$/PVA film. Reproduced with permission from ref. 206. Copyright 2026 Wiley-VCH GmbH.

rates of 187.53 and 196.25 μmol g^{-1} h^{-1}, respectively (Fig. 40d and e). A definitive link between the SBF-plasmonic properties and the catalytic output was evidenced by the monochromatic apparent quantum efficiency (AQE) measurements; the AQE profiles for both NH_3 and H_2O_2 exhibited a high degree of overlap with the catalyst's broadband absorption spectrum (Fig. 40f and g). This spectral matching confirmed that the vacancy-induced and Mo-enhanced LSPR effectively drives the redox chemistry across the entire visible-to-NIR range. Ultimately, the Mo-$H_{0.23}WO_{3-x}$ photocatalyst achieved a significant solar-to-chemical conversion efficiency of 0.090%, demonstrating the practical potential of integrating multiple defect-engineering strategies into a single barrier-free semiconductor framework.

To improve the light utilization of the system, the authors integrated the Mo-$H_{0.23}WO_{3-x}$ nanoplates into the same floatable PVA-based biphasic platform previously described. This interfacial engineering resulted in a 1.64-fold and 1.66-fold enhancement in NH_3 and H_2O_2 production rates, reaching 308.41 and 325.27 μmol g^{-1} h^{-1}, respectively, compared to the powdered slurry (Fig. 40h and i). The underlying mechanism, elucidated through DFT calculations and carrier dynamics studies, revealed a sophisticated two-photon excitation process. Upon absorbing an initial photon, a hot electron was transferred to a mid-gap doping state, subsequently migrating to the high-energy region of the conduction band after absorbing a second photon. This sequential excitation was enhanced by the LSPR of the Mo-$H_{0.23}WO_{3-x}$ framework, which significantly augments the generation of hot charge carriers. While the photogenerated holes in the valence band drive the oxidation of H_2O to H_2O_2, the accumulation of hot electrons, combined with the OV-mediated chemisorption and activation of N_2, facilitated high-efficiency nitrogen reduction. Collectively, these two studies highlight the transformative potential of Schottky-barrier-free architectures, where the synergy between metallic-like carrier densities, and defect-induced active sites

Table 1 Summary table of all the discussed photocatalysts

S. no.	Catalyst	Reaction	Reaction conditions	Product yield	Reference
1	In_2O_{3-x}/In_2O_3	CO_2 reduction with hydrogen	Batch reactor, $P = 2$ bar, H_2/CO_2 ratio = 1 : 1; Xe lamp (2 W cm^{-2}), $T = 262$ °C; external heating – no; reaction time = 30 min	CO: 1.87462 mmol h^{-1} m^{-2}	463
2	In_2O_{3-x}/In_2O_3	CO_2 reduction with hydrogen	Flow reactor, $P = 1$ bar, H_2/CO_2 ratio = 1 : 1; total flow = 1 mL min^{-1}; Xe lamp (0.8 W cm^{-2}), $T = 300$ °C; external heating – yes	CO: 0.161 mmol h^{-1} m^{-2}	463
3	0.4%GDY-IO	CO_2 reduction with hydrogen	Batch reactor, $P = 1.6$ bar, H_2/CO_2 ratio = 3 : 1; Xe lamp (2 W cm^{-2}), $T = 120$ °C; external heating – no; reaction time = 4 h	CO: 0.018 mmol g^{-1} CH_4: 0.011 mmol g^{-1} C_2H_4: 0.0007 mmol g^{-1} C_2H_6: 0.0009 mmol g^{-1} C_3H_6: 0.0001 mmol g^{-1} C_3H_8: 0.0001 mmol g^{-1}	466
4	Pd/TiO_2	CO_2 reduction with hydrogen	Batch reactor, $P = 25$ bar, H_2/CO_2 ratio = 4 : 1; 150 W mercury lamp, $T = 130$ °C; external heating – no; reaction time = 3 h	CO: 0.3556 mmol g^{-1} CH_4: 0.0463 mmol g^{-1} C_2H_6: 0.0396 mmol g^{-1}	467
5	R-Au/MnO_x-2%-PTPO (PTPO-Pt doped $PbTiO_3$)	CO_2 reduction with hydrogen	Flow reactor, $P = 1$ bar, H_2/CO_2 ratio = 3 : 1; total flow = 24 L g_{cat}^{-1} h^{-1}; Xe lamp (20 mW cm^{-2}), $T = 550$ °C; external heating – yes	CO: 235.7 mmol g^{-1} h^{-1}	70
6	Rh/Al_2O_3	CO_2 reduction with hydrogen	Flow reactor, $P = 1$ bar, H_2/CO_2 ratio = 5.5 : 1; total flow = 71 mL min^{-1}; blue LED (4.9 W cm^{-2}), $T = 350$ °C; external heating – yes	CH_4: 36 mmol h^{-1} g^{-1}	471
7	Black gold-Ni	CO_2 reduction with hydrogen	Flow reactor, $P = 1$ bar, H_2/CO_2 ratio = 1 : 10; total flow = 11 mL min^{-1}; Xe lamp (2.7 W cm^{-2}), $T = 223$ °C; external heating – no	CO: 2464 ± 40 mmol g_{Ni}^{-1} h^{-1}	248
8	Au@AuRu/g-C_3N_4	CO_2 reduction with hydrogen	Batch reactor, $P = 10$ bar, H_2/CO_2 ratio = 3 : 1; Xe lamp (1.1 W cm^{-2}), $T = 150$ °C; external heating – yes; reaction time = 4 h	CH_4: 0.103 mmol h^{-1} g^{-1}	477
9	$Al@Cu_2O$	CO_2 reduction with hydrogen	Flow reactor, $P = 1$ bar, H_2/CO_2 ratio = 1 : 1; total flow = 10 mL min^{-1}; supercontinuum fiber laser (10 W cm^{-2}), $T = 175$ °C; external heating – no	CO: 0.360 mmol cm^{-2} h^{-1}	238
10	$Ru_{0.1}Cu_1$-$MgAl_2O_4$	CO_2 reduction with hydrogen	Flow reactor, $P = 1$ bar, $CO_2/H_2/Ar$ ratio = 1 : 3:1; total flow = 3 mL min^{-1}; Xe lamp (1.7 W cm^{-2}), $T = 190$ °C; external heating – no	CH_3OH: 640 μL g^{-1} h^{-1}	162
11	$CuIn_5S_8$	CO_2 reduction with water	Batch reactor, $P = 1$ bar; UV Xe lamp (0.05 W cm^{-2}); external heating – no	CH_4: 0.0087 mmol h^{-1} g^{-1}	527
12	BiOCl nanosheets	CO_2 reduction with water		CO: 0.1882 mmol h^{-1} g^{-1}	528

Table 1 (*Contd.*)

S. no.	Catalyst	Reaction	Reaction conditions	Product yield	Reference
			Batch reactor, $P = 1$ bar; Xe lamp (400 nm cutoff filter); external heating – no		
13	$Pb_{0.6}Bi_{1.4}O_2Cl_{1.4}$	CO_2 reduction with water	Batch reactor, $P = 1$ bar; CO_2 (*ca.*1500 ppm); Xe lamp (420 nm cutoff filter); external heating – no; reaction time = 4 h	CO: 0.01791 mmol g^{-1} CH_3OH: 0.02653 mmol g^{-1}	529
14	Carbon-doped SnS_2	CO_2 reduction with water	Flow reactor, halogen lamp; reaction time = 13 h	Acetaldehyde: 1.2566 mmol g_{cat}^{-1}	530
15	Mn, C-codoped ZnO	CO_2 reduction with water	Batch reactor, $P = 0.8$ bar; Xe lamp; external heating – no; reaction time = 4 h	CO: 0.00083 mmol g^{-1}	531
16	Cu_2O-Pt/SiC/IrO_x	CO_2 reduction with water	Batch reactor, $P = 0.8$ bar; Xe lamp ($\lambda \geq 420$ nm); external heating – no; reaction time = 2 h	HCOOH: 0.8967 mmol g^{-1} h^{-1}	457
17	Single-atom cobalt in Bi_3O_4Br	CO_2 reduction with water	Batch reactor, $P = 0.8$ bar; Xe lamp; external heating – no	CO: 0.1071 mmol g^{-1} h^{-1}	532
18	$SrNb_2O_{6-x}$-3	CO_2 reduction with water	Batch reactor, $P = 1$ bar; Xe lamp (320 nm < λ < 780 nm); external heating – no	CO: 0.066 mmol g^{-1} h^{-1}	53
19	2D $BiFeO_3$	CO_2 reduction with water	Batch reactor, $P = 1$ bar; Xe lamp (500 mW cm^{-2}); external heating – no; reaction time = 1.5 h	CO: 0.17 mmol g^{-1} h^{-1}	19
20	Ag@Li_xTiO_2	CO_2 reduction with water	Batch reactor, $P = 1$ bar; Xe lamp (0.1 W cm^{-2}); external heating – no; reaction time = 10 h	CH_4: 0.049 mmol g^{-1}	533
21	AgX/g-C_3N_4 (X = Cl and Br)	CO_2 reduction with water	Flow reactor, $P = 1$ bar; low-power 15 W energy-saving daylight lamp (0.0085 W cm^{-2}); external heating – no; total flow = 5 mL min^{-1}	CH_4: 0.001092 mmol $g_{catalyst}^{-1}$	534
22	Au@TiO_2	CO_2 reduction with water	Batch reactor, $P = 1$ bar; Xe lamp,; external heating – no	CH_4: 0.00252 mmol g^{-1} h^{-1} C_2H_6: 0.00167 mmol g^{-1} h^{-1}	535
23	Au NR@ZnO	CO_2 reduction with water	Batch reactor, $P = 1.01$ bar; Xe lamp; external heating – no	CH_4: 0.017 mmol h^{-1} $(g_{Au})^{-1}$ CO: 0.032 mmol h^{-1} $(g_{Au})^{-1}$	536
24	Au nanoparticles	CO_2 reduction with water	Batch reactor, $P = 1$ bar; 420 nm LED (0.07 W cm^{-2}); external heating – no, reation time = 3 h	CO: 4.73 mmol g^{-1} h^{-1}	459
25	Au rod@CuPd	CO_2 reduction with water	Batch reactor, $P = 1$ bar; Xe lamp (0.4 W cm^{-2}), $T = 200$ °C; external heating – yes	CH_4: 0.55 mmol h^{-1} g^{-1}	412
26	Pt/black TiO_2	DRM	Flow reactor, $CH_4/CO_2 = 1:1$; $P = 1$ bar; total flow = 10 mL min^{-1}; AM 1.5G Newport solar simulator (0.1 W cm^{-2}), T = 700 °C; external heating – yes	CO: 480 mmol g^{-1} h^{-1} H_2: 237 mmol g^{-1} h^{-1}	552
27	Rh/STO	DRM	Flow reactor, $CH_4 : CO_2 : Ar$ (1 : 1 : 98 in vol%); $P = 1$ bar; total flow = 10 mL min^{-1}; Hg–Xe lamp (absorbed	CO: 0.27 mmol h^{-1} H_2: 0.27 mmol h^{-1}	553

Table 1 (*Contd.*)

S. no.	Catalyst	Reaction	Reaction conditions	Product yield	Reference
			photon number 1.25×10^{17} quanta per cm^2 per s); external heating – no		
28	SA-Ru/Cu	DRM	Flow reactor, $CH_4 : CO_2 = 1 : 1$; $P = 1$ bar; total flow = 16 mL min^{-1}; supercontinuum laser (19.2 W cm^{-2}); external heating – no	CO: 1980 mmol g^{-1} h^{-1} H_2: 1980 mmol g^{-1} h^{-1}	223
29	$NiCo/SiO_2$	DRM	Flow reactor, $CH_4 : CO_2 = 1 : 1$; $P = 1$ bar; total flow = 20 mL min^{-1}; Xe lamp (9 W cm^{-2}), $T = 700$ °C; external heating – yes	CO: 1446.1 mmol g^{-1} h^{-1} H_2: 1293.7 mmol g^{-1} h^{-1}	556
30	BiOBr-OV	N_2 reduction	Batch reactor; $P = 1$ bar; Xe lamp (420 nm cutoff); external heating – no; detection: spectrophotometry (Nessler's reagent)	NH_3: 0.104 mmol h^{-1} g_{cat}^{-1}	601
31	MoS_2/CdS	N_2 reduction	Batch reactor; $P = 3$ bar; Xe lamp (420 nm cutoff, 1.13 W cm^{-2}); external heating – no; reaction time = 4 h; detection: spectrophotometry (Nessler's reagent)	NH_3: 249.7 mg L^{-1} g_{cat}^{-1}	602
32	$AuRu_x$	N_2 reduction	Batch reactor; $P = 2$ bar; Xe lamp (0.4 W cm^{-2}); external heating – no; reaction time = 2 h; detection: spectrophotometry (indophenol blue)	NH_3: 0.101 mmol g^{-1} h^{-1}	281
33	Au/TiO_2	N_2 reduction	Flow reactor; $P = 1$ bar; total flow = 20 mL min^{-1} of N_2; Xe lamp (800 nm cutoff filter); external heating – no; detection: spectrophotometry (indophenol blue), ion chromatography, and ^1H NMR	NH_3: 10.1 nmol cm^{-2} h^{-1}	603
34	MoO_{3-x}	N_2 reduction	Flow reactor; $P = 1$ bar; total flow = 50 mL min^{-1} of N_2; Xe lamp (0.1 W cm^{-2}); external heating – no; reaction time = 2 h; detection: spectrophotometry (Nessler's reagent)	NH_3: 0.435 mmol h^{-1} g^{-1}	604
35	MoO_{3-x}/Ag	N_2 reduction	Flow reactor; $P = 1$ bar; Xe lamp (AM 1.5 G filter, 0.1 W cm^{-2}); external heating – no; reaction time = 2 h; detection: spectrophotometry (Nessler's reagent)	NH_3: 0.30 mmol h^{-1} g_{cat}^{-1}	605
36	Mo-$H_{0.23}WO_{3-x}$	N_2 reduction	Flow reactor; $P = 1$ bar; Xe lamp (AM 1.5 G filter, 0.1 W cm^{-2}); external heating – no; reaction time = 2 h; detection: spectrophotometry (Nessler's reagent)	NH_3: 0.308 mmol h^{-1} g^{-1} H_2O_2: 0.325 mmol h^{-1} g^{-1}	206

overcomes the traditional kinetic and thermodynamic barriers of plasmonic photocatalysis.[206]

4.5. Summary of catalytic insights: semiconductors and plasmonics

The examination of CO_2 reduction, dry reforming of methane, and N_2 fixation reactions reveals fundamental differences in how semiconductor and plasmonic photocatalysts approach chemical transformations, yet also uncovers convergent strategies that both systems employ to overcome their individual limitations. Semiconductor photocatalysts demonstrate their strength in sustained, multi-electron processes where their long carrier lifetimes (nanoseconds to microseconds) and well-defined band edge positions enable predictable thermodynamic control over reaction selectivity. This is exemplified in the selective CH_4 production from CO_2 reduction over defect-engineered $CuIn_5S_8$ layers, where discrete energy levels and extended carrier lifetimes facilitate the challenging 8-electron reduction pathway. In contrast, plasmonic photocatalysts excel in activating thermodynamically and kinetically challenging reactions through their ability to generate high-energy hot carriers and create intense local electric fields. The quantum-sized Au nanoparticles achieving 4.73 mmol g^{-1} h^{-1} CO production from CO_2 reduction with 100% selectivity demonstrate how plasmonic systems can provide both the energy and lifetime necessary for efficient catalysis, while the AuRu core-antenna structures breaking the formidable N≡N triple bond (941 kJ mol^{-1}) at ambient conditions showcase the unique ability of plasmonic hot carriers to overcome kinetic barriers that would be insurmountable for thermal or conventional photocatalytic processes.

One of the most profound insights emerging from recent studies is the shift toward Schottky-barrier-free architectures, such as the Mo-$H_{0.23}$/WO_{3-x} nanoplates. These frameworks represent a shift in how we view the metal–semiconductor interface; by eliminating the traditional depletion region, these systems allow for the seamless transport of hot electrons to catalytic sites. This architecture is particularly potent when coupled with two-photon excitation processes, where sequential energy absorption allows electrons to migrate from mid-gap states to higher-energy regions of the conduction band. This mechanism, significantly augmented by LSPR, exemplifies how researchers are now utilizing the "energy bottleneck" of traditional systems as a stepping stone to achieve higher quantum efficiencies.

Furthermore, the transition from laboratory benchmarks to practical systems has highlighted the importance of interfacial reactor engineering. The integration of catalysts into floatable PVA-based biphasic platforms addresses a critical bottleneck in traditional photocatalysis: the simultaneous optimization of light utilization and mass transport. By confining the reaction to a biphasic interface, these systems minimize light scattering by the solvent while ensuring that gaseous reactants like CO_2 and N_2 have direct access to the active sites. This coupling of materials science and reactor design demonstrates that the next generation of photocatalytic enhancement will likely come from the spatial management of both photons and molecules.

However, the most profound insight emerges from the recognition that both material classes converge on similar optimization strategies to transcend their individual limitations, revealing universal principles of photocatalytic enhancement that surpass the semiconductor–plasmonic divide. Both systems rely heavily on defect engineering, oxygen vacancies in semiconductors (black TiO_2, In_2O_{3-x}, BiOBr) and surface defects in plasmonic metals (MoO_{3-x}), to extend carrier lifetimes, create active sites, and modify electronic structures for enhanced catalytic performance. The ubiquitous use of heterostructure architectures, from semiconductor Z-schemes (Cu_2O-Pt/SiC/IrO_x) to plasmonic antenna–reactor systems (Au@AuRu/g-C_3N_4, DPC-C4-Ni), demonstrates that spatial separation of charge generation and utilization represents a fundamental design principle regardless of the underlying excitation mechanism. Most remarkably, the emergence of hybrid semiconductor–plasmonic systems (Au@TiO_2, Ag@$Li_{0.075}TiO_2$, Au NR@ZnO) reveals that the future of photocatalytic design lies not in choosing between these paradigms, but in utilizing their synergistic combination where plasmonic intensity provides the initial activation energy while semiconductor persistence ensures sustained chemical conversion, ultimately achieving performance levels that exceed the sum of their individual contributions, a testament to the complementary rather than competitive nature of these two fundamental approaches to solar-driven chemistry. Further broadening this scope, the emergence of doped semiconductor nanocrystals and transition metal nitrides has introduced a versatile platform for dynamically tunable, earth-abundant plasmonic systems.[606–608]

A summary table compiling all photocatalyst examples discussed in this section is provided to facilitate direct comparison (Table 1).

5. Semiconductor *vs.* plasmonics: charge dynamics

Understanding the differences and overlaps in charge dynamics between semiconductors and plasmonic systems is essential for interpreting their catalytic behavior. Both platforms rely on photoexcited carriers to drive chemical transformations, but the timescales, relaxation pathways, and interaction mechanisms with adsorbates can vary significantly. A discussion on representative examples from the literature helps clarify how hot carriers are generated, how long they persist, and how efficiently they couple into surface reactions. This section, therefore, sets the stage for discussing specific cases, highlighting both the shared principles and the distinct features that govern semiconductor and plasmonic photocatalysts.

5.1. Ultrafast dynamics in semiconductors

In the absence of external influences such as electromagnetic radiation, electrons and phonons in semiconductors or metals remain in thermal equilibrium, continually exchanging energy and momentum between them with average momentum equal

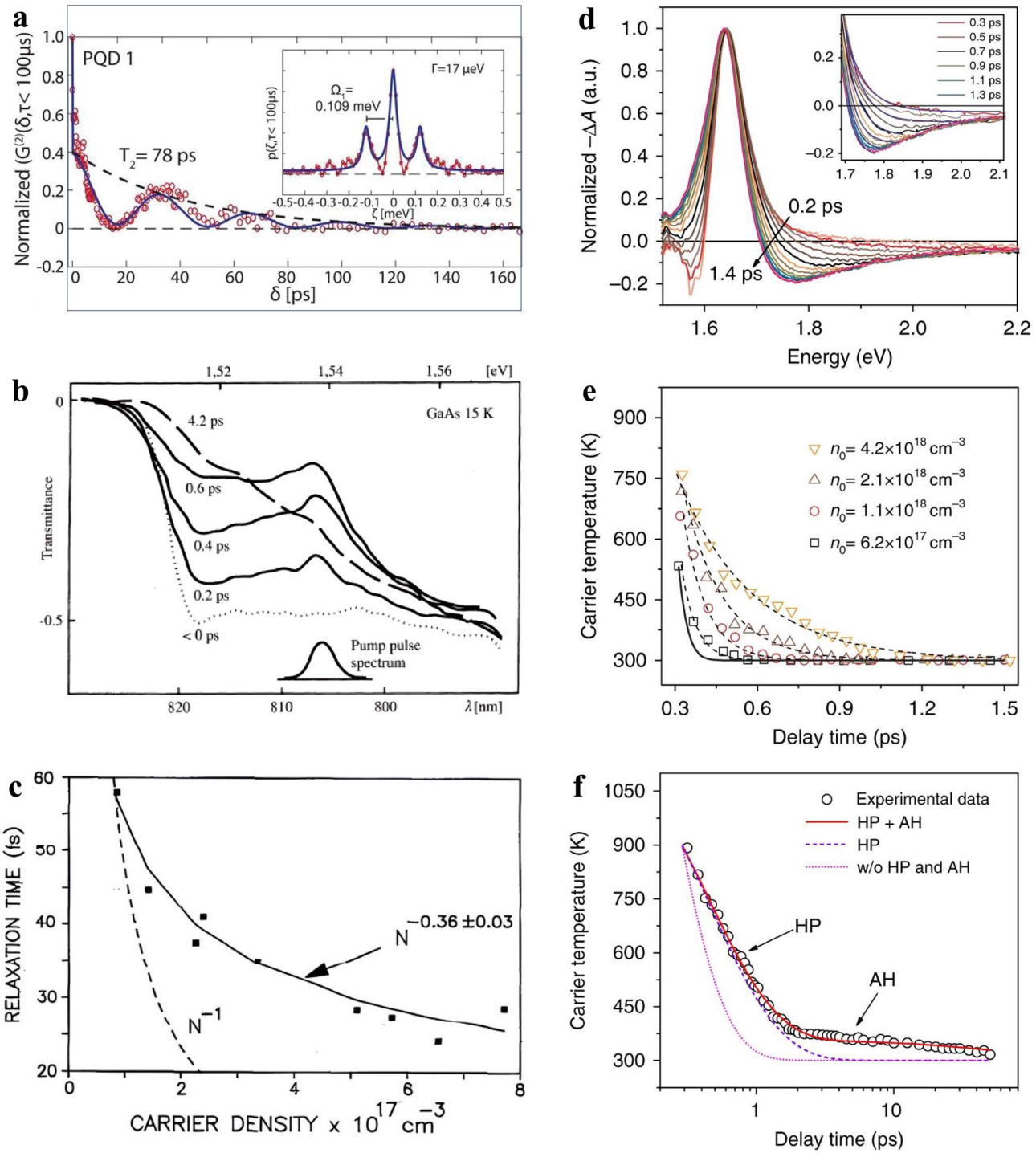

Fig. 41 TA spectroscopy for coherence time, relaxation dynamics, and hot carrier temperature. (a) Interferogram envelope squared for $CsPbBr_3$ NC (red circles) with best fit (blue line) and dephasing component (black dashed lines) decaying with $e^{-2/T_2\delta}$. Γ is the exciton linewidth, and $p(\zeta, \tau)$ is the spectral intensity, (b) time-resolved transmittance spectra of GaAs at 15 K for different time delays between the pump and probe pulses, (c) dephasing time in GaAs as a function of the carrier density. The dashed line represents the prediction by a simple Drude model, (d) normalized TA spectra with variable delays from 0.2 ps to 1.4 ps, and the inset shows fitted high energy tails using the Maxwell–Boltzmann distribution function to extract the HC temperature, (e) extracted HC temperature with a delay at different carrier density. Black line: calculated HC cooling dynamics in the absence of hot-phonon effect. All the dashed lines are calculated HC cooling dynamics in the presence of the hot-phonon effect, (f) HC cooling dynamics with a carrier density of 10.4×10^{18} cm^{-3} at RT. Black circles: HC temperature extracted from TA spectra. The lines show the calculated HC cooling dynamics for $\tau_{ph} = 0.6$ ps: with hot-phonon (HP) effect only (violet dashed line); with both HP and Auger heating (AH) effects (bright red line); and without HP and AH effects (magenta dotted line). Part (a) is reproduced with permission from ref. 613, copyright 2019 AAAS. Part (b) is reproduced with permission from ref. 614, copyright 1985 American Physical Society. Part (c) is reproduced with permission from ref. 615, copyright 1992 American Institute of Physics. Part (d–f) are reproduced with permission from ref. 616, copyright 2017 Springer Nature Publishing Group.

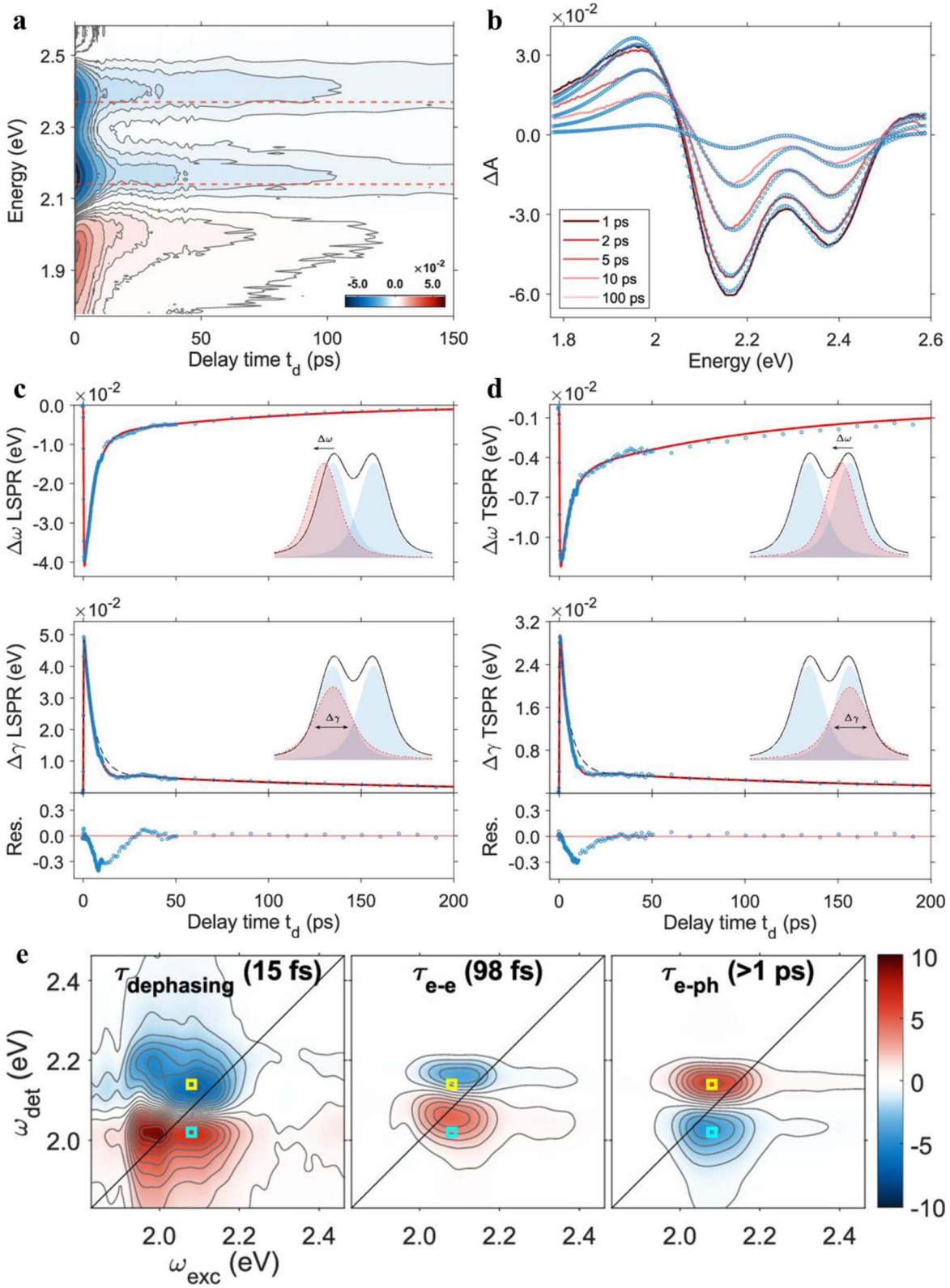

Fig. 42 TAS and 2DES for scattering lifetimes in Au nanorods. (a) 2D map representation of ΔA (colorscale) as a function of probing energy (eV) and pump-probe time delay (ps) with a pump pulse centered at 3.10 eV with a fluence of 700 μJ cm^{-2} and red horizontal lines indicate the spectral position of LSPR (2.14 eV) and TSPR (2.37 eV), (b) TA spectra at different delay times t_d (blue dots) and the respective fitting curves obtained using Voigt profile, (c) time evolution of $\Delta\omega$ (upper panel) and $\Delta\gamma$ (central panel) for LSPR. Blue dots, experimental points; red lines, fitting lines. (d) Same as (c) but for TSPR, (e) Decay associated spectra (DAS) for the three time constants extracted by the global fitting. The values of the time constants are reported in each plot. Reproduced with permission from ref. 628, copyright 2024 American Chemical Society.

to zero and average energy corresponding to the ambient lattice temperature. When either material is irradiated with electromagnetic radiation, the electronic distribution is perturbed, leading to the excitation of charge carriers (in a semiconductor) or interband transition and/or LSPR in metals (coherent regime). The average energy and momentum of these charge carriers are relaxed through various scattering processes and can be divided into four temporally overlapping regimes.[609,610] In this section, we discuss these four regimes with some examples.

5.1.1 Coherent regime. Immediately after photoexcitation, materials enter the coherent regime, where excited states retain a well-defined phase relationship with the driving electromagnetic field. In semiconductors, photon absorption creates excitons that generate a macroscopic interband polarization. This coherence decays extremely rapidly due to scattering. For example, in bulk GaAs (~0.1 μm), Becker *et al.*[611] used ultrafast four-wave mixing to measure decay constants of 3.5–11 fs as carrier density increased. Although short-lived, coherence remains technologically important, particularly in quantum information applications.[612] Utzat *et al.*[613] demonstrated this using photon–correlation Fourier spectroscopy, showing that $CsPbBr_3$ nanocrystals exhibit an optical coherence time of 78 ps at 3.6 K (Fig. 41a), which is a significant portion of their radiative lifetime ($T_1 = 210$ ps) at the same temperature.

5.1.2 Non-thermal regime. As coherence decays, carriers form a highly energetic, non-equilibrium distribution in which electrons typically gain more kinetic energy than holes. This regime was first observed by Oudar *et al.*[614] in 0.75 μm GaAs, where a 1.538 eV pump produced transient bleaching from state filling (Fig. 41b) that decayed over ~4.2 ps as carriers thermalized. The dephasing time (T_2) observed was ≈0.3 ps, which depends strongly on carrier density. Portella *et al.*[615] reported T_2 values of 25–60 fs for densities between 8×10^{16} and 8×10^{17} cm^{-3} in bulk GaAs, demonstrating that higher excitation densities increase charged carrier populations and enhance carrier–carrier scattering (Fig. 41c). Excitation energy also influences relaxation, with Lin *et al.*,[617] using a 2 eV excitation source, observed that increasing the Al mole fraction in Al_x-$Ga_{1-x}As$, which widens the band gap, resulted in a prolonged non-thermal distribution time. Collectively, these findings suggest that maximizing the lifetime of the non-thermal hot carrier distribution requires lower excitation densities and photon energies closer to the conduction band minimum.

5.1.3 Quasi-equilibrium regime. The hot carriers, generated through photoexcitation, undergo rapid carrier–carrier scattering, which redistributes energy among the carrier population and drives thermalization toward a common carrier temperature. This causes the system to reach a quasi-equilibrium state where carriers follow a Fermi–Dirac distribution with a temperature T_c still above the lattice temperature T_L.[618] This regime is particularly significant as slow carrier cooling holds greater promise for designing high-efficiency catalysts. This cooling proceeds primarily through the emission of optical phonons. Because carrier–carrier scattering scales with carrier density, the relative contribution of different scattering processes varies significantly with excitation conditions.

Further relaxation occurs through carrier–phonon coupling until carrier energies fall below the optical phonon threshold. Although high excitation densities generally accelerate thermalization *via* increased carrier–carrier scattering, cooling in semiconductor nanocrystals is often slowed by competing high-density effects. These include the hot-phonon bottleneck, where non-equilibrium longitudinal optical (LO) phonons accumulate and are reabsorbed because carrier–phonon scattering outpaces phonon decay, and Auger recombination, which recycles recombination energy back into the carrier system rather than emitting photons.[616,619]

One prominent example illustrating these phenomena at higher excitation densities was reported by Fu *et al.*[616] who examined hot-carrier cooling in methylammonium lead triiodide at carrier densities ~10^{18} cm^{-3} using transient absorption spectroscopy with 2.48 eV excitation. They observed an initial photobleach at 1.64 eV from band filling that evolved into photoinduced absorption within 0.6 ps (Fig. 41d). Hot-carrier temperatures were estimated using a Maxwell–Boltzmann approximation, and the cooling curves flattened at higher carrier concentrations, indicating slower energy loss (Fig. 41e). The dominant cooling mechanism was attributed to polar Fröhlich electron–phonon coupling, where delayed emission of zone-center LO phonons (lifetime ≈ 0.6 ± 0.1 ps) produced a hot-phonon bottleneck. At still higher densities (~10^{18} cm^{-3}), Auger heating further suppressed relaxation, leading to pronounced cooling slowdown (Fig. 41f). These results reveal the strong influence of carrier density, phonon bottlenecks, and Auger processes on hot-carrier cooling.

5.1.4 Isothermal regime. Following hot-carrier relaxation, the system approaches thermal equilibrium as the thermalized electron–hole population and the coupled phonon modes progressively cool toward the lattice temperature. Phonon–phonon interaction is one of the most fundamental scattering processes that drives this equilibrium. Excess electrons and holes persist, and recombination proceeds *via* radiative pathways (photon emission) or non-radiative decay through optical phonons. As illustrated by the examples above, the timescales of each relaxation step depend sensitively on band structure, initial excess energy, excitation type, carrier density, and lattice temperature.

5.2. Ultrafast dynamics in plasmonic nanostructures

In plasmonic nanomaterials, coherent excitation occurs when the incident photon frequency matches the plasma frequency, generating LSPR. The electric field enhancement scales with the quality factor $Q = \omega/\gamma$, typically 10–20 for Au and Ag.[620,621] Khurgin *et al.*[620] showed that over half of the electromagnetic energy resides in charge oscillations, free electrons in metals *versus* bound valence electrons in semiconductors.

LSPR damping initiates hot-carrier generation. Classical Drude theory describes this as gradual energy loss per oscillation cycle caused mainly by frictional loss (or electron–phonon scattering),[622–626] though electron–electron interactions and

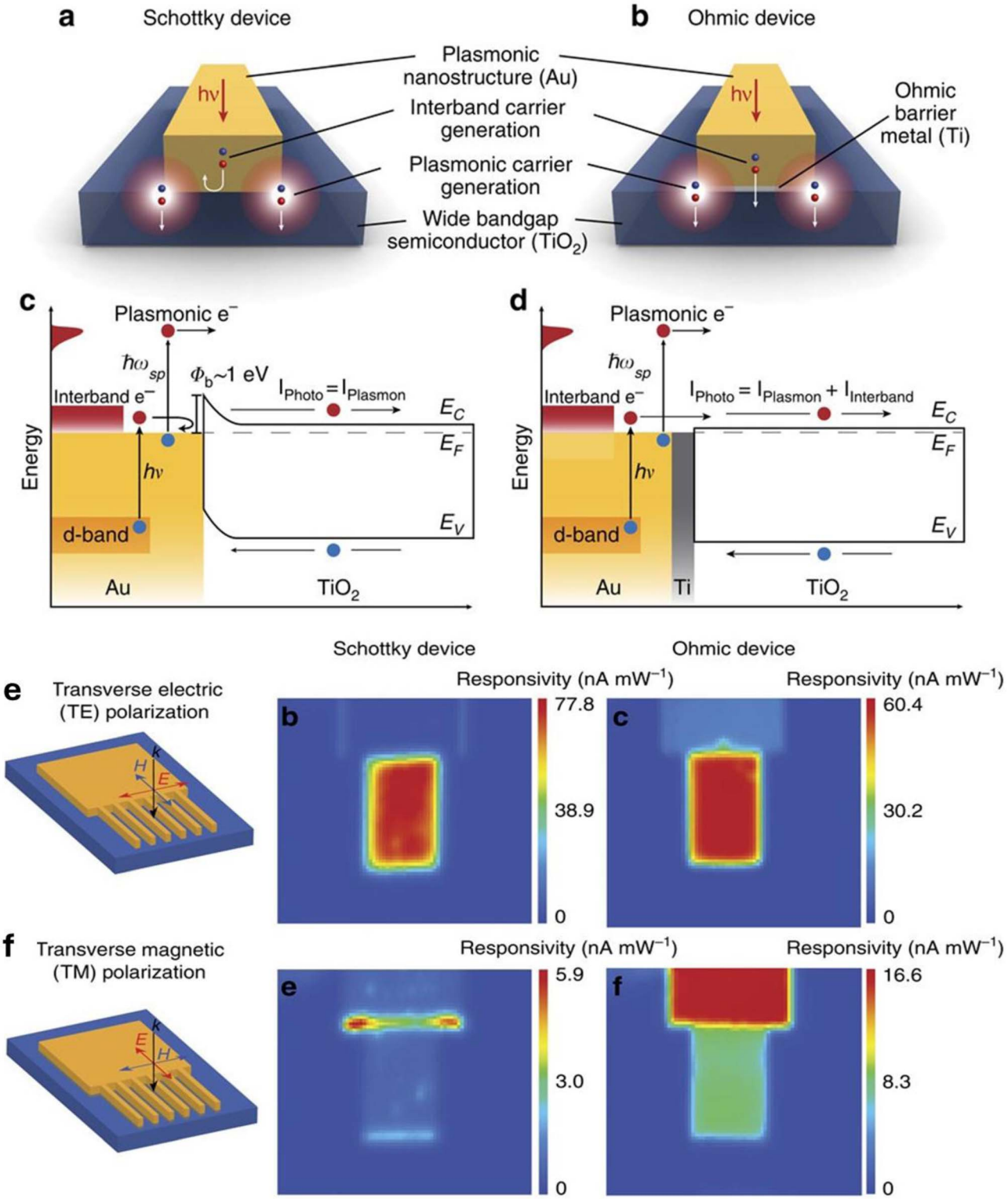

Fig. 43 Carriers' route, band diagrams, and photocurrent mapping in Schottky and ohmic devices. Schematic of hot-carrier generation and collection. (a) Schottky and (b) ohmic barrier. Plasmonic hot-carrier generation is localized to areas of high-field enhancement, while interband absorption occurs throughout the bulk. Band diagrams show (c) an Au-TiO_2 Schottky device where low-energy carriers cannot cross the barrier, and (d) an Au-Ti-TiO_2 ohmic device, where carriers are freely collected due to the absence of a barrier. The wide semiconductor band gap enables preferential electron collection. (e) Schematic of TE excitations used to generate photocurrent map of a Schottky and an ohmic device using TE-polarized light. The laser wavelength is tuned to the resonance of the plasmonic nanowires (~675 nm, wire width 273 nm). (f) Schematic of TM-polarized light excitation used to generate photocurrent maps of a Schottky and an ohmic device. Reproduced with permission from ref. 637, Copyright 2015 Springer Nature Publishing Group.

rapid decay of d-band holes due to larger effective mass in noble metals also contribute.[627] Hot-carrier relaxation then follows the same sequence of electron–electron, electron–phonon, and phonon–phonon scattering as in semiconductors, though with faster e–e scattering due to higher carrier density. While the formal sequence of relaxation steps is similar, the underlying excitation origin, characteristic timescales, and consequences for energy transfer and catalysis differ fundamentally between plasmonic metals and semiconductors. Toffoletti *et al.*[628] investigated these dynamics in colloidal Au nanorods using transient absorption and 2D electronic spectroscopy (2DES). Pump–probe measurements revealed photobleaching at both plasmon modes (LSPR at 2.14 eV, TSPR at 2.37 eV) and a red-shifted, broadened positive signal from electron heating (Fig. 42a and b). Voigt-profile fits[629] enabled the extraction of time-dependent plasmon shifts ($\Delta\omega$) and broadenings ($\Delta\gamma$) (Fig. 42c and d). A breathing mode with a 53 ± 5 ps period was observed, attributed to lattice expansion, and it modulated $\Delta\gamma$ more strongly than $\Delta\omega$. From fluence-dependent dynamics, the electron–phonon scattering time was determined as $\tau_{e\text{–}ph} \approx 1.16 \pm 0.36$ ps, and the phonon–phonon scattering time as $\tau_{ph\text{–}ph} \approx 145 \pm 40$ ps.

To resolve earlier processes within the first few hundred femtoseconds, the authors employed 2DES, which separates homogeneous and inhomogeneous linewidth contributions.[630–634] The homogeneous linewidth before scattering was $\gamma_{LSPR} = 52 \pm 5$ meV at $t_2 = 0$, where t_2 represents the delay between the second pump pulse and the probe pulse, and it broadened with increasing t_2 due to electron–electron scattering. From the time dependence of $\gamma_{LSPR(t2)}$, the authors extracted $\tau_{e\text{–}e} \approx 65 \pm 42$ fs, refined to $\sim 98 \pm 26$ fs using global fitting, along with $\tau_{e\text{–}ph} \approx 1603 \pm 40$ fs (Fig. 42e). The authors also identified a coherent dephasing time of ~15 fs (45 meV linewidth). This coherent regime represents a fascinating parallel between plasmonic nanostructures and semiconductors; both systems can maintain quantum coherence on similar timescales. However, unlike semiconductors, plasmonic nanostructures exhibit significant electron–electron scattering, allowing them to achieve a Fermi–Dirac distribution much more quickly.

5.2.1 Damping mechanisms in LSPR. There are two broader categories of damping mechanisms in plasmonic nanostructures: interband excitation and intraband excitation.

5.2.1.1 Interband decay. Interband excitation represents a direct quantum transition from a filled d-band below the Fermi level to an empty sp-band. In silver, this involves the transition from 4d-band to 5s-band, while in gold, it involves the 5d-band to 6s-band. These transitions require specific energies: the interband gap of Au and Ag is 2.4 eV and 3.8 eV, respectively.[635,636]

To provide an electron with the kinetic energy between 0.5 and 1 eV necessary for ejection from the surface, blue and UV radiation are needed for gold and silver, respectively. This requirement creates a fundamental challenge: in the visible spectrum, interband absorption competes with other absorption processes, reducing the efficiency of hot-electron extraction.

Zheng *et al.*[637] provided clear experimental evidence separating carrier generation from direct interband excitation *versus* plasmon decay. Using electron-beam lithography, they fabricated devices with square Au pads and periodic Au nanowire arrays (50 nm thickness, 500 nm spacing) on ⟨100⟩ TiO_2 substrates, forming either Schottky (Au/TiO_2) or ohmic (Au/Ti/TiO_2) contacts (Fig. 43a and b). This configuration allowed selective probing of carrier injection pathways. Because metals exhibit low interband absorption cross-sections but strong plasmonic absorption, Schottky contacts primarily detect high-energy carriers generated from plasmon decay, whereas ohmic contacts allow both low- and high-energy carriers to contribute (Fig. 43c and d).

Using 675 nm excitation (1.84 eV), well below the TiO_2 band gap (3.03 eV), ensured that only Au was photoexcited. Under transverse electric (TE) polarization, which efficiently excites surface plasmon polaritons, Schottky devices generated localized photocurrent near the edges of nanostructures, while ohmic devices produced uniform current (Fig. 43e). Under transverse magnetic (TM) polarization, Schottky devices showed minimal signal, whereas ohmic devices still produced uniform current (Fig. 43f). These polarization-dependent responses confirm that plasmonic excitation yields significantly greater photocurrent than direct interband transitions. This work established an important design principle: interband transitions largely produce low-energy carriers, while plasmon decay provides the high-energy carriers more relevant for photocatalysis and photodetection.

5.2.1.2 Intraband decay. Intraband processes involve transitions between electronic states of different momenta and require phonons, defects, electron–electron scattering, or surfaces to satisfy momentum conservation. Phonon- or defect-mediated pathways dephase the LSPR and generate hot carriers analogously to indirect semiconductors. Electron–electron interactions redistribute plasmon energy among many carriers, especially at higher frequencies where the e–e scattering rate increases. Surface-assisted damping (Landau damping) becomes prominent in nanoscale structures: strong field confinement at the surface broadens the available momentum range and enables coupling to high-momentum electronic states. This mechanism efficiently generates hot carriers near the interface, precisely where carrier extraction or catalytic reactions occur, making it highly relevant to photocatalysis.[609]

Brown *et al.*[638] provided a quantitative framework for these processes *via* first-principles calculations based on experimentally measured dielectric functions. They evaluated contributions from direct (interband), surface-assisted, phonon-assisted, and resistive decay channels to the plasmon linewidth (Fig. 44a–d). Their results show that, above the interband threshold (~1.6–1.8 eV for Al, Au, Cu; ~3.5 eV for Ag), direct transitions dominate the plasmon damping. Near the Fermi level, however, phonon-assisted decay is the primary mechanism, as electron–electron scattering is negligible, making carrier lifetime and mean free path maximum. Carrier lifetimes peak at ~30 fs for Ag, Cu, and Au, with mean free paths of ~50 nm (Ag > Cu > Au), while Al exhibits shorter lifetimes (~10 fs) and shorter mean free paths (~20 nm) (Fig. 44e–h). At

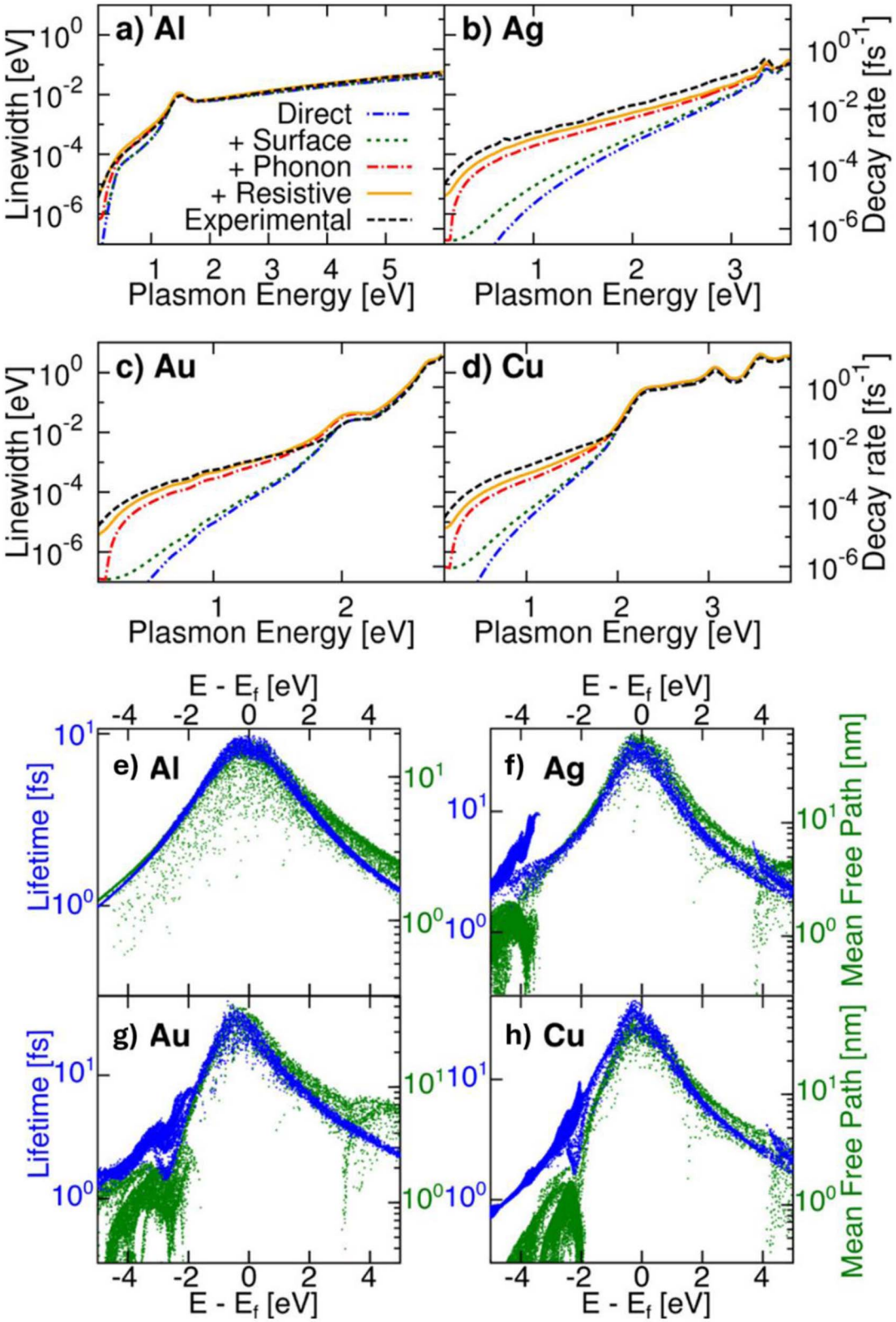

Fig. 44 Comparison of experimental and calculated line widths, decay rates, and hot carrier lifetimes in Al, Ag, Au, and Cu. Calculated and experimental line widths (left axis) and decay rates (right axis) in (a) Al, (b) Ag, (c) Au, and (d) Cu. The theoretical curves indicate cumulative contributions from direct (or interband) transitions alone ("Direct"), including surface-assisted transitions ("+Surface"), including phonon-assisted transitions ("+Phonon"), and including resistive losses ("+Resistive"). Hot carrier lifetimes as a function of energy, accounting for electron–electron and electron–phonon contributions for (e) Al, (f) Ag, (g) Au, and (h) Cu. For each panel, the left axis measures lifetime (blue) and the right axis measures mean free path (green). The spread in the results is because of multiple electronic states at each energy with different scattering rates due to anisotropy at the microscopic level. Reproduced with permission from ref. 638, Copyright 2015 American Chemical Society.

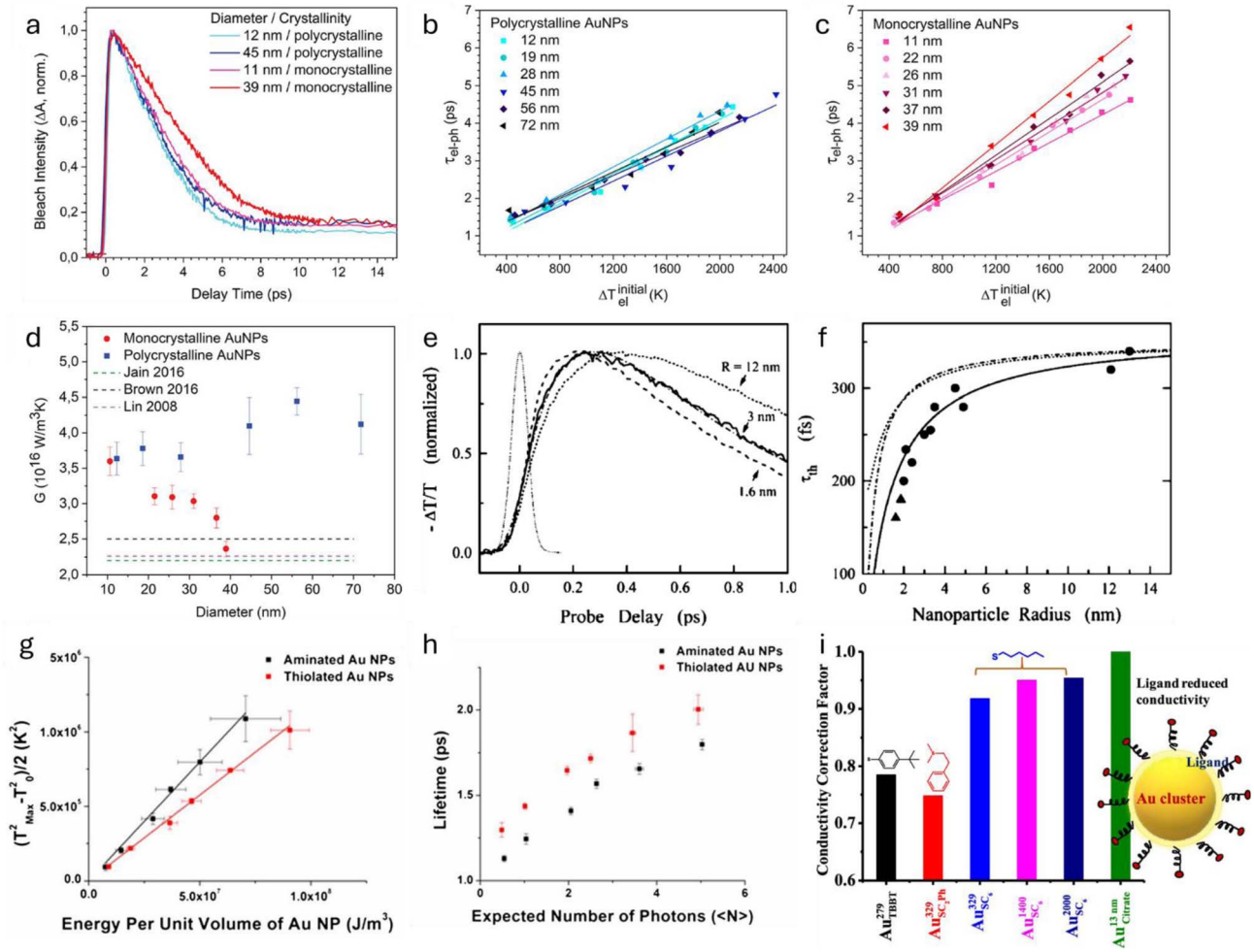

Fig. 45 Size and ligand-dependent carrier dynamics in Au nanocrystals. (a) Dynamics of the TA bleach recovery of different AuNPs after excitation with 100 μJ cm^{-2} pulses. Electron–phonon coupling times *vs.* initial electron temperature for (b) polycrystalline and (c) monocrystalline AuNPs, (d) electron–phonon coupling constants as a function of particle diameter. Literature bulk gold values are plotted as dashed lines for comparison, (e) time behavior of the induced transmission change $-\Delta T/T$ measured for the pump ≈ 3.95 eV and probe ≈ 1.32 eV in Ag nanoparticle samples, (f) size dependence of the electron thermalization time τ_{th} (or τ_{e-e}) for Ag nanoparticles in a $BaO-P_2O_5$ (dots) and Al_2O_3 (triangles) matrix. The full line shows the computed τ_{th} considering both the spillout and d-electron localization effects, and the dash-dotted and dotted lines of their respective contributions, (g) $\frac{1}{2}(T_E^{max2} - {T_0}^2)$ *vs. U* normalized by the unit volume of the Au NP, (h) the observed lifetime of hot electrons *versus* the average number of photons absorbed per NP, for the aminated (black) and thiolated (red) Au NPs, (i) electrical conductivity of various Au nanoclusters obtained using three-layered Mie theory. Part (a–d) is reproduced with permission from ref. 647, copyright 2021 American Chemical Society. Part (e and f) is reproduced with permission from ref. 646, copyright 2000 American Physical Society. Part (g and h) is reproduced with permission from ref. 651, copyright 2013 Proceedings of the National Academy of Sciences of the United States of America. Part (i) is reproduced with permission from ref. 652, copyright 2019 American Chemical Society.

energies >1 eV above the Fermi level, electron–electron scattering becomes increasingly significant, reducing mean free paths to ~10 nm at 2 eV.

This analysis suggests that aluminum might be the most promising option for plasmonic hot carrier generation, as it not only efficiently produces hot carriers over the broadest frequency range but also generates high-energy electrons and holes with equal probability. Compared to noble metals, it demonstrates superior transport properties for high-energy holes. However, aluminum's lower absorption cross-section compared to noble metals (Au, Ag) and its poor stability due to oxidation limit its widespread use in applications.

5.3. Size and ligand effect on carrier dynamics in plasmonic and semiconductor nanostructures

The ultrafast dynamics become even more intricate when we consider how nanoparticle size and surface chemistry can dramatically alter the temporal behavior of excited carriers. These parameters provide powerful tools for controlling carrier lifetimes and optimizing photocatalytic performance.

5.3.1 Plasmonic nanoparticles. Measuring electron–phonon (e–ph) and electron–electron (e–e) scattering times *via* ultrafast spectroscopy is challenging because these processes depend on pump fluence. Two strategies are commonly used:

low-intensity excitation to minimally perturb the electron distribution, or measurements across multiple pump powers extrapolated to zero fluence.

The size dependence of e–ph scattering in noble metal nanoparticles has been widely studied, though early reports were contradictory.[152,164,639–650] Staechelin *et al.*[647] clarified that crystallinity is the key factor: polycrystalline Au nanoparticles show negligible size dependence, whereas monocrystalline AuNPs exhibit a clear decrease in e–ph scattering rate with decreasing size. Using TA spectroscopy, they tracked spectral dynamics as a "spectral thermometer" of electron temperature (Fig. 45a). At high initial electron temperatures (~2000 K), e–ph coupling times were ~4.4 ps for polycrystalline AuNPs and ranged from 4.6 ps (11 nm) to 6.5 ps (39 nm) for monocrystalline particles. At low electron temperatures (~450 K), the coupling times converge (~1.5 ps) (Fig. 45b and c). The linear relationship between τ_{e-ph} and initial electron temperature allows the extraction of electron–phonon coupling constants. The e–ph coupling constant in polycrystalline AuNPs is size-independent, remaining approximately 4×10^{16} W m^{-3} K^{-1}. However, monocrystalline AuNPs show size-dependent behavior, decreasing from 3.6×10^{16} W m^{-3} K^{-1} (11 nm) to 2.4×10^{16} W m^{-3} K^{-1} (39 nm), approaching bulk values (~$2.2–2.5 \times 10^{16}$ W m^{-3} K^{-1}) (Fig. 45d). This effect arises from electron-surface scattering: monocrystalline particles have longer electron mean free paths, making surface-to-volume ratio important, whereas grain boundaries in polycrystalline NPs dominate scattering, rendering size less significant. Consequently, monocrystalline AuNPs exhibit longer hot-electron lifetimes, which can enhance catalytic efficiency.

Voisin *et al.*[646] studied size-dependent e–e scattering in Ag nanoparticles (1.5–13 nm) using IR pump pulses (950 nm) for intraband excitation, which alters the occupation number (Δf) around Fermi level E_F and UV probe pulses for interband detection, which is sensitive to this change. Smaller particles showed faster thermalization (shorter τ_{e-e}), while τ_{e-e} increased by a factor of two as particle size increased from 3 to 26 nm (Fig. 45e). In small nanoparticles, the high surface-to-volume ratio exposes a larger electron density to inefficient Coulomb screening, thereby enhancing e–e scattering. This reduced screening efficiency stems from (i) electron spillout at the surface and (ii) core confinement of bound d-electron, which collectively lower the electron density near the surface. By accounting for electron density spillout and d-electron surface exclusion, the model (Fig. 45f) successfully reproduces the experimental size dependence. This confirms the critical role of these surface effects, though deviations occur for particles ≤2 nm due to strong confinement.

The chemical environment surrounding nanoparticles acts like a molecular atmosphere that can dramatically affect hot carrier lifetimes. Coating nanoparticle surfaces with ligands stabilizes the particles and, in the case of metals, can alter LSPR properties by changing the effective optical refractive index in the near field.[653–655] The influence of the chemical environment on hot carrier lifetime has been explored in various plasmonic nanostructures.[651,656–660]

Aruda *et al.*[651] sought to clarify the mechanism behind lifetime changes when switching ligands passivating Au NPs from a dative bonded alkylamine ligand (hexadecylamine) to covalently bonded alkylthiolates (hexadecanethiolate), both of similar dimensions but different bonding characteristics. They applied a temperature-dependent Mie theory model to fit TA spectra, utilizing three fitting parameters: electronic temperature T_e and two temperature-dependent damping constants. The electronic heat capacity γ relates to the initial electronic temperature T_e^{max} through electronic population by laser pulse (U) *via*:

$$U = \frac{1}{2}\gamma\left(T_E^{max2} - T_0{}^2\right) \quad (3)$$

The reciprocal slope of $\frac{1}{2}(T_E^{max2} - T_0{}^2)$ *versus* U (Fig. 45g) gives the electronic heat capacity γ. They observed that γ for thiolated AuNPs is 40% higher than that of aminated AuNPs. Using the general form of the two-temperature model (TTM), the temperature-dependent electron–phonon coupling constant ($g = g_o + g_1(\Delta T)$ where $\Delta T = T_e - T_L$) was found to be 30% larger for thiolated AuNPs than aminated AuNPs. The hot electron lifetime depended on both initial electronic temperature and the number of photons absorbed per particle, as both γ and g are temperature dependent. Thiolated AuNPs exhibited 20% longer hot electron lifetimes than aminated AuNPs (Fig. 45h).

This occurs because higher γ means reduced energy exchange between electrons and lattice, thus increasing hot electron lifetime, while larger g means increased energy transfer rate, thereby decreasing hot electron lifetime. These two effects partially cancel each other, leading to a net 20% increase in hot electron lifetime. The greater impact of thiolate on both g and γ compared to amine was attributed to covalently bound thiolate enhancing the density of states near the Fermi level more than amine.

Shabaninezhad *et al.*[652] investigated passivating ligand roles on electron–phonon relaxation dynamics in the smallest-sized gold nanoclusters. They found that Au nanoclusters passivated by aromatic rings (TBBT and Sc_2Ph) show greater electron–phonon coupling times compared to nanoclusters passivated with hexane thiol ligand (SC_6) (Fig. 45i). The authors explained this result by noting that in Au nanoclusters passivated by aromatic ligands, electrical conductivity decreases due to Au-π interaction and conjugation, leading to decreased free electron density.

5.3.2 Semiconductor nanocrystals. A key distinction between semiconductors and metal nanocrystals is the presence of a band gap in semiconductors. Even at small sizes, energy spacing in metal nanocrystals remains minimal, resembling bulk behavior, whereas semiconductor optical excitation is dictated by the size-dependent band gap. Consequently, quantum confinement effects in metals only become apparent at much smaller particle sizes compared to semiconductors.[661] Additionally, trap states in semiconductor nanocrystals, arising from dangling bonds, surface defects, and stabilizing adsorbates, provide alternative pathways for exciton recombination, which can either promote or hinder photocatalysis depending on their energy and density.[662]

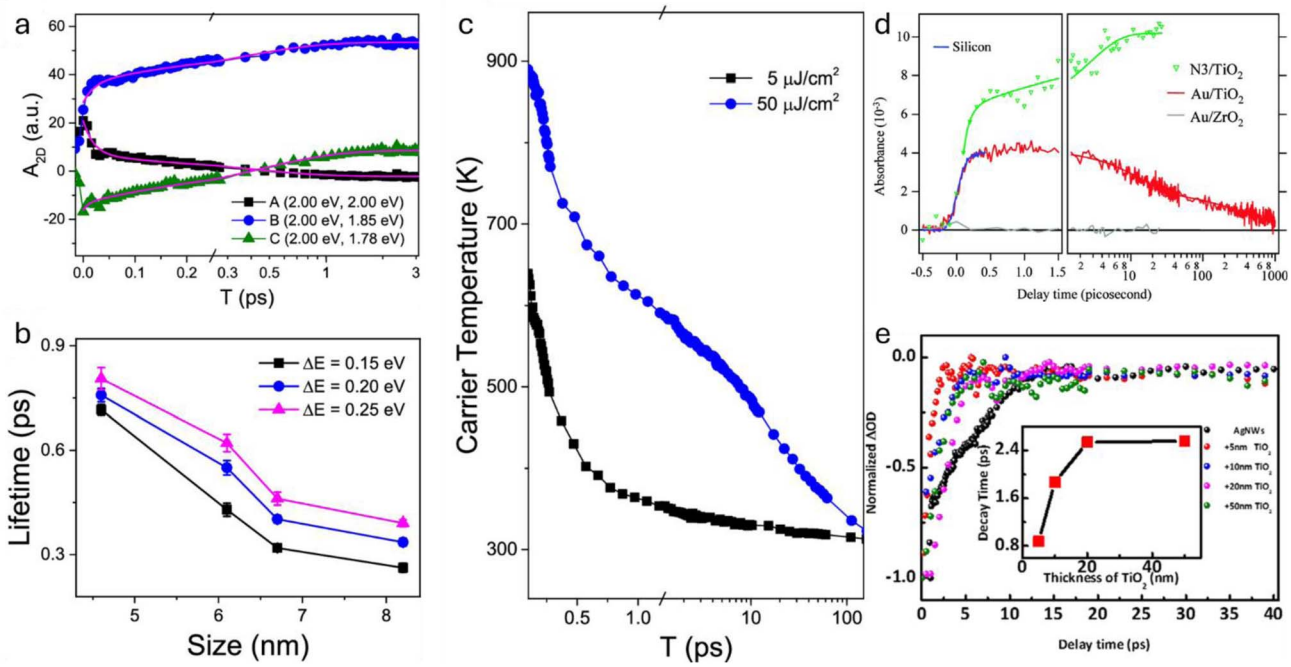

Fig. 46 Size-dependent carrier dynamics in $CsPbI_3$ nanocrystals and electron transfer kinetics in metal/semiconductor hybrid. (a) Temporal dynamics of 2DES signals probed at excitation excess energy of $\Delta E = 0.15$ eV and different emission energy. (b) Size-dependent lifetime parameters for hot carrier dynamics. The cooling process slows down with decreasing nanocrystal size as a signature of the phonon bottleneck effect. (c) The dynamics of hot-carrier temperature with pump fluence of 5 and 50 μJ cm^{-2} for the average size of a nanocrystal sample of 6.7 nm. (d) Transient absorption kinetics at 3500 nm of nanocrystalline films (green: $N3/TiO_2$, red: Au/TiO_2, grey: Au/ZrO_2). The blue line shows the response of the apparatus, obtained using a silicon plate. (e) Normalized curves of shell-thickness dependence of the AgNWs plasmon photobleaching decay dynamics. The probe wavelength is 349 nm. All the experiments were conducted under a pump wavelength of 320 nm (3.87 eV) with an average power of 3 mW. Part (a–c) is reproduced with permission from ref. 668, copyright 2020 American Chemical Society. Part (d) is reproduced with permission from ref. 669, copyright 2007 American Chemical Society. Part (e) is reproduced with permission from ref. 670, copyright 2018 Springer Nature Publishing Group.

The size dependence of carrier–phonon scattering in perovskite nanocrystals has produced apparently contradictory results: some studies report faster hot carrier cooling with decreasing size,[65,663] others show slower cooling,[664,665] or negligible change.[666,667] Yu *et al.*[668] resolved this by using 2D electronic spectroscopy with 10 fs resolution to study $CsPbI_3$ nanocrystals (4.6–8.2 nm, below the exciton Bohr diameter ~12 nm) (Fig. 46). 2DES enabled separation of rapid carrier thermalization (~20 fs) from subsequent cooling *via* carrier–phonon interactions (~260 fs), which is difficult to resolve with standard TA spectroscopy.

Analysis of the 2D signals revealed that smaller nanocrystals exhibited slower cooling, with lifetimes more than doubling as size decreased from 8.2 to 4.6 nm (Fig. 46b). Higher excess excitation energy also prolongs hot carrier lifetimes, due to Auger heating and hot-phonon bottleneck (Fig. 46c). These results highlight the interplay between size, excitation energy, and hot phonon dynamics in controlling carrier relaxation in semiconductor nanocrystals.

Surface ligand modification profoundly influences carrier dynamics in quantum dots, as ligands can change trap states and affect intraband relaxation through various mechanisms such as phonon coupling, Auger recombination, and vibrational relaxation. Surface ligands on semiconductor nanocrystals can significantly affect exciton relaxation processes.[671–675] Zhang *et al.*[671] investigated the role of alkyl ligand chain length in hot-carrier cooling processes in $CsPbBr_3$ nanocrystals. They used two alkyl ligands: octanoic acid, C8 (OcA), and oleic acid, C18 (OA). $CsPbBr_3$-OcA QDs exhibited longer hot-carrier cooling lifetimes (~504 fs) compared to $CsPbBr_3$-OA QDs (~387 fs). This difference demonstrates that molecular vibrations of ligands can affect carrier–phonon coupling during cooling processes. The vibrational modes of the shorter-chain OcA ligand appear to disrupt the coupling between carriers and the relevant phonon modes, impeding efficient thermal relaxation.

Schnitzenbaumer *et al.*[672] showed that capping CdSe QDs with chalcogenides (S^{2-}, Se^{2-}, Te^{2-}) changed hot electron cooling times through Auger recombination, with Te^{2-} showing a drastic decrease in hot carrier lifetime due to trap states that act as additional recombination channels.

In both semiconductor and metal nanoparticles, controlling hot carrier lifetime through nanoparticle size is possible. However, to achieve size dependence in semiconductors, one needs to synthesize nanoparticles with dimensions small enough to show quantum confinement effects, which is clearly not the case in metal nanoparticles, where classical size effects dominate.

5.4. Ultrafast carrier dynamics in metal/semiconductor hybrid nanostructures

Understanding ultrafast dynamics in individual systems is key to designing hybrid architectures that combine the advantages of semiconductors and plasmonic nanostructures. In metal–semiconductor hybrids, hot carriers generated *via* Landau damping near plasmonic nanoparticle surfaces can be injected into semiconductors if they possess sufficient energy to overcome Schottky barriers. Non-thermal electrons relax through electron–electron scattering (<100 fs) to reach a Fermi–Dirac distribution, then undergo electron–phonon scattering (1–10 ps) and finally transfer energy to the surroundings through phonon–phonon interactions (~100 ps). Schottky barriers help prolong hot-electron lifetimes, enabling them to participate in chemical reactions occurring on microsecond-to-second timescales.[676] Electron transfer can also occur from the semiconductor conduction band to a metal if suitable empty states exist and electronic coupling is strong.

TiO_2 is a widely studied semiconductor in such heterostructures. Upon UV excitation, broad infrared absorption arises from intraband transitions and shallow mid-gap states.[677] Furube *et al.*[669,678] demonstrated electron injection from Au nanoparticles into TiO_2 within 50 fs, indicating that injection occurs before or during electron–electron scattering in Au (Fig. 46d). Similarly, Cheng *et al.*[670] showed that electron–phonon scattering times in Ag nanowires decrease when coated with thin TiO_2 shells, reflecting ultrafast electron injection, which opens up an alternate decay channel, while thicker shells enable back-transfer and thus, slower relaxation (Fig. 46e). Graphene represents a unique case due to its zero band gap and, in nanostructured or doped forms, tunable plasmonic resonance in the visible-NIR. Ding *et al.*[679] investigated ultrafast dynamics in a graphene-Ag nanowire (AgNW) hybrid using a 400 nm pump. While isolated components showed faster decays (AgNW plasmon lifetime: 150 ± 7 fs; graphene electron–phonon interaction: 1.4–2.5 ps), the hybrid system exhibited significantly prolonged lifetimes due to hot electron transfer from Ag to graphene. In the visible region, this transfer occurred at 534 ± 108 fs, resulting in a plasmon-induced hot electron lifetime of 3.2 ± 0.8 ps. In the NIR region, dynamics were notably slower: the transfer time increased to 780 ± 92 fs due to lower kinetic energy, and the electron–phonon interaction time extended to 3.9 ± 0.9 ps, attributed to graphene's enhanced optical absorption in this range. When employed as SERS substrates for the reduction of 4-nitrobenzenethiol (4NBT) to 4,4′-dimercaptoazobenzene (DMAB), the graphene-Ag nanowire hybrid demonstrated significantly higher reaction probability and efficiency compared to isolated graphene or Ag nanowires. This superior performance is attributed to a synergistic enhancement arising from the combination of plasmonic hot-electron generation in Ag and the high carrier mobility and broadband optical absorption of graphene.

This section emphasized that the efficiency of photocatalysis is fundamentally a "race against time", where the success of a chemical transformation depends on extracting charge carriers before they relax into heat. These examples highlight the importance of understanding coherent, non-thermal, quasi-equilibrium, and isothermal regimes for optimizing charge extraction. Semiconductor excitons persist in the nanosecond-to-microsecond range, while plasmonic hot carriers exist in the femtosecond-to-picosecond domain. This temporal mismatch is both a challenge and an opportunity: by tuning plasmonic resonance and nanostructure size, high-energy carriers can be effectively injected into semiconductors, extending their useful lifetime for chemical transformations. Smaller semiconductor nanocrystals benefit from quantum confinement and phonon bottlenecks, prolonging exciton lifetimes, whereas larger metal nanocrystals reduce surface scattering to extend hot-electron lifetimes. Hybrid architectures, such as core–shell or metal-loaded semiconductor nanoparticles, provide alternative decay pathways and energy transfer mechanisms that compete with thermalization, allowing energetic carriers to drive reactions more efficiently. Optimizing such systems requires careful consideration of: (i) matching carrier lifetimes with reaction timescales, (ii) ensuring carrier energies exceed activation barriers, (iii) positioning reactive sites within carrier diffusion lengths, and (iv) maximizing interfacial charge transfer.

Ultrafast spectroscopy has transformed our understanding from viewing photocatalysis as a simple light-absorption process to recognizing it as a complex series of temporal steps where success depends on winning the race against relaxation of the excited state. The future of photocatalytic design lies not just in choosing the right materials but in tuning their temporal dynamics to create systems where quantum precision meets classical intensity, and where the excited electrons and holes can be used to drive the chemical transformations.

6. Conclusions

In conclusion, photocatalysis has emerged as a promising solution to global energy and environmental challenges, driven by rapid advancements in both plasmonic and semiconductor materials. This review has analyzed the fundamental differences and complementary features of semiconductor and plasmonic heterogeneous photocatalysts, beginning with their photoexcitation and relaxation behavior and progressing toward their distinct roles in driving light-mediated chemical transformations. Semiconductors primarily operate through band gap excitation to generate electron–hole pairs, which are harnessed for chemical transformations. In contrast, plasmonic materials leverage LSPR to produce energetic charge carriers and enhance local electric fields. These distinct light–matter interaction pathways are responsible for their differing catalytic behaviors across key reactions such as CO_2 reduction, N_2 fixation, and dry reforming of methane.

Excited-state dynamics play a central role in both systems. While semiconductor photocatalysis depends on efficient charge separation and transport, plasmonic photocatalysis capitalizes on short-lived hot carriers and photothermal effects. The ongoing debate around thermal *versus* non-thermal contributions emphasizes the complexity of plasmonic systems and the need for deeper mechanistic insights.

Throughout the review, we have stressed upon the importance of advanced characterization tools in elucidating the intricate mechanisms governing photocatalysis. These techniques are essential for mapping reaction intermediates, activation energies, and transient charge dynamics.

Looking forward, the integration of plasmonic and semiconductor functionalities offers exciting opportunities for rational catalyst design. To fully realize this potential, the field must embrace emerging computational tools like predictive modeling through machine-learning-assisted design. By establishing robust descriptors, such as d-band centers, LSPR peak positions, and interfacial charge-transfer resistance, machine learning algorithms can navigate the high-dimensional design space of hybrid catalysts. This approach allows researchers to simulate thousands of material combinations, such as complex ternary alloys or hierarchical architectures, identifying optimal configurations that would take years to discover through traditional laboratory experimentation. Simultaneously, a shift toward *in situ* and *operando* spectroscopy is essential to move beyond the "black box" understanding of the catalyst surface. Future research should prioritize multi-modal *operando* setups that combine vibrational spectroscopy with electronic probes, such as *in situ* X-ray absorption or ambient-pressure XPS. Such techniques are critical for observing the real-time reconstruction of the catalyst surface and the transient stability of active sites under high-intensity illumination.

Finally, the transition from lab-scale success to industrial application hinges on addressing scalability and the cost of noble metals. Expanding the use of earth-abundant plasmonic materials requires a focus on surface passivisation and protective encapsulation to prevent oxidative deactivation without sacrificing LSPR intensity. Beyond material innovation, the development of optimized reactor geometries is essential for maximizing photon utilization efficiency. Enhancing the light-harvesting architecture of the reactor is a critical step in translating these technologies from laboratory-scale prototypes to viable industrial-scale systems. By bridging the gap between computational prediction, rigorous *operando* mechanistic analysis, and the development of cost-effective materials, the field of photocatalysis is poised to move toward a new era of efficient and sustainable light-driven chemistry.

Author contributions

V. P. proposed the idea and guided the project. R. V. wrote the initial draft assisted by, V. P., G. S., R. B., C. S., and S. S. R. V. and V. P. wrote the final article.

Conflicts of interest

The authors declare no competing interests.

Data availability

No primary research results, software or code have been included, and no new data were generated or analyzed as part of this review.

Acknowledgements

We acknowledge the funding support of the Department of Atomic Energy TIFR-RTI 4015 and Anusandhan National Research Foundation (ANRF). We acknowledge the use of ChatGPT (OpenAI) for refining the English language and grammar in the preparation of this manuscript.

References

1 S. A. Rawool, K. K. Yadav and V. Polshettiwar, Defective TiO_2 for Photocatalytic CO_2 Conversion to Fuels and Chemicals, *Chem. Sci.*, 2021, **12**, 4267–4299.
2 Ž. Kovačič, B. Likozar and M. Huš, Photocatalytic CO_2 Reduction: A Review of AB Initio Mechanism, Kinetics, and Multiscale Modeling Simulations, *ACS Catal.*, 2020, **10**, 14984–15007.
3 P. Melchiorre, Introduction: Photochemical Catalytic Processes, *Chem. Rev.*, 2022, **122**, 1483–1484.
4 L. Candish, K. D. Collins, G. C. Cook, J. J. Douglas, A. Gómez-Suárez, A. Jolit and S. Keess, Photocatalysis in the Life Science Industry, *Chem. Rev.*, 2021, **122**, 2907–2980.
5 D.-E. Lee, M.-K. Kim, M. Danish and W.-K. Jo, State-of-the-Art Review on Photocatalysis for Efficient Wastewater Treatment: Attractive Approach in Photocatalyst Design and Parameters Affecting the Photocatalytic Degradation, *Catal. Commun.*, 2023, **183**, 106764.
6 C. Xu, P. R. Anusuyadevi, C. Aymonier, R. Luque and S. Marre, Nanostructured Materials for Photocatalysis, *Chem. Soc. Rev.*, 2019, **48**, 3868–3902.
7 A. Fujishima and K. Honda, Electrochemical Photolysis of Water at a Semiconductor Electrode, *Nature*, 1972, **238**, 37–38.
8 A. V. Akimov, A. J. Neukirch and O. V. Prezhdo, Theoretical Insights into Photoinduced Charge Transfer and Catalysis at Oxide Interfaces, *Chem. Rev.*, 2013, **113**, 4496–4565.
9 O. P. Dimitriev, Dynamics of Excitons in Conjugated Molecules and Organic Semiconductor Systems, *Chem. Rev.*, 2022, **122**, 8487–8593.
10 Q. Li, K. Wu, H. Zhu, Y. Yang, S. He and T. Lian, Charge Transfer from Quantum-Confined 0D, 1D, and 2D Nanocrystals, *Chem. Rev.*, 2024, **124**, 5695–5763.
11 S. Bai, J. Jiang, Q. Zhang and Y. Xiong, Steering Charge Kinetics in Photocatalysis: Intersection of Materials Syntheses, Characterization Techniques and Theoretical Simulations, *Chem. Soc. Rev.*, 2015, **44**, 2893–2939.
12 F. P. G. De Arquer, D. V. Talapin, V. I. Klimov, Y. Arakawa, M. Bayer and E. H. Sargent, Semiconductor Quantum Dots: Technological Progress and Future Challenges, *Science*, 2021, **373**, eaaz8541.
13 C. S. Ponseca, P. Chábera, J. Uhlig, P. Persson and V. Sundström, Ultrafast Electron Dynamics in Solar Energy Conversion, *Chem. Rev.*, 2017, **117**, 10940–11024.
14 A. Balapure, J. R. Dutta and R. Ganesan, Recent Advances in Semiconductor Heterojunctions: A Detailed Review of The Fundamentals of Photocatalysis, Charge Transfer

Mechanism and Materials, *RSC Appl. Interfaces*, 2024, **1**, 43–69.
15 T. Hisatomi, J. Kubota and K. Domen, Recent Advances in Semiconductors for Photocatalytic and Photoelectrochemical Water Splitting, *Chem. Soc. Rev.*, 2014, **43**, 7520–7535.
16 Z. Zhang and J. T. Yates, Band Bending in Semiconductors: Chemical and Physical Consequences at Surfaces and Interfaces, *Chem. Rev.*, 2012, **112**, 5520–5551.
17 M. A. Fox and M. T. Dulay, Heterogeneous Photocatalysis, *Chem. Rev.*, 1993, **93**, 341–357.
18 M. R. Hoffmann, S. T. Martin, W. Choi and D. W. Bahnemann, Environmental Applications of Semiconductor Photocatalysis, *Chem. Rev.*, 1995, **95**, 69–96.
19 Z. Ren, Z. Chen, B. Gao and Q. Xu, Band Gap Tuning via Supercritical CO_2-Induced Exciton Effect in $BiFeO_3$ for Photocatalytic CO_2 Reduction, *Nano Lett.*, 2025, **25**, 8043–8048.
20 J. Tang, J. Pang, X. Lv and X. Wang, Photocatalytic CO_2 Reduction with 100% CO Selectivity Using In_2O_3/CuO/g-C_3N_4 Ternary Composites, *ACS Appl. Energy Mater.*, 2025, **8**, 9683–9690.
21 A. Kudo and Y. Miseki, Heterogeneous Photocatalyst Materials for Water Splitting, *Chem. Soc. Rev.*, 2008, **38**, 253–278.
22 J. Schneider, M. Matsuoka, M. Takeuchi, J. Zhang, Y. Horiuchi, M. Anpo and D. W. Bahnemann, Understanding TiO_2 Photocatalysis: Mechanisms and materials, *Chem. Rev.*, 2014, **114**, 9919–9986.
23 M. G. Walter, E. L. Warren, J. R. McKone, S. W. Boettcher, Q. Mi, E. A. Santori and N. S. Lewis, Solar Water Splitting Cells, *Chem. Rev.*, 2010, **110**, 6446–6473.
24 A. L. Linsebigler, G. Lu and J. T. Yates, Photocatalysis on TiO_2 Surfaces: Principles, Mechanisms, and Selected Results, *Chem. Rev.*, 1995, **95**, 735–758.
25 Y. Wang, X. Cheng, N. Ma, W. Cheng, P. Zhang, F. Luo, W. Shi, S. Yao, T. Lu and Z. Zhang, In Situ Growth of Metal-Organic Layer on Polyoxometalate-etching Cu_2O to Boost CO_2 Reduction with High Stability, *Angew. Chem., Int. Ed.*, 2025, **64**, e202423204.
26 S. M. Sze and K. K. Ng, *Physics of Semiconductor Devices*, Wiley, 1st edn, 2006.
27 V. M. Huxter, L. Huang, A. Wolcott, J. Z. Zhang, R. J. Saykally and R. A. Mathies, Hot Carrier Dynamics in Semiconductor Quantum Dots, *Acc. Chem. Res.*, 2013, **46**, 2205–2213.
28 M. C. Beard, J. M. Luther and A. J. Nozik, The Promise and Challenge of Nanostructured Solar Cells, *Nat. Nanotechnol.*, 2014, **9**, 951–954.
29 X. Xuanwen, S. Wang, P. Wu, P. Dong, R. Jiang and Z. Wang, Photocatalytic Conversion of CO_2 by H_2O as an Electron Donor over $NaTaO_3$ with Controlled Morphologies Using a Series of Cocatalysts, *Chem.–Asian J.*, 2025, **20**, e2024016622025.
30 E. H. Sargent, Colloidal Quantum Dot Solar Cells, *Nat. Photon.*, 2012, **6**, 133–135.
31 X.-B. Li, C.-H. Tung and L.-Z. Wu, Semiconducting Quantum Dots for Artificial Photosynthesis, *Nat. Rev. Chem*, 2018, **2**, 160–173.
32 X.-X. Ding, X.-Y. Tong, Y. Lu, W.-K. Yan, Z.-G. Jiang and C.-H. Zhan, Silver-Polyoxometalates Schottky Junction: Charge Manipulation and Photocatalysis, *Inorg. Chem.*, 2025, **64**, 18960–18967.
33 S. T. Gebre, L. Martinez-Gomez, C. J. Miller, C. P. Kubiak, R. F. Ribeiro and T. Lian, Fano Resonance in CO_2 Reduction Catalyst Functionalized Quantum Dots, *J. Am. Chem. Soc.*, 2025, **147**, 10966–10973.
34 R. Ma, T. Wang, B. Qian, Z. Xia, S. Chen, W. Shi, Q. Yang, G. Xie and S. Chen, Ultrathin Hf-MOF with Dinitrogen Chelating Sites Stabilizing and Inducing Generation of Single-Rod $Cs_3Bi_2Br_9$ Nanocrystals for Efficient Photocatalytic CO_2 Reduction, *J. Am. Chem. Soc.*, 2025, **147**, 32625–32639.
35 Y. Zhang, Z. Mu, C. Zhou, H. Abdelsalam, X. Zhou, L. Shi, Z. Chen, Y. Liang, Z. Wang and Q. Zhang, Synergistic Surface Charge Channel and Oxygen Vacancy Engineering in Sillén–Aurivillius $Bi_7Fe_2Ti_2O_{17}Cl$ Oxyhalides Using In Situ Ag Clusters for Boosting Photocatalytic Activity, *J. Mater. Chem. A*, 2025, **13**, 7989–7998.
36 H. Luo, X. Lu, Y. Cao, Z. Lyu, S. Ding, Y. Lin, Y. Zhou, W. Zhu and Y. Wang, Boosted CO_2 Photoreduction Performance by CdSe Nanoplatelets via Se Vacancy Engineering, *Adv. Sci.*, 2025, **12**, 2413684.
37 Q. Mo, R. Xiong, B. Ning, P. Su, Q. Chen, J. Dong, B. Sa, J. Zheng, Y. Wu and F. Xiao, Maneuvering Charge Transport via Insulating Polymer Interface for Steering Photoredox Catalysis, *Adv. Sci.*, 2025, **12**, e07670.
38 X. Li, L. Cheng, R. Hu, Q. Wu, P. Liang, S. Qin, Z. Yang, B. Yang, J. Zou, T. Jia, Z. Sun and D. Feng, Copper Doping Enables Superior Charge Separation for Enhanced Spin Coherence and CO_2 Photoreduction in $CsPbBr_3$ Quantum Dots, *J. Phys. Chem. Lett.*, 2025, **16**, 10363–10370.
39 Q. Li, C. Lu, J. D. Karin, Y. Zhang, C. Ling, X. Zhang, Z. Zhou, J. Wang and O. V. Prezhdo, Dual-Defect Donor-Acceptor Pairing in Metal Oxide Semiconductors for Enhanced CO_2 Photoreduction, *Nano Lett.*, 2025, **25**, 16507–16514.
40 J. M. Pietryga, Y.-S. Park, J. Lim, A. F. Fidler, W. K. Bae, S. Brovelli and V. I. Klimov, Spectroscopic and Device Aspects of Nanocrystal Quantum Dots, *Chem. Rev.*, 2016, **116**, 10513–10622.
41 N. Zhang, Y. Wang, Z. Xing, Z. Li and W. Zhou, Carbon Doping and Oxygen Vacancy-Tungsten Trioxide/Cu_3SnS_4 S-Scheme Heterojunctions for Boosting Visible-Light-Driven Photocatalytic Performance, *ACS Appl. Mater. Interfaces*, 2025, **17**, 18296–18306.
42 Y. Nosaka and A. Y. Nosaka, Generation and Detection of Reactive Oxygen Species in Photocatalysis, *Chem. Rev.*, 2017, **117**, 11302–11336.
43 W.-J. Ong, L.-L. Tan, Y. H. Ng, S.-T. Yong and S.-P. Chai, Graphitic Carbon Nitride (G-C_3N_4)-Based Photocatalysts for Artificial Photosynthesis and Environmental

Remediation: Are We a Step Closer to Achieving Sustainability?, *Chem. Rev.*, 2016, **116**, 7159–7329.
44 H. Wang, L. Zhang, Z. Chen, J. Hu, S. Li, Z. Wang, J. Liu and X. Wang, Semiconductor Heterojunction Photocatalysts: Design, Construction, and Photocatalytic Performances, *Chem. Soc. Rev.*, 2014, **43**, 5234.
45 H. Mai, D. Chen, Y. Tachibana, H. Suzuki, R. Abe and R. A. Caruso, Developing Sustainable, High-Performance Perovskites in Photocatalysis: Design Strategies and Applications, *Chem. Soc. Rev.*, 2021, **50**, 13692–13729.
46 R. Woods-Robinson, Y. Han, H. Zhang, T. Ablekim, I. Khan, K. A. Persson and A. Zakutayev, Wide Band Gap Chalcogenide Semiconductors, *Chem. Rev.*, 2020, **120**, 4007–4055.
47 A. Hagfeldt and M. Graetzel, Light-Induced Redox Reactions in Nanocrystalline Systems, *Chem. Rev.*, 1995, **95**, 49–68.
48 Y. H. Zhang, G. H. Wu, F. Liu, C. Ding, Z. G. Zou and Q. Shen, Photoexcited Carrier Dynamics in Colloidal Quantum Dot Solar Cells: Insights into Individual Quantum Dots, Quantum Dot Solid Films and Devices, *Chem. Soc. Rev.*, 2020, **49**, 49–84.
49 R. D. Harris, S. Bettis Homan, M. Kodaimati, C. He, A. B. Nepomnyashchii, N. K. Swenson, S. Lian, R. Calzada and E. A. Weiss, Electronic Processes within Quantum Dot-Molecule Complexes, *Chem. Rev.*, 2016, **116**, 12865–12919.
50 H. Zhu, Y. Yang, K. Wu and T. Lian, Charge Transfer Dynamics from Photoexcited Semiconductor Quantum Dots, *Annu. Rev. Phys. Chem.*, 2016, **67**, 259–281.
51 J. K. Utterback, J. L. Ruzicka, H. R. Keller, L. M. Pellows and G. Dukovic, Electron Transfer from Semiconductor Nanocrystals to Redox Enzymes, *Annu. Rev. Phys. Chem.*, 2020, **71**, 335–359.
52 K. Wu and T. Lian, Quantum Confined Colloidal Nanorod Heterostructures for Solar-to-Fuel Conversion, *Chem. Soc. Rev.*, 2016, **45**, 3781–3810.
53 L. Yu, Q. Wang, C. Zhuang, J.-D. Huang, Y. Zhu, X. Jing, Y. Guo, Y.-X. Tong and Z. Zhang, Periodic Frustrated Lewis Pairs on Bimetallic Oxide Semiconductors for CO_2 Adsorption and Photocatalytic Conversion, *ACS Nano*, 2025, **19**, 7239–7252.
54 D. M. Arias-Rotondo and J. K. McCusker, The Photophysics of Photoredox Catalysis: A Roadmap for Catalyst Design, *Chem. Soc. Rev.*, 2016, **45**, 5803–5820.
55 K.-Y. Hsiao, F.-Y. Liu, C.-C. Chen and I.-C. Chen, Probing Photocatalytic Reduction Pathways of CO_2 by Catalyst $PbBiO_2Br$ Using In-Situ Raman Spectroscopy, *ACS Catal.*, 2025, **15**, 3153–3161.
56 P. Liu, J.-R. Chen, F. Du, L. Duan, W. Luo, G. Chen, X. Liu, R. Ma, H. Li, T.-S. Chan, M. Liu and N. Zhang, Interfacial Cation-Driven Bond-Length Engineering for Selective CO_2 Photoreduction to Syngas, *ACS Catal.*, 2025, **15**, 20899–20908.
57 Y. Yan, R. W. Crisp, J. Gu, B. D. Chernomordik, G. F. Pach, A. R. Marshall, J. A. Turner and M. C. Beard, Multiple Exciton Generation for Photoelectronchemical Hydrogen Evolution Reactions with Quantum Yields Exceeding 100%, *Nat. Energy*, 2017, **2**, 17052.
58 M. Zhou, K. Zhang, Y. Ouyang, K. Wang, Y. Zhang, X. Chen, J. Zhao, Q. Wang, H.-M. Shen, Y.-F. Yang, J. Xia, H. Li and Y. She, Substituent Polarity-Regulated Interfacial Polarization in Bismuth Oxyhalide/Metalloporphyrin Composites for Enhanced Charge Transfer and CO_2 Photoreduction, *ACS Catal.*, 2026, **16**, 646–657.
59 G. Dos Santos, L. Tian, R. Gonçalves, H. García and L. Rossi, Boosting CO_2 Photoreduction Efficiency of Carbon Nitride via S-scheme g-C_3N_4/Fe_2TiO_5 Heterojunction, *Adv. Funct. Mater.*, 2025, **35**, 2422055.
60 S. H. Putwa, S. A. Martell, B. Reis, S. Schwarz and M. Dasog, Photocatalytic Versus Stoichiometric Hydrogen Generation Using Mesoporous Silicon Catalysts: The Complex Role of Sacrificial Reagents, *Adv. Funct. Mater.*, 2025, 2507914.
61 R. Yalavarthi, S. B. Mishra, O. Henrotte and E. Cortes, Defects Dynamic in Photo-Excited CeO_2 and Their Influence on CO_2 Photoreduction, *Adv. Funct. Mater.*, 2025, e13933.
62 A. M. Smith, A. M. Mohs and S. Nie, Tuning the Optical and Electronic Properties of Colloidal Nanocrystals by Lattice Strain, *Nat. Nanotechnol.*, 2009, **4**, 56–63.
63 J. Wang, T. Ding, K. Gao, L. Wang, P. Zhou and K. Wu, Marcus Inverted Region of Charge Transfer from Low-Dimensional Semiconductor Materials, *Nat. Commun.*, 2021, **12**, 6333.
64 G. Grimaldi, R. W. Crisp, S. ten Brinck, F. Zapata, M. van Ouwendorp, N. Renaud, N. Kirkwood, W. H. Evers, S. Kinge, I. Infante, *et al.*, Hot-electron Transfer in Quantum-Dot Heterojunction Films, *Nat. Commun.*, 2018, **9**, 2310.
65 M. Li, S. Bhaumik, T. W. Goh, M. S. Kumar, N. Yantara, M. Grätzel, S. Mhaisalkar, N. Mathews and T. C. Sum, Slow Cooling and Highly Efficient Extraction of Hot Carriers in Colloidal Perovskite Nanocrystals, *Nat. Commun.*, 2017, **8**, 14350.
66 J. Q. Grim, S. Christodoulou, F. Di Stasio, R. Krahne, R. Cingolani, L. Manna and I. Moreels, Continuous-Wave Biexciton Lasing at Room Temperature using Solution-Processed Quantum Wells, *Nat. Nanotechnol.*, 2014, **9**, 891–895.
67 J. J. H. Pijpers, R. Ulbricht, K. J. Tielrooij, A. Osherov, Y. Golan, C. Delerue, G. Allan and M. Bonn, Assessment of Carrier Multiplication Efficiency in Bulk PbSe and PbS, *Nat. Phys.*, 2009, **5**, 811–814.
68 C. M. Cirloganu, L. A. Padilha, Q. Lin, N. S. Makarov, K. A. Velizhanin, H. Luo, I. Robel, J. M. Pietryga and V. I. Klimov, Enhanced Carrier Multiplication in Engineered Quasi-Type-II Quantum Dots, *Nat. Commun.*, 2014, **5**, 4148.
69 M. Aerts, T. Bielewicz, C. Klinke, F. C. Grozema, A. J. Houtepen, J. M. Schins and L. D. A. Siebbeles, Highly Efficient Carrier Multiplication in PbS Nanosheets, *Nat. Commun.*, 2014, **5**, 3789.
70 Z. Li, X. Xu, R. Ma, Z. Xie and Q. Kuang, Synergistic Bulk-Surface Engineering of Ferroelectric $PbTiO_3$: Polarization

Amplification and Surface Carrier Confinement for Efficient Photo-Thermal Coupled Catalytic CO_2-to-Fuel Conversion, *Adv. Funct. Mater.*, 2025, e22013.

71 D. Zhu, L. Zhang, R. E. Ruther and R. J. Hamers, Photoilluminated Diamond as a Solid-State Source of Solvated Electrons in Water for Nitrogen Reduction, *Nat. Mater.*, 2013, **12**, 836–841.

72 T. He, Y. Zhao, D. Benetti, B. Moss, L. Tian, S. Selim, R. Li, F. Fan, Q. Li, X. Wang, C. Li and J. R. Durrant, Facet-Engineered $BiVO_4$ Photocatalysts for Water Oxidation: Lifetime Gain Versus Energetic Loss, *J. Am. Chem. Soc.*, 2024, **146**, 27080–27089.

73 T. Simon, N. Bouchonville, M. J. Berr, A. Vaneski, A. Adrović, D. Volbers, R. Wyrwich, M. Döblinger, A. S. Susha, A. L. Rogach, *et al.*, Redox Shuttle Mechanism Enhances Photocatalytic H_2 Generation on Ni-Decorated CdS Nanorods, *Nat. Mater.*, 2014, **13**, 1013–1018.

74 D. W. Wakerley, M. F. Kuehnel, K. L. Orchard, K. H. Ly, T. E. Rosser and E. Reisner, Solar-Driven Reforming of Lignocellulose to H_2 with a CdS/CdOx Photocatalyst, *Nat. Energy*, 2017, **2**, 17021.

75 X. Luo, Y. Han, Z. Chen, Y. Li, G. Liang, X. Liu, T. Ding, C. Nie, M. Wang, F. N. Castellano and K. Wu, Mechanisms of Triplet Energy Transfer Across the Inorganic Nanocrystal/Organic Molecule Interface, *Nat. Commun.*, 2020, **11**, 28.

76 Y. Jiang, C. Wang, C. R. Rogers, M. S. Kodaimati and E. A. Weiss, Regio- and diastereoselective Intermolecular [2 + 2] Cycloadditions Photocatalysed By Quantum Dots, *Nat. Chem.*, 2019, **11**, 1034–1040.

77 W. Liang, C. Nie, J. Du, Y. Han, G. Zhao, F. Yang, G. Liang and K. Wu, Near-Infrared Photon Upconversion and Solar Synthesis using Lead-Free Nanocrystals, *Nat. Photonics*, 2023, **17**, 346–353.

78 M. G. Kibria, S. Zhao, F. A. Chowdhury, Q. Wang, H. P. T. Nguyen, M. L. Trudeau, H. Guo and Z. Mi, Tuning the Surface Fermi Level on p-Type Gallium Nitride Nanowires for Efficient Overall Water Splitting, *Nat. Commun.*, 2014, **5**, 3825.

79 R. Li, F. Zhang, D. Wang, J. Yang, M. Li, J. Zhu, X. Zhou, H. Han and C. Li, Spatial Separation of Photogenerated Electrons and Holes Among {010} and {110} Crystal Facets of $BiVO_4$, *Nat. Commun.*, 2013, **4**, 1432.

80 A. Paracchino, V. Laporte, K. Sivula, M. Grätzel and E. Thimsen, Highly Active Oxide Photocathode for Photoelectrochemical Water Reduction, *Nat. Mater.*, 2011, **10**, 456–461.

81 H. Tada, T. Mitsui, T. Kiyonaga, T. Akita and K. Tanaka, All-Solid-State Z-Scheme in CdS–Au–TiO_2 Three-Component Nanojunction System, *Nat. Mater.*, 2006, **5**, 782.

82 Y. Li, M. Duan, S. Wu, R. A. Taylor and S. C. E. Tsang, Harnessing Solar Energy for Ammonia Synthesis from Nitrogen and Seawater Using Oxynitride Semiconductors, *Adv. Energy Mater.*, 2025, 2406160.

83 R. Rossetti, S. M. Beck and L. E. Brus, Direct Observation of Charge-Transfer Reactions Across Semiconductor: Aqueous Solution Interfaces using Transient Raman Spectroscopy, *J. Am. Chem. Soc.*, 1984, **106**, 980–984.

84 I. Robel, M. Kuno and P. V. Kamat, Size-Dependent Electron Injection from Excited CdSe Quantum Dots into TiO_2 Nanoparticles, *J. Am. Chem. Soc.*, 2007, **129**, 4136–4137.

85 I. Robel, V. Subramanian, M. Kuno and P. V. Kamat, Quantum Dot Solar Cells. Harvesting Light Energy with CdSe Nanocrystals Molecularly Linked to Mesoscopic TiO_2 Films, *J. Am. Chem. Soc.*, 2006, **128**, 2385–2393.

86 A. Kongkanand, K. Tvrdy, K. Takechi, M. Kuno and P. V. Kamat, Quantum Dot Solar Cells. Tuning Photoresponse through Size and Shape Control of CdSe–TiO_2 Architecture, *J. Am. Chem. Soc.*, 2008, **130**, 4007–4015.

87 M. Sykora, M. A. Petruska, J. Alstrum-Acevedo, I. Bezel, T. J. Meyer and V. I. Klimov, Photoinduced Charge Transfer between CdSe Nanocrystal Quantum Dots and Ru–Polypyridine Complexes, *J. Am. Chem. Soc.*, 2006, **128**, 9984–9985.

88 J. Huang, D. Stockwell, Z. Huang, D. L. Mohler and T. Lian, Photoinduced Ultrafast Electron Transfer from CdSe Quantum Dots to Re-bipyridyl Complexes, *J. Am. Chem. Soc.*, 2008, **130**, 5632–5633.

89 A. Issac, S. Jin and T. Lian, Intermittent Electron Transfer Activity from Single CdSe/ZnS QDs, *J. Am. Chem. Soc.*, 2008, **130**, 11280–11281.

90 Q. Li, B. Guo, J. Yu, J. Ran, B. Zhang, H. Yan and J. R. Gong, Highly Efficient Visible-Light-Driven Photocatalytic Hydrogen Production of CdS-Cluster-Decorated Graphene Nanosheets, *J. Am. Chem. Soc.*, 2011, **133**, 10878–10884.

91 V. Subramanian, E. E. Wolf and P. V. Kamat, Catalysis with TiO_2/Gold Nanocomposites. Effect of Metal Particle Size on the Fermi Level Equilibration, *J. Am. Chem. Soc.*, 2004, **126**, 4943.

92 D. Yang, H. Liu, Z. Zheng, Y. Yuan, J.-C. Zhao, E. R. Waclawik, X. Ke and H. Zhu, An Efficient Photocatalyst Structure: TiO_2(B) Nanofibers with a Shell of Anatase Nanocrystals, *J. Am. Chem. Soc.*, 2009, **131**, 17885–17893.

93 T. W. Woolerton, S. Sheard, E. Reisner, E. Pierce, S. W. Ragsdale and F. A. Armstrong, Efficient and Clean Photoreduction of CO_2 to CO by Enzyme-Modified TiO_2 Nanoparticles using Visible Light, *J. Am. Chem. Soc.*, 2010, **132**, 2132–2133.

94 S. Karlsson, J. Boixel, Y. Pellegrin, E. Blart, H.-C. Becker, F. Odobel and L. Hammarström, Accumulative Charge Separation Inspired by Photosynthesis, *J. Am. Chem. Soc.*, 2010, **132**, 17977–17979.

95 Q. Xiang, J. Yu and M. Jaroniec, Synergetic Effect of MoS_2 and Graphene as Cocatalysts for Enhanced Photocatalytic H_2 Production Activity of TiO_2 Nanoparticles, *J. Am. Chem. Soc.*, 2012, **134**, 6575–6578.

96 X. Zong, H. Yan, G. Wu, G. Ma, F. Wen, L. Wang and C. Li, Enhancement of Photocatalytic H_2 Evolution on CdS by Loading MoS_2 as Cocatalyst under Visible Light Irradiation, *J. Am. Chem. Soc.*, 2008, **130**, 7176–7177.

97 T. R. Gordon, M. Cargnello, T. Paik, F. Mangolini, R. T. Weber, P. Fornasiero and C. B. Murray, Nonaqueous Synthesis of TiO_2 Nanocrystals using TiF_4 to Engineer Morphology, Oxygen Vacancy Concentration, and Photocatalytic Activity, *J. Am. Chem. Soc.*, 2012, **134**, 6751–6761.

98 M. Guan, C. Xiao, J. Zhang, S. Fan, R. An, Q. Cheng, J. Xie, M. Zhou, B. Ye and Y. Xie, Vacancy Associates Promoting Solar-Driven Photocatalytic Activity of Ultrathin Bismuth Oxychloride Nanosheets, *J. Am. Chem. Soc.*, 2013, **135**, 10411–10417.

99 J. Jiang, K. Zhao, X. Xiao and L. Zhang, Synthesis and Facet-Dependent Photoreactivity of BiOCl Single-Crystalline Nanosheets, *J. Am. Chem. Soc.*, 2012, **134**, 4473–4476.

100 M. Kong, Y. Li, X. Chen, T. Tian, P. Fang, F. Zheng and X. Zhao, Tuning the Relative Concentration Ratio of Bulk Defects to Surface Defects in TiO_2 Nanocrystals Leads to High Photocatalytic Efficiency, *J. Am. Chem. Soc.*, 2011, **133**, 16414–16417.

101 W. Zhou, W. Li, J.-Q. Wang, Y. Qu, Y. Yang, Y. Xie, K. Zhang, L. Wang, H. Fu and D. Zhao, Ordered Mesoporous Black TiO_2 as Highly efficient Hydrogen Evolution Photocatalyst, *J. Am. Chem. Soc.*, 2014, **136**, 9280–9283.

102 Y. Bi, S. Ouyang, N. Umezawa, J. Cao and J. Ye, Facet Effect of Single-Crystalline Ag_3PO_4 Sub-Microcrystals on Photocatalytic Properties, *J. Am. Chem. Soc.*, 2011, **133**, 6490–6492.

103 X. Han, Q. Kuang, M. Jin, Z. Xie and L. Zheng, Synthesis of Titania Nanosheets with a High Percentage of Exposed (001) Facets and Related Photocatalytic Properties, *J. Am. Chem. Soc.*, 2009, **131**, 3152–3153.

104 W.-N. Wang, W.-J. An, B. Ramalingam, S. Mukherjee, D. M. Niedzwiedzki, S. Gangopadhyay and P. Biswas, Size and Structure Matter: Enhanced CO_2 Photoreduction Efficiency by Size-Resolved Ultrafine Pt Nanoparticles on TiO_2 Single Crystals, *J. Am. Chem. Soc.*, 2012, **134**, 11276–11281.

105 A. Iwase, Y. H. Ng, Y. Ishiguro, A. Kudo and R. Amal, Reduced Graphene Oxide as a Solid-State Electron Mediator in Z-Scheme Photocatalytic Water Splitting under Visible Light, *J. Am. Chem. Soc.*, 2011, **133**, 11054–11057.

106 B. Liu, H. M. Chen, C. Liu, S. C. Andrews, C. Hahn and P. Yang, Large-Scale Synthesis of Transition-Metal-Doped TiO_2 Nanowires with Controllable Overpotential, *J. Am. Chem. Soc.*, 2013, **135**, 9995–9998.

107 C. Xia, W. Wu, T. Yu, X. Xie, C. Van Oversteeg, H. C. Gerritsen and C. De Mello Donega, Size-Dependent Band-Gap and Molar Absorption Coefficients of Colloidal $CuInS_2$ Quantum Dots, *ACS Nano*, 2018, **12**, 8350–8361.

108 Q. Guo, C. Xu, Z. Ren, W. Yang, Z. Ma, D. Dai, H. Fan, T. K. Minton and X. Yang, Stepwise Photocatalytic Dissociation of Methanol and Water on TiO_2(110), *J. Am. Chem. Soc.*, 2012, **134**, 13366–13373.

109 Q. Yuan, Z. Wu, Y. Jin, L. Xu, F. Xiong, Y. Ma and W. Huang, Photocatalytic Cross-Coupling of Methanol and Formaldehyde on a Rutile TiO_2(110) Surface, *J. Am. Chem. Soc.*, 2013, **135**, 5212–5219.

110 Y. Bai, W. Zhang, Z. Zhang, J. Zhou, X. Wang, C. Wang, W. Huang, J. Jiang and Y. Xiong, Controllably Interfacing with Metal: A Strategy for Enhancing CO Oxidation on Oxide Catalysts by Surface Polarization, *J. Am. Chem. Soc.*, 2014, **136**, 14650–14653.

111 G. N. Schrauzer and T. D. Guth, Photolysis of Water and Photoreduction of Nitrogen on Titanium Dioxide, *J. Am. Chem. Soc.*, 1977, **99**, 7189–7193.

112 K. Wu, Q. Li, Y. Jia, J. R. McBride, Z.-x. Xie and T. Lian, Efficient and Ultrafast Formation of Long-Lived Charge-Transfer Exciton State in Atomically Thin Cadmium Selenide/Cadmium Telluride Type-II Heteronanosheets, *ACS Nano*, 2015, **9**, 961–968.

113 Y. Yang, K. Wu, A. Shabaev, A. L. Efros, T. Lian and M. C. Beard, Direct Observation of Photoexcited Hole Localization in CdSe Nanorods, *ACS Energy Lett.*, 2016, **1**, 76–81.

114 Y.-C. Pu, H. Ma, N. Sajben, G. Xia, J. Zhang, Y. Li and J. Z. Zhang, Dependence of Interfacial Charge Transfer on Bifunctional Aromatic Molecular Linkers in CdSe Quantum Dot Sensitized TiO_2 Photoelectrodes, *ACS Appl. Electron. Mater.*, 2018, **1**, 2907–2917.

115 B.-R. Hyun, Y.-W. Zhong, A. C. Bartnik, L. Sun, H. D. Abruña, F. W. Wise, J. D. Goodreau, J. R. Matthews, T. M. Leslie and N. F. Borrelli, Electron Injection from Colloidal PbS Quantum Dots into Titanium Dioxide Nanoparticles, *ACS Nano*, 2008, **2**, 2206–2212.

116 J. H. Olshansky, A. D. Balan, T. X. Ding, X. Fu, Y. V. Lee and A. P. Alivisatos, Temperature-Dependent Hole Transfer from Photoexcited Quantum Dots to Molecular Species: Evidence for Trap-Mediated Transfer, *ACS Nano*, 2017, **11**, 8346–8355.

117 W. K. Bae, L. A. Padilha, Y.-S. Park, H. McDaniel, I. Robel, J. M. Pietryga and V. I. Klimov, Controlled Alloying of the Core−Shell Interface in CdSe/CdS Quantum Dots for Suppression of Auger Recombination, *ACS Nano*, 2013, **7**, 3411–3419.

118 E. A. Weiss, Designing the Surfaces of Semiconductor Quantum Dots for Colloidal Photocatalysis, *ACS Energy Lett.*, 2017, **2**, 1005–1013.

119 J. Zhao, M. A. Holmes and F. E. Osterloh, Quantum Confinement Controls Photocatalysis: A Free Energy Analysis for Photocatalytic Proton Reduction at CdSe Nanocrystals, *ACS Nano*, 2013, **7**, 4316–4325.

120 M. Zhukovskyi, P. Tongying, H. Yashan, Y. Wang and M. Kuno, Efficient Photocatalytic Hydrogen Generation from Ni Nanoparticle Decorated CdS Nanosheets, *ACS Catal.*, 2015, **5**, 6615–6623.

121 T. O'Connor, M. S. Panov, A. Mereshchenko, A. N. Tarnovsky, R. Lorek, D. Perera, G. Diederich, S. Lambright, P. Moroz and M. Zamkov, The Effect of the Charge-Separating Interface on Exciton Dynamics in Photocatalytic Colloidal Heteronanocrystals, *ACS Nano*, 2012, **6**, 8156–8165.

122 F. Costantino and P. V. Kamat, Do Sacrificial Donors Donate H_2 in Photocatalysis?, *ACS Energy Lett.*, 2022, **7**, 242–246.
123 A. S. Hainer, J. S. Hodgins, V. Sandre, M. Vallieres, A. E. Lanterna and J. C. Scaiano, Photocatalytic Hydrogen Generation Using Metal-Decorated TiO_2: Sacrificial Donors vs True Water Splitting, *ACS Energy Lett.*, 2018, **3**, 542–545.
124 T. Simon, M. T. Carlson, J. K. Stolarczyk and J. Feldmann, Electron Transfer Rate vs Recombination Losses in Photocatalytic H_2 Generation on Pt-Decorated CdS Nanorods, *ACS Energy Lett.*, 2016, **1**, 1137–1142.
125 A. K. Simlandy, B. Bhattacharyya, A. Pandey and S. Mukherjee, Picosecond Electron Transfer from Quantum Dots Enables a General and Efficient Aerobic Oxidation of Boronic Acids, *ACS Catal.*, 2018, **8**, 5206–5211.
126 Z. Xu, Z. Huang, C. Li, T. Huang, F. A. Evangelista, M. L. Tang and T. Lian, Tuning the Quantum Dot (QD)/Mediator Interface for Optimal Efficiency of QD-Sensitized Near-Infrared-to-Visible Photon Upconversion Systems, *ACS Appl. Mater. Interfaces*, 2020, **12**, 36558–36567.
127 H. J. Yun, H. Lee, N. D. Kim, D. M. Lee, S. Yu and J. Yi, A combination of Two Visible-Light Responsive Photocatalysts for Achieving the Z-Scheme in the Solid State, *ACS Nano*, 2011, **5**, 4084–4090.
128 L. Ye, J. Liu, C. Gong, L. Tian, T. Peng and L. Zan, Two Different Roles of Metallic Ag on Ag/AgX/BiOX (X = Cl, Br) Visible Light Photocatalysts: Surface Plasmon Resonance and Z-Scheme Bridge, *ACS Catal.*, 2012, **2**, 1677.
129 H. Zhang, X. Lv, Y. Li, Y. Wang and J. Li, P25-Graphene Composite as a High Performance Photocatalyst, *ACS Nano*, 2009, **4**, 380–386.
130 X. Chen, J. Ye, S. Ouyang, T. Kako, Z. Li and Z. Zou, Enhanced Incident Photon-to-Electron Conversion Efficiency of Tungsten Trioxide Photoanodes Based on 3D-Photonic Crystal Design, *ACS Nano*, 2011, **5**, 4310–4318.
131 L. Liu, H. Zhao, J. M. Andino and Y. Li, Photocatalytic CO_2 Reduction with H_2O on TiO_2 Nanocrystals: Comparison of Anatase, Rutile, and Brookite Polymorphs and Exploration of Surface Chemistry, *ACS Catal.*, 2012, **2**, 1817–1828.
132 Y. Tang, W. Di, X. Zhai, R. Yang and W. Qin, NIR-Responsive Photocatalytic Activity and Mechanism of $NAYF_4$:YB,Tm@TiO_2 Core–Shell nanoparticles, *ACS Catal.*, 2013, **3**, 405–412.
133 R. Singh, N. Bayal, A. Maity, D. J. Pradeep, J. Trébosc, P. K. Madhu, O. Lafon and V. Polshettiwar, Probing the Interfaces in Nanosilica-Supported TiO_2 Photocatalysts by Solid-State NMR and *in situ* FTIR, *ChemNanoMat*, 2018, **4**, 1231–1239.
134 R. Singh, R. Bapat, L. Qin, H. Feng and V. Polshettiwar, Atomic Layer Deposited (ALD) TiO_2 on Fibrous Nano-Silica (KCC-1) for Photocatalysis: Nanoparticle Formation and Size Quantization Effect, *ACS Catal.*, 2016, **6**, 2770–2784.
135 R. Rahal, A. Wankhade, D. Cha, A. Fihri, S. Ould-Chikh, U. Patil and V. Polshettiwar, Synthesis of Hierarchical Anatase TiO_2 Nanostructures with Tunable Morphology and Enhanced Photocatalytic Activity, *RSC Adv.*, 2012, **2**, 7048.
136 O. E. Semonin, J. M. Luther, S. Choi, H.-Y. Chen, J. Gao, A. J. Nozik and M. C. Beard, Peak External Photocurrent Quantum Efficiency Exceeding 100% via MEG in a Quantum Dot Solar Cell, *Science*, 2011, **334**, 1530–1533.
137 P. Y. Yu and M. Cardona, *Fundamentals of Semiconductors: Physics and Materials Properties; Graduate Texts in Physics*, Springer, Berlin, Heidelberg, 2010.
138 V. I. Klimov, A. A. Mikhailovsky, D. W. McBranch, C. A. Leatherdale and M. G. Bawendi, Quantization of multiparticle Auger rates in semiconductor quantum dots, *Science*, 2000, **287**, 1011–1013.
139 A. P. Alivisatos, Semiconductor Clusters, Nanocrystals, and Quantum Dots, *Science*, 1996, **271**, 933–937.
140 V. V. Klimov, A. A. Mikhailovsky, D. W. McBranch, C. A. Leatherdale and M. G. Bawendi, Quantization of Multiparticle Auger Rates in Semiconductor Quantum Dots, *Science*, 2000, **287**, 1011–1013.
141 N. J. Borys, M. J. Walter, J. Huang, D. V. Talapin and J. M. Lupton, The Role of Particle Morphology in Interfacial Energy Transfer in CdSe/CdS Heterostructure Nanocrystals, *Science*, 2010, **330**, 1371–1374.
142 W. A. Tisdale, K. J. Williams, B. A. Timp, D. J. Norris, E. S. Aydil and X.-Y. Zhu, Hot-Electron Transfer from Semiconductor Nanocrystals, *Science*, 2010, **328**, 1543–1547.
143 V. Sukhovatkin, S. Hinds, L. Brzozowski and E. H. Sargent, Colloidal Quantum-Dot Photodetectors Exploiting Multiexciton Generation, *Science*, 2009, **324**, 1542–1544.
144 J. B. Sambur, T. Novet and B. A. Parkinson, Multiple Exciton Collection in a Sensitized Photovoltaic System, *Science*, 2010, **330**, 63–66.
145 Z. Han, F. Qiu, R. Eisenberg, P. L. Holland and T. D. Krauss, Robust Photogeneration of H_2 in Water using Semiconductor Nanocrystals and a Nickel Catalyst, *Science*, 2012, **338**, 1321–1324.
146 K. A. Brown, D. F. Harris, M. B. Wilker, A. Rasmussen, N. Khadka, H. Hamby, S. Keable, G. Dukovic, J. W. Peters, L. C. Seefeldt and P. W. King, Light-driven dinitrogen reduction catalyzed by a CdS:nitrogenase MoFe protein biohybrid, *Science*, 2016, **352**, 448–450.
147 M. T. Pirnot, D. A. Rankic, D. B. C. Martin and D. W. C. MacMillan, Photoredox Activation for the Direct β-Arylation of Ketones and Aldehydes, *Science*, 2013, **339**, 1593–1596.
148 D. M. Schultz and T. P. Yoon, Solar Synthesis: Prospects in Visible Light Photocatalysis, *Science*, 2014, **343**, 6174.
149 X. Chen, L. Liu, P. Y. Yu and S. S. Mao, Increasing Solar Absorption for Photocatalysis with Black Hydrogenated Titanium Dioxide Nanocrystals, *Science*, 2011, **331**, 746–750.
150 R. Asahi, T. Morikawa, T. Ohwaki, K. Aoki and Y. Taga, Visible-Light Photocatalysis in Nitrogen-Doped Titanium Oxides, *Science*, 2001, **293**, 269–271.

151 P. H. C. Camargo and E. Cortés, *Plasmonic Catalysis: From Fundamentals to Applications*, Wiley-VCH, Weinheim, 2021, ISBN: 978-3-527-34750-6.
152 U. Aslam, V. G. Rao, S. Chavez and S. Linic, Catalytic Conversion of Solar to Chemical Energy on Plasmonic Metal Nanostructures, *Nat. Catal.*, 2018, **1**, 656–665.
153 E. Cortés, L. V. Besteiro, A. Alabastri, A. Baldi, G. Tagliabue, A. Demetriadou and P. Narang, Challenges in Plasmonic Catalysis, *ACS Nano*, 2020, **14**, 16202–16219.
154 G. V. Hartland, Optical Studies of Dynamics in Noble Metal Nanostructures, *Chem. Rev.*, 2011, **111**, 3858–3887.
155 R. Verma, R. Belgamwar and V. Polshettiwar, Plasmonic Photocatalysis for CO_2 Conversion to Chemicals and Fuels, *ACS Mater. Lett.*, 2021, **3**, 574–598.
156 E. Cortés, R. Grzeschik, S. A. Maier and S. Schlücker, Experimental Characterization Techniques for Plasmon-Assisted Chemistry, *Nat. Rev. Chem*, 2022, **6**, 259–274.
157 R. Verma, G. Sharma and V. Polshettiwar, The Paradox of Thermal vs. Non-Thermal Effects in Plasmonic Photocatalysis, *Nat. Commun.*, 2024, **15**, 7974.
158 A. Stefancu, N. J. Halas, P. Nordlander and E. Cortés, Electronic Excitations at the Plasmon–Molecule Interface, *Nat. Phys.*, 2024, **20**, 1065–1077.
159 N. J. Halas, S. Lal, W.-S. Chang, S. Link and P. Nordlander, Plasmons in Strongly Coupled Metallic Nanostructures, *Chem. Rev.*, 2011, **111**, 3913–3961.
160 A. Manjavacas, J. G. Liu, V. Kulkarni and P. Nordlander, Plasmon-Induced Hot Carriers in Metallic Nanoparticles, *ACS Nano*, 2014, **8**, 7630–7638.
161 S. Li, H. Huang, L. Shao and J. Wang, How to Utilize Excited Plasmon Energy Efficiently, *ACS Nano*, 2021, **15**, 10759–10768.
162 S. Ning, Y. Zhu, S. Zhang, X. Wu, X. Yin, L. Tang, R. Liu, S. Chen, L. Li, C. Yang, Z. Hu and J. Ye, Light-Driven Electronic Restructuring in RuCu Alloy Catalysts for Selective CO_2-to-Methanol Conversion, *Adv. Funct. Mater.*, 2026, **36**, e14006.
163 M. L. Brongersma, N. J. Halas and P. Nordlander, Plasmon-Induced Hot Carrier Science and Technology, *Nat. Nanotechnol.*, 2015, **10**, 25–34.
164 J. H. Hodak, I. Martini and G. V. Hartland, Spectroscopy and Dynamics of Nanometer-Sized Noble Metal Particles, *J. Phys. Chem. B*, 1998, **102**, 6958–6967.
165 S. Link and M. A. El-Sayed, Optical Properties and Ultrafast Dynamics of Metallic Nanoparticles, *Annu. Rev. Phys. Chem.*, 2003, **54**, 331–366.
166 J. A. Schuller, E. S. Barnard, W. Cai, Y. C. Jun, J. S. White and M. L. Brongersma, Plasmonics for Extreme Light Concentration and Manipulation, *Nat. Mater.*, 2010, **9**, 193–204.
167 W. L. Barnes, A. Dereux and T. W. Ebbesen, Surface Plasmon Subwavelength Optics, *Nature*, 2003, **424**, 824–830.
168 D. Tan, T. Wei, B. Xu, W. Wang, H. Li, Y. Zhou, B. Lin and G. Yang, Ag-Au Antenna-Reactor System with Enhanced Superimposed LSPR-Induced Electric Fields for Plasmon-Mediated CO_2 Photoreduction, *ACS Catal.*, 2025, **15**, 15629–15639.
169 X. Fu, Y. Zhang, S. Yang, Q. Chai, Z. Liu, H. Wang, K. Wang, Z. Zhao, N. Li, H. Huang and J. Li, Interface-Engineering-Induced Reactive Hydrogen Supply in the Dual-Plasmon Heterojunction for Efficient CO_2-to-CH_4 Photosynthesis, *ACS Catal.*, 2026, **16**, 1091–1102.
170 C. Zhan, X.-J. Chen, J. Yi, J.-F. Li, D.-Y. Wu and Z.-Q. Tian, From Plasmon-Enhanced Molecular Spectroscopy to Plasmon-Mediated Chemical Reactions, *Nat. Rev. Chem*, 2018, **2**, 216–230.
171 R. Sundararaman, P. Narang, A. S. Jermyn, W. A. Goddard III and H. A. Atwater, Theoretical Predictions for Hot-Carrier Generation from Surface Plasmon Decay, *Nat. Commun.*, 2014, **5**, 5788.
172 E. Cortés, W. Xie, J. Cambiasso, A. S. Jermyn, R. Sundararaman, P. Narang, S. Schlücker and S. A. Maier, Plasmonic Hot Electron Transport Drives Nano-Localized Chemistry, *Nat. Commun.*, 2017, **8**, 14880.
173 K. Yu, K. Feng, M. Cai, H. Li, Y. Zhou, J. Shen, S. Liu, Z. Zhu, M. Sohail, V. Tolstoy, X. An, C. Li and L. He, Nature-Inspired Nanoarray Catalyst toward Balanced Heat and Mass Transport in Photothermal Catalysis, *ACS Nano*, 2025, **19**, 18674–18685.
174 X. Li, B. Wu, X. Zhang, A. Chen, J. Wang, H. Wang, A. Ciesielski, J. Liu and J. Zhang, Plasmon Mediated Photocatalysis: Engineering Interfaces for Effective Hot Carrier Utilization, *ACS Energy Lett.*, 2025, **10**, 1347–1356.
175 G. Joshi, A. Q. Mir, A. Layek, A. Ali, S. T. Aziz, S. Khatua and A. Dutta, Plasmon-Based Small-Molecule Activation: A New Dawn in the Field of Solar-Driven Chemical Transformation, *ACS Catal.*, 2022, **12**, 1052–1067.
176 Z. Sun, S. Cheng, R. Luo, X. Jing, H. Yin, K. Liu, A. A. Wibowo, K. H. Lim, H. T. Nguyen, N. Cox, G. K. Li, W. Zhou, S. Kawi and Z. Yin, Local Electric Field Modulation of Surface Vacancies Enhances CO_2 Methanation in Pure Water, *ACS Catal.*, 2025, **15**, 2250–2261.
177 M. Cao, Y. Zhang, H. Feng, M. Liu, D. Liu and Q. Li, Synergistic Plasmonic and Molecular Engineering of Carbon Nitride: Breaking Photocatalytic Trade-Offs for Efficient Noble-Metal-Free Solar CO_2 Reduction, *Adv. Funct. Mater.*, 2025, e19444.
178 J. Liu, C. Xia, S. Zaman, Y. Su, L. Tan and S. Chen, Surface Plasmon Assisted Photoelectrochemical Carbon Dioxide Reduction: Progress and Perspectives, *J. Mater. Chem. A*, 2023, **11**, 16918–16932.
179 M. Li, Z. Han, J. Kong, Q. Hu, W. Liu, J. Xu, W. Yan, J. Hu, J. Zhu, Y. Pan, M. Zhou, Q. Chen and X. Jiao, Infrared Photothermal Catalytic Reduction of Atmospheric CO_2 Into CO with 100% Selectivity via Dual-Plasmon Resonance Conductor, *Adv. Mater.*, 2025, **37**, 2503021.
180 F. Rathmann, I. Abdelsalam, S. Wang, M. M. Kubik, S. Frindy, T. V. Alves, M. Chundak, M. Ritala, A. Reznichenko, M. Reinikainen and P. H. C. Camargo, Plasmon-Enhanced CO_2 Methanation over Au@Ru/TiO_2

via Nanoscale Control of Ru Shell Thickness, *Angew. Chem., Int. Ed.*, 2025, **64**, e18748.

181 M. Bernardi, J. Mustafa, J. B. Neaton and S. G. Louie, Theory and Computation of Hot Carriers Generated by Surface Plasmon Polaritons in Noble Metals, *Nat. Commun.*, 2015, **6**, 7044.

182 A. O. Govorov and H. Zhang, Kinetic Density Functional Theory for Plasmonic Nanostructures: Breaking of the Plasmon Peak in the Quantum Regime and Generation of Hot Electrons, *J. Phys. Chem. C*, 2015, **119**, 6181–61942.

183 E.-R. Newmeyer, J. D. North and D. F. Swearer, Hot Carrier Photochemistry on Metal Nanoparticles, *J. Appl. Phys.*, 2022, **132**, 230901.

184 L. Yuan, B. B. Bourgeois, C. C. Carlin, F. H. da Jornada and J. A. Dionne, Sustainable Chemistry with Plasmonic Photocatalysts, *Nanophotonics*, 2023, **12**, 2745–2762.

185 I. Jung, J. Kim, S. Lee, W. Park and S. Park, Multiple Stepwise Synthetic Pathways Toward Complex Plasmonic 2D and 3D Nanoframes for Generation of Electromagnetic Hot Zones in a Single Entity, *Acc. Chem. Res.*, 2023, **56**, 270–283.

186 H. Kim, H. Park, M. Kang and J. Y. Park, Plasmonic Hot Carrier-Driven Photoelectrochemical Water Splitting on Antenna–Reactor Pt/Ag/TiO_2 Schottky Nanodiodes, *J. Chem. Phys.*, 2022, **157**, 084701.

187 H. Lee, J. Park, K. Song and J. Y. Park, Surface Plasmon-Induced Hot Carriers: Generation, Detection, and Applications, *Acc. Chem. Res.*, 2022, **55**, 3727–3737.

188 Y. Liu, X. He, X. Liu, B. Li, J. Ma and P. Cheng, Light-induced Enhancement of Energetic Charge Carrier Extraction and Modulation of Local Charge Density to Impact Selectivity in Plasmonic Nanometals, *Angew. Chem., Int. Ed.*, 2025, **64**, e202422034.

189 F. Wang, Z. Lu, H. Guo, G. Zhang, Y. Li, Y. Hu, W. Jiang and G. Liu, Plasmonic Photocatalysis for CO_2 Reduction: Advances, Understanding and Possibilities, *Chem.–Eur. J.*, 2023, **29**, e202202716.

190 T. Huang, J. Han, Z. Li, Y. Hong, X. Gu, Y. Wu, Y. Zhang and S. Liu, Unraveling the Essential Role of Consecutive Protonation Steps in Photocatalytic CO_2 Reduction when using Au Nanorods in a MOF, *Angew. Chem., Int. Ed.*, 2025, **64**, e202500269.

191 J. Yang, Z. Chen, Z. Wang, Q. Qian, B. Pan, Q. Zhang, C. Xiao and Y. Xie, Plasmon-Ferroelectric Induced Multifield Coupling Effect Accelerates Charge Spatial Separation for Boosting Tandem Photoredox Catalysis, *Angew. Chem., Int. Ed.*, 2025, **64**, e202507396.

192 Y. Wang, F. Xue, W. Zhang, D. Cao, M. Zhang, Z. Li, C. Zhan, Q. Kuang and Z. Xie, Overcoming Copper Instability via Nickel Alloying for Efficient Plasmon-Catalytic CO_2 Hydrogenation, *Angew. Chem., Int. Ed.*, 2026, **65**, e21576.

193 X. Chen, Y. Su, Z. Zheng, J. Chen, T. Zhou, Z. Wei, W. Yang, Z. Deng and Y. Peng, Highly Dispersed Antenna-Single-Atom-Reactor on Metal-Organic Frameworks Support for Efficient Photocatalytic CO_2 Reduction, *Chem. Commun.*, 2025, **61**, 5790–5793.

194 R. Belgamwar, C. Singhvi, G. Sharma, V. K. Paidi, P. Glatzel, S. Yamazoe, P. Sarawade and V. Polshettiwar, Synthesis of Synergistic Catalysts: Integrating Defects, SMSI, and Plasmonic Effects for Enhanced Photocatalytic CO_2 Reduction, *Chem. Sci.*, 2025, **16**, 9766–9784.

195 J. Gargiulo, R. Berté, Y. Li, S. A. Maier and E. Cortés, From Optical to Chemical Hot Spots in Plasmonics, *Acc. Chem. Res.*, 2019, **52**, 2525–2535.

196 X. Zhang, W. Xie, Z. Wang, Y. Liu, P. Wang, H. Cheng, Y. Dai, B. Huang and Z. Zheng, Highly Thermally Stable Au-Rh NRs for Plasmon-Enhanced Photothermal Catalytic CO_2 Hydrogenation to C_2, *Energy Fuels*, 2025, **39**, 17029–17037.

197 G. C. Phan-Quang, X. Han, C. S. L. Koh, H. Y. F. Sim, C. L. Lay, S. X. Leong, Y. H. Lee, N. Pazos-Perez, R. A. Alvarez-Puebla and X. Y. Ling, Three-Dimensional Surface-Enhanced Raman Scattering Platforms: Large-Scale Plasmonic Hotspots for New Applications in Sensing, Microreaction, and Data Storage, *Acc. Chem. Res.*, 2019, **52**, 1844–1854.

198 Y. Jiang, Y. Li, G. Wang, Z. Huo, L.-H. Shao, Y. Wang, H. Dong and F.-M. Zhang, Plasmonic Bi/COF Nanoheterojunction for Enhanced Artificial Photosynthetic CO_2 Reduction, *Inorg. Chem.*, 2026, **65**, 1264–1273.

199 A. J. Offen, Z. Geng, Y. Yu and J. Liu, "A Lot's in a Name": Insights from Debates on Thermal and Nonthermal Effects in Plasmonic Catalysis, *ACS Appl. Energy Mater.*, 2023, **6**, 11762–11772.

200 V. Jain, R. K. Kashyap and P. P. Pillai, Plasmonic Photocatalysis: Activating Chemical Bonds Through Light and Plasmon, *Adv. Opt. Mater.*, 2022, **10**, 2200463.

201 A. J. Bagnall, S. Ganguli and A. Sekretareva, Hot or Not? Reassessing Mechanisms of Photocurrent Generation in Plasmon-Enhanced Electrocatalysis, *Angew. Chem., Int. Ed.*, 2024, **63**, e202314352.

202 S. Singh, G. Sharma, M. Joshi and V. Polshettiwar, Solar-Driven Upcycling of Plastic Waste Using Plasmonic Black Gold, *Chem. Sci.*, 2026, **17**, 1592–1603.

203 G. Yu, N. Li, X. Li, Y. Guo and T. Yan, Synergetic Effect of Surface Frustrated Lewis Pair and Localized Surface Plasmon Resonance on Tuning the Catalyst from Inert to Highly Reactive for Photocatalytic CO_2 Hydrogenation, *J. Mater. Chem. A*, 2025, **13**, 13843–13855.

204 M. Ahlawat, D. Mittal and V. G. Rao, Plasmon-Induced Hot-Hole Generation and Extraction at Nano-Heterointerfaces for Photocatalysis, *Commun. Mater.*, 2021, **2**, 114.

205 G. Sharma, C. Singhvi, G. Mishra, A. Nandi, G. Schuck, N. Grimm, D. Wallacher, A. Kumar, P. Nukala, S. Nath, S. Ghosh and V. Polshettiwar, Hot Electron-Driven Tandem CO_2 Reduction and Propane Dehydrogenation over Plasmonic Black Gold Nanoreactors, *Proc. Natl. Acad. Sci. U. S. A*, 2025, **122**, e2520317122.

206 K. An, B. Wu, J. Hu, X. Bai, P. Wang, Y. Fang, R. Jiang and J. Wang, Schottky-Barrier-Free Plasmonic WO_3-Based Photocatalysts for Simultaneous N_2 Fixation and H_2O_2 Generation, *Adv. Mater.*, 2026, **38**, e15476.

207 D. B. Ingram and S. Linic, Water Splitting on Composite Plasmonic-Metal/Semiconductor Photoelectrodes: Evidence for Selective Plasmon-Induced Formation of Charge Carriers Near the Semiconductor Surface, *J. Am. Chem. Soc.*, 2011, **133**, 5202–5205.

208 X. Wan, Y. Pan, Y. Xu, J. Liu, H. Chen, R. Pan, Y. Zhao, P. Su, Y. Li, X. Zhang, S. Zhang, H. Li, D. Su, Y. Weng and J. Zhang, Ultralong Lifetime of Plasmon-Excited Electrons Realized in Nonepitaxial/Epitaxial Au@CdS/$CsPbBr_3$ Triple-Heteronanocrystals, *Adv. Mater.*, 2023, **35**, 2207555.

209 K. Wang and T. He, Plasmon Photocatalytic CO_2 Reduction Reactions Over Au Particles on Various Substrates, *Nanoscale*, 2023, **15**, 12398–12405.

210 S. Yu and P. K. Jain, Plasmonic Photosynthesis of C_1–C_3 Hydrocarbons from Carbon Dioxide Assisted by an Ionic Liquid, *Nat. Commun.*, 2019, **10**, 2022.

211 Z. Lian, M. Sakamoto, H. Matsunaga, J. J. M. Vequizo, A. Yamakata, M. Haruta, H. Kurata, W. Ota, T. Sato and T. Teranishi, Near Infrared Light Induced Plasmonic Hot Hole Transfer at a Nano-Heterointerface, *Nat. Commun.*, 2018, **9**, 2314.

212 S. S. E. Collins, E. K. Searles, L. J. Tauzin, M. Lou, L. Bursi, Y. Liu, J. Song, C. Flatebo, R. Baiyasi, Y. Y. Cai, B. Foerster, T. Lian, P. Nordlander, S. Link and C. F. Landes, Plasmon Energy Transfer in Hybrid Nanoantennas, *ACS Nano*, 2021, **15**, 9522–9530.

213 X. Wan, Y. Gao, M. Eshete, M. Hu, R. Pan, H. Wang, L. Liu, J. Liu, J. Jiang, S. Brovelli and J. Zhang, Simultaneous Harnessing of Hot Electrons and Hot Holes Achieved via N-Metal-p Janus Plasmonic Heteronanocrystals, *Nano Energy*, 2022, **98**, 107217.

214 C. Zhan, B.-W. Liu, Y.-F. Huang, S. Hu, B. Ren, M. Moskovits and Z.-Q. Tian, Disentangling Charge Carrier from Photothermal Effects in Plasmonic Metal Nanostructures, *Nat. Commun.*, 2019, **10**, 2671.

215 P. Christopher, H. Xin, A. Marimuthu and S. Linic, Singular Characteristics and Unique Chemical Bond Activation Mechanisms of Photocatalytic Reactions on Plasmonic Nanostructures, *Nat. Mater.*, 2012, **11**, 1044–1050.

216 X. An, J. C. Kays, I. V. Lightcap, T. Ouyang, A. M. Dennis and B. M. Reinhard, Wavelength-Dependent Bifunctional Plasmonic Photocatalysis in Au/Chalcopyrite Hybrid Nanostructures, *ACS Nano*, 2022, **16**, 6813–6824.

217 A. Stefancu, J. Gargiulo, G. Laufersky, B. Auguié, V. Chiș, E. C. L. Ru, M. Liu, N. Leopold and E. Cortés, Interface-Dependent Selectivity in Plasmon- Driven Chemical Reactions, *ACS Nano*, 2023, **17**, 3119–3127.

218 A. G. M. da Silva, T. S. Rodrigues, V. G. Correia, T. V. Alves, R. S. Alves, R. A. Ando, F. R. Ornellas, J. L. Wang, L. H. Andrade and P. H. C. Camargo, Plasmonic Nanorattles as Next Generation Catalysts for Surface Plasmon Resonance-Mediated Oxidations Promoted by Activated Oxygen, *Angew. Chem., Int. Ed.*, 2016, **55**, 7111–7115.

219 C. Tiburski, A. Boje, S. Nilsson, Z. Say, J. Fritzsche, H. Ström, A. Hellman and C. Langhammer, Light-off in Plasmon-Mediated Photocatalysis, *ACS Nano*, 2021, **15**, 11535–11542.

220 F. D. Swearer, H. Zhao, L. Zhou, C. Zhang, H. Robatjazi, P. M. J. Martirez, M. C. Krauter, S. Yazdi, J. M. McClain, E. Ringe, A. E. Carter, P. Nordlander and J. N. Halas, Heterometallic Antenna−Reactor Complexes for Photocatalysis, *Proc. Natl. Acad. Sci. U. S. A.*, 2016, **113**, 8916–8920.

221 U. Aslam, S. Chavez and S. Linic, Controlling Energy Flow in Multimetallic Nanostructures for Plasmonic Catalysis, *Nat. Nanotechnol.*, 2017, **12**, 1000–1005.

222 D. F. Swearer, H. Robatjazi, J. M. P. Martirez, M. Zhang, L. Zhou, E. A. Carter, P. Nordlander and N. J. Halas, Plasmonic Photocatalysis of Nitrous Oxide into N_2 and O_2 Using Aluminum–Iridium Antenna–Reactor Nanoparticles, *ACS Nano*, 2019, **13**, 8076–8086.

223 L. Zhou, J. M. P. Martirez, J. Finzel, C. Zhang, D. F. Swearer, S. Tian, H. Robatjazi, M. Lou, L. Dong, L. Henderson, P. Christopher, E. A. Carter, P. Nordlander and N. J. Halas, Light-Driven Methane Dry Reforming with Single Atomic Site Antenna-Reactor Plasmonic Photocatalysts, *Nat. Energy*, 2020, **5**, 61–70.

224 P. D. Dongare, Y. Zhao, D. Renard, J. Yang, O. Neumann, J. Metz, L. Yuan, A. Alabastri, P. Nordlander and N. J. Halas, A 3D Plasmonic Antenna-Reactor for Nanoscale Thermal Hotspots and Gradients, *ACS Nano*, 2021, **15**, 8761–8769.

225 H. Robatjazi, J. L. Bao, M. Zhang, L. Zhou, P. Christopher, E. A. Carter, P. Nordlander and N. J. Halas, Plasmon-Driven Carbon–Fluorine ($C(sp^3)$–F) Bond Activation with Mechanistic Insights into Hot-Carrier-Mediated Pathways, *Nat. Catal.*, 2020, **3**, 564–573.

226 M. Dhiman, A. Maity, A. Das, R. Belgamwar, B. Chalke, Y. Lee, K. Sim, J.-M. Nam and V. Polshettiwar, Plasmonic Colloidosomes of Black Gold for Solar Energy Harvesting and Hotspots Directed Catalysis for CO_2 to Fuel Conversion, *Chem. Sci.*, 2019, **10**, 6594–6603.

227 S. Mukherjee, F. Libisch, N. Large, O. Neumann, V. L. Brown, J. Cheng, L. J. Lassiter, A. E. Carter, P. Nordlander and J. N. Halas, Hot Electrons Do the Impossible: Plasmon-Induced Dissociation of H_2 on Au, *Nano Lett.*, 2013, **13**, 240–247.

228 S. He, J. Huang, J. L. Goodsell, A. Angerhofer and W. D. Wei, Plasmonic Nickel–TiO_2 Heterostructures for Visible-Light-Driven Photochemical Reactions, *Angew. Chem., Int. Ed.*, 2019, **58**, 6038–6041.

229 P. Han, T. Tana, Q. Xiao, S. Sarina, E. R. Waclawik, D. E. Gomez and H. Zhu, Promoting Ni(II) Catalysis with Plasmonic Antennas, *Chem*, 2019, **5**, 2879–2899.

230 S. Linic, S. Chavez and R. Elias, Flow and Extraction of Energy and Charge Carriers in Hybrid Plasmonic Nanostructures, *Nat. Mater.*, 2021, **20**, 916–924.

231 P. V. Kumar, T. P. Rossi, M. Kuisma, P. Erhart and D. J. Norris, Direct Hot-Carrier Transfer in Plasmonic Catalysis, *Faraday Discuss.*, 2019, **214**, 189–197.

232 Y. Kim, J. G. Smith and P. K. Jain, Harvesting Multiple Electron–Hole Pairs Generated Through Plasmonic

Excitation of Au Nanoparticles, *Nat. Chem.*, 2018, **10**, 763–769.

233 L. Zhou, D. F. Swearer, C. Zhang, H. Robatjazi, H. Zhao, L. Henderson, L. Dong, P. Christopher, E. A. Carter, P. Nordlander and N. J. Halas, Quantifying Hot Carrier and Thermal Contributions in Plasmonic Photocatalysis, *Science*, 2018, **362**, 69–72.

234 J. Zhao, S. C. Nguyen, R. Ye, B. Ye, H. Weller, G. A. Somorjai, A. P. Alivisatos and F. D. Toste, A Comparison of Photocatalytic Activities of Gold Nanoparticles Following Plasmonic and Interband Excitation and a Strategy for Harnessing Interband Hot Carriers for Solution Phase Photocatalysis, *ACS Cent. Sci.*, 2017, **3**, 482–488.

235 G. Tagliabue, J. S. DuChene, M. Abdellah, A. Habib, D. J. Gosztola, Y. Hattori, W.-H. Cheng, K. Zheng, S. E. Canton, R. Sundararaman, J. Sá and H. A. Atwater, Ultrafast Hot-Hole Injection Modifies Hot-Electron Dynamics in Au/P-GaN Heterostructures, *Nat. Mater.*, 2020, **19**, 1312–1318.

236 P. M. Molina, N. Meulendijks, M. Xu, M. A. Verheijen, T. den Hartog, P. Buskens and F. Sastre, Low Temperature Sunlight-Powered Reduction of CO_2 to CO using a Plasmonic Au/TiO_2 Nanocatalyst, *ChemCatChem*, 2021, **13**, 4507–4513.

237 H. Zhang, T. Wang, J. Wang, H. Liu, T. D. Dao, M. Li, G. Liu, X. Meng, K. Chang, L. Shi, T. Nagao and J. Ye, Surface-Plasmon-Enhanced Photodriven CO_2 Reduction Catalyzed by Metal–Organic-Framework-Derived Iron Nanoparticles Encapsulated by Ultrathin Carbon Layers, *Adv. Mater.*, 2016, **28**, 3703–3710.

238 H. Robatjazi, H. Zhao, D. F. Swearer, N. J. Hogan, L. Zhou, A. Alabastri, M. J. McClain, P. Nordlander and N. J. Halas, Plasmon-Induced Selective Carbon Dioxide Conversion on Earth-Abundant Aluminum-Cuprous Oxide Antenna-Reactor Nanoparticles, *Nat. Commun.*, 2017, **8**, 27.

239 W. Li, F. Yue, M. Shi, L. Zhang, S. Zhang, Y. Xie, F. Liu, W. Zhou, H. Chao, S. Tang, N. Liu and H. Zhang, Thermally Assisted Photocatalytic Industrial Flue Gas CO_2 Conversion: 100% Selective CO Production via Synergistic Adsorption-Conversion in NH_2-MXene-MOF Hierarchical Interfaces, *J. Mater. Chem. A*, 2025, **13**, 33233–33244.

240 S. Yu, J. A. Wilson, J. Heo and K. P. Jain, Plasmonic Control of Multi-Electron Transfer and C–C Coupling in Visible-Light-Driven CO_2 Reduction on Au Nanoparticles, *Nano Lett.*, 2018, **18**, 2189–21942.

241 S. Yu and K. P. Jain, Selective Branching of Plasmonic Photosynthesis into Hydrocarbon Production and Hydrogen Generation, *ACS Energy Lett.*, 2019, **4**, 2295–2300.

242 X. Cui, J. Wang, B. Liu, S. Ling, R. Long and Y. Xiong, Turning Au Nanoclusters Catalytically Active for Visible-Light-Driven CO_2 Reduction through Bridging Ligands, *J. Am. Chem. Soc.*, 2018, **140**, 16514–16520.

243 G. Kumari, X. Zhang, D. Devasia, J. Heo and K. P. Jain, Watching Visible Light-Driven CO_2 Reduction on a Plasmonic Nanoparticle Catalyst, *ACS Nano*, 2018, **12**, 8330–8340.

244 S. Mukherjee, L. Zhou, A. M. Goodman, N. Large, C. Ayala-Orozco, Y. Zhang, P. Nordlander and N. J. Halas, Hot-Electron-Induced Dissociation of H_2 on Gold Nanoparticles Supported on SiO_2, *J. Am. Chem. Soc.*, 2014, **136**, 64–67.

245 P. Christopher, H. Xin and S. Linic, Visible-Light-Enhanced Catalytic Oxidation Reactions on Plasmonic Silver Nanostructures, *Nat. Chem.*, 2011, **3**, 467–472.

246 S. Singh, R. Verma, N. Kaul, J. Sa, A. Punjal, S. Prabhu and V. Polshettiwar, Surface Plasmon-Enhanced Photo-Driven CO_2 Hydrogenation by Hydroxy-Terminated Nickel Nitride Nanosheets, *Nat. Commun.*, 2023, **14**, 2551.

247 T. Olsen and J. Schiotz, Origin of Power Laws for Reactions at Metal Surfaces Mediated by Hot Electrons, *Phys. Rev. Lett.*, 2009, **103**, 238301.

248 R. Verma, R. Belgamwar, P. Chatterjee, R. B. Vadell, J. Sa and V. Polshettiwar, Nickel-Laden Dendritic Plasmonic Colloidosomes of Black Gold: Forced Plasmon Mediated Photocatalytic CO_2 Hydrogenation, *ACS Nano*, 2023, **17**, 4526–4538.

249 E. L. Keller and R. R. Frontierra, Ultrafast Nanoscale Raman Thermometry Proves Heating is not a Primary Mechanism for Plasmon-Driven Photocatalysis, *ACS Nano*, 2018, **12**, 5848–5855.

250 J. Wohlwend, O. Wipf, D. Kiwic, S. Käch, B. Mächler, G. Haberfehlner, R. Spolenak and H. Galinski, CO_2 Conversion in Cu-Pd Based Disordered Network Metamaterials with Ultrasmall Mode Volumes, *Nano Lett.*, 2025, **25**, 3740–3746.

251 Y. Negrín-Montecelo, A. Sousa-Castillo, N. Cardeñoso-Garrido, L. Guillade, L. V. Besteiro, M. Vázquez-González, R. A. Alvarez-Puebla, B. Puértolas and M. A. Correa-Duarte, Plasmon-Driven Nitrogen Photoreduction to Ammonia Using Silica-Encapsulated Au Nanostar/TiO_2 Nanohybrids, *Adv. Energy Mater.*, 2025, **15**, 2501526.

252 P. Li, S. H. C. Askes, E. d. P. Rosendo, F. Ariese, C. Ramanan, E. von Hauff and A. N. Baldi, Nanoscale Thermometry of Plasmonic Structures via Raman Shifts in Copper Phthalocyanine, *J. Phys. Chem. C*, 2023, **127**, 9690–9698.

253 H. Shin, J. Jeong, Y. Nam, K. S. Lee, G. J. Yeon, H. Lee, S. Y. Lee, S. Park, H. Park, J. Y. Lee and Z. H. Kim, Vibrationally Hot Reactants in a Plasmon-Assisted Chemical Reaction, *J. Am. Chem. Soc.*, 2023, **145**, 12264–12274.

254 R. Kamarudheen, G. J. Aalbers, R. F. Hamans, L. L. Kamp and A. Baldi, Distinguishing Among All Possible Activation Mechanisms of a Plasmon-Driven Chemical Reaction, *ACS Energy Lett.*, 2020, **5**, 2605–2613.

255 Q. Zhang, Y. Zhou, X. Fu, E. Villarreal, L. Sun, S. Zou and H. Wang, Photothermal Effect, Local Field Dependence, And Charge Carrier Relaying Species in Plasmon-Driven Photocatalysis: A Case Study of Aerobic Nitrothiophenol Coupling Reaction, *J. Phys. Chem. C*, 2019, **123**, 26695–26704.

256 P. Bainova, J. P. Joly, M. Urbanova, D. Votkina, M. Erzina, B. Vokata, A. Trelin, P. Fitl, G. Audran, N. Vanthuyne,

J. Vinklarek, V. Svorcik, P. Postnikov, S. R. A. Marque and O. Lyutakov, Plasmon-Assisted Chemistry using Chiral Gold Helicoids: Toward Asymmetric Organic Catalysis, *ACS Catal.*, 2023, **13**, 12859–12867.

257 Z. Y. Li, R. Devasenathipathy, J. Wang, L. Y. Yu, H. Sheng, Y. Zhu, H. Li, H. Uji-i, X. Huang and G. Lu, Direct Observation of the Plasmon-Enhanced Palladium Catalysis with Single-Molecule Fluorescence Microscopy, *Nano Res.*, 2023, **16**, 8817–8826.

258 D. Gilea, R. G. Ciocarlan, E. M. Seftel, P. Cool and G. Carja, Engineering Heterostructures of Layered Double Hydroxides and Metal Nanoparticles for Plasmon-Enhanced Catalysis, *Catalysts*, 2022, **12**, 1210.

259 O. A. Douglas-Gallardo, C. L. Box and R. J. Maurer, Plasmonic Enhancement of Molecular Hydrogen Dissociation on Metallic Magnesium Nanoclusters, *Nanoscale*, 2021, **13**, 11058–11068.

260 Y. Wei, Q. Hao, X. Fan, M. Li, L. Yao, G. Li, X. Zhao, H. Huang and T. Qiu, Investigation of the Plasmon-Activated C-C Coupling Reactions by Liquid-State SERS Measurement, *ACS Appl. Mater. Interfaces*, 2022, **14**, 54320–54327.

261 S. Ezendam, J. Gargiulo, A. Sousa-Castillo, J. B. Lee, Y. S. Nam, S. A. Maier and E. Cortés, Spatial Distributions of Single-Molecule Reactivity in Plasmonic Catalysis, *ACS Nano*, 2024, **18**, 451–460.

262 D. Votkina, P. Petunin, E. Miliutina, A. Trelin, O. Lyutakov, V. Svorcik, G. Audran, J. Havot, R. Valiev, L. I. Valiulina, J.-P. Joly, Y. Yamauchi, J. H. Mokkath, J. Henzie, O. Guselnikova, S. R. A. Marque and P. Postnikov, Uncovering the Role of Chemical and Electronic Structures in Plasmonic Catalysis: The Case of Homolysis of Alkoxyamines, *ACS Catal.*, 2023, **13**, 2822–2833.

263 Y. Li, H. Gu, Z. Lu, H. Zhang, M. Su, X. Zhang, J. Liu, W. Shi and J. Zhang, Cu_2FeS_2: Discovery of an Exceptional Thermoplasmonic Semiconductor via Arrested Cation Exchange, *Adv. Mater.*, 2026, **38**, e22120.

264 F. X. Tong, C. Cui, X. Z. Liang, Z. Y. Wang, Y. Y. Liu, P. Wang, H. F. Cheng, Y. Dai, Z. K. Zheng and B. B. Huang, Boosting Hot Electrons Transfer via Laser-Induced Atomic Redistribution for Plasmon-Enhanced Nitroreduction and Single-Particle Study, *J. Catal.*, 2022, **407**, 115–125.

265 J. Huang, W. Guo, S. He, J. R. Mulcahy, A. Montoya, J. Goodsell, N. Wijerathne, A. Angerhofer and W. D. Wei, Elucidating the Origin of Plasmon-Generated Hot Holes in Water Oxidation, *ACS Nano*, 2023, **17**, 7813–7820.

266 Y. H. Zhao, F. Wu, J. Wei, H. Sun, Y. Yuan, H. Bao, F. Li, Z. Zhang, S. Han and W. Niu, Designer Gold-Framed Palladium Nanocubes for Plasmon-Enhanced Electrocatalytic Oxidation of Ethanol, *Chem.–Eur. J.*, 2022, **28**, e202200494.

267 R. J. Maurer and P. K. Jain, Hot Electrons in Catalysis, *J. Phys. Chem. C*, 2024, **128**, 1863–1866.

268 T. Salavati-Fard and B. Wang, Plasmon-Assisted Direct Interfacial Charge Transfer Enables Molecular Photodissociation on Metal Surfaces, *ACS Catal.*, 2022, **12**, 12869–12878.

269 A. Zabelina, J. Dedek, O. Guselnikova, D. Zabelin, A. Trelin, E. Miliutina, Z. Kolska, J. Siegel, V. Svorcik, J. Vana and O. Lyutakov, Photoinduced CO_2 Conversion under Arctic Conditions: The High Potential of Plasmon Chemistry under Low Temperature, *ACS Catal.*, 2023, **13**, 3830–3840.

270 G. Ghimire, J. Guo, R. Halmagian and J. He, Reversibly Modulating Plasmon-Mediated Chemical Reaction via Electrode Potential on Reliable Copper Nanoelectrode, *Angew. Chem., Int. Ed.*, 2023, **62**, e202302215.

271 E. Peiris, S. Hanauer, T. Le, J. Wang, T. Salavati-Fard, P. Brasseur, E. V. Formo, B. Wang and P. H. C. Camargo, Controlling Selectivity in Plasmonic Catalysis: Switching Reaction Pathway from Hydrogenation to Homocoupling Under Visible-Light Irradiation, *Angew. Chem., Int. Ed.*, 2022, **62**, e202216398.

272 P. Verma, K. Mori, Y. Kuwahara, M. Manzoli, S. Morandi, C. Fukuhara, R. Raja and H. Yamashita, Amine Functionalization Within Hierarchically-Porous Zeotype Framework for Plasmonic Catalysis over PdAu Nanoparticles, *ChemCatChem*, 2023, **15**, e202201182.

273 Z. Tao, J. Feng, F. Yang, L. Zhang, H. Shen, Q. Cheng and L. Liu, Plasmon-Enhanced Photocatalysis using Gold Nanoparticles Encapsulated in Nanoscale Molybdenum Oxide Shell, *Nanotechnol*, 2023, **34**, 155604.

274 W. Guo, Y. Zhang, J. Tian, Z. Liu, B. Liu and J. Li, Atomic-Scale Interface Engineering in Bi/Bi_2O_3 Heterojunctions for Selective CO_2 Photoreduction to Methanol, *Nat. Commun.*, 2025, **17**, 983.

275 Z. Geng, Y. Yu, A. J. Offen and J. Liu, Achieving Maximum Overall Light Enhancement in Plasmonic Catalysis by Combining Thermal and Non-Thermal Effects, *Nat. Catal.*, 2023, **6**, 1241–1247.

276 S. Wu and M. Sheldon, Mechanisms of Photothermalization in Plasmonic Nanostructures: Insights into the Steady State, *Annu. Rev. Phys. Chem.*, 2023, **74**, 521–545.

277 X. Li, H. O. Everitt and J. Liu, Confirming Nonthermal Plasmonic Effects Enhance CO_2 Methanation on Rh/TiO_2 Catalysts, *Nano Res.*, 2019, **12**, 1906–1911.

278 Y. Hattori, J. Meng, K. Zheng, A. Meier de Andrade, J. Kullgren, P. Broqvist, P. Nordlander and J. Sá, Phonon-Assisted Hot Carrier Generation in Plasmonic Semiconductor Systems, *Nano Lett.*, 2021, **21**, 1083–1089.

279 G. Baffou, I. Bordacchini, A. Baldi and R. Quidant, Simple Experimental Procedures to Distinguish Photothermal from Hot-Carrier Processes in Plasmonics, *Light Sci. Appl.*, 2020, **9**, 108.

280 C. Zhang, T. Kong, Z. Fu, Z. Zhang and H. Zheng, Hot Electron and Thermal Effects in Plasmonic Catalysis of Nanocrystal Transformation, *Nanoscale*, 2020, **12**, 8768–8774.

281 C. Hu, X. Chen, J. Jin, Y. Han, S. Chen, H. Ju, J. Cai, Y. Qiu, C. Gao, C. Wang, Z. Qi, R. Long, L. Song, Z. Liu and Y. Xiong, Surface Plasmon Enabling Nitrogen Fixation in

Pure Water Through a Dissociative Mechanism Under Mild Conditions, *J. Am. Chem. Soc.*, 2019, **141**, 7807.

282 R. Verma, R. Tyagi, V. K. Voora and V. Polshettiwar, Black Gold-Based "Antenna–Reactor" to Activate Non-Plasmonic Nickel: Photocatalytic Hydrodechlorination and Hydrogenation Reactions, *ACS Catal.*, 2023, **13**, 7395–7406.

283 Y. Dubi and Y. Sivan, "Hot" Electrons in Metallic Nanostructures—Non-Thermal Carriers or Heating?, *Light Sci. Appl.*, 2019, **8**, 89.

284 G. Fu, M. Jiang, J. Liu, K. Zhang, Y. Hu, Y. Xiong, A. Tao, Z. Tie and Z. Jin, Rh/Al Nanoantenna Photothermal Catalyst for Wide-Spectrum Solar-Driven CO_2 Methanation with Nearly 100% Selectivity, *Nano Lett.*, 2021, **21**, 8824–8830.

285 K. Chen and H. Wang, Origin of Superlinear Power Dependence of Reaction Rates in Plasmon-Driven Photocatalysis: A Case Study of Reductive Nitrothiophenol Coupling Reactions, *Nano Lett.*, 2023, **23**, 2870–2876.

286 G. Meng, J. Gardner, N. Hertl, W. Dou, R. J. Maurer and B. Jiang, First-Principles Nonadiabatic Dynamics of Molecules at Metal Surfaces with Vibrationally Coupled Electron Transfer, *Phys. Rev. Lett.*, 2024, **133**, 036203.

287 R. Kamarudheen, G. W. Catellanos, L. J. P. Kamp, H. J. H. Clercx and A. Baldi, Quantifying Photothermal and Hot Charge Carrier Effects in Plasmon-Driven Nanoparticle Syntheses, *ACS Nano*, 2018, **12**, 8447–8455.

288 Y. Sivan, J. Baraban, I. Wai Un and Y. Dubi, Comment on "Quantifying Hot Carrier and Thermal Contributions in Plasmonic Photocatalysis.", *Science*, 2019, **364**, eaaw9367.

289 M. Virk, K. Xiong, M. Svedendahl, M. Käll and A. B. Dahlin, A Thermal Plasmonic Sensor Platform: Resistive Heating of Nanohole Arrays, *Nano Lett.*, 2014, **14**, 3544–3549.

290 X. Li, X. Zhang, H. O. Everitt and J. Liu, Light-Induced Thermal Gradients in Ruthenium Catalysts Significantly Enhance Ammonia Production, *Nano Lett.*, 2019, **19**, 1706–1711.

291 V. Lomonosov, T. M. R. Wayman, E. R. Hopper, Y. P. Ivanov, G. Divitini and E. Ringe, Plasmonic Magnesium Nanoparticles Decorated with Palladium Catalyse Thermal and Light-Driven Hydrogenation of Acetylene, *Nanoscale*, 2023, **15**, 7420.

292 I. W. Un, Y. Dubi and Y. Sivan, Photothermal Nonlinearity in Plasmon-Assisted Photocatalysis, *Nanoscale*, 2022, **14**, 5022.

293 Y. Sivan, I. W. Un and Y. Dubi, Assistance of Metal Nanoparticles in Photocatalysis–Nothing More Than a Classical Heat Source, *Faraday Discuss.*, 2019, **214**, 215.

294 Y. Dubi, I. W. Un and Y. Sivan, Distinguishing Thermal from Nonthermal ("Hot") Carriers in Illuminated Molecular Junctions, *Nano Lett.*, 2022, **22**, 2127–2133.

295 C. Wang, O. Ranasingha, S. Natesakhawat, P. R. Ohodnicki, M. Andio, J. P. Lewis and C. Matranga, Visible Light Plasmonic Heating of Au–ZnO for the Catalytic Reduction of CO_2, *Nanoscale*, 2013, **5**, 6968.

296 J. Gardner, D. Corken, S. M. Janke, S. Habershon and R. J. Maurer, Efficient Implementation and Performance Analysis of the Independent Electron Surface Hopping Method for Dynamics at Metal Surfaces, *J. Chem. Phys.*, 2023, **158**, 064101.

297 A. A. Golubev, B. N. Khlebtsov, R. D. Rodriguez, Y. Chen and D. R. T. Zahn, Plasmonic Heating Plays a Dominant Role in the Plasmon-Induced Photocatalytic Reduction of 4-Nitrobenzenethiol, *J. Phys. Chem. C*, 2018, **122**, 5657–5663.

298 L. K. Khorashad, L. V. Besteiro, Z. Wang, J. Valentine and A. O. Govorov, Localization of Excess Temperature using Plasmonic Hot Spots in Metal Nanostructures: Combining Nano-Optical Antennas with The Fano Effect, *J. Phys. Chem. C*, 2016, **120**, 13215–13226.

299 R. Xiong, C. Tang, K. Li, J. Wan, W. Jia, Y. Xiao, B. Cheng and S. Lei, Plasmon Photothermal-Promoted Solar Photocatalytic Hydrogen Production Over a $CoCr_2O_4$/g-C_3N_4 Heterojunction, *J. Mater. Chem. A*, 2022, **10**, 22819–2283.

300 S. Hu, B. Liu, J. Feng, C. Zong, K. Lin, X. Wang, D. Wu and B. Ren, Quantifying Surface Temperature of Thermoplasmonic Nanostructures, *J. Am. Chem. Soc.*, 2018, **140**, 13680–13686.

301 I. Un and Y. Sivan, The Role of Heat Generation and Fluid Flow in Plasmon-Enhanced Reduction-Oxidation Reactions, *ACS Photonics*, 2021, **8**, 1183–1190.

302 J. G. Quintana, J. Crespo, A. Falqui, J. M. López-De-Luzuriaga, M. E. Olmos, M. Rodríguez-Castillo and M. Monge, Mini AuAg Wavy Nanorods Displaying Plasmon-Induced Photothermal and Photocatalytic Properties, *Adv. Photonics*, 2023, **4**, 2200246.

303 N. B. Schorr, M. J. Counihan, R. Bhargava and J. Rodríguez-López, Impact of Plasmonic Photothermal Effects on the Reactivity of Au Nanoparticle Modified Graphene Electrodes Visualized using Scanning Electrochemical Microscopy, *Anal. Chem.*, 2020, **92**, 3666–3673.

304 R. K. Kashyap, I. Dwivedi, S. Roy, S. Roy, A. Rao, C. Subramaniam and P. P. Pillai, Insights into the Utilization and Quantification of Thermoplasmonic Properties in Gold Nanorod Arrays, *Chem. Mater.*, 2022, **34**, 7369–7378.

305 G. Wang, X. Chen, B. Li and L. Wu, Near-Infrared Photothermal Conversion of Polyoxometalate-Modified Gold Nanorods for Plasmon-Enhanced Catalysis, *Inorg. Chem. Front.*, 2023, **10**, 1852–1862.

306 G. Wang, B. Li, B. Li and L. Wu, Gold Nanocrystal-Loaded 2D Supramolecular Network for Plasmon-Enhanced Nitrogen Fixation, *Green Chem.*, 2023, **25**, 10556–10566.

307 D. Mateo, J. C. Navarro, I. S. Khan, J. Ruiz-Martinez and J. Gascon, Plasmonic Titanium Nitride Tubes Decorated with Ru Nanoparticles as Photo-Thermal Catalyst for CO_2 Methanation, *Molecules*, 2022, **27**, 2701.

308 Y. Wei, Z. Mao, X. Y. Ma, C. Zhan and W. B. Cai, Plasmon-Enhanced C-C Bond Cleavage Toward Efficient Ethanol Electrooxidation, *J. Phys. Chem. Lett.*, 2022, **13**, 11288–11294.

309 M. Xu, T. Den Hartog, L. Cheng, M. Wolfs, R. Habets, J. Rohlfs, J. Van Den Ham, N. Meulendijks, F. Sastre and P. Buskens, Using Fiber Bragg Grating Sensors to

Quantify Temperature Non-Uniformities in Plasmonic Catalyst Beds Under Illumination, *ChemPhotoChem*, 2022, **6**, e202100289.

310 H. Ge, Y. Kuwahara, K. Kusu, Z. Bian and H. Yamashita, Ru/H_xMoO_{3-y} with Plasmonic Effect for Boosting Photothermal Catalytic CO_2 Methanation, *Appl. Catal., B*, 2022, **317**, 121734.

311 G. Zerjav, Z. Say, J. Zavasnik, M. Finsgar, C. Langhammer and A. Pintar, Photo, Thermal and Photothermal Activity of TiO_2 Supported Pt Catalysts for Plasmon-Driven Environmental Applications, *J. Environ. Chem. Eng.*, 2023, **11**, 110209.

312 J. Gargiulo, M. Herran, I. L. Violi, A. Sousa-Castillo, L. P. Martinez, S. Ezendam, M. Barella, H. Giesler, R. Grzeschik, S. Schlücker, S. A. Maier, F. D. Stefani and E. Cortés, Impact of Bimetallic Interface Design on Heat Generation in Plasmonic Au/Pd Nanostructures Studied by Single-Particle Thermometry, *Nat. Commun.*, 2023, **14**, 3813.

313 C. Tiburski, F. A. A. Nugroho and C. Langhammer, Optical Hydrogen Nanothermometry of Plasmonic Nanoparticles Under Illumination, *ACS Nano*, 2022, **16**, 6233–6243.

314 N. Lemcoff, N. B. Nechmad, O. Eivgi, E. Yehezkel, O. Shelonchik, R. S. Phatake, D. Yesodi, A. Vaisman, A. Biswas, N. G. Lemcoff and Y. Weizmann, Plasmonic Visible-Near Infrared Photothermal Activation of Olefin Metathesis Enabling Photoresponsive Materials, *Nat. Chem.*, 2023, **15**, 475–482.

315 K. Okada, R. Mashita, A. Fukatsu and M. Takahashi, Polarization-Dependent Plasmonic Heating in Epitaxially Grown Multilayered Metal-Organic Framework Thin Films Embedded with Ag Nanoparticles, *Nanoscale Adv.*, 2023, **5**, 1795–1801.

316 A. Cao, L. Sang, Z. Yu, Y. Zhao, X. Wang, C. Wang and M. Ma, Investigation of The Local Photothermal Effects by Fabricating A CQDs/Au/TiO_2 Photoelectrode in a PEC Water Splitting System, *Catal. Sci. Technol.*, 2022, **12**, 1859–1868.

317 Z. Li, Y. Xiao, F. Liu, X. Yan, D. You, K. Li, L. Zeng, M. Zhu, G. Xiao, J. Albert and T. Guo, Operando Optical Fiber Monitoring of Nanoscale and Fast Temperature Changes During Photo-Electrocatalytic Reactions, *Light Sci. Appl.*, 2022, **11**, 220.

318 Y. Li, Y. Song, X. Zhang, T. Liu, T. Xu, H. Wang, D. E. Jiang and R. Jin, Atomically Precise Au_{42} Nanorods with Longitudinal Excitons for an Intense Photothermal Effect, *J. Am. Chem. Soc.*, 2022, **144**, 12381–12389.

319 R. M. Sarhan, S. Kogikoski Jr, R. M. Schürmann, Y. Zhao, A. Krause, B. Schmidt, I. Bald and Y. Lu, Colloidal Black Gold with Broadband Absorption for Plasmon-Induced Dimerization of 4-Nitrothiophenol and Cross-Linking of Thiolated Diazonium Compound, *J. Phys. Chem. C*, 2023, **127**, 10051–10061.

320 H. Inoue, S. Naya, A. Akita, H. Sugime and H. Tada, Photothermal Oxidation of Cinnamyl Alcohol with Hydrogen Peroxide Catalyzed by Gold Nanoparticle/Antimony-Doped Tin Oxide Nanocrystals, *Chem.–Eur. J.*, 2022, **28**, e202201653.

321 M. Ivanchenko, A. L. Carroll, A. B. Brothers and H. Jing, Plasmonic Ag@Cu_2O Core-Shell Nanostructures Exhibiting Near-Infrared Photothermal Effect, *RSC Adv.*, 2023, **13**, 31569–31577.

322 M. Ji, H. Liu, M. Cheng, L. Huang, G. Yang, F. Bao, G. Huang, Y. Huang, Y. Hu, G. Cong, J. Yu, C. Zhu and J. Xu, Plasmonic Metal Nanoparticle Loading to Enhance the Photothermal Conversion of Carbon Fibers, *J. Phys. Chem. C*, 2022, **126**, 2454.

323 R. Verma, S. Kundu and V. Polshettiwar, One-Pot Synthesized Plasmonic Black Gold Nanoparticles for Efficient Photocatalytic CO Oxidation, *J. Mater. Chem. A*, 2024, **12**, 27235–27245.

324 D. D. S. Lopes, D. D. S. Abreu, R. A. Ando and P. Corio, Regioselective Plasmon-Driven Decarboxylation of Mercaptobenzoic Acids Triggered by Distinct Reactive Oxygen Species, *ACS Catal.*, 2022, **12**, 14619–14628.

325 A. G. M. da Silva, T. S. Rodrigues, J. Wang and P. H. C. Camargo, Plasmonic Catalysis with Designer Nanoparticles, *Chem. Commun.*, 2022, **58**, 2055–2074.

326 J. A. Wisch, X. Liu, P. J. Sarver, C. N. P. Kullmer, A. Millet, D. W. C. MacMillan and B. P. Rand, Plasmon Mediated Near-Field Energy Transfer from Solid-State, Electrically Injected Excitons to Solution Phase Chromophores, *Adv. Funct. Mater.*, 2023, **33**, 2214367.

327 Y. Chen, Y. Zhu, H. Sheng, J. Wang, C. Zhang, Y. Chen, W. Huang and G. Lu, Molecular Coadsorption of p-Hydroxythiophenol on Silver Nanoparticles Boosts the Plasmon-Mediated Decarboxylation Reaction, *ACS Catal.*, 2022, **12**, 2938–2946.

328 H. Lee, Y. Park, S. Nah, M. Kang, M. Lee and J. Y. Park, Reconfiguring Hot-Hole Flux via Polarity Modulation of p-GaN in Plasmonic Schottky Architectures, *Sci. Adv.*, 2025, **11**, eadu0086.

329 T. Le and B. Wang, Solvent-Induced Local Environment Effect in Plasmonic Catalysis, *Nanoscale Adv.*, 2023, **5**, 5774–5779.

330 Y. Fan, A. Girard, M. Waals, C. Salzemann and A. Courty, Ag@Pt Core-Shell Nanoparticles for Plasmonic Catalysis, *ACS Appl. Nano Mater.*, 2023, **6**, 1193–1202.

331 A. Zabelina, E. Miliutina, J. Dedek, A. Trelin, D. Zabelin, R. Valiev, R. Ramazanov, V. Burtsev, D. Popelkova, M. Stastny, V. Svorcik and O. Lyutakov, Nitrogen Photoelectrochemical Reduction on TiB_2 Surface Plasmon Coupling Allows us to Reach Enhanced Efficiency of Ammonia Production, *ACS Catal.*, 2023, **13**, 10916–10926.

332 W. Jiang, H. Zhang, Y. An, Y. Mao, Z. Wang, Y. Liu, P. Wang, Z. Zheng, W. Wei, Y. Dai, H. Cheng and B. Huang, Free-Standing Nanoarrays with Energetic Electrons and Active Sites for Efficient Plasmon-Driven Ammonia Synthesis, *Small*, 2022, **18**, 2201269.

333 G. K. Joshi, A. Saha, A. Dutta and S. Khatua, NIR-Driven Photocatalytic Hydrogen Production by Silane- and Tertiary Amine-Bound Plasmonic Gold Nanoprisms, *ACS Appl. Mater. Interfaces*, 2022, **14**, 38815–38823.

334 R. Zhang, J. Zhang, H. You, M. U. Amin, J.-F. Li and J. Fang, Driving Reactant Molecules to Plasmonic Active Sites Using Electric Field for Enhanced Catalytic Reaction, *ACS Catal.*, 2023, **13**, 12021–12029.

335 F. Tong, X. Liang, M. Liu, Z. Wang, Y. Liu, P. Wang, H. Cheng, Y. Dai, Z. Zheng and B. Huang, Plasmon-Enhanced Water Activation for Hydrogen Evolution from Ammonia-Borane Studied at a Single-Particle Level, *ACS Catal.*, 2022, **12**, 3558–3565.

336 S. Zhang, D. Chen, P. Chen, R. Zhang, Y. Hou, Y. Guo, P. Li, X. Liang, T. Xing, J. Chen, Y. Zhao, Z. Huang, D. Lei and C. Zhi, Concurrent Mechanisms of Hot Electrons and Interfacial Water Molecule Ordering in Plasmon-Enhanced Nitrogen Fixation, *Adv. Mater.*, 2024, **36**, 2310776.

337 S. W. Lee, H. Kim and J. Y. Park, How Hot Electron Generation at the Solid-Liquid Interface is Different from the Solid–Gas Interface, *Nano Lett.*, 2023, **23**, 5373–5380.

338 G. K. Joshi, R. Kashyap, K. Patrikar, A. Mondal and S. Khatua, Ligand-Mediated Electron Transport Channels Enhance Photocatalytic Activity of Plasmonic Nanoparticles, *Nanoscale*, 2023, **15**, 16552–16560.

339 M. P. S. Rodrigues, A. H. B. Dourado, A. G. S. de Oliveira-Filho, A. P. D. L. Batista, M. Feil, K. Krischer and S. I. C. de Torresi, Gold-Rhodium Nanoflowers for the Plasmon-Enhanced CO_2 Electroreduction Reaction upon Visible Light, *ACS Catal.*, 2023, **13**, 267–279.

340 H. Chen, J. Chen, H. He, X. Chen, C. Jia, D. Chen, J. Liang, D. Yu, X. Yao, L. Qin, Y. Huang and Z. Wen, Amorphous CoFeB Nanosheets with Plasmon-Regulated Dynamic Active Sites for Electrocatalytic Water Oxidation, *Appl. Catal., B*, 2023, **323**, 122187.

341 T. E. Li and S. Hammes-Schiffer, Nuclear-Electronic Orbital Quantum Dynamics of Plasmon-Driven H_2 Photodissociation, *J. Am. Chem. Soc.*, 2023, **145**, 18210–18214.

342 L. Cheng, F. Wu, Y. Tian, X. Lv, F. Li, G. Xu, H.-Y. Hsu, Y. Zhang and W. Niu, Gap Engineering of Sandwich Plasmonic Gap Nanostructures for Boosting Plasmon-Enhanced Electrocatalysis, *Nano Res.*, 2023, **16**, 8961–8969.

343 J. Guo, G. Ghimire, J. Zhou, L. Yu, Z. Wang, S. Chang and J. He, Potential Controlled Redox Cycling of 4-Aminothiophenol by Coupling Plasmon-Mediated Chemical Reaction with Electrochemical Reaction, *J. Catal.*, 2023, **418**, 256–262.

344 C. Cheng, J. Zhang, R. Zeng, F. Xing and C. Huang, Schottky Barrier Tuning via Surface Plasmon and Vacancies for Enhanced Photocatalytic H_2 Evolution in Seawater, *Appl. Catal., B*, 2022, **310**, 121321.

345 R. Singh, V. Yadav and S. Siddhanta, Probing Plasmon-Induced Surface Reactions using Two-Dimensional Correlation Vibrational Spectroscopy, *Phys. Chem. Chem. Phys.*, 2023, **25**, 6032–6043.

346 L. Nan, J. Giráldez-Martínez, A. Stefancu, L. Zhu, M. Liu, A. O. Govorov, L. V. Besteiro and E. Cortés, Investigating Plasmonic Catalysis Kinetics on Hot-Spot Engineered Nanoantennae, *Nano Lett.*, 2023, **23**, 2883–2889.

347 J. H. Mokkath, Plasmon Induced Hot Carrier Generation in a Pyridine@Au_{20} Composite, *Phys. Chem. Chem. Phys.*, 2023, **25**, 28750–28760.

348 E. Landaeta, N. I. Kadosh and Z. D. Schultz, Mechanistic Study of Plasmon-Assisted In Situ Photoelectrochemical CO_2 Reduction to Acetate with a Ag/Cu_2O Nanodendrite Electrode, *ACS Catal.*, 2023, **13**, 1638–1648.

349 S. N. Bonvicini and Y. Shi, Formation and Removal of Alloyed Bimetallic Au-Ag Nanoparticles from Silicon Substrates for Tunable Surface Plasmon Resonance, *ACS Appl. Nano Mater.*, 2022, **5**, 14850–14861.

350 H. Li, S. Wang, M. Wang, Y. Gao, J. Tang, S. Zhao, H. Chi, P. Zhang, J. Qu, F. Fan and C. Li, Enhancement of plasmon-induced photoelectrocatalytic water oxidation over Au/TiO_2 with lithium intercalation, *Angew. Chem., Int. Ed.*, 2022, **61**, e202204272.

351 M. Herran, S. Juergensen, M. Kessens, D. Hoeing, A. Köppen, A. Sousa-Castillo, W. J. Parak, H. Lange, S. Reich, F. Schulz and E. Cortés, Plasmonic Bimetallic Two-Dimensional Supercrystals for H_2 Generation, *Nat. Catal.*, 2023, **6**, 1205–1214.

352 J. Yao, Y. Jiang, X. Gu, X. Guo, Y. Ying, Y. Wen, X. L. Liu, H. F. Yang and Y. Wu, Surface Plasmon Resonance-Triggered Local Electromagnetic Field Advances Photocatalytic and Photoelectrochemical Performance of Plasmonic Metal/Semiconductor Composite, *J. Phys. Chem. C*, 2023, **127**, 248–255.

353 Y. Nishijima, K. Ueno, Y. Kotake, K. Murakoshi, H. Inoue and H. Misawa, Near-Infrared Plasmon-Assisted Water Oxidation, *J. Phys. Chem. Lett.*, 2012, **3**, 1248–1252.

354 L. Hammoud, C. Strebler, J. Toufaily, T. Hamieh, V. Keller and V. Caps, The Role of the Gold-Platinum Interface in AuPt/TiO_2-Catalyzed Plasmon-Induced Reduction of CO_2 with Water, *Faraday Discuss.*, 2023, **242**, 443.

355 L. Shi, H. Liu, S. Ning and J. Ye, Localized Surface Plasmon Resonance Effect Enhanced Cu/TiO_2 Core-Shell Catalyst for Boosting CO_2 Hydrogenation Reaction, *Catal. Sci. Technol.*, 2022, **12**, 6155–6162.

356 Q. Hao, Z. Li, Y. Shi, R. Li, Y. Li, L. Wang, H. Yuan, S. Ouyang and T. Zhang, Plasmon-Induced Radical-Radical Heterocoupling Boosts Photodriven Oxidative Esterification of Benzyl Alcohol over Nitrogen-Doped Carbon-Encapsulated Cobalt Nanoparticles, *Angew. Chem., Int. Ed.*, 2023, **135**, e202312808.

357 M. Berdakin, G. Soldano, F. P. Bonafé, V. Liubov, B. Aradi, T. Frauenheim and C. G. Sánchez, Dynamical Evolution of the Schottky Barrier as a Determinant Contribution to Electron-Hole Pair Stabilization and Photocatalysis of Plasmon-Induced Hot Carriers, *Nanoscale*, 2022, **14**, 2816–2825.

358 Y. Li, Z. Zhang, A. Du, X. Du, A. Zhu, C. Zhang, Y. Gao, Y. Hu, Y. Wang, X. Yang, L. Yang and W. Xie, Hot-Electron-Driven Interfacial Chemistry Using Non-Noble Plasmonic Cu Under Visible-Light Irradiation, *ACS Photonics*, 2023, **10**, 3181–3187.

359 S. Swaminathan, J. K. Bera and M. Chandra, Simultaneous Harvesting of Multiple Hot Holes via Visible-Light

Excitation of Plasmonic Gold Nanospheres for Selective Oxidative Bond Scission of Olefins to Carbonyls, *Angew. Chem., Int. Ed.*, 2023, **62**, e202215933.

360 B. Zhou, J. Zhong, X. Tang, J.-H. Liu, J. Shen, C. Wang, W. Ou, H. Wang, L. Liu, J. Pan, J. Lu and Y. Y. Li, In Situ Surface-Enhanced Raman Spectroscopy Monitoring of Molecular Reorientation in Plasmon-Mediated Chemical Reactions, *J. Catal.*, 2022, **413**, 527–533.

361 J. Zhu, J. Huang, J. Dai, R. Chen, X. Fu, Z. Wang, H. Liu and G. Li, Size Effect on Formic Acid Dehydrogenation over Plasmonic Au@Pd Core-Satellite Nanostructures, *ACS Appl. Energy Mater.*, 2022, **5**, 10013–10022.

362 T. Le, T. Salavati-Fard and B. Wang, Plasmonic Energetic Electrons Drive CO_2 Reduction on Defective Cu_2O, *ACS Catal.*, 2023, **13**, 6328–6337.

363 L.-W. Wu, C. Liu, Y. Han, Y. Yu, Z. Liu and Y.-F. Huang, A Spectroscopic Study of the Mechanism of Au(III) (hydro-) Oxides in Promoting Plasmon-Mediated Photoelectrochemical Water-Oxidation, *J. Chem. Phys.*, 2023, **158**, 151102.

364 J. Zhao, Y. Bai, Z. Li, J. Liu, W. Wang, P. Wang, B. Yang, R. Shi, G. I. N. Waterhouse, X.-D. Wen, Q. Dai and T. Zhang, Plasmonic Cu Nanoparticles for the Low-Temperature Photo-Driven Water-Gas Shift Reaction, *Angew. Chem., Int. Ed.*, 2023, **62**, e202219299.

365 S. Wang, P. Liu, C. Meng, Y. Wang, L. Zhang, L. Pan, Z. Yin, N. Tang and J. Zou, Boosting Photoelectrochemical Water Splitting by Au@Pt Modified ZnO/CdS with Synergy of Au-S Bonds and Surface Plasmon Resonance, *J. Catal.*, 2022, **408**, 196–205.

366 Y. Xiao, Z. Wang, B. Yao, M. Cao and Y. Wang, Guiding the Driving Factors on Plasma Super-Photothermal S-Scheme Core-Shell Nanoreactor to Enhance Photothermal Catalytic H_2 Evolution and Selective CO_2 Reduction, *Small*, 2023, **20**, 2304843.

367 S. Swaminathan, V. G. Rao, J. K. Bera and M. Chandra, The Pivotal Role of Hot Carriers in Plasmonic Catalysis of C−N Bond Forming Reaction of Amines, *Angew. Chem., Int. Ed.*, 2021, **133**, 12640–12646.

368 Y. Gao, Q. Zhu, S. He, S. Wang, W. Nie, K. Wu, F. Fan and C. Li, Observation of Charge Separation Enhancement in Plasmonic Photocatalysts Under Coupling Conditions, *Nano Lett.*, 2023, **23**, 3540–3548.

369 I. Ullah, S. Habib, X.-J. Lu, J.-H. Li, S. Chen, A. Habib and A.-W. Xu, Bimetallic Nitride NiMoN Loaded On Graphitic Carbon Nitride for Plasmon-Enhanced Visible Light-Driven Photocatalytic Hydrogen Evolution from Water Splitting, *Catal. Sci. Technol.*, 2024, **14**, 912–918.

370 T. Li, Y. Liu, R. Jia and L. Huang, Fabrication of Heterogeneous Bimetallic Nanochains through Photochemical Welding for Promoting the Electrocatalytic Hydrogen Evolution Reaction, *J. Colloid Interface Sci.*, 2024, **656**, 399–408.

371 S. Rizevsky and D. Kurouski, Tip-Enhanced Raman Imaging of Photocatalytic Processes at the Nanoscale, *J. Phys. Chem. C*, 2022, **126**, 14781–14790.

372 Y. Yu, Y. Xie, P. Zhang, W. Zhang, W. Wang, S. Zhang, Q. Ou and W. Li, Hot Spots Engineering by Dielectric Support for Enhanced Photocatalytic Redox Reactions, *Nano Res.*, 2023, **16**, 239–247.

373 Z. Li, J. Rigor, S. Ehtesabi, S. Gojare, S. Kupfer, S. Gräfe, N. Large and D. Kurouski, Role of Plasmonic Antenna in Hot Carrier-Driven Reactions on Bimetallic Nanostructures, *J. Phys. Chem. C*, 2023, **127**, 22635–22645.

374 W. Zhang, X. Li, S. Liu, J. Qiu, J. An, J. Yao, S. Zuo, B. Zhang, H. Xia and C. Li, Photocatalytic Oxidation of 5-Hydroxymethylfurfural Over Interfacial-Enhanced Ag/TiO_2 Under Visible Light Irradiation, *ChemSusChem*, 2022, **15**, e202102158.

375 G. Bharath, G. Karthikeyan, A. Kumar, J. Prakash, D. Venkatasubbu, A. K. Nadda, V. K. Gupta, M. Abu Haija and F. Banata, Surface Engineering of Au Nanostructures for Plasmon-Enhanced Electrochemical Reduction of N_2 and CO_2 into Urea in the Visible-NIR Region, *Appl. Energy*, 2022, **318**, 119244.

376 P. yu, R. Espinoza and S. C. Nguyen, Photocatalysis of Metallic Nanoparticles: Interband vs Intraband Induced Mechanisms, *J. Phys. Chem. C*, 2023, **127**, 15685–15698.

377 H. Xie, Z. Li, J. Zhu, H. Li, Q. Yang, Y. Yang and C. Li, Charge Separation Between Pt Co-catalysts and Plasmonic Au in Pt-Au/C_3N_4 Photocatalysts, *J. Phys. Chem. Lett.*, 2022, **13**, 11982–11989.

378 J. Xu, H. Xu, L. Xu, Q. Ruan, X. Zhu, C. Kan and D. Shi, Plasmonic and Catalytic Au NBP@AgPd Nanoframes for Highly Efficient Photocatalytic Reactions, *Phys. Chem. Chem. Phys.*, 2023, **25**, 13189–13197.

379 A. Muravitskaya, A. Movsesyan, O. Avalos-Ovando, V. A. B. Lorca, M. A. Correa-Duarte, L. V. Besteiro, T. Liedl, P. Yu, Z. Wang, G. Markovich and A. O. Govorov, Hot Electrons and Electromagnetic Effects in the Broadband Au, Ag, and Ag-Au Nanocrystals: The UV, Visible, and NIR Plasmons, *ACS Photonics*, 2024, **11**, 68–84.

380 J. Yang, S. He, H. Liu, E. Jaatinen, E. Waclawik, J. Quan, S. Sarina, C. He, S. Huang, H. Zhu and M. Wu, Enhancing Visible-Light Photocatalytic Performance of Au/TiO_2 Catalysts Through Light Reflection-Promoted Optical Absorption with Oriented Anatase Mesocrystals, *J. Mater. Chem. A*, 2023, **11**, 4751–4757.

381 P. Han, X. Mao, Y. Jin, S. Sarina, J. Jia, E. R. Waclawik, A. Du, S. E. Bottle, J.-C. Zhao and H.-Y. Zhu, Plasmonic Silver-Nanoparticle-Catalysed Hydrogen Abstraction from the C(sp^3)-H Bond of the Benzylic Cα Atom for Cleavage of Alkyl Aryl Ether Bonds, *Angew. Chem., Int. Ed.*, 2023, **62**, e202215201.

382 S. Wang, Y. Zhang, Y. Zheng, Y. Xu, G. Yang, S. Zhong, Y. Zhao and S. Bai, Plasmonic Metal Mediated Charge Transfer in Stacked Core-Shell Semiconductor Heterojunction for Significantly Enhanced CO_2 Photoreduction, *Small*, 2023, **19**, 2204774.

383 Z. Wang and H. Wang, Au@C/Pt Core@Shell/Satellite Supra-Nanostructures: Plasmonic Antenna-Reactor Hybrid Nanocatalysts, *Nanoscale Adv.*, 2023, **5**, 5435–5448.

384 J. Li, Z. Lu, C. Jin, J. Shen, H. Jiang, X. Yu, L. Sun, W. Wang, L. Wang and Q. Liu, Plasmonic Ni_3N Cocatalyst Boosting Directional Charge Transfer and Separation Toward Synergistic Photocatalytic-Photothermal Performance of Hydrogen and Benzaldehyde Production as Well as Bacterial Inactivation, *Inorg. Chem.*, 2022, **61**, 18979–18989.

385 G. Sharma, R. Verma, S. Masuda, K. Badawy, N. Singh, T. Tsukuda and V. Polshettiwar, Pt-Doped Ru Nanoparticles Loaded on 'Black Gold' Plasmonic Nanoreactors as Air Stable Reduction Catalysts, *Nat. Commun.*, 2024, **15**, 713.

386 Q. Zhang, A. Mirzaei, Y. Wang, G. Song, C. Wang, L. V. Besteiro, A. O. Govorov, M. Chaker and D. Ma, Extracting Hot Holes from Plasmonic Semiconductors for Photocatalysis, *Appl. Catal., B*, 2022, **317**, 121792.

387 H. Zhang, J. Diao, Y. Liu, H. Zhao, B. K. Y. Ng, Z. Ding, Z. Guo, H. Li, J. Jia, C. Yu, F. Xie, G. Henkelman, M.-M. Titirici, J. Robertson, P. Nellist, C. Duan, Y. Guo, D. J. Riley and J. Qiu, In-Situ-Grown Cu Dendrites Plasmonically Enhance Electrocatalytic Hydrogen Evolution on Facet-Engineered Cu_2O, *Adv. Mater.*, 2023, **35**, 2305742.

388 J. Guan, S. Wu, L. Li, X. Wang, W. Ji and Y. Ozaki, New Insights of Charge Transfer at Metal/Semiconductor Interfaces for Hot-Electron Generation Studied by Surface-Enhanced Raman Spectroscopy, *J. Phys. Chem. Lett.*, 2022, **13**, 3571–3578.

389 H. Deng, Z. Gu, W. Zheng, T. Sun and G. Gao, Engineering Dumbbell-Shaped Au Nanobipyramid/Ag-CeO_2 Plasmonic Bimetal-Semiconductor Heterostructures for Nitroaromatic Reduction, *ACS Appl. Nano Mater.*, 2023, **6**, 11581–11589.

390 J. Fang, C. Zhu, Y. Ni, C. Lu and Z. Xu, Double Local Electromagnetic Fields Collaboratively Enhanced Triplet-Triplet Annihilation Upconversion for Efficient Photocatalysis, *Catal. Sci. Technol.*, 2023, **13**, 2151–2159.

391 G. Li, M. Wang, H. Shao, W. Liu, S. Yang, W. Sun, T. Ishihara, Y. Sun and X. Zhou, Light-Driven Carbon Dioxide Reduction Over the Ag-Decorated Modified TS-1 Zeolite, *Catal. Sci. Technol.*, 2022, **12**, 2490–2499.

392 S. Guo, Y. Qiao, J. Ding, Y. Guo, C. Han and X. Gu, Regulating the Electronic Structure of Plasmonic Co/Cu Catalysts Through Morphology Engineering to Enhance Visible-Light-Driven Hydrogen Generation from Aqueous Ammonia Borane, *Catal. Sci. Technol.*, 2023, **13**, 7068–7075.

393 T. Zhang, Y. Chen, X. Yang, J. Chen, J. Zhong, J. Li, M. Li and Z. Wan, Enhanced Photocatalytic Detoxication Properties of OVs-Rich Pd/N-TiO_2 Heterojunctions: Excellent Charge Separation and Mechanism Insight, *Mater. Today Chem.*, 2023, **28**, 101358.

394 R. F. Hamans, M. Parente, A. Garcia-Etxarri and A. Baldi, Optical Properties of Colloidal Silver Nanowires, *J. Phys. Chem. C*, 2022, **126**, 8703–8709.

395 J. Liu, Y. Xie, Y. Wang, K. Yang, S. Su, Y. Ling and P. Chen, Synergistic Coupling of Interface Ohmic Contact and LSPR Effects Over Au/$Bi_{24}O_{31}Br_{10}$ Nanosheets for Visible-Light-Driven Photocatalytic CO_2 Reduction to CO, *Chem. Sci.*, 2023, **14**, 13518–13529.

396 J. E. Kuszynski, C. J. Fabiano, E. T. Nguyen, K. Mao, A. K. Ahuja, R. D. Schaller and G. F. Strouse, Plasmon-Induced Hot-Carrier Excited-State Dynamics in Plasmonic Semiconductor Nanocrystals, *J. Phys. Chem. C*, 2023, **127**, 22654–22661.

397 W. Ou, Y. Fan, J. Shen, Y. Xu, D. Huang, B. Zhou, T. W. Lo, S. Li, Y. Y. Li, D. Lei and J. Lu, Plasmoelectric Potential in Plasmon-Mediated Electrochemistry, *Nano Lett.*, 2022, **22**, 8397–8405.

398 X. Zang, X. Shi, Y. Suganami, Y. Liu, T. Oshikiri and H. Misawa, Investigation of Enhanced Water Oxidation Under Plasmon-Nanocavity Strong Coupling Using In Situ Electrochemical Surface-Enhanced Raman Spectroscopy, *J. Phys. Chem. C*, 2023, **127**, 15087–15095.

399 Y. Wang, Y. Wang, I. Aravind, Z. Cai, L. Shen, B. Zhang, B. Wang, J. Chen, B. Zhao, H. Shi, J. M. Dawlaty and S. B. Cronin, In Situ Investigation of Ultrafast Dynamics of Hot Electron-Driven Photocatalysis in Plasmon-Resonant Grating Structures, *J. Am. Chem. Soc.*, 2022, **144**, 3517–3526.

400 J. Yang, L. Li, C. Xiao and Y. Xie, Dual-Plasmon Resonance Coupling Promoting Directional Photosynthesis of Nitrate from Air, *Angew. Chem., Int. Ed.*, 2023, **62**, e202311911.

401 E. Contreras, R. Nixon, C. Litts, W. Zhang, F. M. Alcorn and P. K. Jain, Plasmon-Assisted Ammonia Electrosynthesis, *J. Am. Chem. Soc.*, 2022, **144**, 10743–10751.

402 D. Solti, K. D. Chapkin, D. Renard, A. Bayles, B. D. Clark, G. Wu, J. Y. Zhou, A. L. Tsai, L. Kürti, P. Nordlander and N. J. Halas, Plasmon-Generated Solvated Electrons for Chemical Transformations, *J. Am. Chem. Soc.*, 2022, **144**, 20183–20189.

403 T. Tang, M. Li, Z. Liang, Y.-W. Hu, J. Chen, G. Wang, J. Chen, K.-H. Ye and Z. Lin, Promoting Plasmonic Hot Hole Extraction and Photothermal Effect for The Oxygen Evolution Reactions, *Chem.–Eur. J.*, 2023, **29**, e202300225.

404 Y. Wang and C. M. Aikens, Effects of Field Strength and Silver Nanowire Size on Plasmon-Enhanced N_2 Dissociation, *J. Phys. Chem. A*, 2023, **127**, 5609–5619.

405 R. Schürmann, A. Nagel, S. Juergensen, A. Pathak, S. Reich, C. Pacholski and I. Bald, Microscopic Understanding of Reaction Rates Observed in Plasmon Chemistry of Nanoparticle-Ligand Systems, *J. Phys. Chem. C*, 2022, **126**, 5333–5342.

406 M. Chen, Z. Ye, L. Wei, J. Yuan and L. Xiao, Shining at the Tips: Anisotropic Deposition of Pt Nanoparticles Boosting Hot Carrier Utilization for Plasmon-Driven Photocatalysis, *J. Am. Chem. Soc.*, 2022, **144**, 12842–12849.

407 M. Romain, P. Roman, L. Saviot, N. Millot and W. Boireau, Inferring the Interfacial Reactivity of Gold Nanoparticles by Surface Plasmon Resonance Measurements, *Langmuir*, 2023, **39**, 13058–13067.

408 M. Kang, B. Jeon and J. Y. Park, Catalytic Boosting by Surface-Plasmon-Driven Hot Electrons On Antenna-Reactor Schottky Nanodiodes, *Nano Lett.*, 2023, **23**, 5116–5122.

409 H. Jia, F. Li, T. H. Chow, X. Liu, H. Zhang, Y. Lu, J. Wang and C.-Y. Zhang, Construction of Spatially Separated Gold Nanocrystal/Cuprous Oxide Architecture for Plasmon-Driven CO_2 Reduction, *Nano Lett.*, 2022, **22**, 7268–7274.

410 S. Kim, L. T. M. Huynh and S. Yoon, Which Nanoparticle Shape is the Most Effective in Generating Hot Charge Carriers from Plasmon Excitation?, *J. Phys. Chem. C*, 2023, **127**, 14776–14783.

411 J. Zhou, J. Guo, A. M. Mebel, G. Ghimire, F. Liang, S. Chang and J. He, Probing the Intermediates of Catalyzed Dehydration Reactions of Primary Amide to Nitrile in Plasmonic Junctions, *ACS Catal.*, 2022, **12**, 7737–7747.

412 C. Hu, X. Chen, J. Low, Y.-W. Yang, H. Li, D. Wu, S. Chen, J. Jin, H. Li, H. Ju, C.-H. Wang, Z. Lu, R. Long, L. Song and Y. Xiong, Near-Infrared-Featured Broadband CO_2 Reduction with Water to Hydrocarbons by Surface Plasmon, *Nat. Commun.*, 2023, **14**, 221.

413 L. Wang, D. Zare, T. H. Chow, J. Wang, M. Magnozzi and M. Chergui, Disentangling Light- and Temperature-Induced Thermal Effects in Colloidal Au Nanoparticles, *J. Phys. Chem. C*, 2022, **126**, 3591–3599.

414 P. Peerakiatkhajohn, J.-H. Yun, T. Butburee, W. Nisspa and S. Thaweesak, Surface Plasmon-Driven Photoelectrochemical Water Splitting of a Ag/TiO_2 Nanoplate Photoanode, *RSC Adv.*, 2022, **12**, 2652–2661.

415 Y.-Q. Su, J. Liu, R. Huang, H.-T. Yang, M.-X. Li, R. Pang, M. Zhang, M.-H. Yang, H.-F. Su, R. Devasenathipathy, Y.-F. Wu, J.-Z. Zhou, D.-Y. Wu, S.-Y. Xie, B.-W. Mao and Z.-Q. Tian, Plasmon-Mediated Photoelectrochemical Hot-Hole Oxidation Coupling Reactions of Adenine on Nanostructured Silver Electrodes, *J. Phys. Chem. Lett.*, 2023, **14**, 5163–5171.

416 S. K. Giri and G. C. Schatz, Photodissociation of H_2 on Ag and Au Nanoparticles: Effect of Size and Plasmon versus Interband Transitions on Threshold Intensities for Dissociation, *J. Phys. Chem. C*, 2023, **127**, 4115–4123.

417 Z. Lian, F. Wu, J. Zi, G. Li, W. Wang and H. Li, Infrared Light-Induced Anomalous Defect-Mediated Plasmonic Hot Electron Transfer for Enhanced Photocatalytic Hydrogen Evolution, *J. Am. Chem. Soc.*, 2023, **145**, 15482–15487.

418 L. Zhai, S. Gebre, B. Chen, D. Xu, J. Chen, Z. Li, Y. Liu, H. Yang, C. Ling, Y. Ge, W. Zhai, C. Chen, L. Ma, Q. Zhang, X. Li, Y. Yan, X. Huang, L. Li, Z. Guan, C.-L. Tao, Z. Huang, H. Wang, J. Liang, Y. Zhu, C. Lee, P. Wang, C. Zhang, L. Gu, Y. Du, T. Lian, H. Zhang and X.-J. Wu, Epitaxial Growth of Highly Symmetrical Branched Noble Metal-Semiconductor Heterostructures with Efficient Plasmon-Induced Hot-Electron Transfer, *Nat. Commun.*, 2023, **14**, 2538.

419 G. T. Forcherio, B. Ostovar, J. Boltersdorf, Y.-Y. Cai, A. C. Leff, K. N. Grew, C. A. Lundgren, S. Link and D. R. Baker, Single-Particle Insights into Plasmonic Hot Carrier Separation Augmenting Photoelectrochemical Ethanol Oxidation with Photocatalytically Synthesized Pd-Au Bimetallic Nanorods, *ACS Nano*, 2022, **16**, 12377–12389.

420 S. Lin, J.-B. Ma, J.-J. Fu, L. Sun, H. Zhang, J. Cheng and J.-F. Li, Constructing The V_o-TiO_2/Ag/TiO_2 Heterojunction for Efficient Photoelectrochemical Nitrogen Reduction to Ammonia, *J. Phys. Chem. C*, 2023, **127**, 1345–1354.

421 Y. Kim, D. H. Wi, J. W. Hong and S. W. Han, Plasmonic Nanocrystal Assembly-Semiconductor Hybrids for Boosting Visible to Near-Infrared Photocatalysis, *ACS Nano*, 2023, **17**, 18641–18651.

422 H. Tang, Z. A. Chen, C. Ouyang, Z. Ye, S. Li, Z. Hong and M. Zhi, Coupling the Surface Plasmon Resonance of WO_{3-x} and Au for Enhancing the Photocatalytic Activity of the Nonoxidative Methane Coupling Reaction, *J. Phys. Chem. C*, 2022, **126**, 20036–20048.

423 S. Wang, L. Wu, J. Li, C. Deng, J. Xue, D. Tang, H. Ji, C. Chen, Y. Zhang and J. Zhao, In Situ Observation of Hot Carrier Transfer at Plasmonic Au/Metal-Organic Frameworks (MOFs) Interfaces, *Chem.–Eur. J.*, 2022, **28**, e202200919.

424 H. Sheng, J. Wang, J. Huang, Z. Li, G. Ren, L. Zhang, L. Yu, M. Zhao, X. Li, G. Li, N. Wang, C. Shen and G. Lu, Strong Synergy Between Gold Nanoparticles and Cobalt Porphyrin Induces Highly Efficient Photocatalytic Hydrogen Evolution, *Nat. Commun.*, 2023, **14**, 1528.

425 P. K. Jain, Taking The Heat Off of Plasmonic Chemistry, *J. Phys. Chem. C*, 2019, **123**, 24347–24351.

426 L. Zhou, D. F. Swearer, H. Robatjazi, A. Alabastri, P. Christopher, E. A. Carter, P. Nordlander and N. J. Halas, Response to Comment On "Quantifying Hot Carrier and Thermal Contributions in Plasmonic Photocatalysis", *Science*, 2019, **364**, eaaw9545.

427 Y. Dubi, I. W. Un, J. Baraban and Y. Sivan, Distinguishing Thermal from Non-Thermal Contributions to Plasmonic Hydrodefluorination, *Nat. Catal.*, 2022, **5**, 244–246.

428 H. Robatjazi, A. Schirato, A. Alabastri, P. Christopher, E. A. Carter, P. Nordlander and N. J. Halas, Reply to: Distinguishing Thermal from Non-Thermal Contributions to Plasmonic Hydrodefluorination, *Nat. Catal.*, 2022, **5**, 247–250.

429 Y. Dubi, I. W. Un and Y. Sivan, Thermal Effects – An Alternative Mechanism for Plasmon-Assisted Photocatalysis, *Chem. Sci.*, 2020, **11**, 5017.

430 P. K. Jain, Comment On "Thermal Effects – An Alternative Mechanism for Plasmon-Assisted Photocatalysis" By Y. Dubi, I. W. Un and Y. Sivan, Chem. Sci., 2020, 11, 5017, *Chem. Sci.*, 2020, **11**, 9022.

431 Y. Dubi, I. W. Un and Y. Sivan, Reply to the 'Comment on "Thermal Effects – An Alternative Mechanism for Plasmon-Assisted Photocatalysis"' by P. Jain, *Chem. Sci.*, 2020, **11**, 9024–9025.

432 Y. Sivan, J. H. Baraban and Y. Dubi, Experimental Practices Required to Isolate Thermal Effects in Plasmonic Photo-Catalysis: Lessons from Recent Experiments, *OSA Continuum*, 2019, **3**, 483.

433 Y. Sivan and Y. Dubi, Recent Developments in Plasmon-Assisted Photocatalysis-A Personal Perspective, *Appl. Phys. Lett.*, 2020, **117**, 130501.

434 K. Metwally, S. Mensah and G. Baffou, Isosbestic Thermoplasmonic Nanostructures, *ACS Photonics*, 2018, **4**, 1544–1551.

435 S. Yu and P. K. Jain, Isotope Effects in Plasmonic Photosynthesis, *Angew. Chem., Int. Ed.*, 2020, **59**, 22480–22483.

436 N. W. Ashcroft and N. D. Mermin, *Solid State Physics*, Saunders College Publ, Fort Worth, 21st edn, 1995.

437 R. Huebener, *Conductors, Semiconductors, Superconductors: An Introduction to Solid State Physics*, Undergraduate lecture notes in physics, Springer, Cham, 3rd edn, 2019.

438 C. Kittel, *Introduction to Solid State Physics*, John Wiley & Sons, 8th edn, 2004.

439 S. H. Simon, *The Oxford Solid State Basics*, Oxford University Press, Oxford, 1st edn, 2013.

440 S. Fang, M. Rahaman, J. Bharti, E. Reisner, M. Robert, G. A. Ozin and Y. H. Hu, Photocatalytic CO_2 Reduction, *Nat. Rev. Methods Primers*, 2023, **3**, 61.

441 J. Albero, Y. Peng and H. Garcia, Photocatalytic CO_2 Reduction to C_{2+} Products, *ACS Catal.*, 2020, **10**, 5734–5749.

442 L. Liu, S. Wang, H. Huang, Y. Zhang and T. Ma, Surface Sites Engineering on Semiconductors to Boost Photocatalytic CO_2 Reduction, *Nano Energy*, 2020, **75**, 104959.

443 X. Li, J. Yu, M. Jaroniec and X. Chen, Cocatalysts for Selective Photoreduction of CO_2 into Solar Fuels, *Chem. Rev.*, 2019, **119**, 3962–4179.

444 L. Wang, W. Chen, D. Zhang, Y. Du, R. Amal, S. Qiao, J. Wu and Z. Yin, Surface Strategies for Catalytic CO_2 Reduction: from Two-Dimensional Materials to Nanoclusters to Single Atoms, *Chem. Soc. Rev.*, 2019, **48**, 5310–5349.

445 T. Inoue, A. Fujishima, S. Konishi and K. Honda, Photoelectrocatalytic Reduction of Carbon Dioxide in Aqueous Suspensions of Semiconductor Powders, *Nature*, 1979, **277**, 637–638.

446 S. Saeidi, N. A. S. Amin and M. R. Rahimpour, Hydrogenation of CO_2 to Value-Added Products—A Review and Potential Future Developments, *J. CO_2 Util.*, 2014, **5**, 66–81.

447 J. Ma, N. Sun, X. Zhang, N. Zhao, F. Xiao, W. Wei and Y. A. Sun, Short Review of Catalysis for CO_2 Conversion, *Catal. Today*, 2009, **148**, 221–231.

448 C.-H. Huang and C.-S. Tan, A Review: CO_2 Utilization, *Aerosol Air Qual. Res.*, 2014, **14**, 480–499.

449 J. Jia, H. Wang, Z. Lu, P. G. O'Brien, M. Ghoussoub, P. Duchesne, Z. Zheng, P. Li, Q. Qiao and L. Wang, Photothermal Catalyst Engineering: Hydrogenation of Gaseous CO_2 with High Activity and Tailored Selectivity, *Adv. Sci.*, 2017, **4**, 1700252.

450 L. Hurtado, R. Natividad and H. García, Photocatalytic Activity of Cu_2O Supported on Multi Layers Graphene for CO_2 Reduction by Water Under Batch and Continuous Flow, *Catal. Commun.*, 2016, **84**, 30–35.

451 D. Mateo, J. Albero and H. García, Graphene Supported NiO/Ni Nanoparticles as Efficient Photocatalyst for Gas Phase CO_2 Reduction with Hydrogen, *Appl. Catal., B*, 2018, **224**, 563–571.

452 J. Zhao, Q. Yang, R. Shi, G. I. N. Waterhouse, X. Zhang, L.-Z. Wu, C.-H. Tung and T. Zhang, FeO–CeO_2 Nanocomposites: An Efficient and Highly Selective Catalyst System for Photothermal CO_2 Reduction to CO, *NPG Asia Mater.*, 2020, **12**, 5.

453 N. Li, B. Wang, Y. Si, F. Xue, J. Zhou, Y. Lu and M. Liu, Toward High-Value Hydrocarbon Generation by Photocatalytic Reduction of CO_2 in Water Vapor, *ACS Catal.*, 2019, **9**, 5590–5602.

454 K. Li, B. Peng and T. Peng, Recent Advances in Heterogeneous Photocatalytic CO_2 Conversion to Solar Fuels, *ACS Catal.*, 2016, **6**, 7485–7527.

455 Q. Wang, J. Warnan, S. Rodríguez-Jiménez, J. J. leung, S. Kalathil, V. Andrei, K. Domen and E. Reisner, Molecularly Engineered Photocatalyst Sheet for Scalable Solar Formate Production from Carbon Dioxide and Water, *Nat. Energy*, 2020, **5**, 703–710.

456 S. Wang, M. Xu, T. Peng, C. Zhang, T. Li, I. Hussain, J. Wang and B. Tan, Porous Hypercrosslinked Polymer-TiO_2-Graphene Composite Photocatalysts for Visible-Light-Driven CO_2 Conversion, *Nat. Commun.*, 2019, **10**, 676.

457 Y. Wang, X. Shang, J. Shen, Z. Zhang, D. Wang, J. Lin, J. C. S. Wu, X. Fu, X. Wang and C. Li, Direct and Indirect Z-Scheme Heterostructure-Coupled Photosystem Enabling Cooperation of CO_2 Reduction and H_2O Oxidation, *Nat. Commun.*, 2020, **11**, 3043.

458 T. Yan, N. Li, L. Wang, Y. Xu, Y. Liang, Y. Dai, B. Huang, J. You and G. A. Ozin, How to Make an Efficient Gas-Phase Heterogeneous CO_2 Hydrogenation Photocatalyst, *Energy Environ. Sci.*, 2020, **13**, 3054–3063.

459 W. Shangguan, Q. Liu, Y. Wang, N. Sun, Y. Liu, R. Zhao, Y. Li, C. Wang and J. Zhao, Molecular-Level Insight into Photocatalytic CO_2 Reduction with H_2O over Au Nanoparticles by Interband Transitions, *Nat. Commun.*, 2022, **13**, 3894.

460 Y. Li, D. Hui, Y. Sun, Y. Wang, Z. Wu, C. Wang and J. Zhao, Boosting Thermo-Photocatalytic CO_2 Conversion Activity by Using Photosynthesis-Inspired Electron-Proton-Transfer Mediators, *Nat. Commun.*, 2021, **12**, 123.

461 D. Devasia, A. J. Wilson, J. Heo, V. Mohan and P. K. Jain, A Rich Catalog of C–C Bonded Species Formed In CO_2 Reduction on a Plasmonic Photocatalyst, *Nat. Commun.*, 2021, **12**, 2612.

462 T. Billo, F. Y. Fu, P. Raghunath, I. Shown, W. F. Chen, H. T. Lien, T. H. Shen, J. F. Lee, T. S. Chan, K. Y. Huang, C. I. Wu, M. C. Lin, J. S. Hwang, C. H. Lee, L. C. Chen and K. H. Chen, Ni-Nanocluster Modified Black TiO_2 with Dual Active Sites for Selective Photocatalytic CO_2 Reduction, *Small*, 2018, **14**, 1702928.

463 L. Wang, Y. Dong, T. Yan, Z. Hu, F. M. Ali, D. M. Meira, P. N. Duchesne, J. Y. Y. Loh, C. Qiu, E. E. Storey, Y. Xu, W. Sun, M. Ghoussoub, N. P. Kherani, A. S. Helm and G. A. Ozin, Black Indium Oxide a Photothermal CO_2 Hydrogenation Catalyst, *Nat. Commun.*, 2020, **11**, 2432.

464 J. Strand, M. Kaviani, D. Gao, A. M. El-Sayed, V. Afanes'ev and A. L. Shluger, Intrinsic Charge Trapping in

Amorphous Oxide Films: Status and Challenges, *J. Phys. Condens. Matter*, 2018, **30**, 233001.

465 Z. Zhang, C. Mao, D. M. Meira, P. N. Duchesne, A. A. Tountas, Z. Li, C. Qiu, S. Tang, R. Song, X. Ding, J. Sun, J. Yu, J. Y. Howe, W. Tu, L. Wang and G. A. Ozin, New Black Indium Oxide—Tandem Photothermal CO_2-H_2 Methanol Selective Catalyst, *Nat. Commun.*, 2022, **13**, 1512.

466 W. Li, Y. Zhang, Y. Wang, W. Ran, Q. Guan, W. Yi, L. Zhang, D. Zhang, N. Li and T. Yan, Graphdiyne Facilitates Photocatalytic CO_2 Hydrogenation into C_{2+} Hydrocarbons, *Appl. Catal., B*, 2024, **340**, 123267.

467 N. Li, M. Liu, B. Yang, W. Shu, Q. Shen, M. Liu and J. Zhou, Enhanced Photocatalytic Performance toward CO_2 Hydrogenation over Nanosized TiO_2-Loaded Pd under UV Irradiation, *J. Phys. Chem. C*, 2017, **121**, 2923–2932.

468 G. D. Gesesse, C. Wang, B. K. Chang, S. H. Tai, P. Beaunier, R. Wojcieszak, H. Remita, C. Colbeau-Justin and M. N. Ghazzal, A Soft-Chemistry Assisted Strong Metal–Support Interaction on a Designed Plasmonic Core–Shell Photocatalyst for Enhanced Photocatalytic Hydrogen Production, *Nanoscale*, 2020, **12**, 7011–7023.

469 T. L. Thompson and J. T. Yates, Monitoring Hole Trapping in Photoexcited TiO_2(110) using a Surface Photoreaction, *J. Phys. Chem. B*, 2005, **109**, 18230–18236.

470 K. A. Willets and R. P. Van Duyne, Localized Surface Plasmon Resonance Spectroscopy and Sensing, *Annu. Rev. Phys. Chem.*, 2007, **58**, 267–297.

471 X. Zhang, X. Li, D. Zhang, N. Q. Su, W. Yang, H. O. Everitt and J. Liu, Product Selectivity in Plasmonic Photocatalysis for Carbon Dioxide Hydrogenation, *Nat. Commun.*, 2017, **8**, 14542.

472 T. Shao, X. Wang, H. Dong, S. Liu, D. Duan, Y. Li, P. Song, H. Jiang, Z. Hou, C. Gao and Y. Xiong, A Stacked Plasmonic Metamaterial with Strong Localized Electric Field Enables Highly Efficient Broadband Light-Driven CO_2 Hydrogenation, *Adv. Mater.*, 2022, **34**, 2202367.

473 X. Zhang, Y. Fan, E. You, Z. Li, Y. Dong, L. Chen, Y. Yang, Z. Xie, Q. Kuang and L. Zheng, MOF Encapsulated Sub-Nm Pd Skin/Au Nanoparticles as Antenna-Reactor Plasmonic Catalyst for Light Driven CO_2 Hydrogenation, *Nano Energy*, 2021, **84**, 105950.

474 T. Butburee, Z. Sun, A. Centeno, F. Xie, Z. Zhao, D. Wu, P. Peerakiatkhajohn, S. Thaweesak, H. Wang and L. Wang, Improved CO_2 Photocatalytic Reduction Using a Novel 3-Component Heterojunction, *Nano Energy*, 2019, **62**, 426–433.

475 W. Zhang, L. Wang, K. Wang, M. U. Khan, M. Wang, H. Li and J. Zeng, Integration of Photothermal Effect and Heat Insulation to Efficiently Reduce Reaction Temperature of CO_2 Hydrogenation, *Small*, 2016, **13**, 1602583.

476 I. García-García, E. C. Lovell, R. J. Wong, V. L. Barrio, J. Scott, J. F. Cambra and R. Amal, Silver-Based Plasmonic Catalysts for Carbon Dioxide Reduction, *ACS Sustainable Chem. Eng.*, 2020, **8**, 1879–1887.

477 X. Zhang, H. Liu, Y. Wang, S. Yang, Q. Chen, Z. Zhao, Y. Yang, Q. Kuang and Z. Xie, Hot-Electron-Induced CO_2 Hydrogenation on Au@AuRu/g-C_3N_4 Plasmonic Bimetal–Semiconductor Heterostructure, *Chem. Eng. J.*, 2022, **443**, 136482.

478 Y.-F. Xu, M.-Z. Yang, B.-X. Chen, X.-D. Wang, H.-Y. Chen, D.-B. Kuang and C.-Y. Su, A $CsPbBr_3$ Perovskite Quantum Dot/Graphene Oxide Composite for Photocatalytic CO_2 Reduction, *J. Am. Chem. Soc.*, 2017, **139**, 5660–5663.

479 A. Li, T. Wang, C. Li, Z. Huang, Z. Luo and J. Gong, Adjusting the Reduction Potential of Electrons by Quantum Confinement for Selective Photoreduction of CO_2 to Methanol, *Angew. Chem., Int. Ed.*, 2019, **58**, 3804–3808.

480 J. Di, X. Zhao, C. Lian, M. Ji, J. Xia, J. Xiong, W. Zhou, X. Cao, Y. She, H. Liu, K. P. Loh, S. J. Pennycook, H. Li and Z. Liu, Atomically-Thin Bi_2MoO_6 Nanosheets with Vacancy Pairs for Improved Photocatalytic CO_2 Reduction, *Nano Energy*, 2019, **61**, 54–59.

481 Y. Zhang, L. Li, Q. Han, L. Tang, X. Chen, J. Hu, Z. Li, Y. Zhou, J. Liu and Z. Zou, Bi_2 MoO_6 Nanostrip Networks for Enhanced Visible-Light Photocatalytic Reduction of CO_2 to CH_4, *ChemPhysChem*, 2017, **18**, 3240–3244.

482 X. Li, J. Yu, M. Jaroniec and X. Chen, Cocatalysts for Selective Photoreduction of CO_2 into Solar Fuels, *Chem. Rev.*, 2019, **119**, 3962–4179.

483 J. Ran, M. Jaroniec and S.-Z. Qiao, Cocatalysts in Semiconductor-Based Photocatalytic CO_2 Reduction: Achievements, Challenges, and Opportunities, *Adv. Mater.*, 2018, **30**, 1704649.

484 K.-L. Bae, J. Kim, C. K. Lim, K. M. Nam and H. Song, Colloidal Zinc Oxide-Copper(I) Oxide Nanocatalysts for Selective Aqueous Photocatalytic Carbon Dioxide Conversion into Methane, *Nat. Commun.*, 2017, **8**, 1156.

485 S. Wang, B. Y. Guan and X. W. D. Lou, Construction of ZnIn2S4–In2O3 Hierarchical Tubular Heterostructures for Efficient CO_2 Photoreduction, *J. Am. Chem. Soc.*, 2018, **140**, 5037–5040.

486 M. E. Aguirre, R. Zhou, A. J. Eugene, M. I. Guzman and M. A. Grela, Cu_2O/TiO_2 Heterostructures for CO_2 Reduction through a Direct Z-Scheme: Protecting Cu_2O from Photocorrosion, *Appl. Catal., B*, 2017, **217**, 485–493.

487 X. Jiao, Z. Chen, X. Li, Y. Sun, S. Gao, W. Yan, C. Wang, Q. Zhang, Y. Lin, Y. Luo and Y. Xie, Defect-Mediated Electron–Hole Separation in One-Unit-Cell $ZnIn_2S_4$ Layers for Boosted Solar-Driven CO_2 Reduction, *J. Am. Chem. Soc.*, 2017, **139**, 7586–7594.

488 J. Di, C. Zhu, M. Ji, M. Duan, R. Long, C. Yan, K. Gu, J. Xiong, Y. She, J. Xia, H. Li and Z. Liu, Defect-Rich Bi_{12} O_{17} Cl_2 Nanotubes Self-Accelerating Charge Separation for Boosting Photocatalytic CO_2 Reduction, *Angew. Chem., Int. Ed.*, 2018, **57**, 14847–14851.

489 J. Wu, X. Li, W. Shi, P. Ling, Y. Sun, X. Jiao, S. Gao, L. Liang, J. Xu, W. Yan, C. Wang and Y. Xie, Efficient Visible-Light-Driven CO_2 Reduction Mediated by Defect-Engineered BiOBr Atomic Layers, *Angew. Chem., Int. Ed.*, 2018, **130**, 8855–8859.

490 J. Wang, T. Xia, L. Wang, X. Zheng, Z. Qi, C. Gao, J. Zhu, Z. Li, H. Xu and Y. Xiong, Enabling Visible-Light-Driven Selective CO_2 Reduction by Doping Quantum Dots:

Trapping Electrons and Suppressing H_2 Evolution, *Angew. Chem., Int. Ed.*, 2018, **57**, 16447–16451.

491 J. Yu, J. Low, W. Xiao, P. Zhou and M. Jaroniec, Enhanced Photocatalytic CO_2 -Reduction Activity of Anatase TiO_2 by Coexposed {001} and {101} Facets, *J. Am. Chem. Soc.*, 2014, **136**, 8839–8842.

492 S. Wang, B. Y. Guan, Y. Lu and X. W. Lou, Formation of Hierarchical In_2S_3–$CdIn_2S_4$ Heterostructured Nanotubes for Efficient and Stable Visible Light CO_2 Reduction, *"D"J. Am. Chem. Soc.*, 2017, **139**, 17305–17308.

493 X. Jiao, K. Zheng, L. Liang, X. Li, Y. Sun and Y. Xie, Fundamentals and Challenges of Ultrathin 2D Photocatalysts in Boosting CO_2 Photoreduction, *Chem. Soc. Rev.*, 2020, **49**, 6592–6604.

494 Ș. Neaț u, J. A. Maciá-Agulló, P. Concepción and H. Garcia, Gold–Copper Nanoalloys Supported on TiO_2 as Photocatalysts for CO_2 Reduction by Water, *J. Am. Chem. Soc.*, 2014, **136**, 15969–15976.

495 H.-C. Hsu, I. Shown, H.-Y. Wei, Y.-C. Chang, H.-Y. Du, Y.-G. Lin, C.-A. Tseng, C.-H. Wang, L.-C. Chen, Y.-C. Lin and K.-H. Chen, Graphene Oxide as a Promising Photocatalyst for CO_2 to Methanol Conversion, *Nanoscale*, 2013, **5**, 262–268.

496 C. Gao, S. Chen, Y. Wang, J. Wang, X. Zheng, J. Zhu, L. Song, W. Zhang and Y. Xiong, Heterogeneous Single-Atom Catalyst for Visible-Light-Driven High-Turnover CO_2 Reduction: The Role of Electron Transfer, *Adv. Mater.*, 2018, **30**, 1704624.

497 A. Meng, S. Wu, B. Cheng, J. Yu and J. Xu, Hierarchical TiO_2/$Ni(OH)_2$ Composite Fibers with Enhanced Photocatalytic CO_2 Reduction Performance, *J. Mater. Chem. A*, 2018, **6**, 4729–4736.

498 S. Gao, B. Gu, X. Jiao, Y. Sun, X. Zu, F. Yang, W. Zhu, C. Wang, Z. Feng, B. Ye and Y. Xie, Highly Efficient and Exceptionally Durable CO2 Photoreduction to Methanol over Freestanding Defective Single-Unit-Cell Bismuth Vanadate Layers, *J. Am. Chem. Soc.*, 2017, **139**, 3438–3445.

499 M. Li, L. Zhang, X. Fan, Y. Zhou, M. Wu and J. Shi, Highly Selective CO2 Photoreduction to CO over G-C_3N_4/Bi_2WO_6 Composites under Visible Light, *J. Mater. Chem. A*, 2015, **3**, 5189–5196.

500 C. Bie, B. Zhu, F. Xu, L. Zhang and J. Yu, In Situ Grown Monolayer N-Doped Graphene on CdS Hollow Spheres with Seamless Contact for Photocatalytic CO_2 Reduction, *Adv. Mater.*, 2019, **31**, 1902868.

501 R. Long, Y. Li, Y. Liu, S. Chen, X. Zheng, C. Gao, C. He, N. Chen, Z. Qi, L. Song, J. Jiang, J. Zhu and Y. Xiong, Isolation of Cu Atoms in Pd Lattice: Forming Highly Selective Sites for Photocatalytic Conversion of CO_2 to CH_4, *J. Am. Chem. Soc.*, 2017, **139**, 4486–4492.

502 J. L. White, M. F. Baruch, J. E. Pander, Y. Hu, I. C. Fortmeyer, J. E. Park, T. Zhang, K. Liao, J. Gu, Y. Yan, T. W. Shaw, E. Abelev and A. B. Bocarsly, Light-Driven Heterogeneous Reduction of Carbon Dioxide: Photocatalysts and Photoelectrodes, *Chem. Rev.*, 2015, **115**, 12888–12935.

503 D. Voiry, H. S. Shin, K. P. Loh and M. Chhowalla, Low-Dimensional Catalysts for Hydrogen Evolution and CO_2 Reduction, *Nat. Rev. Chem*, 2018, **2**, 0105.

504 F. Chen, Z. Ma, L. Ye, T. Ma, T. Zhang, Y. Zhang and H. Huang, Macroscopic Spontaneous Polarization and Surface Oxygen Vacancies Collaboratively Boosting CO_2 Photoreduction on $BiOIO_3$ Single Crystals, *Adv. Mater.*, 2020, **32**, 1908350.

505 X. Lin, S. Wang, W. Tu, H. Wang, Y. Hou, W. Dai and R. Xu, Magnetic Hollow Spheres Assembled from Graphene-Encapsulated Nickel Nanoparticles for Efficient Photocatalytic CO_2 Reduction, *ACS Appl. Energy Mater.*, 2019, **2**, 7670–7678.

506 S. Xie, Y. Wang, Q. Zhang, W. Deng and Y. Wang, MgO- and Pt-Promoted TiO_2 as an Efficient Photocatalyst for the Preferential Reduction of Carbon Dioxide in the Presence of Water, *ACS Catal.*, 2014, **4**, 3644–3653.

507 S. Chen, H. Wang, Z. Kang, S. Jin, X. Zhang, X. Zheng, Z. Qi, J. Zhu, B. Pan and Y. Xie, Oxygen Vacancy Associated Single-Electron Transfer for Photofixation of CO_2 to Long-Chain Chemicals, *Nat. Commun.*, 2019, **10**, 788.

508 X. Jiao, X. Li, X. Jin, Y. Sun, J. Xu, L. Liang, H. Ju, J. Zhu, Y. Pan, W. Yan, Y. Lin and Y. Xie, Partially Oxidized SnS_2 Atomic Layers Achieving Efficient Visible-Light-Driven CO_2 Reduction, *J. Am. Chem. Soc.*, 2017, **139**, 18044–18051.

509 Y.-X. Pan, Y. You, S. Xin, Y. Li, G. Fu, Z. Cui, Y.-L. Men, F.-F. Cao, S.-H. Yu and J. B. Goodenough, Photocatalytic CO_2 Reduction by Carbon-Coated Indium-Oxide Nanobelts, *J. Am. Chem. Soc.*, 2017, **139**, 4123–4129.

510 S. N. Habisreutinger, L. Schmidt-Mende and J. K. Stolarczyk, Photocatalytic Reduction of CO_2 on TiO_2 and Other Semiconductors, *Angew. Chem., Int. Ed.*, 2013, **52**, 7372–7408.

511 K. Li, B. Peng and T. Peng, Recent Advances in Heterogeneous Photocatalytic CO_2 Conversion to Solar Fuels, *ACS Catal.*, 2016, **6**, 7485–7527.

512 A. Anouar, R. García-Aboal, P. Atienzar, A. Franconetti, N. Katir, A. El Kadib, A. Primo and H. Garcia, Remarkable Activity of 002 Facet of Ruthenium Nanoparticles Grown on Graphene Films on the Photocatalytic CO_2 Methanation, *Adv. Sustainable Syst.*, 2022, **6**, 2100487.

513 X. Zu, Y. Zhao, X. Li, R. Chen, W. Shao, L. Li, P. Qiao, W. Yan, Y. Pan, Q. Xu, J. Zhu, Y. Sun and Y. Xie, Reversible Switching Cu^{II}/Cu^{I} Single Sites Catalyze High-rate and Selective CO_2 Photoreduction, *Angew. Chem., Int. Ed.*, 2023, **62**, e202215247.

514 Y. Li, J. Hao, H. Song, F. Zhang, X. Bai, X. Meng, H. Zhang, S. Wang, Y. Hu and J. Ye, Selective Light Absorber-Assisted Single Nickel Atom Catalysts for Ambient Sunlight-Driven CO_2 Methanation, *Nat. Commun.*, 2019, **10**, 2359.

515 M. Marszewski, S. Cao, J. Yu and M. Jaroniec, Semiconductor-Based Photocatalytic CO_2 Conversion, *Mater. Horiz.*, 2015, **2**, 261–278.

516 Y. Shi, G. Zhan, H. Li, X. Wang, X. Liu, L. Shi, K. Wei, C. Ling, Z. Li, H. Wang, C. Mao, X. Liu and L. Zhang, Simultaneous Manipulation of Bulk Excitons and Surface

Defects for Ultrastable and Highly Selective CO_2 Photoreduction, *Adv. Mater.*, 2021, **33**, 2100143.

517 L. Liang, F. Lei, S. Gao, Y. Sun, X. Jiao, J. Wu, S. Qamar and Y. Xie, Single Unit Cell Bismuth Tungstate Layers Realizing Robust Solar CO_2 Reduction to Methanol, *Angew. Chem., Int. Ed.*, 2015, **54**, 13971–13974.

518 Q. Liu, D. Wu, Y. Zhou, H. Su, R. Wang, C. Zhang, S. Yan, M. Xiao and Z. Zou, Single-Crystalline, Ultrathin $ZnGa_2O_4$ Nanosheet Scaffolds to Promote Photocatalytic Activity in CO_2 Reduction into Methane, *ACS Appl. Mater. Interfaces*, 2014, **6**, 2356–2361.

519 L. Hao, L. Kang, H. Huang, L. Ye, K. Han, S. Yang, H. Yu, M. Batmunkh, Y. Zhang and T. Ma, Surface-Halogenation-Induced Atomic-Site Activation and Local Charge Separation for Superb CO_2 Photoreduction, *Adv. Mater.*, 2019, **31**, 1900546.

520 H. Yu, J. Li, Y. Zhang, S. Yang, K. Han, F. Dong, T. Ma and H. Huang, Three-in-One Oxygen Vacancies: Whole Visible-Spectrum Absorption, Efficient Charge Separation, and Surface Site Activation for Robust CO_2 Photoreduction, *Angew. Chem., Int. Ed.*, 2019, **58**, 3880–3884.

521 H. Huang, R. Shi, Z. Li, J. Zhao, C. Su and T. Zhang, Triphase Photocatalytic CO_2 Reduction over Silver-Decorated Titanium Oxide at a Gas–Water Boundary, *Angew. Chem., Int. Ed.*, 2022, **61**, e202200802.

522 F. Xu, K. Meng, B. Cheng, S. Wang, J. Xu and J. Yu, Unique S-Scheme Heterojunctions in Self-Assembled TiO2/CsPbBr3 Hybrids for CO_2 Photoreduction, *Nat. Commun.*, 2020, **11**, 4613.

523 Y. Wang, Z. Zhang, L. Zhang, Z. Luo, J. Shen, H. Lin, J. Long, J. C. S. Wu, X. Fu, X. Wang and C. Li, Visible-Light Driven Overall Conversion of CO_2 and H_2O to CH_4 and O_2 on 3D-SiC@2D-MoS_2 Heterostructure, *J. Am. Chem. Soc.*, 2018, **140**, 14595–14598.

524 B. AlOtaibi, S. Fan, D. Wang, J. Ye and Z. Mi, Wafer-Level Artificial Photosynthesis for CO_2 Reduction into CH_4 and CO Using GaN Nanowires, *ACS Catal.*, 2015, **5**, 5342–5348.

525 A. Iwase, S. Yoshino, T. Takayama, Y. H. Ng, R. Amal and A. Kudo, Water Splitting and CO_2 Reduction under Visible Light Irradiation Using Z-Scheme Systems Consisting of Metal Sulfides, CoOx-Loaded $BiVO_4$, and a Reduced Graphene Oxide Electron Mediator, *J. Am. Chem. Soc.*, 2016, **138**, 10260–10264.

526 W. Zhang, A. R. Mohamed and W. Z. Ong, Scheme Photocatalytic Systems for Carbon Dioxide Reduction: Where Are We Now?, *Angew. Chem., Int. Ed.*, 2020, **59**, 22894–22915.

527 X. Li, Y. Sun, J. Xu, Y. Shao, J. Wu, X. Xu, Y. Pan, H. Ju, J. Zhu and Y. Xie, Selective Visible-Light-Driven Photocatalytic CO_2 Reduction to CH_4 Mediated by Atomically Thin $CuIn_5S_8$ Layers, *Nat. Energy*, 2019, **4**, 690–699.

528 Y. Shi, J. Li, C. Mao, S. Liu, X. Wang, X. Liu, S. Zhao, X. Liu, Y. Huang and L. Zhang, Van Der Waals Gap-Rich BiOCl Atomic Layers Realizing Efficient, Pure-Water CO_2-to-CO Photocatalysis, *Nat. Commun.*, 2021, **12**, 5923.

529 X. Feng, R. Zheng, C. Gao, W. Wei, J. Peng, R. Wang, S. Yang, W. Zou, X. Wu, Y. Ji and H. Chen, Unlocking Bimetallic Active Sites via a Desalination Strategy for Photocatalytic Reduction of Atmospheric Carbon Dioxide, *Nat. Commun.*, 2022, **13**, 2146.

530 I. Shown, S. Samireddi, Y.-C. Chang, R. Putikam, P.-H. Chang, A. Sabbah, F.-Y. Fu, W.-F. Chen, C.-I. Wu, T.-Y. Yu, P.-W. Chung, M. C. Lin, L.-C. Chen and K.-H. Chen, Carbon-Doped SnS_2 Nanostructure as a High-Efficiency Solar Fuel Catalyst under Visible Light, *Nat. Commun.*, 2018, **9**, 169.

531 M. Sayed, F. Xu, P. Kuang, J. Low, S. Wang, L. Zhang and J. Yu, Sustained CO_2-Photoreduction Activity and High Selectivity over Mn, C-Codoped ZnO Core-Triple Shell Hollow Spheres, *Nat. Commun.*, 2021, **12**, 4936.

532 J. Di, C. Chen, S.-Z. Yang, S. Chen, M. Duan, J. Xiong, C. Zhu, R. Long, W. Hao, Z. Chi, H. Chen, Y.-X. Weng, J. Xia, L. Song, S. Li, H. Li and Z. Liu, Isolated Single Atom Cobalt in Bi_3O_4Br Atomic Layers to Trigger Efficient CO_2 Photoreduction, *Nat. Commun.*, 2019, **10**, 2840.

533 J. Y. Do, R. K. Chava, K. K. Mandari, N.-K. Park, H.-J. Ryu, M. W. Seo, D. Lee, T. S. Senthil and M. Kang, Selective Methane Production from Visible-Light-Driven Photocatalytic Carbon Dioxide Reduction Using the Surface Plasmon Resonance Effect of Superfine Silver Nanoparticles Anchored on Lithium Titanium Dioxide Nanocubes (Ag@LixTiO$_2$), *Appl. Catal., B*, 2018, **237**, 895–910.

534 W.-J. Ong, L. K. Putri, L.-L. Tan, S.-P. Chai and S.-T. Yong, Heterostructured AgX/g-C_3N_4 (X = Cl and Br) Nanocomposites via a Sonication-Assisted Deposition-Precipitation Approach: Emerging Role of Halide Ions in the Synergistic Photocatalytic Reduction of Carbon Dioxide, *Appl. Catal., B*, 2016, **180**, 530–543.

535 W. Tu, Y. Zhou, H. Li, P. Li and Z. Zou, Au@TiO_2 Yolk–Shell Hollow Spheres for Plasmon-Induced Photocatalytic Reduction of CO_2 to Solar Fuel via a Local Electromagnetic Field, *Nanoscale*, 2015, **7**, 14232–14236.

536 J. Shen, Z. Chen, S. Han, H. Zhang, H. Xu, C. Xu, Z. Ding, R. Yuan, J. Chen and J. Long, Plasmonic Electrons-Driven Solar-to-Hydrocarbon Conversion over Au NR@ZnO Core-Shell Nanostructures, *ChemCatChem*, 2020, **12**, 2989–2994.

537 S. Yu, A. J. Wilson, J. Heo and P. K. Jain, Plasmonic Control of Multi-Electron Transfer and C–C Coupling in Visible-Light-Driven CO_2 Reduction on Au Nanoparticles, *Nano Lett.*, 2018, **18**, 2189–2194.

538 D. Devasia, A. J. Wilson, J. Heo, V. Mohan and P. K. Jain, A Rich Catalog of C–C Bonded Species Formed in CO_2 Reduction on a Plasmonic Photocatalyst, *Nat. Commun.*, 2021, **12**, 2612.

539 H. Lai, W. Xiao, Y. Wang, T. Song, B. Long, S. Yin, A. Ali and G.-J. Deng, Plasmon-Induced Carrier Separation Boosts High-Selective Photocatalytic CO_2 Reduction on Dagger-Axe-like Cu@Co Core–Shell Bimetal, *Chem. Eng. J.*, 2021, **417**, 129295.

540 S. Li, P. Miao, Y. Zhang, J. Wu, B. Zhang, Y. Du, X. Han, J. Sun and P. Xu, Recent Advances in Plasmonic Nanostructures for Enhanced Photocatalysis and Electrocatalysis, *Adv. Mater.*, 2021, **33**, 2000086.

541 Y. Li, M. Wen, Y. Wang, G. Tian, C. Wang and J. Zhao, Plasmonic Hot Electrons from Oxygen Vacancies for Infrared Light-Driven Catalytic CO_2 Reduction on Bi_2O_{3-x}, *Angew. Chem.*, 2021, **133**, 923–929.

542 B. László, K. Baán, E. Varga, A. Oszkó, A. Erdőhelyi, Z. Kónya and J. Kiss, Photo-Induced Reactions in the CO_2 -Methane System on Titanate Nanotubes Modified with Au and Rh Nanoparticles, *Appl. Catal., B*, 2016, **199**, 473–484.

543 B. Tahir, M. Tahir and N. A. S. Amin, Photo-Induced CO_2 Reduction by CH_4/H_2O to Fuels Over Cu-Modified g-C_3N_4 Nanorods Under Simulated Solar, *Energy Appl. Surf. Sci.*, 2017, **419**, 875–885.

544 F. Pan, X. Xiang, W. Deng, H. Zhao, X. Feng and Y. Li, A Novel Photo-Thermochemical Approach for Enhanced Carbon Dioxide Reforming of Methane, *ChemCatChem*, 2018, **10**, 940–945.

545 Q. Zhang, M. Mao, Y. Li, Y. Yang, H. Huang, Z. Jiang, Q. Hu, S. Wu and X. Zhao, Novel Photoactivation Promoted Light-Driven CO_2 Reduction by CH_4 On Ni/CeO_2 Nanocomposite with High Light-To-Fuel Efficiency and Enhanced Stability, *Appl. Catal., B*, 2018, **239**, 555–564.

546 H. Liu, X. Meng, T. D. Dao, H. Zhang, P. Li, K. Chang, T. Wang, M. Li, T. Nagao and J. Ye, Conversion of Carbon Dioxide by Methane Reforming under Visible-Light Irradiation: Surface-Plasmon-Mediated Nonpolar Molecule Activation, *Angew. Chem., Int. Ed.*, 2015, **54**, 11545–11549.

547 H. Liu, M. Li, T. D. Dao, Y. Liu, W. Zhou, L. Liu, X. Meng, T. Nagao and J. Ye, Design of PdAu Alloy Plasmonic Nanoparticles for Improved Catalytic Performance in CO_2 Reduction with Visible Light Irradiation, *Nano Energy*, 2016, **26**, 398–404.

548 H. Liu, T. D. Dao, L. Liu, X. Meng, T. Nagao and J. Ye, Light Assisted CO_2 Reduction with Methane Over Group VIII Metals: Universality of Metal Localized Surface Plasmon Resonance in Reactant Activation, *Appl. Catal., B*, 2017, **209**, 183–189.

549 H. Huang, M. Mao, Q. Zhang, Y. Li, J. Bai, Y. Yang, M. Zeng and X. Zhao, Solar-Light-Driven CO_2 Reduction by CH_4 on Silica-Cluster-Modified Ni Nanocrystals with a High Solar-to-Fuel Efficiency and Excellent Durability, *Adv. Energy Mater.*, 2018, **8**, 1–11.

550 H. Liu, X. Meng, T. D. Dao, L. Liu, P. Li, G. Zhao, T. Nagao, L. Yang and J. Ye, Light Assisted CO_2 Reduction with Methane over SiO_2 Encapsulated Ni Nanocatalysts for Boosted Activity and Stability, *J. Mater. Chem. A*, 2017, **5**, 10567–10573.

551 H. Liu, H. Song, W. Zhou, X. Meng and J. A. Ye, Promising Application of Optical Hexagonal TaN in Photocatalytic Reactions, *Angew. Chem., Int. Ed.*, 2018, **57**, 16781–16784.

552 B. Han, W. Wei, L. Chang, P. Cheng and Y. H. Hu, Efficient Visible Light Photocatalytic CO_2 Reforming of CH_4, *ACS Catal.*, 2016, **6**, 494–497.

553 S. Shoji, X. Peng, A. Yamaguchi, R. Watanabe, C. Fukuhara, Y. Cho, T. Yamamoto, S. Matsumura, M. W. Yu, S. Ishii, T. Fujita, H. Abe and M. Miyayuchi, Photocatalytic Uphill Conversion of Natural Gas Beyond the Limitation of Thermal Reaction Systems, *Nat. Catal.*, 2020, **3**, 148–153.

554 A. C. Luntz, M. Persson, S. Wagner, C. Frischkorn and M. Wolf, Femtosecond Laser Induced Associative Desorption of H_2 from Ru(0001): Comparison of "First Principles" Theory with Experiment, *J. Chem. Phys.*, 2006, **124**, 244702.

555 V. A. Spata and E. A. Carter, Mechanistic Insights into Photocatalyzed Hydrogen Desorption from Palladium Surfaces Assisted by Localized Surface Plasmon Resonances, *ACS Nano*, 2018, **12**, 3512–3522.

556 J. Zhang, K. Xie, Y. Jiang, M. Li, X. Tan, Y. Yang, X. Zhao, L. Wang, Y. Wang, X. Wang, Y. Zhu, H. Chen, M. Wu, H. Sun and S. Wang, Photoinducing Different Mechanisms on a Co-Ni Bimetallic Alloy in Catalytic Dry Reforming of Methane, *ACS Catal.*, 2023, **13**, 10855–10865.

557 H. Li, C. Mao, H. Shang, Z. Yang, Z. Ai and L. Zhang, New Opportunities for Efficient N_2 Fixation by Nanosheet Photocatalysts, *Nanoscale*, 2018, **10**, 15429–15435.

558 X. Chen, N. Li, Z. Kong, W.-J. Ong and X. Zhao, Photocatalytic Fixation of Nitrogen to Ammonia: State-of-the-art Advancements and Future Prospects, *Mater. Horiz.*, 2018, **5**, 9–27.

559 L. Wang, M. K. Xia, H. Wang, K. F. Huang, C. X. Qian, C. T. Maravelias and G. A. Ozin, Greening Ammonia Toward the Solar Ammonia Refinery, *Joule*, 2018, **2**, 1055–1074.

560 S. M. Sun, Q. An, W. Z. Wang, L. Zhang, J. J. Liu and W. A. Goddard, Efficient Photocatalytic Reduction of Dinitrogen to Ammonia On Bismuth Monoxide Quantum Dots, *J. Mater. Chem. A*, 2017, **5**, 201–209.

561 Y. Hao, X. Dong, S. Zhai, H. Ma, X. Wang and X. Zhang, Hydrogenated Bismuth Molybdate Nanoframe for Efficient Sunlight-Driven Nitrogen Fixation from Air, *Chem.–Eur. J.*, 2016, **22**, 18722–18728.

562 L. Zhang, R. Gu, J. Zhang, H. Liu, S. Zhu, D. Su, T. Wang, Y. Mou and C. Wang, Plasmonic Bi-Doped Bi-$Bi_2Sn_2O_7$/Bi-g-C_3N_4 Photothermal Catalysis for Nitrogen Fixation, *Green Chem.*, 2025, **27**, 2138–2149.

563 C. Xu, P. Qiu, L. Li, H. Chen, F. Jiang and X. Wang, Bismuth Subcarbonate with Designer Defects for Broad-Spectrum Photocatalytic Nitrogen Fixation, *ACS Appl. Mater. Interfaces*, 2018, **10**, 25321–25328.

564 J. Wang, G. Ran, J. Gao, D. Li, G. I. N. Waterhouse, R. Shi, W. Zhang, J. Tang, L. Wu, Y. Zhao and T. Zhang, Solar-Driven Conversion of Nitrogen and Water to Solid Fertilizer in an Outdoor 1 m^2 Panel Reactor, *Adv. Mater.*, 2025, **37**, 2420199.

565 Y. Bai, L. Ye, T. Chen, L. Wang, X. Shi, X. Zhang and D. Chen, Facet-Dependent Photocatalytic N_2 Fixation of Bismuth-Rich Bi_5O_7I Nanosheets, *ACS Appl. Mater. Interfaces*, 2016, **8**, 27661–27668.

566 J. Wang, W. Lin, Y. Ran, J. Cui, L. Wang, X. Yu and Y. Zhang, Nanotubular TiO_2 with Remedied Defects for Photocatalytic Nitrogen Fixation, *J. Phys. Chem. C*, 2020, **124**, 1253–1259.

567 S. H. Cao, H. Chen, F. Jiang and X. Wang, Nitrogen Photofixation by Ultrathin Amine-Functionalized Graphitic Carbon Nitride Nanosheets as a Gaseous Product from Thermal Polymerization of Urea, *Appl. Catal., B*, 2018, **224**, 222–229.

568 G. Dong, W. Ho and C. Wang, Selective Photocatalytic N_2 Fixation Dependent on g-C_3N_4 Induced by Nitrogen Vacancies, *J. Mater. Chem. A*, 2015, **3**, 23435–23441.

569 X. Li, X. Sun, L. Zhang, S. Sun and W. Wang, Efficient Photocatalytic Fixation of N_2 By KOH-treated g-C_3N_4, *J. Mater. Chem. A*, 2018, **6**, 3005–3011.

570 X. Feng, H. Chen, F. Jiang and X. Wang, Enhanced Visible-Light Photocatalytic Nitrogen Fixation over Semicrystalline Graphitic Carbon Nitride: Oxygen and Sulfur Co-Doping for Crystal and Electronic Structure Modulation, *J. Colloid Interface Sci.*, 2018, **509**, 298–306.

571 Q. X. Liu, L. H. Ai and J. Jiang, Mxene-Derived TiO_2@C/g-C_3N_4 Heterojunctions for Highly Efficient Nitrogen Photofixation, *J. Mater. Chem. A*, 2018, **6**, 4102–4110.

572 P. X. Xing, P. F. Chen, Z. Q. Chen, X. Hu, H. J. Lin, Y. Wu, L. H. Zhao and Y. M. He, Novel Ternary MoS_2/C-ZnO Composite with Efficient Performance in Photocatalytic NH_3 Synthesis under Simulated Sunlight, *ACS Sustainable Chem. Eng.*, 2018, **6**, 14866–14879.

573 S. H. Cao, N. Zhou, F. H. Gao, H. Chen and F. Jiang, All-Solid-State Z-Scheme 3,4-Dihydroxybenzaldehyde-Functionalized Ga_2O_3/Graphitic Carbon Nitride Photocatalyst with Aromatic Rings as Electron Mediators for Visible-Light Photocatalytic Nitrogen Fixation, *Appl. Catal., B*, 2017, **218**, 600–610.

574 P. X. Qiu, C. M. Xu, N. Zhou, H. Chen and F. Jiang, Metal-Free Black Phosphorus Nanosheets-Decorated Graphitic Carbon Nitride Nanosheets with C-P Bonds for Excellent Photocatalytic Nitrogen Fixation, *Appl. Catal., B*, 2018, **221**, 27–35.

575 Z.-K. Shen, Y.-J. Yuan, P. Wang, W. Bai, L. Pei, S. Wu, Z.-T. Yu and Z. Zou, Few-Layer Black Phosphorus Nanosheets: A Metal-Free Cocatalyst for Photocatalytic Nitrogen Fixation, *ACS Appl. Mater. Interfaces*, 2020, **12**, 17343–17352.

576 Q. Zhang, S. Hu, Z. Fan, D. Liu, Y. Zhao, H. Ma and F. Li, Preparation of g-C_3N_4/ZnMoCdS Hybrid Heterojunction Catalyst with Outstanding Nitrogen Photofixation Performance under Visible Light via Hydrothermal Post-Treatment, *Dalton Trans.*, 2016, **45**, 3497–3505.

577 W. R. Zhao, J. Zhang, X. Zhu, M. Zhang, J. Tang, M. Tan and Y. Wang, Enhanced Nitrogen Photofixation on Fe-Doped TiO_2 with Highly Exposed (101) Facets in the Presence of Ethanol as Scavenger, *Appl. Catal., B*, 2014, **144**, 468–477.

578 M. Lashgari and P. Zeinalkhani, Photocatalytic N_2 Conversion to Ammonia using Efficient Nanostructured Solar-Energy-Materials in Aqueous Media: A Novel Hydrogenation Strategy and Basic Understanding of the Phenomenon, *Appl. Catal., A*, 2017, **529**, 91–97.

579 W. Zhao, H. Xi, M. Zhang, Y. Li, J. Chen, J. Zhang and X. Zhu, Enhanced Quantum Yield of Nitrogen Fixation for Hydrogen Storage with in Situ-Formed Carbonaceous Radicals, *Chem. Commun.*, 2015, **51**, 4785–4788.

580 S. Z. Hu, W. D. Zhang, J. Bai, G. Lu, L. Zhang and G. Wu, Construction of A 2D/2D g-C_3N_4/rGO Hybrid Heterojunction Catalyst with Outstanding Charge Separation Ability and Nitrogen Photofixation Performance via a Surface Protonation Process, *RSC Adv.*, 2016, **6**, 25695–25702.

581 N. Zhang, A. Jalil, D. Wu, S. Chen, Y. Liu, C. Gao, W. Ye, Z. Qi, H. Ju, C. Wang, X. Wu, L. Song, J. Zhu and Y. Xiong, Refining Defect States in $W_{18}O_{49}$ by Mo Doping: A Strategy for Tuning N_2 Activation Towards Solar-Driven Nitrogen Fixation, *J. Am. Chem. Soc.*, 2018, **140**, 9434–9443.

582 X. Xue, R. Chen, H. Chen, Y. Hu, Q. Ding, Z. Liu, L. Ma, G. Zhu, W. Zhang, Q. Yu, J. Liu, J. Ma and Z. Jin, Oxygen Vacancy Engineering Promoted Photocatalytic Ammonia Synthesis on Ultrathin Two-Dimensional Bismuth Oxybromide Nanosheets, *Nano Lett.*, 2018, **18**, 7372–7377.

583 S. Wang, X. Hai, X. Ding, K. Chang, Y. Xiang, X. Meng, Z. Yang, H. Chen and J. Ye, Light-Switchable Oxygen Vacancies in Ultrafine Bi_5O_7Br Nanotubes for Boosting Solar-Driven Nitrogen Fixation in Pure Water, *Adv. Mater.*, 2017, **29**, 1701774.

584 P. Li, Z. Zhou, Q. Wang, M. Guo, S. Chen, J. Low, R. Long, W. Liu, P. Ding, Y. Wu and Y. Xiong, Visible-Light-Driven Nitrogen Fixation Catalyzed by Bi_5O_7Br Nanostructures: Enhanced Performance by Oxygen Vacancies, *J. Am. Chem. Soc.*, 2020, **142**, 12430–12439.

585 M. Lan, N. Zheng, X. Dong, C. Hua, H. Ma and X. Zhang, Bismuth-Rich Bismuth Oxyiodide Microspheres with Abundant Oxygen Vacancies as an Efficient Photocatalyst for Nitrogen Fixation, *Dalton Trans.*, 2020, **49**, 9123–9129.

586 J. Di, J. Xia, M. F. Chisholm, J. Zhong, C. Chen, X. Cao, F. Dong, Z. Chi, H. Chen, Y. X. Weng, J. Xiong, S. Z. Yang, H. Li, Z. Liu and S. Dai, Defect-Tailoring Mediated Electron-Hole Separation in Single-Unit-Cell Bi_3O_4Br Nanosheets for Boosting Photocatalytic Hydrogen Evolution and Nitrogen Fixation, *Adv. Mater.*, 2019, **31**, 1807576.

587 X. Gao, L. An, D. Qu, W. Jiang, Y. Chai, S. Sun, X. Liu and Z. Sun, Enhanced Photocatalytic N_2 Fixation by Promoting N_2 Adsorption with a Co-Catalyst, *Sci. Bull.*, 2019, **64**, 918–925.

588 L. Q. Ye, C. Q. Han, Z. Y. Ma, Y. M. Leng, J. Li, X. X. Ji, D. Q. Bi, H. Q. Xie and Z. X. Huang, Ni_2P Loading on $Cd_{0.5}Zn_{0.5}S$ Solid Solution for Exceptional Photocatalytic Nitrogen Fixation Under Visible Light, *Chem. Eng. J.*, 2017, **307**, 311–318.

589 Y. Zhao, Y. Zhao, G. I. N. Waterhouse, L. Zheng, X. Cao, F. Teng, L. Z. Wu, C. H. Tung, D. O'Hare and T. Zhang, Layered-Double-Hydroxide Nanosheets as Efficient Visible-Light-Driven Photocatalysts for Dinitrogen Fixation, *Adv. Mater.*, 2017, **29**, 1703828.

590 N. Zhang, L. Li, Q. Shao, T. Zhu, X. Huang and X. Xiao, Fe-Doped Biocl Nanosheets with Light-Switchable Oxygen Vacancies for Photocatalytic Nitrogen Fixation, *ACS Appl. Energy Mater.*, 2019, **2**, 8394–8398.

591 Y. Liao, J. N. Lin, B. H. Cui, G. Xie and S. Hu, Well-Dispersed Ultrasmall Ruthenium On TiO_2(P25) For Effective Photocatalytic N_2 Fixation in Ambient Condition, *J. Photochem. Photobiol., A*, 2020, **387**, 112100.

592 Y. Shiraishi, M. Hashimoto, K. Chishiro, K. Moriyama, S. Tanaka and T. Hirai, Photocatalytic Dinitrogen Fixation with Water on Bismuth Oxychloride in Chloride Solutions for Solar-To-Chemical Energy Conversion, *J. Am. Chem. Soc.*, 2020, **142**, 7574–7583.

593 Y. Shiraishi, K. Chishiro, S. Tanaka and T. Hirai, Photocatalytic Dinitrogen Reduction with Water on Boron-Doped Carbon Nitride Loaded with Nickel Phosphide Particles, *Langmuir*, 2020, **36**, 734–741.

594 Y. Li, X. Chen, M. Zhang, Y. Zhu, W. Ren, Z. Mei, M. Gu and F. Pan, Oxygen Vacancy-Rich MoO_{3-X} Nanobelts for Photocatalytic N_2 Reduction to NH_3 in Pure Water, *Catal. Sci. Technol.*, 2019, **9**, 803–810.

595 H. Mou, J. Wang, D. Yu, D. Zhang, W. Chen, Y. Wang, D. Wang and T. Mu, Fabricating Amorphous G-C_3N_4/ZrO_2 Photocatalysts by One-Step Pyrolysis for Solar-Driven Ambient Ammonia Synthesis, *ACS Appl. Mater. Interfaces*, 2019, **11**, 44360–44365.

596 H. Hirakawa, M. Hashimoto, Y. Shiraishi and T. Hirai, Photocatalytic Conversion of Nitrogen to Ammonia with Water on Surface Oxygen Vacancies of Titanium Dioxide, *J. Am. Chem. Soc.*, 2017, **139**, 10929–10936.

597 J. R. Christianson, D. Zhu, R. J. Hamers and J. R. Schmidt, Mechanism of N_2 Reduction to NH_3 by Aqueous Solvated Electrons, *J. Phys. Chem. B*, 2014, **118**, 195–203.

598 J. Yang, Y. Guo, W. Lu, R. Jiang and J. Wang, Emerging Applications of Plasmons in Driving CO_2 Reduction and N_2 Fixation, *Adv. Mater.*, 2018, **30**, 1802227.

599 R. Huang, X. Li, W. Gao, X. Zhang, S. Liang and M. Luo, Recent Advances in Photocatalytic Nitrogen Fixation: From active Sites to Ammonia Quantification Methods, *RSC Adv.*, 2021, **11**, 14844–14861.

600 D. Zhu, L. Zhang, R. E. Ruther and R. J. Hamers, Photo-Illuminated Diamond as a Solid-State Source of Solvated Electrons in Water for Nitrogen Reduction, *Nat. Mater.*, 2013, **12**, 836–841.

601 H. Li, J. Shang, Z. Ai and L. Zhang, Efficient Visible Light Nitrogen Fixation with BiOBr Nanosheets of Oxygen Vacancies on the Exposed {001} Facets, *J. Am. Chem. Soc.*, 2015, **137**, 6393–6399.

602 X. Zheng, H. Han, J. Liu, Y. Yang, L. Pan, S. Zhang, S. Meng and S. Chen, Sulfur Vacancy-Mediated Electron–Hole Separation at MoS_2/CdS Heterojunctions for Boosting Photocatalytic N_2 Reduction, *ACS Appl. Energy Mater.*, 2022, **5**, 4475–4485.

603 H. Huang, S. Wang, X. Fan, D. Philo, L. Fang, W. Tu, T. Qiu, Z. Zou and J. Ye, Near-Infrared Plasmon-Driven Nitrogen Photofixation Achieved by Assembling Size-Controllable Gold Nanoparticles on TiO_2 Nanocavity Arrays, *ACS Sustainable Chem. Eng.*, 2023, **11**, 10993–11001.

604 H. Bai, S. H. Lam, J. Yang, X. Cheng, S. Li, R. Jiang, L. Shao and J. Wang, A Schottky-Barrier-Free Plasmonic Semiconductor Photocatalyst for Nitrogen Fixation in a "One-Stone-Two-Birds" Manner, *Adv. Mater.*, 2022, **34**, 2104226.

605 J. Hu, K. An, Y. Ren, F. R. Wang, Y. Guo, X. Bai, D. Wang and J. Wang, Plasmonic MoO_{3-x}/Ag Photocatalyst for the Fixation of N_2 from Air with the Solar Energy Conversion Efficiency Reaching over 0.28%, *Adv. Mater.*, 2025, **37**, e09652.

606 G. Garcia, R. Buonsanti, E. L. Runnerstrom, R. J. Mendelsberg, A. Llordes, A. Anders, T. J. Richardson and D. J. Milliron, Dynamically Modulating the Surface Plasmon Resonance of Doped Semiconductor Nanocrystals, *Nano Lett.*, 2011, **11**, 4415–4420.

607 U. Guler, V. M. Shalaev and A. Boltasseva, Nanoparticle Plasmonics: Going Practical with Transition Metal Nitrides, *Mater. Today*, 2015, **18**, 227–237.

608 I. Kriegel, F. Scotognella and L. Manna, Plasmonic Doped Semiconductor Nanocrystals: Properties, Fabrication, Applications and Perspectives, *Phys. Rep.*, 2017, **674**, 1–52.

609 J. Shah, Ultrafast Spectroscopy of Semiconductors and Semiconductor Nanostructures, *Springer Series in Solid-State Sciences*, Springer, Berlin, Heidelberg, 1999, vol. 115.

610 R. R. Alfano, *Semiconductors Probed by Ultrafast Laser Spectroscopy*, Academic Press, 1984.

611 P. C. Becker, H. L. Fragnito, C. H. B. Cruz, R. L. Fork, J. E. Cunningham, J. E. Henry and C. V. Shank, Femtosecond Photon Echoes from Band-to-Band Transitions in GaAs, *Phys. Rev. Lett.*, 1988, **61**, 1647–1649.

612 J. Zhu, Y. Li, X. Lin, Y. Han and K. Wu, Coherent Phenomena and Dynamics of Lead Halide Perovskite Nanocrystals for Quantum Information Technologies, *Nat. Mater.*, 2024, **23**, 1027–1040.

613 H. Utzat, W. Sun, A. E. K. Kaplan, F. Krieg, M. Ginterseder, B. Spokoyny, N. D. Klein, K. E. Shulenberger, C. F. Perkinson, M. V. Kovalenko and M. G. Bawendi, Coherent Single-Photon Emission from Colloidal Lead Halide Perovskite Quantum Dots, *Science*, 2019, **363**, 1068–1072.

614 J. L. Oudar, D. Hulin, A. Migus, A. Antonetti and F. Alexandre, Subpicosecond Spectral Hole Burning due to Nonthermalized Photoexcited Carriers in GaAs, *Phys. Rev. Lett.*, 1985, **55**, 2074–2077.

615 M. T. Portella, J.-Y. Bigot, R. W. Schoenlein, J. E. Cunningham and C. V. Shank, k-space Carrier Dynamics in GaAs, *Appl. Phys. Lett.*, 1992, **60**(17), 2123–2125.

616 J. Fu, Q. Xu, G. Han, B. Wu, C. H. A. Huan, M. L. Leek and T. C. Sum, Hot Carrier Cooling Mechanisms in Halide Perovskites, *Nat. Commun.*, 2017, **8**, 1300.

617 W.-Z. Lin, R. W. Schoenlein, J. G. Fujimoto and E. P. Ippen, Femtosecond Absorption Saturation Studies of Hot Carriers in GaAs and AlGaAs, *IEEE J. Quantum Electron.*, 1988, **24**, 267–275.

618 H. Reddy, K. Wang, Z. Kudyshev, L. Zhu, S. Yan, A. Vezzoli, S. J. Higgins, V. Gavini, A. Boltasseva, P. Reddy, V. M. Shalaev and E. Meyhofer, Determining Plasmonic Hot-Carrier Energy Distributions via Single-Molecule Transport Measurements, *Science*, 2020, **369**, 423–426.

619 I. Ahmed, L. Shi, H. Pasanen, P. Vivo, P. Maity, M. Hatamvand and Y. Zhan, There is Plenty of Room at the Top: Generation of Hot Charge Carriers and Their Applications in Perovskite and other Semiconductor-based Optoelectronic Devices, *Light Sci. Appl.*, 2021, **10**, 174.
620 J. B. Khurgin, G. Sun and R. A. Soref, Practical Limits of Absorption Enhancement near Metal Nanoparticles, *Appl. Phys. Lett.*, 2009, **94**, 071103.
621 P. B. Johnson and R. W. Christy, Optical Constants of the Noble Metals, *Phys. Rev. B*, 1972, **6**, 4370–4379.
622 A. O. Govorov, H. Zhang and Y. K. Gun'ko, Theory of Photoinjection of Hot Plasmonic Carriers from Metal Nanostructures into Semiconductors and Surface Molecules, *J. Phys. Chem. C*, 2013, **117**, 16616–16631.
623 R. Sundararaman, P. Narang, A. S. Jermyn, W. A. Goddard III and H. A. Atwater, Theoretical Predictions for Hot-Carrier Generation from Surface Plasmon Decay, *Nat. Commun.*, 2014, **5**, 5788.
624 C. Boerigter, R. Campana, M. Morabito and S. Linic, Evidence and Implications of Direct Charge Excitation as the Dominant Mechanism in Plasmon-Mediated Photocatalysis, *Nat. Commun.*, 2016, **7**, 10545.
625 L. V. Besteiro, X.-T. Kong, Z. Wang, G. Hartland and A. O. Govorov, Understanding Hot-Electron Generation and Plasmon Relaxation in Metal Nanocrystals: Quantum and classical mechanisms, *ACS Photonics*, 2017, **4**, 2759–2781.
626 S. A. Maier, *Plasmonics: Fundamentals and Applications*, Springer US, New York, 2007.
627 J. B. Khurgin, Hot Carriers Generated by Plasmons: Where are they Generated and Where do they go from there?, *Faraday Discuss.*, 2019, **214**, 35–58.
628 F. Toffoletti and E. Collini, Coherent and Incoherent Ultrafast Dynamics in Colloidal Gold Nanorods, *J. Phys. Chem. Lett.*, 2024, **15**, 339–348.
629 G. K. Wertheim, M. A. Butler, K. W. West and D. N. E. Buchanan, Determination of the Gaussian and Lorentzian Content of Experimental Line Shapes, *Rev. Sci. Instrum.*, 1974, **45**, 1369–1371.
630 A. Lietard, C.-S. Hsieh, H. Rhee and M. Cho, Electron Heating and Thermal Relaxation of Gold Nanorods Revealed by Two-Dimensional Electronic Spectroscopy, *Nat. Commun.*, 2018, **9**, 891.
631 W. R. Jeffries, K. Park, R. A. Vaia and K. L. Knappenberger, Resolving Electron–Electron Scattering in Plasmonic Nanorod Ensembles using Two-Dimensional Electronic Spectroscopy, *Nano Lett.*, 2020, **20**, 7722–7727.
632 D. Finkelstein-Shapiro, P.-A. Mante, S. Sarisozen, L. Wittenbecher, I. Minda, S. Balci, T. Pullerits and D. Zigmantas, Understanding Radiative Transitions and Relaxation Pathways in Plexcitons, *Chem*, 2021, **7**, 1092–1107.
633 E. Fresch, F. V. A. Camargo, Q. Shen, C. C. Bellora, T. Pullerits, G. S. Engel, G. Cerullo and E. Collini, Two-Dimensional Electronic Spectroscopy, *Nat. Rev. Methods Primers*, 2023, **3**, 84.
634 S. Biswas, J. Kim, X. Zhang and G. D. Scholes, Coherent Two-Dimensional and Broadband Electronic Spectroscopies, *Chem. Rev.*, 2022, **122**, 4257–4321.
635 K. Kolwas and A. Derkachova, Impact of the Interband Transitions in Gold and Silver on the Dynamics of Propagating and Localized Surface Plasmons, *Nanomaterials*, 2020, **10**, 1411.
636 H. U. Yang, J. D'Archangel, M. L. Sundheimer, E. Tucker, G. D. Boreman and M. B. Raschke, Optical Dielectric Function of Silver, *Phys. Rev. B: Condens. Matter Mater. Phys.*, 2015, **91**, 235137.
637 B. Y. Zheng, H. Zhao, A. Manjavacas, M. McClain, P. Nordlander and N. J. Halas, Distinguishing Between Plasmon-Induced and Photoexcited Carriers in a Device Geometry, *Nat. Commun.*, 2015, **6**, 7797.
638 A. M. Brown, R. Sundararaman, P. Narang, W. A. Goddard and H. A. Atwater, Nonradiative Plasmon Decay and Hot Carrier Dynamics: Effects of Phonons, Surfaces, and Geometry, *ACS Nano*, 2015, **10**, 957–966.
639 J. B. Khurgin and G. Sun, Comparative Analysis of Spasers, Vertical-Cavity Surface-Emitting Lasers and Surface-Plasmon-Emitting Diodes, *Nat. Photonics*, 2014, **8**, 468–473.
640 J. H. Hodak, A. Henglein and G. V. Hartland, Electron-Phonon Coupling Dynamics in Very Small (Between 2 and 8 nm Diameter) Au Nanoparticles, *J. Chem. Phys.*, 2000, **112**, 5942–5947.
641 S. Link, C. Burda, Z. L. Wang and M. A. El-Sayed, Electron Dynamics in Gold and Gold–Silver Alloy Nanoparticles: The Influence of a Nonequilibrium Electron Distribution and the Size Dependence of the Electron–Phonon Relaxation, *J. Chem. Phys.*, 1999, **111**, 1255–1264.
642 E. Minutella, F. Schulz and H. Lange, Excitation-Dependence of Plasmon-Induced Hot Electrons in Gold Nanoparticles, *J. Phys. Chem. Lett.*, 2017, **8**, 4925–4929.
643 A. Arbouet, C. Voisin, D. Christofilos, P. Langot, N. Del Fatti, F. Vallée, J. Lermé, G. Celep, E. Cottancin, M. Gaudry, M. Pellarin, M. Broyer, M. Maillard, M. P. Pileni and M. Treguer, Electron-Phonon Scattering in Metal Clusters, *Phys. Rev. Lett.*, 2003, **90**, 177401.
644 J. Z. Zhang, Ultrafast Studies of Electron Dynamics in Semiconductor and Metal Colloidal Nanoparticles: Effects of Size and Surface, *Acc. Chem. Res.*, 1997, **30**, 423–429.
645 B. A. Smith, J. Z. Zhang, U. Giebel and G. Schmid, Direct Probe of Size-Dependent Electronic Relaxation in Single-Sized Au and Nearly Monodisperse Pt Colloidal Nano-Particles, *Chem. Phys. Lett.*, 1997, **270**, 139–144.
646 C. Voisin, D. Christofilos, N. Del Fatti, F. Vallée, B. Prével, E. Cottancin, J. Lermé, M. Pellarin and M. Broyer, Size-Dependent Electron-Electron Interactions in Metal Nanoparticles, *Phys. Rev. Lett.*, 2000, **85**, 2200–2203.
647 Y. U. Staechelin, D. Hoeing, F. Schulz and H. Lange, Size-dependent Electron–Phonon Coupling in Monocrystalline Gold Nanoparticles, *ACS Photonics*, 2021, **8**, 752–757.
648 S. Link and M. A. El-Sayed, Size and Temperature Dependence of the Plasmon Absorption of Colloidal Gold Nanoparticles, *J. Phys. Chem. B*, 1999, **103**, 4212–4217.

649 W. Ekardt, Work Function of Small Metal Particles: Self-Consistent Spherical Jellium-Background Model, *Phys. Rev. B: Condens. Matter Mater. Phys.*, 1984, **29**, 1558–1564.
650 A. Liebsch, Surface-Plasmon Dispersion and Size Dependence of Mie Resonance: Silver versus Simple Metals, *Phys. Rev. B: Condens. Matter Mater. Phys.*, 1993, **48**, 11317–11328.
651 K. O. Aruda, M. Tagliazucchi, C. M. Sweeney, D. C. Hannah, G. C. Schatz and E. A. Weiss, Identification of Parameters through which Surface Chemistry Determines the Lifetimes of Hot Electrons in Small Au Nanoparticles, *Proc. Natl. Acad. Sci. U. S. A.*, 2013, **110**, 4212–4217.
652 M. Shabaninezhad, A. Abuhagr, N. A. Sakthivel, C. Kumara, A. Dass, K. Kwak, K. Pyo, D. Lee and G. Ramakrishna, Ultrafast Electron Dynamics in Thiolate-Protected Plasmonic Gold Clusters: Size and Ligand Effect, *J. Phys. Chem. C*, 2019, **123**, 13344–13353.
653 K. Kwak, S. S. Kumar and D. Lee, Selective Determination of Dopamine using Quantum-Sized Gold Nanoparticles Protected with Charge Selective Ligands, *Nanoscale*, 2012, **4**, 4240.
654 M. S. Devadas, J. Kim, E. Sinn, D. Lee, T. Goodson and G. Ramakrishna, Unique Ultrafast Visible Luminescence in Monolayer-Protected Au_{25} Clusters, *J. Phys. Chem. C*, 2010, **114**, 22417–22423.
655 J. Romann, J. Wei and M.-P. Pileni, Computational Matching of Surface Plasmon Resonance: Interactions between Silver Nanoparticles and Ligands, *J. Phys. Chem. C*, 2015, **119**, 11094–11099.
656 S. L. Westcott, R. D. Averitt, J. A. Wolfgang, P. Nordlander and N. J. Halas, Adsorbate-Induced Quenching of Hot Electrons in Gold Core−Shell Nanoparticles, *J. Phys. Chem. B*, 2001, **105**, 9913–9917.
657 M. Hu and G. V. Hartland, Heat Dissipation for Au Particles in Aqueous Solution: Relaxation Time versus Size, *J. Phys. Chem. B*, 2003, **107**, 1284.
658 W. Huang, W. Qian, M. A. El-Sayed, Y. Ding and Z. L. Wang, Effect of the Lattice Crystallinity on the Electron−Phonon Relaxation Rates in Gold Nanoparticles, *J. Phys. Chem. C*, 2007, **111**, 10751–10757.
659 S. Link, A. Furube, M. B. Mohamed, T. Asahi, H. Masuhara and M. A. El-Sayed, Hot Electron Relaxation Dynamics of Gold Nanoparticles Embedded in $MgSO_4$ Powder Compared to Solution: The Effect of the Surrounding Medium, *J. Phys. Chem. B*, 2002, **106**, 945–955.
660 H. J. Shin, I.-W. Hwang, Y.-N. Hwang, D. Kim, S. H. Han, J.-S. Lee and G. Cho, Comparative Investigation of Energy Relaxation Dynamics of Gold Nanoparticles and Gold−Polypyrrole Encapsulated Nanoparticles, *J. Phys. Chem. B*, 2003, **107**, 4699–4704.
661 W. A. De Heer, The Physics of Simple Metal Clusters: Experimental Aspects and Simple Models, *Rev. Mod. Phys.*, 1993, **65**, 611–676.
662 J. Z. Zhang, Ultrafast Studies of Electron Dynamics in Semiconductor and Metal Colloidal Nanoparticles: Effects of Size and Surface, *Acc. Chem. Res.*, 1997, **30**, 423–429.
663 J. Butkus, P. Vashishtha, K. Chen, J. K. Gallaher, S. K. K. Prasad, D. Z. Metin, G. Laufersky, N. Gaston, J. E. Halpert and J. M. Hodgkiss, The Evolution of Quantum Confinement in $CsPbBr_3$ Perovskite Nanocrystals, *Chem. Mater.*, 2017, **29**, 3644–3652.
664 Y. Li, R. Lai, X. Luo, X. Liu, T. Ding, X. Lu and K. Wu, On the Absence of a Phonon Bottleneck in Strongly Confined $CsPbBr_3$ Perovskite Nanocrystals, *Chem. Sci.*, 2019, **10**, 5983–5989.
665 Y. Li, T. Ding, X. Luo, Y. Tian, X. Lu and K. Wu, Synthesis and Spectroscopy of Monodispersed, Quantum-Confined $FAPbBr_3$ Perovskite Nanocrystals, *Chem. Mater.*, 2019, **32**, 549–556.
666 B. T. Diroll and R. D. Schaller, Intraband Cooling in All-Inorganic and Hybrid Organic–Inorganic Perovskite Nanocrystals, *Adv. Funct. Mater.*, 2019, **29**, 1901725.
667 M. Cong, B. Yang, J. Chen, F. Hong, S. Yang, W. Deng and K. Han, Carrier Multiplication and Hot-Carrier Cooling Dynamics in Quantum-Confined CsPbI3 Perovskite Nanocrystals, *J. Phys. Chem. Lett.*, 2020, **11**, 1921–1926.
668 B. Yu, L. Chen, Z. Qu, C. Zhang, Z. Qin, X. Wang and M. Xiao, Size-Dependent Hot Carrier Dynamics in Perovskite Nanocrystals Revealed by Two-Dimensional Electronic Spectroscopy, *J. Phys. Chem. Lett.*, 2020, **12**, 238–244.
669 A. Furube, L. Du, K. Hara, R. Katoh and M. Tachiya, Ultrafast Plasmon-Induced Electron Transfer from Gold Nanodots into TiO_2 Nanoparticles, *J. Am. Chem. Soc.*, 2007, **129**, 14852–14853.
670 J. Cheng, Y. Li, M. Plissonneau, J. Li, J. Li, R. Chen, Z. Tang, L. Pautrot-d'Alençon, T. He, M. Tréguer-Delapierre and M.-H. Delville, Plasmon-Induced Hot Electron Transfer in AgNW@TiO_2@AuNPs Nanostructures, *Sci. Rep.*, 2018, **8**, 14136.
671 W. G. Delmas, E. T. Vickers, A. C. DiBenedetto, C. Lum, I. N. Hernandez, J. Z. Zhang and S. Ghosh, Modulating Charge Carrier Dynamics and Transfer via Surface Modifications in Organometallic Halide Perovskite Quantum Dots, *J. Phys. Chem. Lett.*, 2020, **11**, 7886–7892.
672 K. J. Schnitzenbaumer, T. Labrador and G. Dukovic, Impact of Chalcogenide Ligands on Excited State Dynamics in CdSe Quantum Dots, *J. Phys. Chem. C*, 2015, **119**, 13314–13324.
673 P. Guyot-Sionnest, B. Wehrenberg and D. Yu, Intraband Relaxation in CdSe Nanocrystals and the Strong Influence of the Surface Ligands, *J. Chem. Phys.*, 2005, **123**, 074709.
674 A. Pandey and P. Guyot-Sionnest, Slow Electron Cooling in Colloidal Quantum Dots, *Science*, 2008, **322**, 929–932.
675 M. D. Peterson, L. C. Cass, R. D. Harris, K. Edme, K. Sung and E. A. Weiss, The Role of Ligands in Determining the Exciton Relaxation Dynamics in Semiconductor Quantum Dots, *Annu. Rev. Phys. Chem.*, 2014, **65**, 317–339.
676 J. Huang, W. Guo, Y. Hu and W. D. Wei, Plasmonic Metal–Semiconductor Heterostructures for Hot-Electron-Driven Photochemistry, *MRS Bull.*, 2020, **45**, 37–42.
677 A. Yamakata, T.-A. Ishibashi and H. Onishi, Time-Resolved Infrared Absorption Spectroscopy of Photogenerated

Electrons in Platinized TiO_2 Particles, *Chem. Phys. Lett.*, 2001, **333**, 271–277.

678 L. Du, A. Furube, K. Yamamoto, K. Hara, R. Katoh and M. Tachiya, Plasmon-Induced Charge Separation and Recombination Dynamics in Gold–TiO_2 Nanoparticle Systems: Dependence on TiO_2 Particle Size, *J. Phys. Chem. C*, 2009, **113**, 6454–6462.

679 Q. Ding, Y. Shi, M. Chen, H. Li, X. Yang, Y. Qu, W. Liang and M. Sun, Ultrafast Dynamics of Plasmon-Exciton Interaction of Ag Nanowire- Graphene Hybrids for Surface Catalytic Reactions, *Sci. Rep.*, 2016, **6**, 32724.